



Thèse présentée pour obtenir le grade de
Docteur de l'Université Paris-Est

Spécialité : Mécanique

par

Samy MOKHTARI

Ecole Doctorale : Sciences, Ingénierie et Environnement

**A wavelet-based multi-scale and
homogenized modeling for pressure waves
propagation in congested media**

Une modélisation multi-échelles et homogénéisée par transformée en
ondelettes continue pour la propagation d'ondes de pression en milieu
congestionné

Thèse soutenue le 06/01/2021 devant le jury composé de :

Bruno TORRESANI	Professeur, Aix-Marseille Université	Président
Patrick FLANDRIN	Directeur de recherche, ENS Lyon	Rapporteur
Stéphane ETIENNE	Professeur, Polytechnique Montréal	Rapporteur
Stéphane PAGANO	Directeur de recherche, CNRS	Examineur
Isabelle RAMIERE	Ingénieur chercheur, CEA Cadarache	Examineur
Pierre ARGOUL	Professeur associé (HDR), ENPC, Paris	Directeur de thèse
Guillaume RICCIARDI	Expert senior (HDR), CEA Cadarache	Co-encadrant
Vincent FAUCHER	Expert senior (HDR), CEA Cadarache	Co-encadrant
Lucas ADELAÏDE	Chargé de recherche, UGE, Paris	Invité

Résumé

La simulation de l'écoulement d'un fluide au sein d'un milieu solide congestionné constitue encore aujourd'hui une problématique scientifique importante dans certains domaines de recherche, notamment l'ingénierie nucléaire. En effet, face à un nombre très important d'interfaces à gérer, les méthodes classiques d'interaction fluide-structure induiraient un coût de calcul prohibitif. Cette problématique des interfaces se cumule par ailleurs avec des phénomènes multi-échelles, qui trouvent leur origine dans l'écoulement fluide, ainsi que dans la micro-structure du milieu solide. Face à cette double problématique interfaces et multi-échelles, une approche milieu poreux ou homogénéisée peut être adoptée.

Dans cet esprit, cette thèse met en avant une modélisation multi-échelles et homogénéisée, en capacité de simuler un écoulement compressible non-visqueux au sein d'un milieu solide congestionné. Afin de s'affranchir des limitations rencontrées dans les méthodes multi-échelles et l'homogénéisation (stricte séparation d'échelles, périodicité, traitement des conditions aux limites, linéarité, équation de fermeture micro-macro...), cette nouvelle modélisation met en avant un formalisme mathématique basé sur la transformée en ondelettes continue. En appliquant, par le biais d'un produit de convolution, une ondelette bien choisie sur les équations aux dérivées partielles (EDP) gouvernant le milieu continu fluide, il est possible d'obtenir des EDPs filtrées décrivant un fluide homogénéisé. Le processus de convolution proposé est également applicable à des EDPs génériques. Par ailleurs, grâce à la transformée en ondelettes inverse, le modèle dispose d'une équation de fermeture analytique en capacité de relier les échelles résolues (i.e. le fluide homogénéisé) et non-résolues (i.e. le fluide réel). Cette relation de fermeture permet d'une part de transférer rigoureusement les conditions aux limites du fluide réel dans le fluide homogénéisé, et d'autre part de traiter explicitement les non-linéarités. Enfin, la résolution numérique des EDPs du fluide homogénéisé permet de reconstruire, à chaque pas de temps, le champ de pression au sein du fluide réel, et ainsi de déduire le chargement dynamique appliqué sur la micro-structure. Cette étape importante, validée sur des solutions numériques 2D de référence avec micro-structures fixes, ouvre ainsi la voie à un solveur fluide-structure intégrant le couplage entre les deux milieux.

Abstract

Computing a flow within a highly congested solid medium is still nowadays an important scientific issue in many research fields, such as nuclear engineering. Indeed, confronted with an overwhelming number of interfaces, the classical Fluid-Structure Interaction (FSI) approach would inevitably lead to cumbersome computations. This important issue of interfaces is also here coupled with multi-scale phenomena, caused both by the fluid and the solid medium micro-structure. In order to deal with these interfaces and multi-scale problematics, a more mesoscopic approach, based on porous media or homogenization, can be put forward.

In this spirit, this work develops a multi-scale and homogenized model able to account for an inviscid compressible flow within a congested solid medium. In order to bypass the classical limitations of multi-scale and homogenization methods (strict scale separation, periodicity, treatment of boundary conditions, linearity, closure equation between scales), this new model promotes an original use of Continuous Wavelet Transform. By applying, by means of a convolution product, a well-designed wavelet to the fluid Partial Differential Equations (PDEs), the model is able to derive spatially-filtered PDEs governing a homogenized fluid. This convolution process is also applicable to generic PDEs. Furthermore, thanks to an inverse wavelet transform, the model benefits from an analytical closure equation which connects resolved (i.e. the homogenized fluid) and unresolved (i.e. the real fluid) scales. This wavelet-based closure equation allows on the one hand, to rigorously transfer the real fluid boundary conditions into the homogenized fluid, and on the other hand to explicitly handle nonlinearities. Finally, the numerical computation of the homogenized fluid PDEs allows to reconstruct, at each time step, the pressure field in the real fluid, which leads to the dynamic load applied to the solid medium micro-structure. This important step, validated on 2D reference numerical solutions with steady micro-structures, thus opens the way to a coupled fluid-structure solver.

Remerciements

Je remercie tout d'abord les membres du jury pour leur participation, aussi bien en présentiel qu'en distanciel. Je remercie MM. Patrick FLANDRIN et Stéphane ETIENNE pour leurs rapports détaillés et commentaires constructifs, éléments indispensables à la préparation de ma soutenance et à l'amélioration du présent mémoire. Je remercie M. Bruno TORRESANI d'avoir volontiers accepté de présider mon jury de thèse. Son expertise sur les ondelettes a été un élément précieux durant la soutenance. Je remercie également M. Stéphane PAGANO et Mme Isabelle RAMIERE pour les remarques pertinentes soulevées lors de la soutenance.

Je tiens par la suite à remercier mon équipe encadrante. Mon directeur de thèse Pierre ARGOUL tout d'abord, qui m'a pris sous son aile dès mon arrivée à l'École des Ponts en 2013. Ses nombreux conseils, et les divers projets réalisés ensemble durant mon cursus, ont confirmé mon intérêt pour la Recherche. Je remercie également mes encadrants CEA, Guillaume RICCIARDI et Vincent FAUCHER, dont j'ai fait la connaissance dès 2016 en stage de césure. La qualité de cette première immersion au CEA, ainsi que leur écoute et expertise m'ont naturellement amené à poursuivre l'aventure avec eux en thèse. Enfin, je remercie Lucas ADELAÏDE, pour son encadrement, ses conseils, et sa grande disponibilité au quotidien durant mes travaux à l'Université Gustave Eiffel.

J'ai bien entendu une pensée toute particulière pour les équipes de mes deux laboratoires d'accueil. Le LTHC au CEA Cadarache tout d'abord, pour son accueil chaleureux dès 2016, et cette belle atmosphère de travail partagée pendant plusieurs années. Je remercie en particulier Maxime DUCOU et Kévin CRUZ pour leur aide précieuse lors de la conception de ma maquette expérimentale. Je remercie Jean PEYBERNES pour son écoute et ses conseils, aussi bien en tant que chef de laboratoire qu'en tant que professeur d'Aïkido au sein du dojo de Cadarache. Je remercie également Yves PHILIBERT pour son accueil chaleureux au sein du club de tennis de table de Saint-Julien. J'ai bien sûr une pensée pour tous mes collègues (ex-)doctorants (Roberto, Mathieu, Chunhui, Naz, Lorenzo, Benjamin, Louise...), et je n'oublie pas le super duo de secrétaires Gaëlle et Marie-Hélène, rouages indispensables au laboratoire. Sans compter tous les autres collègues que je ne pourrais citer dans ces quelques lignes. Je remercie également toute l'équipe du laboratoire EMGCU à l'Université Gustave Eiffel : Pierre, Renaud-Pierre, André, Franziska, Lucas, Minh, Boumediene, Véronique, Victor, Franck, Joël, Damien, Amandine, Silvia...Malgré une présence moins fréquente au sein du laboratoire, ils m'y ont chaleureusement accueilli, m'ont ouvert à des opportunités d'enseignements, m'ont conseillé sur l'après-thèse...Je les en remercie. J'adresse également toute ma gratitude à M. Vegard AUNE et aux techniciens du laboratoire CASA, pour leur accueil et expertise lors des essais à l'université NTNU de Trondheim.

Enfin, je tiens à remercier du fond du cœur mes parents, dont les conseils avisés et le soutien indéfectible ont fait de moi l'homme que je suis, et m'ont guidé jusqu'à ce jour. Et je ne pourrais conclure ces quelques lignes sans remercier ma Kathleen, qui m'accompagne de sa tendresse, de son amour et de son soutien depuis 4 belles années déjà.

Contents

1	Introduction	1
2	State of the art	4
2.1	Introduction	4
2.2	FSI and porous medium : the case of PWR	4
2.2.1	Solid medium modeling at the microscopic scale	6
2.2.2	Fluid modeling at the microscopic scale	8
2.2.3	Modeling at the mesoscopic scale	8
2.3	Homogenization in solid mechanics	11
2.3.1	Mechanical approach	11
2.3.2	Mathematical approach	13
2.4	Multi-scale methods	14
2.4.1	Filtering methods: Large Eddy Simulation	14
2.4.2	Projection-based methods: Variational Multi-Scale	18
2.5	1D Continuous Wavelet Transform	22
2.5.1	A middle ground between time and frequency	22
2.5.2	Analysing wavelet and CWT	23
2.5.3	Localization property	25
2.5.4	Complex analytic wavelets	26
2.5.5	Real and symmetric wavelets	30
2.5.6	Scaling function and low-frequency approximation	31
2.5.7	Inverse wavelet transform	33
2.5.8	CWT and redundancy	34
2.6	2D Continuous Wavelet Transform	35
2.6.1	Analysing wavelet and CWT	35
2.6.2	Complex wavelets: from analytic to directional wavelets	36
2.6.3	Real and isotropic wavelets and scaling functions	37
2.6.4	Inverse wavelet transform	39
2.7	1D Discrete Wavelet Transform and Multi-Resolution Analysis	40
2.8	Wavelets and boundary conditions	44
2.9	Wavelets, signal processing, operator analysis, and PDEs	45
2.10	Conclusion	46
3	A wavelet-based multi-scale and homogenized model	48
3.1	Introduction	48
3.2	Modeling at the microscopic scale	52

3.2.1	Solid medium	53
3.2.2	Fluid	54
3.3	Non-smooth behavior of the fluid PDEs	55
3.4	Wavelet-based homogenization	59
3.4.1	Initial conditions: Riemann problem	60
3.4.2	"Weak-extension" of the fluid PDEs to \mathbb{R}^2	60
3.4.3	"Weak-convolution" wavelets * extended fluid PDEs	70
3.5	Boundary conditions, closure between scales, and nonlinearities	81
3.5.1	Boundary conditions and closure between scales	81
3.5.2	Treatment of nonlinearities	84
3.6	Model convergence and accuracy criteria	85
3.6.1	Convergence towards DNS	86
3.6.2	Accuracy criteria	90
3.7	Analysing wavelet and scaling function	92
3.8	Summary of the model assumptions and equations	96
3.9	Numerical methods	98
3.9.1	Solid medium: Newmark method	99
3.9.2	Homogenized fluid: Godunov's method	100
3.9.3	Stability: explicit VS implicit filtering	103
3.9.4	Sampling, FFT, and aliasing	105
3.10	Conclusion	106
4	Model implementation and analysis	108
4.1	Introduction	108
4.2	Wavelet analysis of a 2D reference pressure wave	109
4.2.1	L^2 -accuracy	112
4.2.2	Force-wise accuracy	114
4.3	Direct computation of the fluid filtered PDEs	118
4.3.1	Preliminary analysis on stability and accuracy	118
4.3.2	2D pressure wave through a 10 x 10 array of disks	130
4.3.3	Equivalent modeling of a fuel assembly cross section	137
4.4	Ongoing works	141
4.4.1	First implementation of a nested grids algorithm	141
4.4.2	Towards a coupled fluid-structure solver	148
4.5	Conclusion	163
5	Conclusion	164
	List of appendices	176
A	Convolution product	177

List of Figures

1.1	Simplified 1D/3D scheme of a PWR in a LOCA context	1
1.2	Pressure wave propagating through a fuel assembly cross section	3
2.1	Cutaway of a French PWR core.	5
2.2	Fuel assemblies design: overview (2.2a) and spacer grid (2.2b).	5
2.3	Cutaway of the control domain around a fuel rod.	9
2.4	Philosophy of the porous medium modeling	9
3.1	Illustration of a 2D {fluid + solid} geometry.	53
3.2	Example of a test function for compactly-supported distributions	72
3.3	2D Mexican hat	93
3.4	2D scaling function	94
3.5	Approximation of the scaling function	95
3.6	Illustration of a 2D {fluid + solid} geometry.	96
4.1	Geometry of the first reference test case.	109
4.2	Reference pressure field snapshots	111
4.3	Reference horizontal pressure profile - 10×10 array	112
4.4	Pressure L^2 -energy recovered	114
4.5	Horizontal force applied to the solid obstacles	116
4.6	Horizontal pressure profiles - 10×10 array	117
4.7	Absolute error $ p_{ref} - p_{recons} $	118
4.8	Scheme of the preliminary test.	119
4.9	Visualization of the 2×2 array	120
4.10	Initial pressure field (10 vs 1 bar).	120
4.11	Reference VS reconstructed pressure fields (1/3)	121
4.12	Reference VS reconstructed pressure profiles (1/3)	122
4.13	Reference VS reconstructed pressure fields (2/3)	123
4.14	Reference VS reconstructed pressure profiles (2/3)	124
4.15	Reference VS reconstructed pressure fields (3/3)	125
4.16	Reference VS reconstructed pressure profiles (3/3)	125
4.17	Evolution of the horizontal force (1/2)	126
4.18	Evolution of the horizontal force (2/2)	127
4.19	Evolution of the relative error \tilde{e}_F (1/3)	128
4.20	Evolution of the relative error \tilde{e}_F (2/3)	129
4.21	Evolution of the relative error \tilde{e}_F (3/3)	129
4.22	2D pressure wave through a 10×10 steady array of disks. . . .	130

4.23	Visualization of the 10×10 array of disks.	131
4.24	Reconstructed VS reference pressure fields snapshots	132
4.25	Horizontal pressure profile - 10×10 array	133
4.26	L^2 -norm accuracy - 10×10 array	134
4.27	Force-wise accuracy - 10×10 array	136
4.28	FFT modulus of the horizontal force (N.m^{-1}) - 10×10 array .	137
4.29	Equivalent arrays of disks (2×2 , 4×4 , 10×10)	138
4.30	Reconstructed pressure field - equivalents arrays (4×4 , 2×2)	139
4.31	Horizontal force and its FFT modulus for equivalent arrays . .	140
4.32	Pressure fields - ref. VS model with multi-grid computations .	147
4.33	Horizontal force with multi-grid computations	147
4.34	Experimental setup	149
4.35	Tube bundle test specimen	150
4.36	Failure of the tube bundle test specimen	152
4.37	Shock wave impacting the test specimen	153
4.38	Visualization of the rods displacement	154
4.39	Solid medium longitudinal displacement	155
4.40	Initial pressure field - 2×2 moving array of disks	156
4.41	Visualization of the 2×2 moving array of disks at $t = 0$	156
4.42	Displacements U_x/U_y - 2×2 moving array	158
4.43	Horizontal pressure profile - 2×2 moving array	161
4.44	Initial and maximum positions of the 2×2 moving array . . .	162

List of Tables

2.1	Analysing wavelet time-frequency support.	26
3.1	Filtering properties of the Mexican hat wavelet (1/2)	93
3.2	Filtering properties of the Mexican hat wavelet (2/2)	93
3.3	Filtering properties of the scaling function	95
3.4	Scaling function cutoff values	96
3.5	Stability - cutoff scale VS mesh size	105
3.6	Mesh sampling properties.	105
3.7	Aliasing - cutoff scale VS mesh size	106
4.1	Geometry - 1st test case.	110
4.2	Pressure loading - 1st test case.	110
4.3	Fluid parameters - 1st test case.	110
4.4	Cutoff scale of the Mexican hat wavelet - 1st test case.	113
4.5	Cutoff scales and number of wavelet coefficients - 1st test case.	117
4.6	Geometry - 2nd test case.	119
4.7	Pressure loading - 2nd test case.	119
4.8	Fluid parameters - 2nd test case.	119
4.9	Spatial and time discretization - 2nd test case.	119
4.10	Geometry - 3rd test case.	130
4.11	Pressure loading - 3rd test case.	130
4.12	Fluid parameters - 3rd test case.	130
4.13	Spatial and time discretization - 3rd test case.	131
4.14	Relative errors on the force and pressure field L^2 -norm.	135
4.15	Relative error on the horizontal force for equivalent arrays.	141
4.16	Relative error on the horizontal force - multi-grid computations.	148
4.17	Test matrix for the experimental setup	151
4.18	Geometry - 2×2 moving array of disks.	156
4.19	Pressure loading - 2×2 moving array of disks.	156
4.20	Fluid parameters - 2×2 moving array of disks.	157
4.21	Solid medium parameters - 2×2 moving array of disks.	157
4.22	Spatial and time discretization - 2×2 moving array of disks.	157

Nomenclature

Ω : open subset of \mathbb{R}^d , $d \in \{1, 2, 3\}$

$L^p(\Omega) = \{f : \Omega \mapsto \mathbb{R} \text{ measurable, } \int_{\Omega} |f|^p < +\infty\}$, $1 \leq p < +\infty$

$L^\infty(\Omega) = \{f : \Omega \mapsto \mathbb{R} \text{ measurable, } \exists M \geq 0, |f| \leq M \text{ almost everywhere}\}$

$L_0^2(\Omega) = \{f \in L^2(\Omega), \int_{\Omega} f = 0\}$

$L_{loc}^1(\Omega)$: Lebesgue space of functions integrable on any compact set $K \subset \Omega$

$L_{loc}^\infty(\Omega)$: Lebesgue space of functions bounded on any compact set of $K \subset \Omega$

$H^1(\Omega) = \{f \in L^2(\Omega), \nabla f \in L^2(\Omega)\}$: Sobolev space

$H^{-1}(\Omega)$: Sobolev space of linear forms on H^1

$\mathcal{V}(\Omega) = [H^1(\Omega)]^3$

$\mathcal{V}'(\Omega) = [H^{-1}(\Omega)]^3$

$D(\mathbb{R}^d) = \{\varphi : \mathbb{R}^d \mapsto \mathbb{R}, C^\infty \text{ with compact support}\}$: space of test functions

$D'(\mathbb{R}^d)$: space of distributions on \mathbb{R}^d

$\mathcal{E}'(\mathbb{R}^d)$: space of distributions with compact support in \mathbb{R}^d

$\langle T, \varphi \rangle_{D', D}$ denotes the action of a distribution $T \in D'(\mathbb{R}^d)$ on $\varphi \in D(\mathbb{R}^d)$

$\text{supp}(f)$ denotes the support of a function or distribution f

List of abbreviations

PWR	Pressurized Water Reactor
LOCA	Loss Of Cooling Accident
FSI	Fluid-Structure Interaction
CWT	Continuous Wavelet Transform
DWT	Discrete Wavelet Transform
PDE	Partial Differential Equation
LES	Large Eddy Simulation
DNS	Direct Numerical Simulation
RVE	Representative Volume Element
RANS	Reynolds Averaged Navier-Stokes
VMS	Variational Multi-Scale
MRA	Multi-Resolution Analysis
FFT	Fast Fourier Transform
CFL	Courant-Friedrichs-Lewy
SSTF	Simlab Shock Tube Facility

Chapter 1

Introduction

The current work finds its starting point in the study of the mechanical consequences of accidental scenarios for Pressurized Water Reactors (PWR), with a focus on the propagation of transverse pressure waves through the fuel assemblies of a nuclear core. Such a phenomenon, called Loss Of Cooling Accident (LOCA), originates from a failure in one of the pipes of the pressurized primary loop (155 bar). An initial plane pressure wave then propagates from the failure towards the main vessel (see Figure 1.1), and is expected to undergo some diffraction at the junction between the 1D pipe and the 3D core. The first mechanical solicitation on the fuel assemblies (see Figure 2.1-2.2) located within the main vessel would then come from the transverse propagation of a (spherical) pressure wave, followed by a second vertical wave guided by the axial water flow.

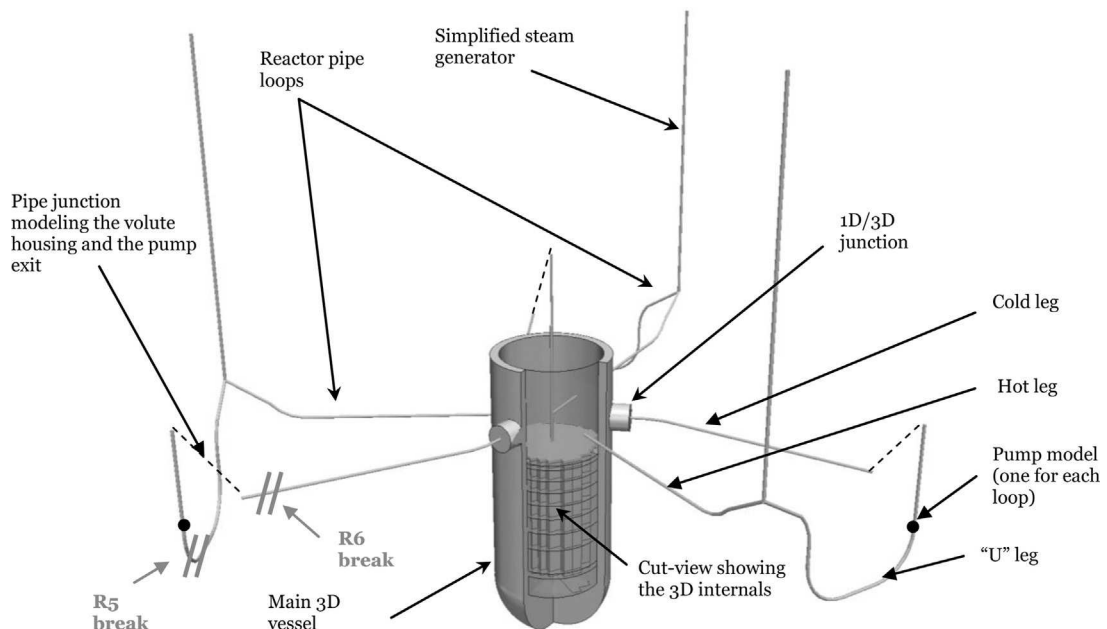


Figure 1.1: Simplified 1D/3D scheme of a PWR in a Loss Of Cooling Accident (LOCA) context - reproduced from [Faucher et al., 2014] with permission.

The physics of interest thus requires to compute a compressible flow within a highly congested solid medium, here the fuel assemblies. Such a computation is still nowadays an important scientific issue in many industrial or research fields. It can for instance also relate to flows within biological tissues, or porous media such as concrete or soil. Confronted with an overwhelming number of interfaces, the classical Fluid-Structure Interaction (FSI) approach, which relies on an explicit representation of all the interfaces, would inevitably lead to cumbersome computations. This important issue of interfaces is also here coupled with multi-scale phenomena: a wide range of spatial scales is for instance contained within a viscous turbulent flow, possibly entangled with the different spatial scales of the congested solid medium. Thus, in order to tackle both the interface and multi-scale problematics, a more mesoscopic approach of FSI can be put forward, inspired by porous media or homogenization theory.

In this spirit, a multi-scale and homogenized modeling is hereafter introduced to account for an inviscid compressible flow within a congested solid medium. In order to build a self-sustained model, bypassing the classical limitations of multi-scale and homogenization methods (strict scale separation, periodicity, treatment of boundary conditions, linearity, closure equation between scales), this work promotes an original use of Continuous Wavelet Transform (CWT). By applying, by means of a convolution product, a well-designed wavelet (or scaling function) to the fluid Partial Differential Equations (PDEs), the model results in spatially-filtered PDEs governing a homogenized fluid in the whole {fluid + solid} domain. Such a convolution process is also applicable to generic PDEs. Furthermore, thanks to an inverse wavelet transform, the model is able to connect analytically resolved (i.e. the homogenized fluid) and unresolved (i.e. the real fluid) scales. This wavelet-based closure equation allows on the one hand, to rigorously transfer the real fluid boundary conditions into the homogenized fluid, and on the other hand to explicitly handle nonlinearities. The numerical computation of the homogenized fluid PDEs then allows to reconstruct, at each time step, the pressure field in the real fluid, which leads to the dynamic load applied to the solid medium.

In this work, the choice has been made to focus the homogenization process on the fluid, as it occupies a connected domain in the geometry of interest. Furthermore, CWT is hereafter applied in a 2D formalism. This work indeed focuses on the propagation of transverse pressure waves through the cross section of fuel assemblies, as displayed in Figure 1.2.

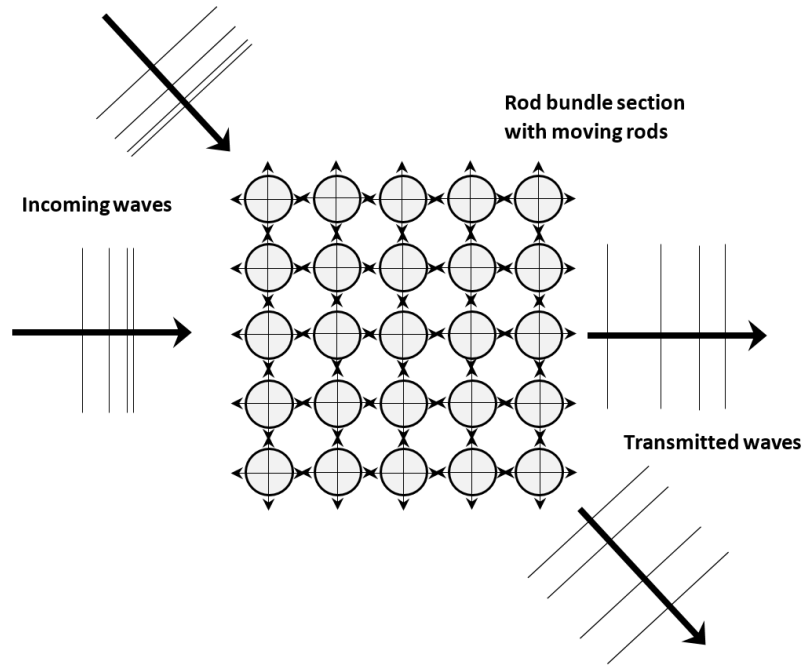


Figure 1.2: Sketch of a 2D transverse pressure wave propagating through a fuel assembly cross section.

The following of this manuscript is organized as follows: chapter 2 is dedicated to an overview of a wide state of the art, starting with porous media approaches, homogenization and multi-scale methods. The core of this bibliography chapter then focuses on wavelets theory. This will allow to connect to chapter 3, which will then thoroughly describe the wavelet-based multi-scale and homogenized modeling. The model capabilities are then assessed in chapter 4, with numerical experiments involving 2D shock waves propagating through different steady solid obstacles. These tests are then supplemented with some ongoing projects: on the one hand, preliminary experimental data acquired on a tube bundle specimen within a shock tube facility, and on the other hand, a first numerical test handling moving solid obstacles. The final chapter is then dedicated to a conclusion.

Chapter 2

Overview of the state of the art

2.1 Introduction

This chapter aims at setting the basis for the wavelet-based model at the core of this work, which comes as a new contribution in an already extensive state of the art. This overview will thus emphasize some of the key methods in the literature of porous media, homogenization and multi-scale methods, with a final and major focus on wavelets. This chapter hereafter emphasizes "analytical" (as opposed to numerical) methods, i.e. methods acting at the continuum medium scale, on Partial Differential Equations (PDEs), and mostly independent from any choice of discretization technique.

The opening section of this chapter presents a porous medium approach designed to compute Fluid-Structure Interaction (FSI) phenomena, in the framework of Pressurized Water Reactors (PWR). It will be followed by the classical literature on homogenization, with its mechanical and mathematical approaches. The third section will then present two important examples of multi-scale methods in the framework of turbulent flows, namely explicit filtering and projection-based methods. This literature on homogenization and multi-scale methods being recalled, the core of this chapter will then be dedicated to wavelets theory, with a first and main focus on Continuous Wavelet Transform (CWT), with its 1D and 2D implementation. The framework of Discrete Wavelet Transform and Multi-Resolution Analysis (MRA) will then follow.

Throughout this chapter, it will be emphasized how homogenization and multi-scale methods struggle with common limitations, among which the treatment of boundary conditions, and the closure equation between resolved and unresolved scales. This will allow to highlight, especially in chapter 3, how Continuous Wavelet Transform (CWT) may tackle these important issues.

2.2 FSI and porous medium : the case of PWR

The interaction between a fluid and a highly congested solid medium, at the core of this work, finds a perfect illustration with the behavior of a French

Pressurized Water Reactor (PWR). As can be seen in Figure 2.1, a PWR core contains numerous fuel assemblies (up to 157 for a 900 MW reactor) submitted to the water flow of the primary loop. These assemblies exhibit a beam-like geometry, with a square cross section ($20\text{ cm}^2 \times 4\text{ m}$). Their inner structure is composed of 264 fuel rods (5 mm radius), 5 instrumentation guide thimbles, and 24 control rod guide thimbles (Figure 2.2a). The latter bring stiffness and cohesion to the structure thanks to 8 spacer grids (Figure 2.2b) placed along the assembly. They can also host the falling control rods (Figure 2.1) in case of an emergency core stop. The design of spacer grids allows to increase turbulence within the water flow, which transports the heat, created by the nuclear fission reaction, towards the steam generators. Under nominal operating conditions, the water flow is mainly vertical when it runs through the fuel assemblies. Water is maintained liquid at around 300°C thanks to a 155 bar pressurization of the primary loop.

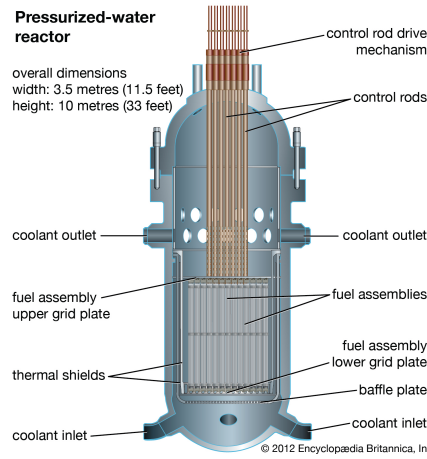


Figure 2.1: Cutaway of a French PWR core.

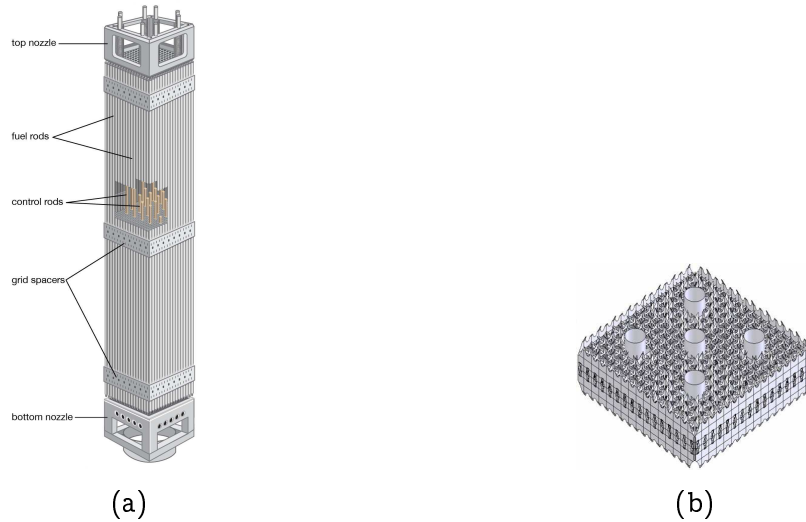


Figure 2.2: Fuel assemblies design: overview (2.2a) and spacer grid (2.2b).

Before introducing the porous medium approach developed to handle FSI phenomena within a PWR, let us first recall the classical approach, where both media are modeled at the microscopic scale, with a continuum medium point of view.

2.2.1 Solid medium modeling at the microscopic scale

In a PWR core, the solid medium occupies a disconnected domain, resulting from the reunion of disjoint fuel assemblies. Neglecting body forces, each fuel assembly satisfies, with a 3D continuum medium modeling, the following momentum balance equation and dynamic boundary condition on the current domain $\Omega_s(t)$:

$$\begin{aligned} \rho_s \underline{\gamma} &= \underline{div}(\underline{\sigma_s}) && \text{in } \Omega_s(t) \\ \underline{\sigma_s} \cdot \underline{n_s} &= \underline{T}_{F \rightarrow S} + \underline{T}_{impact} && \text{on } \partial\Omega_s(t), \end{aligned} \quad (2.1)$$

with:

- ρ_s the solid medium density (kg.m^{-3});
- $\underline{\gamma}$ the Eulerian acceleration (m.s^{-2});
- $\underline{\sigma_s}$ the Cauchy stress tensor (Pa);
- $\underline{T}_{F \rightarrow S}$ the stresses applied by the fluid on the interface $\partial\Omega_s$ (Pa);
- \underline{T}_{impact} the stresses resulting from impacts with other fuel assemblies (Pa);
- $\underline{n_s}$ the outward unit normal vector on the boundary $\partial\Omega_s$.

The Eulerian acceleration $\underline{\gamma}(\underline{x}, t)$ for $\underline{x} \in \Omega_s(t)$ is linked to the Lagrangian acceleration $\underline{\Gamma}(\underline{X}, t)$ for $\underline{X} \in \Omega_s(0)$ via the following equations:

$$\forall t \geq 0, \underline{\gamma}(\underline{x}, t) = \underline{\gamma}(\underline{\varphi}(\underline{X}, t), t), \quad (2.2)$$

$$= \underline{\Gamma}(\underline{X}, t), \quad (2.3)$$

$$= \frac{\partial^2 \underline{U}}{\partial t^2}(\underline{X}, t), \quad (2.4)$$

where:

- $\underline{\varphi}(\cdot, t) : \underline{X} \mapsto \underline{\varphi}(\underline{X}, t) = \underline{x}$ describes the transformation undergone by the reference domain $\Omega_s(0)$;
- $\underline{U}(\underline{X}, t) = \underline{\varphi}(\underline{X}, t) - \underline{X}$ denotes the displacement field.

To solve the problem (2.1), a closure equation between $\underline{\underline{\sigma}}_s$ and the displacement \underline{U} is required. This closure is brought by the mechanical behavior law, which formally writes:

$$\underline{\underline{\sigma}}_s = \underline{\underline{\sigma}}_s(\underline{\underline{e}}(\underline{U})), \quad (2.5)$$

where $\underline{\underline{e}}(\underline{U})$ denotes Green-Lagrange strain tensor, defined by:

$$\underline{\underline{e}}(\underline{U}) = \frac{1}{2} (\underline{\underline{\nabla}} \underline{U} + {}^T \underline{\underline{\nabla}} \underline{U} + {}^T \underline{\underline{\nabla}} \underline{U} \cdot \underline{\underline{\nabla}} \underline{U}). \quad (2.6)$$

The variational formulation associated to the problem (2.1) is known as the Virtual Powers Principle. Given a kinematically admissible and smooth Eulerian velocity field $\underline{\tilde{v}}$, one can integrate the momentum balance equation against $\underline{\tilde{v}}$. Using Green's formula for integration by parts, it comes:

$$\int_{\Omega_s(t)} \rho_s \underline{\underline{\gamma}} \cdot \underline{\tilde{v}} = - \int_{\Omega_s(t)} \underline{\underline{\sigma}}_s : \underline{\underline{\nabla}} \underline{\tilde{v}} + \int_{\partial\Omega_s(t)} (\underline{\underline{\sigma}}_s \cdot \underline{n}_s) \cdot \underline{\tilde{v}}. \quad (2.7)$$

Now, introducing the virtual strain rate tensor $\underline{\underline{d}}(\underline{\tilde{v}}) = \frac{1}{2} (\underline{\underline{\nabla}} \underline{\tilde{v}} + {}^T \underline{\underline{\nabla}} \underline{\tilde{v}})$, and using the symmetry of the Cauchy stress tensor, one can write:

$$\int_{\Omega_s(t)} \rho_s \underline{\underline{\gamma}} \cdot \underline{\tilde{v}} + \int_{\Omega_s(t)} \underline{\underline{\sigma}}_s : \underline{\underline{d}}(\underline{\tilde{v}}) = \int_{\partial\Omega_s(t)} (\underline{T}_{F \rightarrow S} + \underline{T}_{impact}) \cdot \underline{\tilde{v}}. \quad (2.8)$$

The two terms on the left-hand side represent respectively the virtual powers of inertial and internal forces. As for the term on the right-hand side, it represents the virtual power of the external forces applied to the solid medium, here contact forces applied by the fluid and other fuel assemblies.

Such a modeling of the solid medium at the microscopic scale quickly encounters some limitations in the current context. Indeed, as it can be seen in Figure 2.2, fuel assemblies exhibit a complex design, with multiple contacts and friction between inner components, especially within spacer grids. Such a design results in damping and nonlinearities in their mechanical behavior. Modeling all these phenomena at the microscopic scale would be too cumbersome, considering the number of fuel rods and fuel assemblies contained within a PWR core. Thus, beam models are often preferred to describe the solid medium kinematics and mechanical law. In [Ricciardi et al., 2009], a Timoshenko beam model is chosen, motivated by the low shear modulus of fuel assemblies. The local damping and nonlinearities are then taken into account by a global nonlinear visco-elastic behavior of the beam.

In the current work, the choice has been made to focus the homogenized modeling on the fluid, as it occupies a connected domain within the PWR core. The reader may thus refer to [Fontaine and Politopoulos, 2000], [Pisapia et al., 2003] and [Ricciardi et al., 2009, Ricciardi, 2016] for further details on the solid medium modeling.

2.2.2 Fluid modeling at the microscopic scale

Let us now consider the water flow within a PWR core. It is, under nominal operating conditions, almost vertical, incompressible and very turbulent, with a Reynolds number around 10^5 . Such a flow is governed by Navier-Stokes equations:

$$\begin{cases} \rho [\partial_t \underline{v} + \underline{div}(\underline{v} \otimes \underline{v})] &= \eta \Delta \underline{v} - \underline{\nabla} p + \underline{f}, \\ \underline{div}(\underline{v}) &= 0, \end{cases} \quad (2.9)$$

where ρ denotes the fluid density (kg.m^{-3}), \underline{v} its velocity (m.s^{-1}), η the dynamic viscosity ($\text{Pl} = \text{Pa.s}$), p the pressure (Pa), and \underline{f} a body force per unit of volume. These equations translate respectively the conservation of the fluid momentum and mass. They are completed with a no-slip kinematic boundary condition:

$$\underline{v} - \partial_t \underline{U} = \underline{0} \quad \text{on } \partial\Omega_f(t) \cap \partial\Omega_s(t). \quad (2.10)$$

As it will be detailed later in this chapter, in the section dedicated to turbulence and Large Eddy Simulation (LES), the Direct Numerical Simulation (DNS) of a viscous incompressible and turbulent flow (i.e. the direct computation of Navier-Stokes equations) quickly becomes too cumbersome. Indeed, the number of degrees of freedom necessary to catch all the spatial scales contained within the flow increases as a power law of the Reynolds number. Therefore, as the solid medium, the fluid also requires a more mesoscopic modeling.

2.2.3 Modeling at the mesoscopic scale

As it was just highlighted, a mesoscopic modeling is relevant for both the fluid and the congested solid medium in order to discard the smallest spatial scales. Furthermore, the classical Fluid-Structure Interaction (FSI) approach, which can be found in [Faucher and Kokh, 2013, Faucher et al., 2014] or [Etienne and Pelletier, 2012, Yu et al., 2016, Yu et al., 2018], is here confronted with an overwhelming number of interfaces. As a consequence, a homogenized approach of FSI shall be designed to tackle the interaction between the two media. Inspired by works on multiphase flows [Banerjee and Chan, 1980], [Delhay et al., 1993], solid-fluid mixtures [Terada et al., 1998], [Robbe and Bliard, 2002], or Large Eddy Simulation [Barsamian and Hassan, 1997], porous media models were put forward for nuclear in-core structures. Such an approach has been implemented in [Ricciardi et al., 2009, Ricciardi and Boccaccio, 2015, Ricciardi, 2016] for the study of a PWR core dynamics in response to a seismic transient. In such a context, the fluid forces acting on structures come from the incompressible, turbulent, and mostly axial flow through the assemblies. Taking advantage of the quasi-periodicity of the inner components of a PWR core, this porous medium approach relies on:

- the definition of a control domain Ω_c around each fuel rod, in the spirit of a Representative Volume Element (RVE):

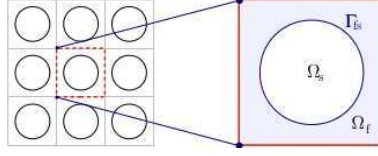


Figure 2.3: Cutaway of the control domain around a fuel rod.

- the definition of equivalent fluid and solid media (see Figure 2.4) by means of a volume averaging of their original PDEs over the control domain:

$$f_{eq} = \frac{1}{|\Omega_c|} \int_{\Omega_c} f \, dV. \quad (2.11)$$

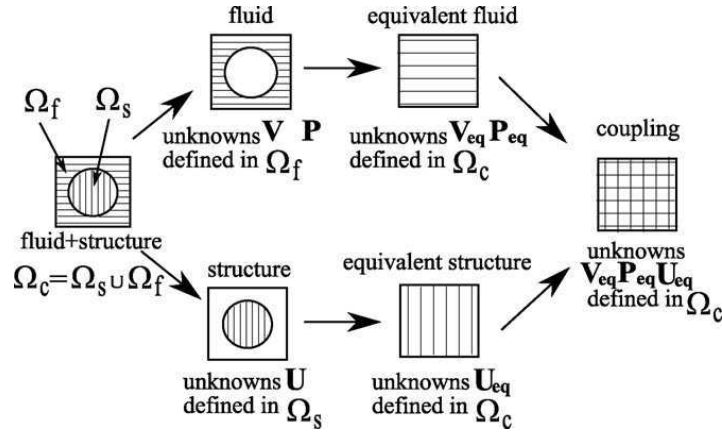


Figure 2.4: Philosophy of the porous medium modeling - reproduced from [Ricciardi et al., 2009] with permission.

The volume averaging operator defined by (2.11) is applied directly onto the PDEs (2.1) and (2.9) governing the two media at the microscopic scale. It allows to derive spatially-filtered PDEs governing the equivalent fluid and solid media. In the process, it transforms contact forces between the two media, defined only on the interfaces, into body forces between their equivalent counterparts. In a second step, the filtered PDEs governing the equivalent solid medium are reduced into a Timoshenko beam model, as described earlier.

It is important to highlight that the original contact forces between the two media depend on the original fluid velocity and pressure fields, and on the original solid medium displacement, which are no longer solved either by the spatially-filtered fluid or solid equations. In order to solve the porous medium problem, a closure expression is thus required to connect unresolved and resolved scales. This expression shall allow to define the body force interaction between the equivalent fluid and solid media as a function depending only on the equivalent fields:

$$\underline{F}_{\mathbf{F} \rightarrow \mathbf{S}} := \underline{F}(\underline{v}, p, \underline{U}), \quad (2.12)$$

$$= \underline{F}^{eq}(\underline{v}_{eq}, p_{eq}, \underline{U}_{eq}). \quad (2.13)$$

As no analytical expression is available to define the functional \underline{F}^{eq} in equation (2.13), an *ad hoc* closure model has to be implemented. In [Ricciardi et al., 2009, Ricciardi, 2016], an empirical model based on the works of [Taylor, 1952], [Lighthill, 1960, Lighthill, 1986] and [Païdoussis, 1966, Païdoussis, 1969, Païdoussis, 2006] is chosen to represent the forces applied by a viscous incompressible turbulent flow to a single cylinder rod. In a similar way, an *ad hoc* contact model is also needed for the new body force describing impacts between fuel assemblies.

Beside these first closure expressions, another one is also required to properly model turbulence effects. Indeed, as it will be detailed later when discussing Large Eddy Simulation (LES), the volume averaging of the nonlinear convective term $\text{div}(\underline{v} \otimes \underline{v})$ requires to define the impact of the fluctuating component of the velocity onto its filtered component. This closure expression is classically defined by means of an *ad hoc* turbulence model (see [Lesieur, 2008]).

Beside this major issue of closure expressions between resolved and unresolved scales, such a porous medium approach also faces, like any other homogenization and multi-scale methods, an important issue with the treatment of boundary conditions. Indeed, in order for the spatially-filtered PDEs to remain local equations, the control domain $\Omega_c(\underline{x})$ shall be defined around each point \underline{x} of the total domain $\Omega_f \cup \Omega_s$. As a result, when \underline{x} is located in the vicinity of the boundary $\partial(\Omega_f \cup \Omega_s)$, the control domain $\Omega_c(\underline{x})$ overlaps the complementary domain $\mathbb{R}^3 \setminus (\Omega_f \cup \Omega_s)$. This fact requires to extend the initial fields to the whole space \mathbb{R}^3 , and thus raises the question on how to properly define the boundary conditions on the equivalent (filtered) fields. It is usually assumed in literature that the filtered fields share the same boundary conditions than the original ones.

Finally, it shall be highlighted that such a porous medium or homogenized modeling for FSI has for now only been applied in the case of a viscous incompressible and turbulent flow. To the author's knowledge, no such work exists for the case of a compressible flow and a fast transient pressure wave interacting with a highly congested solid medium. In the PWR framework, the interaction between a rarefaction wave originating from a pipe break and the core dynamics is for now studied under some strong simplifications, like in [Faucher et al., 2014], where fuel assemblies are considered as an equivalent acoustic impedance, responsible for the global pressure drop through the core. In such a case, where viscosity and turbulence effects can be neglected considering the time scale of interest, the proper evaluation of the loading exerted by the fluid to the solid medium requires to represent pressure gradients within the flow, at the suitable scale, and especially through the cross-section of fuel assemblies. In order to better take into account the local geometric details of the solid medium (without explicitly meshing all interfaces) and their impact

on the propagation of pressure waves, a homogenized and multi-scale model shall also be developed for this new physics of interest. This new model shall be able to deal with the major issues highlighted in the porous medium approach, and further detailed in the following sections dedicated to homogenization and multi-scale methods.

2.3 Homogenization in solid mechanics

The keyword homogenization is usually linked to the study of heterogeneous materials in solid mechanics. The following subsections are dedicated to the two classical approaches of homogenization, namely mechanical and mathematical.

2.3.1 Mechanical approach

The mechanical approach of homogenization was originally developed in the framework of linear elasticity. Confronted with a heterogeneous material, the first step consists in the identification, if possible, of a Representative Volume Element (RVE). This volume V shall be large compared to the material microscopic heterogeneities, and small compared to the material size, in order to allow for spatial averages on the RVE to be considered as local quantities for the material. This RVE being set, the macroscopic and homogenized stiffness (fourth-order) tensor $\underline{\underline{\mathbb{C}}}^{hom}$ can be defined, from its microscopic counterpart $\underline{\underline{\mathbb{C}}}$, as follows:

$$\langle \underline{\underline{\sigma}} \rangle_V = \left\langle \underline{\underline{\mathbb{C}}} : \underline{\underline{\epsilon}} \right\rangle_V, \quad (2.14)$$

$$= \underline{\underline{\mathbb{C}}}^{hom} : \langle \underline{\underline{\epsilon}} \rangle_V, \quad (2.15)$$

where $\langle \underline{\underline{\sigma}} \rangle_V$ and $\langle \underline{\underline{\epsilon}} \rangle_V$ denote the RVE-volume averages of respectively the Cauchy stress tensor and the linearized strain tensor:

$$\langle f \rangle_V = \frac{1}{V} \int_V f \, dV. \quad (2.16)$$

In order to estimate the macroscopic stiffness tensor, boundary conditions have to be defined on the RVE. Following the work of [Hill, 1963], it is known that for uniform stresses ($\underline{\underline{\sigma}}(x) \cdot \underline{\underline{n}} = \underline{\underline{\Sigma}} \cdot \underline{\underline{n}}$) or linear displacements ($\underline{\underline{\xi}}(\underline{\underline{x}}) = \underline{\underline{E}} \cdot \underline{\underline{x}}$) imposed on the RVE boundary, one has $\langle \underline{\underline{\epsilon}} \rangle_V = \underline{\underline{E}}$. Moreover, these specific boundary conditions also allow to estimate bounds on the macroscopic stiffness tensor for any other type of boundary condition, as proved by [Nemat-Nasser and Hori, 1993].

Beside this issue of boundary conditions, a closure equation is also required between the macroscopic (homogenized) stiffness tensor $\underline{\underline{\mathbb{C}}}^{hom}$ and its microscopic counterpart $\underline{\underline{\mathbb{C}}}$. This closure relies on the introduction of a fourth-order concentration tensor $\underline{\underline{\mathbb{A}}}$, defined by:

$$\forall \underline{x} \in V, \underline{\underline{\epsilon}}(\underline{x}) = \underline{\underline{\mathbb{A}}}(\underline{x}) : \langle \underline{\underline{\epsilon}} \rangle_V. \quad (2.17)$$

The pioneering work of [Eshelby, 1959] brought theoretical results, known as Eshelby's tensor, to determine this concentration tensor, in the framework of an elliptic inclusion embedded in an infinite linear elastic and homogeneous medium. This early result has then been generalized in [Tanaka and Mori, 1972] to any general domain Ω contained within two larger and embedded elliptic domains ($\Omega \subset \mathcal{E}_1 \subset \mathcal{E}_2$).

To bypass the strong assumptions required for the computation of the concentration tensor $\underline{\underline{\mathbb{A}}}$, variational approaches have been proposed in literature [Hashin and Shtrikman, 1963, Willis, 1981], to determine, in a different way, the homogenized properties of a material. Following the principle of minimum potential energy, the RVE elastic energy density is defined as:

$$\widetilde{W}(\underline{\underline{\epsilon}}) = \min_{\underline{\underline{\epsilon}} \in K} \frac{1}{V} \int_V W(\underline{x}, \underline{\underline{\epsilon}}) \, d\underline{x}, \quad (2.18)$$

where K is the set of kinematically admissible displacements, and $W(\underline{x}, \underline{\underline{\epsilon}})$ the microscopic elastic energy density of the heterogeneous material. The homogenized stress tensor $\underline{\underline{\mathbb{C}}}^{hom}$ is then defined by:

$$\widetilde{W}(\underline{\underline{\epsilon}}) = \frac{1}{2} \underline{\underline{\epsilon}} : \underline{\underline{\mathbb{C}}}^{hom} : \underline{\underline{\epsilon}}. \quad (2.19)$$

However, as the minimization problem (2.18) cannot be easily solved, a reference homogeneous medium is introduced to estimate a lower bound on $\widetilde{W}(\underline{\underline{\epsilon}})$. This reference material is chosen so as to satisfy a linear elastic behavior, with an additional second-order tensor, known as polarization tensor. This tensor, usually assumed uniform on each phase of the heterogeneous material of interest, is then tuned so as to maximise a lower bound on $\widetilde{W}(\underline{\underline{\epsilon}})$. This variational approach in linear elasticity has then been extended to nonlinear elastic composites [Willis, 1981, Ponte Castañeda, 1991, Ponte Castañeda and Suquet, 1998]. A few years later, a somehow similar variational method has been proposed to deal with nonlinear inelastic composites [Miehe, 2002], where the micro-structure inelastic behavior is handled with an incremental variational formulation on the potential associated to microscopic stresses.

All these works, here included in a mechanical approach of homogenization, share some strong limitations. Indeed, they often rely on strong assumptions regarding the heterogeneities geometry, and require a clear scale separation between the RVE size and the material size. They also face issues with the treatment of boundary conditions (periodicity or infinite medium assumption), explained by the fact that once again a RVE-volume averaging operator does not allow to properly define homogenized fields in the vicinity of the domain

boundary. Finally, this mechanical approach of homogenization is mostly restricted to solid materials, and highly dependent on the mechanical behavior law. This is a major drawback to its extension to other types of physics.

2.3.2 Mathematical approach

In parallel with this mechanical literature, mathematicians have also extensively studied the field of homogenization, with the objective to bring some theoretical foundations to the approximation of a heterogeneous material by an equivalent homogeneous one. The mathematical approach of homogenization deals with phenomena governed by linear elliptic equations (linear elasticity, stationary heat equation, Poisson equation for the electrical potential...), or diffusion processes, with mostly periodically oscillating coefficients. For instance, let Ω be a periodic and bounded open set in \mathbb{R}^n . Let us denote ϵ its period, which is assumed small compared to the size of the domain. Let \underline{A} be a bounded and positive definite second-order tensor. A linear elliptic problem writes, with Dirichlet boundary conditions:

$$\begin{cases} -\operatorname{div} \left(\underline{A} \left(\frac{\underline{x}}{\epsilon} \right) \nabla u_\epsilon \right) &= f & \text{in } \Omega \\ u_\epsilon &= 0 & \text{on } \partial\Omega \end{cases} \quad (2.20)$$

where u_ϵ is the unknown, and f is a source term, usually assumed in $L^2(\Omega)$ to ensure the well-posedness of the problem.

The mathematical approach of homogenization [Bensoussan et al., 1978, Sanchez-Palencia, 1980], often referred to as asymptotic or periodic homogenization, corresponds to the study of the limit of the problem (2.20) as the parameter ϵ tends towards zero. The homogenized problem associated to (2.20) can heuristically be obtained by assuming the following two-scale asymptotic expansion (*ansatz*):

$$u_\epsilon(\underline{x}) = \sum_{i=0}^{+\infty} \epsilon^i u_i \left(\underline{x}, \frac{\underline{x}}{\epsilon} \right), \quad (2.21)$$

where the functions $(\underline{x}, \underline{y}) \mapsto u_i(\underline{x}, \underline{y})$ are assumed smooth and periodic in \underline{y} . Thanks to the linearity of the problem (2.20), this expansion can be used to obtain a series of equations on the new unknowns u_i . The homogenized problem then corresponds to the equation satisfied by u_0 , which can be shown to only depend on the variable \underline{x} :

$$\begin{cases} -\operatorname{div} \left(\underline{A}^* \nabla u_0(\underline{x}) \right) &= f & \text{in } \Omega \\ u_0 &= 0 & \text{on } \partial\Omega \end{cases} \quad (2.22)$$

where \underline{A}^* now denotes the homogenized (and uniform) second-order tensor.

The use of the two-scale expansion (2.21) is supported by theoretical results on the convergence of the unknown u_ϵ as ϵ tends towards zero, known as the oscillating test function method (or energy method) [Tartar, 1979] and the two-scale convergence method [Allaire, 1992]. It is noticeable that this

asymptotic homogenization, while mostly used for periodic materials, can also be extended to the non-periodic case with the notion of G or H -convergence [De Giorgi and Spagnolo, 1973, Murat and Tartar, 1997]. However, the derivation of the homogenized problem is not as straightforward as in the periodic case.

Finally, it shall be highlighted that, despite their apparent differences, the mechanical and mathematical approaches of homogenization do share some common limitations. Indeed, the second one also faces issues with the treatment of boundary conditions, as the periodicity assumption does not stand anymore in the vicinity of the domain boundary. It is for instance well-known that asymptotic expansions are not suited for the proper representation of boundary layers phenomena. Furthermore, the mathematical approach is also highly dependent on a strong scale separation assumption, as the parameter ϵ measuring the ratio between the smaller and larger spatial scales shall tends towards zero. Besides, asymptotic homogenization is mostly applicable to periodic geometries and linear problems. Linearity is indeed required in order to inject the two-scale expansion (2.21) in the problem equation (2.20).

These two major approaches of homogenization being now described, it can be highlighted that, while not always classified within the same literature, the theory of homogenization can be embedded in the wide framework of multi-scale methods. Indeed, homogenization aims at smoothing the microscopic behavior of a material, i.e. the unresolved scales, in order to compute only the macroscopic (low-frequency) behavior, i.e. the resolved scales. And like any multi-scale method, a closure equation is required to describe the interaction between unresolved and resolved scales (cf. the concentration tensor previously described for instance). The following section is thus dedicated to some key examples of multi-scale methods.

2.4 Multi-scale methods

Among the wide family of "analytical" (as opposed to numerical) multi-scale methods, two different but somehow similar approaches will hereafter be highlighted, in the framework of turbulent flows: on the one hand (explicit) filtering methods, such as Large Eddy Simulation, and on the other hand projection-based methods, which are based on a direct-sum decomposition between a "coarse-component" space and a "fine-component" space, such as the Variational Multi-Scale (VMS) method. The framework of Discrete Wavelet Transform and Multi-Resolution Analysis (MRA), which shares similarities with the VMS method, will be discussed in the sections dedicated to wavelets.

2.4.1 Filtering methods: Large Eddy Simulation

To start with explicit filtering methods and Large Eddy Simulation, let us first recall that Newtonian viscous and incompressible fluids are governed by Navier-Stokes equations:

$$\begin{cases} \rho [\partial_t \underline{v} + \underline{div}(\underline{v} \otimes \underline{v})] &= \eta \Delta \underline{v} - \nabla p, \\ \underline{div}(\underline{v}) &= 0. \end{cases} \quad (2.23)$$

Within a viscous incompressible flow, turbulence can be witnessed when the convective component of the flow ($\rho \underline{div}(\underline{v} \otimes \underline{v})$), which is responsible for kinetic energy transport, becomes significantly more important than the viscous component ($\eta \Delta \underline{v}$), which is responsible for kinetic energy dissipation. This competition between nonlinear convection and viscous dissipation is measured by the (dimensionless) Reynolds number:

$$R_e \sim \frac{\|\rho \underline{div}(\underline{v} \otimes \underline{v})\|}{\|\eta \Delta \underline{v}\|}. \quad (2.24)$$

More precisely, if V denotes the characteristic velocity of the flow, L its characteristic length, and $\nu = \frac{\eta}{\rho}$ the fluid kinematic viscosity ($\text{m}^2 \cdot \text{s}^{-1}$), the Reynolds number can be expressed as:

$$R_e = \frac{VL}{\nu}. \quad (2.25)$$

When the Reynolds number satisfies $R_e \lesssim 2000$, diffusion dominates convection, and the flow regime is laminar. When the Reynolds number increases beyond this critical value, the flow progressively becomes turbulent, showing increasing mixing property and coherent structures such as eddies. These eddies possess a wide range of spatial scales, from the characteristic length of the flow L down to the Kolmogorov scale, defined by $LR_e^{-\frac{9}{4}}$ in 3D. Thus, the number of degrees of freedom necessary to catch all the spatial scales contained in a viscous turbulent flow increases as a power law of the Reynolds number.

To cope with the numerical limitation of DNS, multi-scale methods have been developed to compute turbulent flows at less expensive cost. The Reynolds Averaged Navier-Stokes (RANS) method and Large Eddy Simulation (LES) are the most widely used techniques in literature. The first one is based on a time averaging operator which allows to separate the mean and fluctuating components of the flow. Under a stationarity assumption, the ergodic theorem ensures that ensemble, time and spatial averaging are equivalent. As for LES, it relies on a spatial filtering or averaging operator, which allows to separate large and small scales. The scales larger than the filter cutoff length are resolved, while the impact of smaller scales is modeled, and thus requires a closure equation. Given a filter G_δ , where $\delta > 0$ denotes the cutoff length, the filtered component \bar{v} of a field v is defined by the following convolution product:

$$\bar{v}(\underline{x}, t) = \int_{\mathbb{R}^d} G_\delta(\underline{x} - \underline{y}) v(\underline{y}, t) d\underline{y}, \quad (2.26)$$

$$= (G_\delta * v)(\underline{x}, t). \quad (2.27)$$

The filter G_δ can for instance be a box or Gaussian filter in physical space, or a sharp filter in spectral space. The fluctuation v' of the field v is then defined so as to satisfy the following decomposition:

$$v = \bar{v} + v'. \quad (2.28)$$

In turbulence literature [Lesieur, 2008], it is generally assumed that the spatial filtering operator commutes with all time and spatial derivatives. Thus, by applying this operator on Navier-Stokes equations (2.23), one obtains the following filtered momentum balance equation:

$$\forall i \in \{1, 2, 3\}, \rho \left[\frac{\partial \bar{v}_i}{\partial t} + \frac{\partial (\bar{v}_i \bar{v}_j)}{\partial x_j} \right] = -\frac{\partial \bar{p}}{\partial x_i} + \frac{\partial}{\partial x_j} [\eta (\partial_j \bar{v}_i + \partial_i \bar{v}_j) + \rho T_{ij}], \quad (2.29)$$

where $\underline{T} = (T_{ij})_{i,j}$ is called subgrid-scale tensor, and is defined by:

$$T_{ij} = \bar{v}_i \bar{v}_j - \overline{v_i v_j}. \quad (2.30)$$

This additional term results from the application of the filter on the non-linear convective term $\underline{v} \otimes \underline{v}$. Equation (2.29) now drives only the spatial scales larger than δ , i.e. the resolved scales. In order to highlight the impact of smaller scales on this equation, and thus the need of a closure equation between resolved and unresolved scales, the subgrid-scale tensor can be rewritten as follows (see [Lesieur, 2008]):

$$T_{ij} = \bar{v}_i \bar{v}_j - \overline{(\bar{v}_i + v'_i)(\bar{v}_j + v'_j)}, \quad (2.31)$$

$$= (\bar{v}_i \bar{v}_j - \overline{\bar{v}_i \bar{v}_j}) - (\overline{\bar{v}_i v'_j} + \overline{v'_i \bar{v}_j}) - \overline{v'_i v'_j}, \quad (2.32)$$

$$= L_{ij} + C_{ij} + R_{ij}. \quad (2.33)$$

Thus, beside the classical Reynolds-stress term $R_{ij} = -\overline{v'_i v'_j}$, two additional terms appear in the subgrid-scale tensor compared to the RANS method. This is explained by the fact that, conversely to time or ensemble averaging, the spatial filtering operator is not idempotent, that is to say:

$$\bar{\bar{v}} \neq \bar{v}. \quad (2.34)$$

The first term L_{ij} in equation (2.33), called Leonard's term, depends only on the velocity filtered component. However, the cross-term C_{ij} and Reynolds-stress term R_{ij} both exhibit the velocity fluctuating component, i.e. the unresolved scales. In order to solve the filtered equation (2.29), it is thus necessary to add a closure equation, as in the theory of homogenization. As no analytical expression is available to connect unresolved and resolved scales, an *ad hoc* model has to be implemented. One of the first and most famous closure model is Smagorinsky eddy-viscosity model [Smagorinsky, 1963], in which an artificial

turbulent viscosity is introduced to account for the energy dissipation in the subgrid scales. In this model, the deviatoric component of the subgrid-scale tensor is evaluated via the following equations:

$$T_{ij} = -2\nu_t \bar{S}_{ij} + \frac{1}{3} \text{tr}(\underline{T}) \delta_{ij}, \quad (2.35)$$

$$\bar{S}_{ij} = \frac{1}{2} (\partial_{x_j} \bar{v}_i + \partial_{x_i} \bar{v}_j), \quad (2.36)$$

where the eddy-viscosity ν_t is defined according to a mixing-length assumption:

$$\nu_t = (C_s \Delta x)^2 |\bar{S}|, \quad (2.37)$$

$$= (C_s \Delta x)^2 \sqrt{2 \bar{S}_{ij} \bar{S}_{ij}}, \quad (2.38)$$

where Δx is the characteristic length of the subgrid scale, and $\Delta x |\bar{S}|$ can be considered as a turbulent velocity. The parameter C_s can be tuned depending on the case at study. A commonly used value is $C_s = 0.1$. The closure equation being now defined, the spatially-filtered Navier-Stokes equations (2.29) can then be computed.

Nevertheless, despite its common use, LES, like any other multi-scale or homogenization method, is still facing some important issues, among which the treatment of boundary conditions. Indeed, the classical assumption of commutation between the spatial filtering operator and spatial derivatives in the PDEs does not stand for bounded flows. Moreover, convolution product is not properly defined on a bounded domain either. The use of a convolution product requires to extend the original fields to the whole space \mathbb{R}^d . Furthermore, the spatial filtering process brings the original system boundary conditions within the newly extended and filtered problem. The only way to avoid this phenomenon is to decrease the filter cutoff length towards zero near the domain boundaries. This option, however, significantly changes the derivation process of the filtered equations, as the commutation assumption does not stand either with a filter with varying cutoff length. The interested reader may refer to the works of [Ghosal and Moin, 1995, Fureby and Tabor, 1997, Vasilyev et al., 1998, Dunca et al., 2003, Berselli et al., 2006, Leonard et al., 2007] for further details on this topic.

Beside this important issue on boundary conditions, LES is also limited by its need of a turbulence model to close the filtered equations and connect resolved and unresolved scales. This closure model has a huge impact on the LES results, especially around obstacles or near the flow boundaries. Such an *ad hoc* model is here mandatory because a plain spatial filtering technique does not offer an inverse formula able to reconstruct, from the filtered component, the original field. It will be detailed later in this manuscript that, conversely, Continuous Wavelet Transform (CWT) does offer such a reconstruction formula.

To conclude this subsection dedicated to filtering methods, it shall be highlighted that their use has recently spread in homogenization for solid mechanics as well [Yvonnet and Bonnet, 2014, Tognevi et al., 2016]. To the author's knowledge, such works are still limited to linear problems. Furthermore, similar challenges are encountered with boundary conditions, and their consequences on the definition of a closure equation (concentration tensor) between resolved and unresolved scales.

Let us now turn towards another major approach in multi-scale modeling, that is to say projection-based methods.

2.4.2 Projection-based methods: Variational Multi-Scale

Beside filtering methods, turbulence literature has also seen the development of projection-based methods, such as the Variational Multi-Scale method (VMS), which has been put forward as an alternative to LES for the simulation of turbulent flows [Hughes et al., 1998, Hughes et al., 2000, Hughes et al., 2001, Bazilevs et al., 2007]. In a will to bypass some of the limitations of spatial filtering operators (non-commutation with spatial derivatives for bounded flows, treatment of boundary conditions), and the need of a closure model between resolved and unresolved scales (e.g. eddy-viscosity models), VMS promotes the use of a linear projection operator. The starting point is thus the direct-sum decomposition of a linear subspace \mathcal{V} (e.g. a Hilbert space) into a coarse-scale (finite-dimensional) subspace $\overline{\mathcal{V}}$ and a fine-scale (infinite-dimensional) subspace \mathcal{V}' :

$$\mathcal{V} = \overline{\mathcal{V}} \oplus \mathcal{V}'. \quad (2.39)$$

The coarse scale component of a field $f \in \mathcal{V}$ is then defined by:

$$\overline{f} = \mathbb{P}_{\overline{\mathcal{V}}} f, \quad (2.40)$$

where $\mathbb{P}_{\overline{\mathcal{V}}}$ denotes the projection on $\overline{\mathcal{V}}$. It can for instance be the L^2 or H^1 -orthogonal projection.

Remark 2.4.1 *While the use of such a projection operator is intended to replace the filtering operator used in LES, it could be argued that a plain averaging of a T -periodic signal $f \in L^2[0, T]$ is nothing else than a L^2 -orthogonal projection on the linear subspace spanned by the vector $\{t \mapsto e_k(t) = e^{i\frac{2k\pi t}{T}}\}$, for $k = 0$. Indeed, given the Hermitian inner product on $L^2[0, T]$:*

$$\langle f, g \rangle_{L^2} = \frac{1}{T} \int_0^T \overline{f(t)} g(t) dt, \quad (2.41)$$

the family $(e_k)_{k \in \mathbb{Z}}$ clearly constitutes an orthonormal basis for $L^2[0, T]$. The L^2 -orthogonal projection of f on $\overline{\mathcal{V}} = \text{Vect}\{e_0\}$ is thus given by:

$$\mathbb{P}_{\underline{V}} f = \frac{\langle e_0, f \rangle_{L^2}}{\|e_0\|_{L^2}^2} \cdot e_0 \quad (2.42)$$

$$= \left(\frac{1}{T} \int_0^T \overline{e_0(t)} f(t) dt \right) e_0 \quad (2.43)$$

$$= \left(\frac{1}{T} \int_0^T f(t) dt \right) e_0 \quad (2.44)$$

Thus, the plain averaging operator can also be seen as a projection operator. In a similar way, filtering a signal by cutting off all frequencies beyond a value ω_c can be seen as a L^2 -orthogonal projection on $\text{Vect}\{(e_k)_{-k_c \leq k \leq k_c}\}$, with $\frac{2\pi}{T}k_c \leq \omega_c$. To further highlight this link between linear projection and filtering, it is noticeable that in [Koobus and Farhat, 2004], which extends the use of VMS to compressible turbulence on unstructured meshes, a cell agglomeration method and a plain spatial averaging are used to define the coarse-scale components, rather than a projection operator.

This remark on linear projection and filtering being stated, VMS relies on the decomposition of the problem variational formulation into coarse-scale and fine-scale variational formulations. Starting with Navier-Stokes problem on a domain $\Omega \subset \mathbb{R}^d$, with Dirichlet boundary conditions for the velocity:

$$\begin{cases} \rho(\partial_t \underline{v} + (\underline{v} \cdot \nabla) \underline{v}) &= -\nabla p + \eta \Delta \underline{v} + \underline{f} & \text{in } \Omega, \\ \text{div}(\underline{v}) &= 0 & \text{in } \Omega, \\ \underline{v} &= \underline{0} & \text{on } \partial\Omega, \end{cases} \quad (2.45)$$

the variational formulation writes:

for $f \in V^*(\Omega)$, find $(\underline{v}, p) \in V(\Omega) \times Q(\Omega)$ such that, $\forall (\underline{w}, q) \in V(\Omega) \times Q(\Omega)$:

$$\begin{aligned} -\rho \left(\underline{v}, \frac{\partial \underline{w}}{\partial t} \right)_{L^2} + \eta \int_{\Omega} \underline{\nabla} \underline{v} : \underline{\nabla} \underline{w} + \rho \int_{\Omega} ((\underline{v} \cdot \nabla) \underline{v}) \cdot \underline{w} - \int_{\Omega} p \text{div}(\underline{w}) \\ = \langle \underline{f}, \underline{w} \rangle_{V^*, V}, \end{aligned} \quad (2.46)$$

$$\int_{\Omega} \text{div}(\underline{v}) q = 0, \quad (2.47)$$

where $V(\Omega) = [H_0^1(\Omega)]^d$ is a Sobolev space, $V^*(\Omega)$ is the dual space of $V(\Omega)$, and $Q(\Omega) = L_0^2(\Omega)$. If one introduces the following linear, bilinear and trilinear forms:

$$\begin{aligned} L : \quad & V \longmapsto \mathbb{R} \\ & \underline{w} \longmapsto \langle \underline{f}, \underline{w} \rangle_{V^*, V}, \end{aligned} \quad (2.48)$$

$$a : \begin{array}{ccc} V \times V & \longmapsto & \mathbb{R} \\ (\underline{v}, \underline{w}) & \longmapsto & \eta \int_{\Omega} \underline{\nabla} \underline{v} : \underline{\nabla} \underline{w}, \end{array} \quad (2.49)$$

$$b : \begin{array}{ccc} V \times Q & \longmapsto & \mathbb{R} \\ (\underline{v}, q) & \longmapsto & - \int_{\Omega} q \operatorname{div}(\underline{v}), \end{array} \quad (2.50)$$

$$c : \begin{array}{ccc} V \times V \times V & \longmapsto & \mathbb{R} \\ (\underline{v}, \underline{w}, \underline{z}) & \longmapsto & \rho \int_{\Omega} [(\underline{v} \cdot \underline{\nabla}) \underline{w}] \cdot \underline{z}, \end{array} \quad (2.51)$$

then the variational formulation (2.46-2.47) can be rewritten as:

$$\begin{cases} -\rho (\underline{v}, \partial_t \underline{w})_{L^2} + a(\underline{v}, \underline{w}) + b(\underline{w}, p) + c(\underline{v}, \underline{v}, \underline{w}) & = L(\underline{w}), \\ b(\underline{v}, q) & = 0. \end{cases} \quad (2.52)$$

Following [Bazilevs et al., 2007], the coarse and fine scale equations are then obtained by injecting the decomposition of \underline{v} and p into (2.52):

$$\begin{aligned} & -(\bar{\underline{v}} + \underline{v}', \partial_t (\bar{\underline{w}} + \underline{w}'))_{L^2} + a(\bar{\underline{v}} + \underline{v}', \bar{\underline{w}} + \underline{w}') \\ & \quad + b(\bar{\underline{w}} + \underline{w}', \bar{p} + p') + c(\bar{\underline{v}} + \underline{v}', \bar{\underline{v}} + \underline{v}', \bar{\underline{w}} + \underline{w}') \\ & \quad = L(\bar{\underline{w}} + \underline{w}'), \end{aligned} \quad (2.53)$$

$$b(\bar{\underline{v}} + \underline{v}', \bar{q} + q') = 0. \quad (2.54)$$

Thanks to the direct-sum $\mathcal{V} = \bar{\mathcal{V}} \oplus \mathcal{V}'$, equation (2.53) gives rise to the following coarse-scale and fine-scale equations:

$$\begin{aligned} & -(\bar{\underline{v}} + \underline{v}', \partial_t \bar{\underline{w}})_{L^2} + a(\bar{\underline{v}} + \underline{v}', \bar{\underline{w}}) + b(\bar{\underline{w}}, \bar{p} + p') + c(\bar{\underline{v}} + \underline{v}', \bar{\underline{v}} + \underline{v}', \bar{\underline{w}}) \\ & \quad = L(\bar{\underline{w}}), \end{aligned} \quad (2.55)$$

$$\begin{aligned} & -(\underline{v}', \partial_t \underline{w}')_{L^2} + a(\underline{v}', \underline{w}') + b(\underline{w}', \bar{p} + p') + c(\underline{v}' + \bar{\underline{v}}, \underline{v}' + \bar{\underline{v}}, \underline{w}') \\ & \quad = L(\underline{w}'), \end{aligned} \quad (2.56)$$

The fine scale equation (2.56) can be rewritten as:

$$\begin{aligned} & -(\underline{v}', \partial_t \underline{w}')_{L^2} + a(\underline{v}', \underline{w}') + b(\underline{w}', p') + c(\underline{v}', \underline{v}', \underline{w}') + c(\bar{\underline{v}}, \underline{v}', \underline{w}') + c(\underline{v}', \bar{\underline{v}}, \underline{w}') \\ & \quad = L(\underline{w}') + (\bar{\underline{v}}, \partial_t \underline{w}')_{L^2} - a(\bar{\underline{v}}, \underline{w}') - b(\underline{w}', \bar{p}) - c(\bar{\underline{v}}, \bar{\underline{v}}, \underline{w}'), \\ & \quad = \langle \underline{w}', f - \rho \partial_t \bar{\underline{v}} + \eta \Delta \bar{\underline{v}} - \underline{\nabla} \bar{p} - \rho [\bar{\underline{v}} \cdot \underline{\nabla}] \bar{\underline{v}} \rangle_{V^*, V}. \end{aligned} \quad (2.57)$$

Following [Bazilevs et al., 2007], the term in the right-hand side of equation (2.57) $(f - \rho \partial_t \underline{u} + \eta \Delta \underline{u} - \nabla \cdot \underline{p} - \rho [\underline{u} \cdot \nabla] \underline{u})$ can be seen as the residual $Res(\underline{u}, \underline{p})$ obtained when the coarse-scale components are used to approximate the solution of Navier-Stokes equations (2.45). Thus, the fine-scale equation (2.57) theoretically allows to estimate the fine-scale components $(\underline{u}', \underline{p}')$ in terms of the coarse-scale components $(\underline{u}, \underline{p})$ and the residual $Res(\underline{u}, \underline{p})$:

$$(\underline{u}', \underline{p}') = F'[(\underline{u}, \underline{p}), Res(\underline{u}, \underline{p})]. \quad (2.58)$$

Equation (2.58) is exactly the (formal) closure equation that allows to solve the coarse-scale equation (2.55). In LES literature, this closure is brought by a turbulence model, such as Smagorinsky eddy-viscosity model. Conversely, VMS philosophy is rather to approximate the closure functional F' . To this end, it is assumed in [Bazilevs et al., 2007] that, when the residual is small, a perturbation series can be used to approximate F' :

$$X' = \sum_{k=1}^{+\infty} \epsilon^k X'_k, \quad (2.59)$$

where $X' = (\underline{u}', \underline{p}')$, $X = (\underline{u}, \underline{p})$ and $\epsilon = \|Res(X)\|_{V^*}$.

However, as stated in [Bazilevs et al., 2007], a rigorous justification of the convergence of this perturbation series is still, to the author's knowledge, lacking. Furthermore, when used in the fine-scale equation (2.57), this series results in a cascade of linear problems, whose solutions require the introduction of a fine-scale Green's operator, which itself depends on the classical Green's operator, via the projection operator \mathbb{P}_V . The computation of this fine-scale Green's operator brings additional difficulties and approximations, which, to the author's knowledge, still need to be dealt with.

Beside this key issue of closure between resolved and unresolved scales, it shall also be highlighted that the treatment of boundary conditions is, once again, raising some questions. Indeed, periodic boundary conditions are partially used in [Hughes et al., 2001, Bazilevs et al., 2007], with an enforcement of the no-slip condition on the coarse-scale component. In [Hughes et al., 1998], it is rather assumed in the theory of VMS that the velocity coarse-scale component \underline{u} shares the same boundary conditions as the original velocity \underline{u} . This assumption can be questioned as a boundary is by essence a high-frequency phenomenon. Furthermore, one can expect the coarse-scale component not to be able to faithfully represent the boundary layer in the vicinity of an obstacle, or to take into account a boundary rugosity and a logarithmic velocity profile for instance.

To conclude this section on the VMS method, it can be highlighted that a similar philosophy using a projection-based partitioning between coarse-scale and fine-scale components has also been applied in the solid mechanics community, for the study of heterogeneous structures [Ladevèze et al., 2001, Ladevèze and Nouy, 2003, Ladevèze, 2004].

This wide state of the art on porous media, homogenization and multi-scale methods being now recalled, it is high time to tackle the core of this

chapter, that is to say wavelets literature. The following sections will thus summarize some of the key concepts about wavelets theory. The focus will be mainly put on Continuous Wavelet Transform (CWT), with its 1D and 2D implementation. The framework of 1D Discrete Wavelet Transform and Multi-Resolution Analysis (MRA) will then follow to complete the picture.

2.5 1D Continuous Wavelet Transform

Wavelets theory stands at the crossing of multiple research areas, such as signal and image processing, harmonic analysis, mathematical physics... While early works from the 1930's were already trying to develop new techniques to cope with the drawbacks of Fourier transform, wavelets theory, in its current form and denomination, can be tied back to the 1980's. Indeed, the first orthogonal wavelets were introduced by [Strömberg, 1981]. Independently, the theoretical physics community of Marseille (France) introduced and studied the concept of Continuous Wavelet Transform (CWT), via the reference works of [Grossmann and Morlet, 1984, Grossmann et al., 1985] and [Torrésani, 1992, Gonnet and Torrésani, 1994, Torrésani, 1995, Torrésani, 1998]. In parallel with these works, new orthogonal wavelets were put forward by [Lemarié and Meyer, 1986], followed by the framework of Multi-Resolution Analysis (MRA) [Mallat, 1989a, Mallat, 1989b, Mallat, 1989c], and the work of [Daubechies, 1988], who defined the first smooth and compactly-supported wavelets. For a brief history of wavelets theory and a wide overview of its developments and applications, especially in the field of MRA, the reader may refer to [Jawerth and Sweldens, 1994]. The interested reader may also find further information on general mathematical tools for time-frequency analysis in the reference works of [Martin and Flandrin, 1985, Flandrin, 1989, Flandrin, 1999, Flandrin, 2018].

To begin this overview of wavelets theory, the focus is here first put on 1D Continuous Wavelet Transform (CWT).

2.5.1 A middle ground between time and frequency

Following [Flandrin, 2005], one can motivate the introduction of wavelets by highlighting the need to find a middle ground between:

- on the one hand, the time representation of a signal f , which formally writes:

$$\forall t_0 \in \mathbb{R}, f(t_0) = \int_{\mathbb{R}} \delta_{t_0}(t) f(t) dt, \quad (2.60)$$

where $\delta_{t_0}(t) = \delta(t - t_0)$ denotes Dirac distribution;

- on the other hand, the frequency representation $\{\mathcal{F}[f](\omega)\}_{\omega \in \mathbb{R}}$, which allows to formally write:

$$\forall t_0 \in \mathbb{R}, f(t_0) = \frac{1}{2\pi} \int_{\mathbb{R}} \mathcal{F}[f](\omega) e^{it_0\omega} d\omega, \quad (2.61)$$

where $\mathcal{F}[f]$ denotes the Fourier transform of a signal f , defined by:

$$\mathcal{F}[f](\omega) = \int_{\mathbb{R}} f(t) e^{-i\omega t} dt. \quad (2.62)$$

The time representation $\{f(t_0)\}_{t_0 \in \mathbb{R}}$ thus consists in a linear decomposition of the signal $f(t)$ on the individual atoms $\{\delta_{t_0}\}_{t_0 \in \mathbb{R}}$, while the frequency representation $\{\mathcal{F}[f](\omega)\}_{\omega \in \mathbb{R}}$ consists in a linear decomposition on the atoms $\{\omega \mapsto e^{it_0\omega}\}_{t_0 \in \mathbb{R}}$. As a result, the time (respectively frequency) representation exhibits a perfect localization in the time (respectively frequency) domain.

2.5.2 Analysing wavelet and CWT

In order to bridge the gap between these two representations, and cope with the poor localization of Fourier transform in the time domain, the idea of Continuous Wavelet Transform (CWT) is to switch the atoms $\{\omega \mapsto e^{it_0\omega}\}_{t_0 \in \mathbb{R}}$ for a new type of functions, called wavelets, which exhibit good localization properties both in the physical and spectral spaces. In order to be able to study numerous time instants (or positions), and numerous frequencies, these wavelets are built by dilations and translations from an original wavelet, called analysing wavelet. The linear decomposition of a signal f on these wavelets thus results in a well-localized transform, called Continuous Wavelet Transform (CWT), which is now able to study a signal frequency spectrum around local time instants or positions. The mathematical definition of 1D CWT is detailed below.

Definition 2.5.1 *1D Continuous Wavelet Transform* (see [Torr sani, 1995, Mallat, 2008])

Assume $\Psi \in L^1(\mathbb{R}) \cap L^2(\mathbb{R})$, with real or complex values, and satisfying the following zero-average condition:

$$\int_{\mathbb{R}} \Psi(t) dt = 0, \quad (2.63)$$

or equivalently:

$$\mathcal{F}[\Psi](0) = 0. \quad (2.64)$$

In the following, it is also assumed that the function Ψ is L^2 -normalized in the time domain:

$$\|\Psi\|_{L^2(\mathbb{R})} = 1. \quad (2.65)$$

Such a function Ψ is called an analysing wavelet. The above requirements ensure that Ψ will exhibit good localization properties in both the physical and spectral spaces. From this original atom, one can build a family of dilated and translated atoms $\{t \mapsto \frac{1}{\sqrt{s}}\Psi\left(\frac{t-u}{s}\right)\}_{s>0, u \in \mathbb{R}}$, where s is a scale parameter, and u a translation parameter.

The Continuous Wavelet Transform (CWT) of a finite-energy signal $f \in L^2(\mathbb{R})$ is then defined as the linear decomposition of f on the complex-conjugates of these atoms (i.e. a L^2 -inner product), that is to say:

$$\forall s > 0, u \in \mathbb{R},$$

$$\boxed{\mathcal{W}[f](s, u) = \frac{1}{\sqrt{s}} \int_{\mathbb{R}} f(t) \Psi\left(\frac{t-u}{s}\right)^* dt.} \quad (2.66)$$

The (complex) number $\mathcal{W}[f](s, u)$ is called wavelet coefficient. It is here evaluated for a given scale $s > 0$ and a time instant $u \in \mathbb{R}$. If one now introduces the notations $\Psi_s(t) = \frac{1}{\sqrt{s}}\Psi\left(\frac{t}{s}\right)$, and $\tilde{\Psi}(t) = \Psi(-t)$, the above definition (2.66) can be rewritten as a convolution product:

$$\boxed{\mathcal{W}[f](s, u) = (f * \tilde{\Psi}_s^*)(u),} \quad (2.67)$$

or equivalently, in the frequency domain, as:

$$\boxed{\mathcal{F}[\mathcal{W}[f](s, \cdot)](\omega) = \mathcal{F}[f](\omega) \times \mathcal{F}[\tilde{\Psi}_s^*](\omega),} \quad (2.68)$$

$$= \mathcal{F}[f](\omega) \times \sqrt{s} \mathcal{F}[\Psi](s\omega)^*. \quad (2.69)$$

To complete this definition of 1D CWT, a few remarks shall be stated:

Remark 2.5.1 • the definition (2.66), where one can notice the scaling factor $\frac{1}{\sqrt{s}}$, is referred to as an "energy formulation" of CWT; the use of a scaling factor $\frac{1}{s}$, referred to as an "amplitude formulation", can also be found in literature. These formulations preserve respectively the wavelets energy (L^2 norm) and amplitude (L^1 norm), as detailed below:

$$\left\| \frac{1}{\sqrt{s}} \Psi\left(\frac{\cdot}{s}\right) \right\|_{L^2(\mathbb{R})}^2 = \int_{\mathbb{R}} \left| \frac{1}{\sqrt{s}} \Psi\left(\frac{t}{s}\right) \right|^2 dt, \quad (2.70)$$

$$= \frac{1}{s} \int_{\mathbb{R}} |\Psi(\tau)|^2 s d\tau, \quad (2.71)$$

$$= \|\Psi\|_{L^2(\mathbb{R})}^2. \quad (2.72)$$

$$\left\| \frac{1}{s} \Psi \left(\frac{\cdot}{s} \right) \right\|_{L^1(\mathbb{R})} = \int_{\mathbb{R}} \frac{1}{s} \left| \Psi \left(\frac{t}{s} \right) \right| dt, \quad (2.73)$$

$$= \frac{1}{s} \int_{\mathbb{R}} |\Psi(\tau)| s d\tau, \quad (2.74)$$

$$= \|\Psi\|_{L^1(\mathbb{R})}. \quad (2.75)$$

- *to justify the well-posedness of equation (2.69), one can put forward Young's inequality, which ensures that, given a finite-energy signal $f \in L^2(\mathbb{R})$ and a wavelet $\Psi \in L^1(\mathbb{R}) \cap L^2(\mathbb{R})$, the function defined by $u \mapsto \mathcal{W}[f](s, u) = (f * \tilde{\Psi}_s^*)(u)$ belongs to $L^2(\mathbb{R}) \cap L^\infty(\mathbb{R})$. Thus, it indeed admits a Fourier transform.*
- *thanks to the wavelet zero-average condition (2.63), one can also define the CWT of a constant signal, which does not belong in $L^2(\mathbb{R})$.*

These definition and remarks being stated, let us now emphasize the localization property of wavelets.

2.5.3 Localization property

Considering the requirements on the analysing wavelet Ψ , namely the zero-average condition $\mathcal{F}[\Psi](0) = 0$, and the fact that $\Psi \in L^1(\mathbb{R}) \cap L^2(\mathbb{R})$, its Fourier transform $\mathcal{F}[\Psi]$ also belongs in $L^2(\mathbb{R})$, and one can moreover state that:

$$\lim_{|t| \rightarrow +\infty} |\Psi(t)| = 0, \quad (2.76)$$

$$\lim_{|\omega| \rightarrow +\infty} |\mathcal{F}[\Psi](\omega)| = 0. \quad (2.77)$$

As a result, the analysing wavelet Ψ classically exhibits a well-localized support both in the physical and spectral spaces, with an oscillating behavior in the time domain, and a band-pass behavior in the frequency domain. Furthermore, all the dilated wavelets $\{\Psi_s\}_{s>0} = \left\{ \frac{1}{\sqrt{s}} \Psi \left(\frac{\cdot}{s} \right) \right\}_{s>0}$ share a similar localization property, with a bandwidth which is identical for all wavelets.

Indeed, following [Torrésani, 1995, Mallat, 2008, Lilly and Olhede, 2009], the support of a complex and analytic wavelet Ψ (the definition will be detailed later in this section) in the time-frequency plane can be defined by:

- a center in the time domain :

$$t_\Psi = \frac{1}{\|\Psi\|_{L^2(\mathbb{R})}^2} \int_{\mathbb{R}} t |\Psi(t)|^2 dt; \quad (2.78)$$

- a width in the time domain :

$$(\Delta t_\Psi)^2 = \frac{1}{\|\Psi\|_{L^2(\mathbb{R})}^2} \int_{\mathbb{R}} (t - t_\Psi)^2 |\Psi(t)|^2 dt; \quad (2.79)$$

- a center in the frequency domain :

$$\omega_\Psi = \frac{1}{\|\mathcal{F}[\Psi]\|_{L^2(\mathbb{R})}^2} \int_{\mathbb{R}} \omega |\mathcal{F}[\Psi](\omega)|^2 d\omega; \quad (2.80)$$

- a width in the frequency domain :

$$(\Delta \omega_\Psi)^2 = \frac{1}{\|\mathcal{F}[\Psi]\|_{L^2(\mathbb{R})}^2} \int_{\mathbb{R}} (\omega - \omega_\Psi)^2 |\mathcal{F}[\Psi](\omega)|^2 d\omega. \quad (2.81)$$

The wavelet Ψ being L^2 -normalized in the time domain, Parseval-Plancherel identity implies that $\|\mathcal{F}[\Psi]\|_{L^2(\mathbb{R})} = \sqrt{2\pi}$. Furthermore, the wavelet Ψ is usually centered around zero in the time domain ($t_\Psi = t_{\Psi_s} = 0$). Taking into account the scale parameter, the wavelet family $\{\Psi_s\}_{s>0}$ is shown to satisfy the following properties:

Time width	Central frequency	Frequency width
$\Delta t_{\Psi_s} = s \Delta t_\Psi$	$\omega_{\Psi_s} = \frac{\omega_\Psi}{s}$	$\Delta \omega_{\Psi_s} = \frac{\Delta \omega_\Psi}{s}$

Table 2.1: Analysing wavelet time-frequency support.

Thus, by filtering a signal through a wavelet family $\{\Psi_s\}_{s>0}$, it is possible to study numerous frequency ranges, while preserving the time (or spatial) localization via the translation parameter u . The interested reader may refer to [Torr sani, 1995, Mallat, 2008] for a detailed presentation on wavelet transform, and to [Lilly and Olhede, 2009] for an overview of the different frequencies (energy frequency, peak-amplitude frequency, instantaneous frequency) that can be associated to a complex analytic wavelet.

Speaking of such wavelets, it is now time to properly define the concept of complex analytic wavelet.

2.5.4 Complex analytic wavelets

Conversely to Fourier transform, where the atoms $\{\omega \mapsto e^{it_0\omega}\}_{t_0 \in \mathbb{R}}$ are complex-valued, the analysing wavelet Ψ can be either:

- complex analytic;
- real and symmetric.

Let us here start with complex analytic wavelets.

Definition 2.5.2 *Complex analytic wavelet*

A complex-valued wavelet $\Psi \in L^1(\mathbb{R}) \cap L^2(\mathbb{R})$ is said to be analytic if and only if:

$$\forall \omega < 0, \mathcal{F}[\Psi](\omega) = 0. \quad (2.82)$$

Let us illustrate this definition with some examples:

Example 2.5.1 *Complex analytic wavelets*

- *Cauchy wavelet of order $n \in \mathbb{N}$:*

$$\Psi_n(t) = \left(\frac{i}{t+i} \right)^{n+1}, \quad (2.83)$$

$$\mathcal{F}[\Psi_n](\omega) = \frac{2\pi}{n!} \omega^n e^{-\omega} H(\omega), \quad (2.84)$$

where H denotes the Heaviside function.

- *generalized Morse wavelets: $\forall \alpha, \beta > 0$,*

$$\mathcal{F}[\Psi_{\alpha,\beta}] = a_{\alpha,\beta} \omega^\alpha e^{-\omega^\beta} H(\omega), \quad (2.85)$$

where $a_{\alpha,\beta} = 2 \left(\frac{\beta}{\alpha} \right)^{\frac{\alpha}{\beta}}$. The interested reader may refer to [Lilly and Olhede, 2009] for a detailed study of this wavelet family.

- *complex Shannon wavelet:*

$$\Psi(t) = \pi \sin_c(t) e^{i2\pi t}. \quad (2.86)$$

- *Morlet wavelet:*

$$\Psi_\nu(t) = A_\nu e^{-\frac{t^2}{2}} \left[e^{i\nu t} - e^{-\frac{\nu^2}{2}} \right], \quad (2.87)$$

$$\mathcal{F}[\Psi_\nu](\omega) = A_\nu e^{-\frac{(\omega-\nu)^2}{2}} \left[1 - e^{-\omega\nu} \right], \quad (2.88)$$

which is only approximately analytic when the parameter ν is large enough. The parameter A_ν is a normalization constant. Once again, the interested reader may refer to [Lilly and Olhede, 2009] for more details on this wavelet.

- Gabor wavelet ($\eta > 0$):

$$\Psi(t) = g(t)e^{i\eta t}, \quad (2.89)$$

$$\mathcal{F}[\Psi](\omega) = \mathcal{F}[g](\omega - \eta), \quad (2.90)$$

where $g(t) = \frac{1}{(\sigma^2\pi)^{\frac{1}{4}}}e^{-\frac{t^2}{2\sigma^2}}$ is a Gaussian window, whose Fourier transform is given by $\mathcal{F}[g](\omega) = (4\pi\sigma^2)^{\frac{1}{4}}e^{-\frac{\sigma^2\omega^2}{2}}$. Thus, when the frequency ω is sufficiently far away from η , the wavelet Fourier transform is almost zero. Gabor wavelet thus becomes approximately analytic with a well-chosen parameter η .

Such complex and analytic wavelets meet a great success in literature. To emphasize why, some properties on analytic signals and Fourier transform shall first be recalled.

Remark 2.5.2 *Analytic signal, Fourier and wavelet transforms*

Any complex analytic signal $\Psi \in L^2(\mathbb{R}, \mathbb{C})$ admits the following decomposition:

$$\Psi(t) = \mathcal{R}(\Psi)(t) + i\mathcal{H}[\mathcal{R}(\Psi)](t), \quad (2.91)$$

$$\mathcal{F}[\Psi](\omega) = \mathcal{F}[\mathcal{R}(\Psi)](\omega) + \text{sign}(\omega)\mathcal{F}[\mathcal{R}(\Psi)](\omega), \quad (2.92)$$

where $\mathcal{R}(\Psi)$ denotes the real part of Ψ , and \mathcal{H} the Hilbert transform:

$$\mathcal{H}[\Psi](t) = \frac{1}{\pi} \text{p.v.} \left(\int_{\mathbb{R}} \frac{1}{t - \tau} \Psi(\tau) d\tau \right), \quad (2.93)$$

$$= \text{p.v.} \left[\left(\tau \mapsto \frac{1}{\pi\tau} \right) * \Psi \right](t). \quad (2.94)$$

In equation (2.94), p.v. denotes the principal value. It is for instance recalled that the principal value of the function $t \mapsto \frac{1}{t}$ is a distribution, which is defined by:

$$\forall \varphi \in \mathcal{S}(\mathbb{R}), \quad \left\langle \text{p.v.} \left(\frac{1}{t} \right), \varphi \right\rangle_{\mathcal{S}', \mathcal{S}} = \lim_{\epsilon \rightarrow 0} \int_{\mathbb{R} \setminus [-\epsilon, \epsilon]} \frac{\varphi(t)}{t} dt, \quad (2.95)$$

where $\mathcal{S}(\mathbb{R})$ denotes the Schwartz space (i.e. smooth functions with fast decay towards zero).

Following equation (2.92), the Fourier transform of a complex analytic signal $\Psi \in L^2(\mathbb{R}, \mathbb{C})$ satisfies:

$$\mathcal{F}[\Psi](\omega) = \begin{cases} 2\mathcal{F}[\mathcal{R}(\Psi)](\omega) & \text{if } \omega \geq 0 \\ 0 & \text{if } \omega < 0 \end{cases} \quad (2.96)$$

Continuous Wavelet Transform also presents interesting properties with analytic signals. Indeed, if one considers a real-valued finite-energy signal $f \in L^2(\mathbb{R}, \mathbb{R})$, and its complex analytic counterpart $f_a = f + i\mathcal{H}[f]$, it can be shown that their respective wavelet transform satisfies:

$$\forall s > 0, \mathcal{W}[f_a](s, \cdot) = 2\mathcal{W}[f](s, \cdot). \quad (2.97)$$

This remark on analytic signals being stated, it can now be emphasized how complex analytic wavelets allow to catch instantaneous frequencies within a real signal.

Remark 2.5.3 *Complex wavelets and instantaneous frequencies*

The use of a complex analytic wavelet Ψ on a real signal f allows to obtain complex wavelet coefficients, which offer information via their modulus and phase. This ability to keep track of the phase of a signal opens the way to instantaneous frequencies.

Indeed, it has already been underlined that any real signal $f \in L^2(\mathbb{R}, \mathbb{R})$ can be connected, thanks to Hilbert transform \mathcal{H} , to its complex analytic counterpart $f_a \in L^2(\mathbb{R}, \mathbb{C})$:

$$f_a(t) = f(t) + i\mathcal{H}[f](t), \quad (2.98)$$

$$= |f_a(t)| e^{i \arg(f_a(t))}. \quad (2.99)$$

Thus, a real signal f can be linked to the canonical pair $(|f_a|, \arg(f_a))$, with $\arg(f_a(t)) \in [0, 2\pi[$. The instantaneous frequency ω_f of the real signal f is then defined by:

$$\omega_f(t) = \frac{d}{dt} [\arg(f_a(t))]. \quad (2.100)$$

Complex wavelets allow to keep track of the phase of the analytic component f_a . Furthermore, the wavelet coefficients of the analytic signal f_a are closely related to the ones of f , as stated by equation (2.97). As for the computation of the analytic component f_a from the original signal f , it is, in common situations, very easy. Indeed, if the signal f is an asymptotic signal, i.e. if it exhibits a single-component oscillatory behavior:

$$f(t) = A(t) \cos(\varphi(t)), \quad (2.101)$$

with a phase $\varphi(t)$ oscillating much faster than the amplitude $A(t)$, then the following approximation holds:

$$f_a(t) \approx A(t)e^{i\varphi(t)}. \quad (2.102)$$

The interested reader may refer to [Delprat et al., 1992, Carmona et al., 1994, Carmona et al., 1997, Le and Argoul, 2004] for further details on the use of complex analytic wavelets for the study of asymptotic signals.

Now, depending on the signal at study, one can be more interested in a symmetric property of the wavelets, rather than their ability to catch instantaneous frequencies. In such cases, one can turn towards real wavelets.

2.5.5 Real and symmetric wavelets

Classical real and symmetric wavelets are detailed below:

Example 2.5.2 *Real symmetric wavelets*

- *1D Mexican hat, obtained by computing the Laplacian of a Gaussian function $e^{-\frac{t^2}{2\sigma^2}}$, $\sigma > 0$:*

$$\Psi(t) = \frac{2}{\pi^{\frac{1}{4}}\sqrt{3}\sigma} \left(1 - \frac{t^2}{\sigma^2}\right) e^{-\frac{t^2}{2\sigma^2}}, \quad (2.103)$$

$$\mathcal{F}[\Psi](\omega) = \frac{\sqrt{8}\sigma^{\frac{5}{2}}\pi^{\frac{1}{4}}}{\sqrt{3}} \omega^2 e^{-\frac{\sigma^2\omega^2}{2}}. \quad (2.104)$$

- *difference of Gaussian functions ($0 < \sigma < 1$):*

$$\Psi(t) = \frac{1}{\sigma^2} e^{-\frac{\|x\|^2}{2\sigma^2}} - e^{-\frac{\|x\|^2}{2}}. \quad (2.105)$$

Such real and symmetric wavelets are very smooth, and can be used to detect singularities in signals, or to regularize non-smooth behaviors.

A common denominator between all the wavelets described until now, whether they are complex or real, is their band-pass behavior in the frequency domain. However, it is sometimes more suited to use low-pass filters to catch simultaneously all the scales or wavelengths beyond a specific cutoff value, as in Large Eddy Simulation (see [Lesieur, 2008]) for turbulent flows for instance. By aggregating all dilated wavelets $\{\Psi_s\}_s$ for $s \geq 1$, it is possible to build such a low-pass filter, called the scaling function or father wavelet.

2.5.6 Scaling function and low-frequency approximation

Given an (admissible) analysing wavelet Ψ , one defines its associated scaling function Φ as follows:

Definition 2.5.3 *Scaling function (see [Torr sani, 1995, Mallat, 2008])*

If $\Psi \in L^1(\mathbb{R}) \cap L^2(\mathbb{R})$ denotes an (admissible) analysing wavelet, its associated scaling function Φ is defined, in the frequency domain, by:

$$\forall \omega \in \mathbb{R}, |\mathcal{F}[\Phi](\omega)|^2 = \int_1^{+\infty} \frac{|\mathcal{F}[\Psi](s\omega)|^2}{s} ds, \quad (2.106)$$

$$= \int_{\omega}^{+\infty} \frac{|\mathcal{F}[\Psi](\xi)|^2}{\xi} d\xi. \quad (2.107)$$

The phase of the Fourier transform $\mathcal{F}[\Phi]$ can be chosen arbitrarily. Besides, the scaling function satisfies the same normalization (in L^2 norm) as the analysing wavelet.

By aggregating all dilated wavelets $\{\Psi_s\}_s$ for $s \geq 1$, as shown in equation (2.107), one gathers all their successive bandwidths, and thus obtains a low-pass filter.

To complete the above definition of scaling function, a few remarks shall be stated:

Remark 2.5.4 *Admissibility and L^2 -normalization*

- the convergence of the integral in equation (2.107) is ensured when the analysing wavelet Ψ satisfies the following admissibility condition:

$$C_{\Psi} := \int_{\mathbb{R}} \frac{|\mathcal{F}[\Psi](\omega)|^2}{|\omega|} d\omega < +\infty. \quad (2.108)$$

This admissibility criterion will also be encountered when discussing inverse wavelet transform.

- the definition (2.107) ensures that both the analysing wavelet and scaling function are L^2 -normalized in the time domain. Indeed, one can write, using Fubini's theorem:

$$\int_{\mathbb{R}} |\mathcal{F}[\Phi](\omega)|^2 d\omega = \int_{\mathbb{R}} \int_{\omega}^{+\infty} \frac{|\mathcal{F}[\Psi](\xi)|^2}{\xi} d\xi d\omega, \quad (2.109)$$

$$= \int_{\mathbb{R}} \frac{|\mathcal{F}[\Psi](\xi)|^2}{\xi} \left(\int_0^{\xi} d\omega \right) d\xi, \quad (2.110)$$

$$= \int_{\mathbb{R}} |\mathcal{F}[\Psi](\xi)|^2 d\xi, \quad (2.111)$$

$$= 2\pi. \quad (2.112)$$

Parseval-Plancherel identity then allows to state that $\|\Phi\|_{L^2(\mathbb{R})}^2 = 1$.

It is here worth noticing that, conversely to analysing wavelets, scaling functions do not always possess an analytical expression in the time domain. For the Mexican hat wavelet for instance, an analytical expression is only available in the spectral domain, as detailed below.

Example 2.5.3 Mexican hat scaling function

The scaling function associated to the 1D Mexican hat wavelet is defined, in the spectral domain, by:

$$\mathcal{F}[\Phi](\omega) = \frac{2\sigma^{\frac{3}{2}}\pi^{\frac{1}{4}}}{\sqrt{3}} \left(\omega^2 + \frac{1}{\sigma^2} \right)^{\frac{1}{2}} e^{-\frac{\sigma^2\omega^2}{2}}. \quad (2.113)$$

This low-pass filter being defined, let us now turn towards the low-frequency approximation of a signal $f \in L^2(\mathbb{R})$.

Definition 2.5.4 *Low-frequency approximation (see [Torrésani, 1995, Mallat, 2008])*

Given an original scaling function $\Phi \in L^1(\mathbb{R}) \cap L^2(\mathbb{R})$, one can build a family of dilated atoms $\left\{ \frac{1}{\sqrt{s}}\Phi\left(\frac{\cdot}{s}\right) \right\}_{s>0}$. The low-frequency approximation $\mathcal{L}[f]$ of a finite-energy signal $f \in L^2(\mathbb{R})$ is then defined as the linear decomposition of f on the complex-conjugates of these atoms:

$$\forall s > 0, u \in \mathbb{R},$$

$$\boxed{\mathcal{L}[f](s, u) = \frac{1}{\sqrt{s}} \int_{\mathbb{R}} f(t) \Phi\left(\frac{t-u}{s}\right)^* dt.} \quad (2.114)$$

Similarly to Continuous Wavelet Transform (CWT), this definition can be rewritten, in the time and frequency domains, as:

$$\boxed{\mathcal{L}[f](s, u) = (f * \tilde{\Phi}_s^*)(u),} \quad (2.115)$$

$$\boxed{\mathcal{F}[\mathcal{L}[f](s, \cdot)](\omega) = \mathcal{F}[f](\omega) \times \sqrt{s}\mathcal{F}[\Phi](s\omega)^*.} \quad (2.116)$$

Now that both the analysing wavelet Ψ and scaling function Φ are defined, it is high time to emphasize why CWT can be a relevant tool to bypass the limitations of classical homogenization and multi-scale methods, especially the closure between resolved and unresolved scales, and the treatment of boundary conditions.

2.5.7 Inverse wavelet transform

Conversely to classical convolution-based filtering operators, Continuous Wavelet Transform (CWT) offers an inverse formula, which allows to recover a high-resolution signal $f \in L^2(\mathbb{R})$ from its wavelet coefficients $\mathcal{W}[f](s, \cdot)$. The only requirement to fulfill in order to allow for such a reconstruction is to choose an admissible analysing wavelet, as detailed below.

Theorem 2.5.1 1D reconstruction formula (see [Torrésani, 1995, Mallat, 2008])

If the analysing wavelet Ψ satisfies the admissibility condition:

$$C_\Psi := \int_{\mathbb{R}} \frac{|\mathcal{F}[\Psi](\omega)|^2}{|\omega|} d\omega < +\infty, \quad (2.117)$$

then the following reconstruction formula holds:

- *if Ψ is real, then for all $f \in L^2(\mathbb{R})$:*

$$f(t) = \frac{2}{C_\Psi} \int_0^{+\infty} \left(\int_{\mathbb{R}} \mathcal{W}[f](s, u) \frac{1}{\sqrt{s}} \Psi\left(\frac{t-u}{s}\right) du \right) \frac{ds}{s^2}, \quad (2.118)$$

- *if Ψ is complex and analytic, then for all $f \in L^2(\mathbb{R})$:*

$$f(t) = \frac{2}{C_\Psi} \mathcal{R} \left(\int_0^{+\infty} \left(\int_{\mathbb{R}} \mathcal{W}[f](s, u) \frac{1}{\sqrt{s}} \Psi\left(\frac{t-u}{s}\right) du \right) \frac{ds}{s^2} \right). \quad (2.119)$$

Furthermore, in both cases, the following energy identity holds:

$$\|f\|_{L^2(\mathbb{R})}^2 = \frac{2}{C_\Psi} \int_0^{+\infty} \left(\int_{\mathbb{R}} |\mathcal{W}[f](s, u)|^2 du \right) \frac{ds}{s^2}. \quad (2.120)$$

For the sake of completeness, it shall be highlighted that another reconstruction formula can be defined with the scaling function Φ . Indeed, if the analysing wavelet Ψ is real, one has, for all $f \in L^2(\mathbb{R})$:

$$f(t) = \frac{2}{C_\Psi} \int_0^{s_0} \left(\int_{\mathbb{R}} \mathcal{W}[f](s, u) \frac{1}{\sqrt{s}} \Psi\left(\frac{t-u}{s}\right) du \right) \frac{ds}{s^2} + \frac{2}{C_\Psi s_0} \int_{\mathbb{R}} \mathcal{L}[f](s_0, u) \frac{1}{\sqrt{s_0}} \Phi\left(\frac{t-u}{s_0}\right) du, \quad (2.121)$$

where s_0 is a positive scale parameter chosen to compute the low-frequency approximation $\mathcal{L}[f](s_0, \cdot)$. It represents the cutoff scale of the low-pass filter Φ_{s_0} .

Thanks to the above reconstruction formula, it is thus possible, with a well-chosen number of wavelet coefficients $(\mathcal{W}[f](s_k, \cdot))_{1 \leq k \leq N}$, selected on a well-chosen scale range $[s_1, s_N]$, to reconstruct, up to an approximation, the signal f at the microscopic scale. This reconstruction formula thus allows to connect unresolved and resolved scales without any *ad hoc* model. It will also allow, as proven in chapter 3, to properly transfer the boundary conditions of a microscopic field f into its filtered counterpart $\mathcal{W}[f](s, \cdot)$.

Nevertheless, despite this obvious advantage of CWT compared to plain filtering methods, it is important to highlight that CWT exhibits one main drawback: redundancy.

2.5.8 CWT and redundancy

Indeed, the use of CWT transforms a one-variable function $t \mapsto f(t)$ into a two-variables function $(s, u) \mapsto \mathcal{W}[f](s, u)$. Furthermore, correlations between different wavelets of the family $\{\Psi\}_{s>0}$ can be witnessed. This is due to the fact that the supports of wavelets associated to neighboring scale parameters may overlap. The redundancy of a specific analysing wavelet Ψ is measured by its reproducing kernel, as detailed in [Torrésani, 1995, Mallat, 2008].

Definition 2.5.5 Reproducing kernel

The reproducing kernel of a wavelet Ψ is defined by the L^2 -inner product between two dilated wavelets:

$$\forall s_1, s_2 \in \mathbb{R}_+^*, u_1, u_2 \in \mathbb{R},$$

$$K(s_1, s_2, u_1, u_2) = \langle \Psi_{s_2, u_2}, \Psi_{s_1, u_1} \rangle_{L^2}, \quad (2.122)$$

$$= \int_{\mathbb{R}} \frac{1}{\sqrt{s_2}} \Psi\left(\frac{t - u_2}{s_2}\right)^* \frac{1}{\sqrt{s_1}} \Psi\left(\frac{t - u_1}{s_1}\right) dt. \quad (2.123)$$

This expression of the reproducing kernel can be obtained by injecting the reconstruction formula (2.118) into the CWT definition (2.66):

$$\mathcal{W}[f](s_2, u_2) \quad (2.124)$$

$$= \int_{\mathbb{R}} \left(\frac{2}{C_{\Psi}} \int_0^{+\infty} \int_{\mathbb{R}} \mathcal{W}[f](s_1, u_1) \frac{1}{\sqrt{s_1}} \Psi\left(\frac{t - u_1}{s_1}\right) du_1 \frac{ds_1}{s_1^2} \right) \frac{1}{\sqrt{s_2}} \Psi\left(\frac{t - u_2}{s_2}\right)^* dt, \quad (2.125)$$

$$= \frac{2}{C_{\Psi}} \int_0^{+\infty} \int_{\mathbb{R}} \left(\int_{\mathbb{R}} \frac{1}{\sqrt{s_1}} \Psi\left(\frac{t - u_1}{s_1}\right) \frac{1}{\sqrt{s_2}} \Psi\left(\frac{t - u_2}{s_2}\right)^* dt \right) \mathcal{W}[f](s_1, u_1) du_1 \frac{ds_1}{s_1^2}, \quad (2.126)$$

$$= \frac{2}{C_{\Psi}} \int_0^{+\infty} \int_{\mathbb{R}} K(s_1, s_2, u_1, u_2) \mathcal{W}[f](s_1, u_1) du_1 \frac{ds_1}{s_1^2}. \quad (2.127)$$

In order to bypass the redundancy of CWT, efforts have been made in the 1980's and 1990's to develop (discrete) orthogonal wavelet bases. But before introducing Discrete Wavelet Transform and orthogonal Multi-Resolution Analysis (MRA), let us first extend CWT to the 2D case.

2.6 2D Continuous Wavelet Transform

In the 1D case, all the atoms $\{\Psi_{s,u}(t)\}_{s>0, u \in \mathbb{R}} = \left\{ \frac{1}{\sqrt{s}} \Psi\left(\frac{t-u}{s}\right) \right\}_{s>0, u \in \mathbb{R}}$ were built by dilations (s) and translations (u) from an analysing wavelet Ψ . In the 2D case, one shall now take into account 2 degrees of freedom of translation, and 1 degree of freedom of rotation. Thus, all the atoms $\{\Psi_{s,\underline{u},\theta}\}_{s>0, \underline{u} \in \mathbb{R}^2, \theta \in [0, 2\pi[}$ are now defined, with an energy formulation, as:

$$\Psi_{s,\underline{u},\theta}(\underline{x}) = \frac{1}{s} \Psi\left(\left(\underline{R}_\theta\right)^{-1} \frac{\underline{x} - \underline{u}}{s}\right), \quad (2.128)$$

where $\underline{u} \in \mathbb{R}^2$ is now a translation vector, and $\underline{R}_\theta \in \mathbb{R}^{2 \times 2}$ a 2D rotation matrix.

Remark 2.6.1 *In 2D, the previous time ($t \in \mathbb{R}$) and frequency ($\omega \in \mathbb{R}$) notations are replaced by respectively a position ($\underline{x} \in \mathbb{R}^2$) and a wave vector ($\underline{k} \in \mathbb{R}^2$).*

2.6.1 Analysing wavelet and CWT

Based on the atoms (2.128), the definition of 2D CWT follows the same spirit as 1D CWT:

Definition 2.6.1 *2D Continuous Wavelet Transform (see [Gonnet and Torr sani, 1994, Antoine and Murenzi, 1996])*

Assume $\Psi \in L^1(\mathbb{R}^2) \cap L^2(\mathbb{R}^2)$, with real or complex values, and satisfying the following zero-average condition:

$$\int_{\mathbb{R}^2} \Psi(\underline{x}) \, d\underline{x} = 0, \quad (2.129)$$

or equivalently:

$$\mathcal{F}[\Psi](\underline{0}) = 0. \quad (2.130)$$

In the following, it is also assumed that the function Ψ is L^2 -normalized:

$$\|\Psi\|_{L^2(\mathbb{R}^2)} = 1. \quad (2.131)$$

Given this analysing wavelet Ψ , the Continuous Wavelet Transform of a signal $f \in L^2(\mathbb{R}^2)$ is defined, with an energy formulation, as follows:

$$\forall s > 0, \underline{u} \in \mathbb{R}^2, \theta \in [0, 2\pi[,$$

$$\boxed{\mathcal{W}[f](s, \underline{u}, \theta) = \frac{1}{s} \int_{\mathbb{R}^2} f(\underline{x}) \Psi \left(\left(\underline{R}_\theta \right)^{-1} \frac{\underline{x} - \underline{u}}{s} \right)^* d\underline{x}.} \quad (2.132)$$

If one introduces the notations $\tilde{\Psi}(\underline{x}) = \Psi(-\underline{x})$, $\Psi_{s,\theta}(\underline{x}) = \frac{1}{s} \Psi \left(\left(\underline{R}_\theta \right)^{-1} \frac{\underline{x}}{s} \right)$, and $\Psi_\theta(\underline{x}) = \Psi \left(\left(\underline{R}_\theta \right)^{-1} \underline{x} \right)$, the above definition (2.132) can be rewritten as follows:

$$\boxed{\mathcal{W}[f](s, \underline{u}, \theta) = (f * \tilde{\Psi}_{s,\theta}^*)(\underline{u}),} \quad (2.133)$$

$$\mathcal{F}[\mathcal{W}[f](s, \cdot, \theta)](\underline{k}) = \mathcal{F}[f](\underline{k}) \times s \mathcal{F}[\Psi_\theta](s \underline{k})^*. \quad (2.134)$$

In the above definitions, the following notations are used:

- s is a positive scale parameter, $\underline{u} \in \mathbb{R}^2$ a vector, and θ an angle;
- $\mathcal{W}[f](s, \underline{u}, \theta)$ is the wavelet coefficient of f ;
- $\underline{R}_\theta = \begin{pmatrix} \cos(\theta) & -\sin(\theta) \\ \sin(\theta) & \cos(\theta) \end{pmatrix}_{(\underline{e}_1, \underline{e}_2)}$ is the 2D rotation matrix with respect to the $(O, \underline{e}_1 \wedge \underline{e}_2)$ axis, where $(\underline{e}_1, \underline{e}_2)$ is the orthonormal cartesian basis of \mathbb{R}^2 .

As in the 1D case, the requirements imposed on the analysing wavelet Ψ ensure that it will exhibit good localization properties both in the physical and spectral spaces.

Nevertheless, while most properties of CWT naturally extend to the 2D case, it is worth noticing that it is not the case for complex analytic wavelets.

2.6.2 Complex wavelets: from analytic to directional wavelets

In 2D, the definition of analytic wavelets does not stand anymore, as it is no longer possible to properly define and distinguish a positive and a negative wave vector $\underline{k} \in \mathbb{R}^2$. In wavelets literature, the concept of complex directional wavelets has thus been introduced. Such wavelets possess a Fourier transform which is essentially supported within a convex cone in the spatial frequency plane $\{\underline{k} \in \mathbb{R}^2\}$. They thus exhibit an anisotropic behavior, and are especially suited for the detection of oriented features, such as edges in a picture for instance. The interested reader may refer to [Gonnet and Torr sani, 1994] and [Antoine and Murenzi, 1996] for further details on this topic.

Conversely to complex wavelets, 1D real symmetric wavelets are naturally extended into 2D isotropic functions.

2.6.3 Real and isotropic wavelets and scaling functions

One of the most widely used real and isotropic wavelet is the 2D Mexican hat, hereafter defined both in the physical and spectral domains.

Example 2.6.1 2D Mexican hat

$$\Psi(\underline{x}) = \frac{\sqrt{2}}{\sigma\sqrt{\pi}} \left(1 - \frac{\|\underline{x}\|^2}{2\sigma^2}\right) e^{-\frac{\|\underline{x}\|^2}{2\sigma^2}}, \quad (2.135)$$

$$\mathcal{F}[\Psi](\underline{k}) = \sigma^3 \sqrt{2\pi} \|\underline{k}\|^2 e^{-\frac{\sigma^2 \|\underline{k}\|^2}{2}}. \quad (2.136)$$

Such real and isotropic wavelets allow to extend the concept of scaling function to the 2D case, as detailed below.

Definition 2.6.2 2D real and isotropic scaling function

If $\Psi \in L^1(\mathbb{R}^2) \cap L^2(\mathbb{R}^2)$ denotes a real, isotropic and admissible analysing wavelet, one can define its associated (real and isotropic) scaling function as follows:

$$\forall \underline{k} \in \mathbb{R}^2, \quad |\mathcal{F}[\Phi](\underline{k})|^2 = 2 \int_1^{+\infty} \frac{|\mathcal{F}[\Psi](s\|\underline{k}\|)|^2}{s} ds, \quad (2.137)$$

$$= 2 \int_{\|\underline{k}\|}^{+\infty} \frac{|\mathcal{F}[\Psi](\xi)|^2}{\xi} d\xi. \quad (2.138)$$

Once again, the phase of the Fourier transform $\mathcal{F}[\Phi]$ can be chosen arbitrarily. The above definition ensures that the scaling function Φ is real and isotropic.

To complete this definition, a few remarks shall be stated:

Remark 2.6.2 Admissibility, L^2 -normalization and isotropy

- to ensure the well-posedness of the integral in equation (2.138), the analysing wavelet Ψ shall satisfy, as in the 1D case, the following 2D admissibility condition:

$$C_\Psi := \int_{\mathbb{R}^2} \frac{|\mathcal{F}[\Psi](\underline{k})|^2}{\|\underline{k}\|^2} d\underline{k} < +\infty. \quad (2.139)$$

- the definition (2.138) ensures that both the analysing wavelet Ψ and scaling function Φ are L^2 -normalized. Indeed, one can write, for all $\underline{k} \in \mathbb{R}^2$:

$$\int_{\mathbb{R}^2} |\mathcal{F}[\Phi](\underline{k})|^2 d\underline{k} = 2 \int_{\mathbb{R}^2} \int_{\|\underline{k}\|}^{+\infty} \frac{|\mathcal{F}[\Psi](\xi)|^2}{\xi} d\xi d\underline{k}, \quad (2.140)$$

$$= 2 \int_0^{2\pi} \int_0^{+\infty} \left(\int_r^{+\infty} \frac{|\mathcal{F}[\Psi](\xi)|^2}{\xi} d\xi \right) r dr d\theta, \quad (2.141)$$

$$= 4\pi \int_0^{+\infty} \left(\int_r^{+\infty} \frac{|\mathcal{F}[\Psi](\xi)|^2}{\xi} d\xi \right) r dr. \quad (2.142)$$

Thanks to Fubini's theorem, one can then write:

$$\int_{\mathbb{R}^2} |\mathcal{F}[\Phi](\underline{k})|^2 d\underline{k} = 4\pi \int_0^{+\infty} \frac{|\mathcal{F}[\Psi](\xi)|^2}{\xi} \left(\int_0^\xi r dr \right) d\xi, \quad (2.143)$$

$$= 4\pi \int_0^{+\infty} \frac{\xi^2}{2} \times \frac{|\mathcal{F}[\Psi](\xi)|^2}{\xi} d\xi, \quad (2.144)$$

$$= 2\pi \int_0^{+\infty} |\mathcal{F}[\Psi](\xi)|^2 \xi d\xi, \quad (2.145)$$

$$= \int_0^{2\pi} \int_0^{+\infty} |\mathcal{F}[\Psi](\xi)|^2 \xi d\xi d\theta, \quad (2.146)$$

$$= \int_{\mathbb{R}^2} |\mathcal{F}[\Psi](\underline{k})|^2 d\underline{k}, \quad (2.147)$$

$$= 4\pi^2. \quad (2.148)$$

Parseval-Plancherel identity then allows to state that $\|\Phi\|_{L^2(\mathbb{R}^2)}^2 = 1$.

- the isotropy property of the scaling function results from the isotropy of the analysing wavelet. Indeed, one can notice that:

$$\mathcal{F}[\Psi](-\underline{k}) = \int_{\mathbb{R}^2} \Psi(\underline{x}) e^{i\underline{k} \cdot \underline{x}} d\underline{x}, \quad (2.149)$$

$$= \int_{\mathbb{R}^2} \Psi(-\underline{y}) e^{-i\underline{k} \cdot \underline{y}} d\underline{y}. \quad (2.150)$$

$$\mathcal{F}[\Psi](\underline{k})^* = \int_{\mathbb{R}^2} \Psi(\underline{x})^* e^{i\underline{k} \cdot \underline{x}} d\underline{x}, \quad (2.151)$$

$$= \int_{\mathbb{R}^2} \Psi(-\underline{y})^* e^{-i\underline{k} \cdot \underline{y}} d\underline{y}. \quad (2.152)$$

Thus, if the analysing wavelet Ψ is real and isotropic, one has $\Psi(-\underline{y})^* = \Psi(-\underline{y}) = \Psi(\underline{y})$, and its Fourier transform also is real and isotropic, i.e. $\mathcal{F}[\Psi](\underline{k})^* = \mathcal{F}[\Psi](\underline{k}) = \mathcal{F}[\Psi](-\underline{k})$. As a result, the Fourier transform $\mathcal{F}[\Phi]$, and the scaling function Φ itself, share the same properties.

As in the 1D case, scaling functions do not always possess an analytical expression in the physical domain. For the Mexican hat wavelet for instance, one can only define its 2D scaling function in the spectral domain.

Example 2.6.2 *2D Mexican hat scaling function*

The 2D scaling function associated to the isotropic Mexican hat wavelet is defined, in the spectral domain, by:

$$\mathcal{F}[\Phi](\underline{k}) = \sigma^2 \sqrt{2\pi} \left(\|\underline{k}\|^2 + \frac{1}{\sigma^2} \right)^{\frac{1}{2}} e^{-\frac{\sigma^2 \|\underline{k}\|^2}{2}}. \quad (2.153)$$

As stated in the previous remark, one can notice that this scaling function is purely real and isotropic in the spectral domain, and thus also in the physical domain.

The definition of 2D isotropic scaling functions being now stated, one can then extend the concept of low-frequency approximation to the 2D case.

Definition 2.6.3 *2D low-frequency approximation*

Given Ψ a real and isotropic analysing wavelet, and Φ its real and isotropic scaling function, one can naturally extend the definition of low-frequency approximation as follows:

$$\forall s > 0, \underline{u} \in \mathbb{R}^2,$$

$$\boxed{\mathcal{L}[f](s, \underline{u}) = \frac{1}{s} \int_{\mathbb{R}^2} f(\underline{x}) \Phi\left(\frac{\underline{x} - \underline{u}}{s}\right) d\underline{x},} \quad (2.154)$$

By introducing the notations $\Phi_s(\underline{x}) = \frac{1}{s} \Phi\left(\frac{\underline{x}}{s}\right)$ and $\tilde{\Phi}(\underline{x}) = \Phi(-\underline{x})$, the above definition can be rewritten as follows:

$$\boxed{\mathcal{L}[f](s, \underline{u}) = (f * \tilde{\Phi}_s)(\underline{u}),} \quad (2.155)$$

$$\boxed{\mathcal{F}[\mathcal{L}[f](s, \cdot)](\underline{k}) = \mathcal{F}[f](\underline{k}) \times s \mathcal{F}[\Phi](s \|\underline{k}\|).} \quad (2.156)$$

Now that both the analysing wavelet Ψ and scaling function Φ have been extended to the 2D case, it is high time to also extend the inverse wavelet transform.

2.6.4 Inverse wavelet transform

Following [Gonnet and Torr sani, 1994, Antoine and Murenzi, 1996], the inverse wavelet transform is extended to the 2D case as detailed below:

Theorem 2.6.1 *2D reconstruction formula*

If the analysing wavelet Ψ satisfies the admissibility condition

$$C_\Psi := \int_{\mathbb{R}^2} \frac{|\mathcal{F}[\Psi](\underline{k})|^2}{\|\underline{k}\|^2} d\underline{k} < +\infty, \quad (2.157)$$

then, the following reconstruction formula and energy identity hold:

$$f(\underline{x}) = \frac{1}{C_\Psi} \int_0^{+\infty} \int_{\mathbb{R}^2} \int_0^{2\pi} \mathcal{W}[f](s, \underline{u}, \theta) \times \frac{1}{s} \Psi\left(\left(\underline{R}_\theta\right)^{-1} \frac{\underline{x} - \underline{u}}{s}\right) d\theta d\underline{u} \frac{ds}{s^3}, \quad (2.158)$$

$$\|f\|_{L^2(\mathbb{R}^2)}^2 = \frac{1}{C_\Psi} \int_0^{+\infty} \int_{\mathbb{R}^2} \int_0^{2\pi} |\mathcal{W}[f](s, \underline{u}, \theta)|^2 d\theta d\underline{u} \frac{ds}{s^3}. \quad (2.159)$$

If the analysing wavelet Ψ is real and isotropic, the reconstruction formula (2.121), which uses the scaling function Φ and the low-frequency approximation $\mathcal{L}[\Phi](s_0, \cdot)$, can naturally be extended to the 2D case.

Now that all the properties of Continuous Wavelet Transform (CWT) have been extended from the 1D to the 2D case, it is high time to turn towards Discrete Wavelet Transform and Multi-Resolution Analysis (MRA), which offer a framework able to bypass the redundancy of CWT.

2.7 1D Discrete Wavelet Transform and Multi-Resolution Analysis

As already highlighted in the introduction of the previous sections, the development of orthogonal wavelet bases has benefited from the important works of [Strömberg, 1981, Lemarié and Meyer, 1986, Daubechies, 1988, Mallat, 1989b]. This fairly recent literature expanded the pioneering work of [Haar, 1910], who designed the first orthogonal wavelets basis, known as the Haar basis. These early wavelets, however, exhibit a discontinuous behavior, which limits their use for the numerical computation of PDEs for instance.

Before citing some examples of orthogonal wavelets, it is first important to recall the theoretical framework of MRA.

Definition 2.7.1 *Multi-Resolution Approximation of $L^2(\mathbb{R})$*

The concept of Multi-Resolution Approximation (MRA) of $L^2(\mathbb{R})$ was first introduced in [Mallat, 1989b]. It is defined as a sequence of closed subspaces $(V_j)_{j \in \mathbb{Z}}$, which satisfies the following properties:

- $\forall j \in \mathbb{Z}, V_j \subset V_{j+1};$
- $\overline{\cup_{j \in \mathbb{Z}} V_j} = L^2(\mathbb{R}),$ and $\cap_{j \in \mathbb{Z}} V_j = \{0\};$
- $\forall x \in \mathbb{R}, \forall j \in \mathbb{Z}, f(x) \in V_j \iff f(2x) \in V_{j+1};$
- $\forall x \in \mathbb{R}, \forall j, k \in \mathbb{Z}, f(x) \in V_j \iff f(x - 2^{-j}k) \in V_j;$
- *there exists an isomorphism from V_0 onto $l^2(\mathbb{Z})$, which commutes with the action of \mathbb{Z} ;*

where $l^2(\mathbb{Z})$ is the space of square-summable sequences. The action of \mathbb{Z} over V_0 is defined as the translation of functions $f \in V_0$ by integer values, while the action of \mathbb{Z} over $l^2(\mathbb{Z})$ is defined as the usual translation.

It is proven in [Mallat, 1989b] that a function $\varphi \in L^2(\mathbb{R})$ exists, with a non-vanishing integral, such that for all $j \in \mathbb{Z}$:

$$\boxed{(\varphi_{j,k}(x))_{k \in \mathbb{Z}} := (\sqrt{2^j} \varphi(2^j x - k))_{k \in \mathbb{Z}} \text{ is an orthonormal basis of } V_j.} \quad (2.160)$$

This function φ is called an orthogonal scaling function, and is uniquely characterized by:

- a refinement or dilation equation:

$$\varphi(x) = 2 \sum_{k \in \mathbb{Z}} a_k \varphi(2x - k), \quad (2.161)$$

where the real sequence $(a_k)_{k \in \mathbb{Z}}$ is called a scaling sequence, which satisfies $\sum_{k \in \mathbb{Z}} a_k = 1$;

- and the following normalization:

$$\int_{\mathbb{R}} \varphi(x) dx = 1. \quad (2.162)$$

Let us now introduce the complementary space of V_j within V_{j+1} , here denoted W_j , which moreover satisfies an orthogonality condition ($V_j \perp W_j$). One can thus write, for all $j \in \mathbb{Z}$, the following direct-sum:

$$V_{j+1} = V_j \oplus W_j. \quad (2.163)$$

In MRA vocabulary, the space V_j is said to contain the information of a given signal $f \in L^2(\mathbb{R})$ at the resolution level 2^j , while W_j is said to contain the details allowing to go from the resolution level 2^j to 2^{j+1} . The above direct-sum immediately implies that:

$$\forall J \in \mathbb{Z}, V_J = \bigoplus_{j=-\infty}^{J-1} W_j, \quad (2.164)$$

$$\boxed{\bigoplus_{j \in \mathbb{Z}} W_j = L^2(\mathbb{R})}. \quad (2.165)$$

Besides, it is also proven in [Mallat, 1989b] that there exists a function $\psi \in L^2(\mathbb{R})$, called orthogonal wavelet, such that the family $(\sqrt{2^j} \psi(2^j x - k))_{k \in \mathbb{Z}}$ is an orthonormal basis of W_j , for all $j \in \mathbb{Z}$. As a consequence:

$$\boxed{(\psi_{j,k}(x))_{j,k \in \mathbb{Z}} := (\sqrt{2^j} \psi(2^j x - k))_{j,k \in \mathbb{Z}} \text{ is an orthonormal basis of } L^2(\mathbb{R})}. \quad (2.166)$$

Remark 2.7.1 *It can here be noticed that, conversely to wavelet families $(\Psi_s)_{s>0}$ in the CWT framework, orthogonal wavelet bases $(\psi_{j,k})_{j,k \in \mathbb{Z}}$ are now constructed by means of integer translations and dyadic dilations from an analysing wavelet ψ .*

Let us now denote by Q_j the orthogonal projection on W_j and parallel to $\bigoplus_{i \neq j} W_i$. The direct-sum (2.165) implies that, for all $f \in L^2(\mathbb{R})$:

$$\boxed{\forall x \in \mathbb{R}, f(x) = \sum_{j \in \mathbb{Z}} Q_j(f)(x),} \quad (2.167)$$

$$= \sum_{j,k \in \mathbb{Z}} \langle \psi_{j,k}, f \rangle_{L^2} \psi_{j,k}(x). \quad (2.168)$$

Equation (2.168) can be seen as an inverse discrete wavelet transform.

Thus, when going from Continuous Wavelet Transform to Discrete Wavelet Transform and MRA, one switches the correlated atoms $\left\{ \frac{1}{\sqrt{s}} \Psi\left(\frac{\cdot - u}{s}\right) \right\}_{s>0, u \in \mathbb{R}}$ for orthonormal wavelet bases $(\sqrt{2^j} \psi(2^j x - k))_{k,j \in \mathbb{Z}}$, and leaves the "convolution product" point of view for a "linear projection" point of view. Now, to illustrate the concept of orthogonal MRA, let us present some examples of orthogonal wavelets.

Example 2.7.1 Orthogonal wavelets

- Haar analysing wavelet is a real, compactly supported, symmetric and orthogonal wavelet, defined by:

$$\psi(t) = \begin{cases} 1 & \text{if } 0 \leq t < \frac{1}{2} \\ -1 & \text{if } \frac{1}{2} \leq t < 1 \\ 0 & \text{otherwise} \end{cases} \quad (2.169)$$

Its associated scaling function is the box function:

$$\varphi(t) = \begin{cases} 1 & \text{if } 0 \leq t < 1 \\ 0 & \text{otherwise} \end{cases} \quad (2.170)$$

Such a wavelet presents a low interest because of its discontinuous behavior.

- *Shannon wavelet is a real, symmetric and orthogonal wavelet, defined by:*

$$\psi(t) = \frac{\sin(2\pi t) - \sin(\pi t)}{\pi t}. \quad (2.171)$$

Its associated scaling function is defined by:

$$\varphi(t) = \sin_c(\pi t). \quad (2.172)$$

Such a wavelet is not compactly supported, and worse, exhibits a slow decay towards zero when $|t|$ increases.

- *Meyer wavelet [Meyer, 1990] is an orthogonal wavelet with a C^∞ smoothness and a fast decay towards zero;*
- *Daubechies wavelets [Daubechies, 1988] were the first wavelets to possess both a high (but finite) smoothness and a compact support. These wavelets are indexed by a finite but arbitrarily high number of vanishing moments $N \in \mathbb{N}^*$, and their support is given by $[0, 2N - 1]$.*

These examples of orthogonal wavelets being stated, it is worth highlighting the slightly different framework of bi-orthogonal wavelets.

Remark 2.7.2 Bi-orthogonal wavelets

The construction of orthogonal wavelet bases obviously imposes some additional restrictions for the design of both the scaling function φ and analysing wavelet ψ , compared to the CWT framework. To soften these restrictions, bi-orthogonal wavelets have thus been designed. Following [Jawerth and Sweldens, 1994], the idea is to no longer impose that φ and ψ generate orthonormal bases of V_j and W_j respectively. Thus, if one still denotes by Q_j the projection operator on W_j , it can only be stated that, for all $f \in L^2(\mathbb{R})$:

$$Q_j(f) = \sum_{k \in \mathbb{Z}} l_k(Q_j(f)) \psi_{j,k}, \quad (2.173)$$

$$= \sum_{k \in \mathbb{Z}} (l_k \circ Q_j)(f) \psi_{j,k}, \quad (2.174)$$

where:

- $(\psi_{j,k})_{k \in \mathbb{Z}}$ still denotes a (non-orthogonal) basis of W_j ;
- $l_k \circ Q_j : v \in W_j \mapsto (l_k \circ Q_j)(v) \in \mathbb{R} \text{ or } \mathbb{C}$ is the unique linear form on W_j satisfying:

$$\forall k' \in \mathbb{Z}, (l_k \circ Q_j)(\psi_{j,k'}) = \delta_k^{k'}, \quad (2.175)$$

where $\delta_k^{k'}$ denotes the Kronecker symbol.

If one now denotes by $(\tilde{\psi}_{j,k})_{k \in \mathbb{Z}}$ the dual basis of $(\psi_{j,k})_{k \in \mathbb{Z}}$, i.e. the basis that generates the dual space W_j^* of W_j , and which moreover satisfies:

$$\forall j_1, j_2, k_1, k_2 \in \mathbb{Z}, \langle \tilde{\psi}_{j_1, k_1}, \psi_{j_2, k_2} \rangle_{L^2} = \delta_{j_1}^{j_2} \delta_{k_1}^{k_2}, \quad (2.176)$$

then Riesz representation theorem ensures that for all $f \in L^2(\mathbb{R})$, $j, k \in \mathbb{Z}$:

$$(l_k \circ Q_j)(f) = \langle \tilde{\psi}_{j,k}, f \rangle_{L^2}. \quad (2.177)$$

This result allows to rewrite the projection of $f \in L^2(\mathbb{R})$ on W_j as follows:

$$Q_j(f) = \sum_{k \in \mathbb{Z}} \langle \tilde{\psi}_{j,k}, f \rangle_{L^2} \psi_{j,k}. \quad (2.178)$$

Finally, using the still valid (but no longer orthogonal) direct-sum (2.165), the following inverse discrete wavelet transform is obtained for all $f \in L^2(\mathbb{R})$:

$$\boxed{\forall x \in \mathbb{R}, f(x) = \sum_{j,k \in \mathbb{Z}} \langle \tilde{\psi}_{j,k}, f \rangle_{L^2} \psi_{j,k}(x).} \quad (2.179)$$

This remark on bi-orthogonal wavelets thus concludes this section dedicated to Discrete Wavelet Transform and Multi-Resolution Analysis (MRA).

Now, before concluding this bibliography chapter, the next two sections discuss the issue of "wavelets and boundary conditions", and present some of the numerous applications of wavelets theory, in fields such as signal processing, operator analysis and PDEs.

2.8 Wavelets and boundary conditions

Similarly to multi-scale and homogenization methods, MRA and Continuous Wavelet Transform (CWT) also face a challenge with the treatment of boundary conditions. Indeed, both integer translations and convolution product require to be defined on the whole real line \mathbb{R} . Nevertheless, motivated by the numerical computation of PDEs, efforts have been made to

adapt the MRA framework to an interval, and bounded domains in general. Intuitive methods such as "zero-padding" or periodizing introduce discontinuities and high-frequencies on the boundaries. To prevent such phenomena, constructions of wavelet bases on an interval, based on Daubechies compactly-supported wavelets, have been put forward in literature. For further details on this topic, the interested reader may refer to the works of [Meyer, 1992, Auscher, 1993, Cohen et al., 1994, Monasse and Perrier, 1995], and [Chiavassa and Liandrat, 1997]. As for Continuous Wavelet Transform, it will be detailed in chapter 3 how it may take into account PDEs boundary conditions. But for now, let us turn towards some important applications of wavelets.

2.9 Wavelets, signal processing, operator analysis, and PDEs

Wavelets have met an important success in scientific fields such as signal processing, operator analysis and PDEs.

Indeed, in signal or image processing applications, especially if data compression is not the main objective, Continuous Wavelet Transform (CWT) can be used, for instance with complex analytic or directional wavelets, to study instantaneous frequencies contained within a signal, or detect edges and oriented features in a picture. Besides, in the following of this manuscript, it will also be proven that CWT can be used, with smooth and isotropic real-valued wavelets, as a regularizing tool to study heterogeneous media or multi-scale phenomena, leading to a new possible formulation of homogenization and multi-scale methods. As for MRA, it is of course ideally suited for data compression driven applications. The JPEG 2000 image compression format is for instance a good example of the use of orthogonal wavelets.

Beside data compression, orthogonal wavelets have also shown their relevance in operator analysis and PDEs, as they allow to represent, in a sparse way, linear operators. Indeed, thanks to the inverse discrete wavelet transform (2.168) detailed earlier in the framework of orthogonal MRA, the action of any linear operator T on a function $f \in L^2(\mathbb{R})$ can be written as follows:

$$T(f) = \sum_{j,k \in \mathbb{Z}} \langle \psi_{j,k}, f \rangle_{L^2} T(\psi_{j,k}), \quad (2.180)$$

$$= \sum_{j,k \in \mathbb{Z}} \langle \psi_{j,k}, f \rangle_{L^2} \left(\sum_{i,l \in \mathbb{Z}} \langle \psi_{i,l}, T(\psi_{j,k}) \rangle_{L^2} \psi_{i,l} \right), \quad (2.181)$$

$$= \sum_{i,l \in \mathbb{Z}} \left(\sum_{j,k \in \mathbb{Z}} \langle \psi_{i,l}, T(\psi_{j,k}) \rangle_{L^2} \langle \psi_{j,k}, f \rangle_{L^2} \right) \psi_{i,l}. \quad (2.182)$$

Following [Beylkin et al., 1991, Beylkin, 1992], the matrix $(\langle \psi_{i,l}, T(\psi_{j,k}) \rangle_{L^2})_{(i,l),(j,k)}$ is referred to as the standard representation of

the operator T in the orthogonal wavelet basis $(\psi_{j,k})_{j,k \in \mathbb{Z}}$. Ideally, if these wavelets were eigenvectors of the operator T , this matrix would be diagonal. In the general case, it is of course not the case. Nevertheless, as detailed in [Jawerth and Sweldens, 1994], the operator matrix may be considered "almost diagonal", as off-diagonal elements are quickly becoming small, thanks to the fast decay (or ideally compact support) of the wavelets $\psi_{j,k}$, which impacts the decay of $T(\psi_{j,k})$, and thus its L^2 -inner product with $\psi_{i,l}$.

Such sparse representations of linear operators are of course not something brand new. Finite difference or finite element methods already allow to solve sparse linear systems. However, these systems are often ill-conditioned, which slows down iterative methods. The sparse representation of a linear operator in a wavelet basis, conversely, allows to decrease the condition number, as detailed in [Beylkin et al., 1991], which presents the BCR algorithm designed to compress Calderon-Zygmund operators into a sparse form. The interested reader may also refer to [Lazaar et al., 1994, Tchamitchian, 1996, Alpert et al., 2002] and [Piquemal and Liandrat, 2005].

Finally, in the spirit of adaptive grid methods, such as multi-level adaptive techniques [Brandt, 1977] or adaptive mesh refinement [Berger and Oliger, 1984], adaptive wavelet methods have been designed for the computation of PDEs. For an extensive overview of these methods, the reader may refer to the reference works of [Jaffard, 1991, Liandrat et al., 1992, Dahmen, 1997] and [Cohen, 2000]. Basically, such methods mainly spread into two families: on the one hand, wavelet-based Galerkin methods for finite element computations, such as in [Frohlich and Schneider, 1997], [Schneider et al., 2001, Mehraeen and Chen, 2006], and, on the other hand, adaptive multi-resolution schemes for finite volume computations, with numerous works such as the ones of [Berger and Collela, 1989, Harten, 1994] and [Bihari and Harten, 1995, Bihari and Harten, 1997], or more recently the works of [Cohen et al., 2003, Müller, 2003, Roussel et al., 2003], [Bramkamp et al., 2004, Roussel and Schneider, 2005, Dahmen et al., 2013]. Multi-resolution schemes take advantage of the fact that wavelet coefficients contain information on the local regularity and local variations of a function. Indeed, wavelet coefficients tend towards zero in regions where the function is smooth, and increase in regions of steep gradients. Thus, a coarse grid can be used to compute the solution where wavelet coefficients are below a given tolerance, and dyadic nested refinements can be implemented in other regions. For general spatial discretizations and meshes, projection and prediction operators are introduced to go back and forth between each level of the nested grids, in the spirit of multi-grid methods. In the 1D case, or with 2D Cartesian grids, the MRA framework previously described can be used to define the operator going from the grid $(s_j = 2^{-j})$ to the refined grid $(s_{j+1} = 2^{-(j+1)})$.

2.10 Conclusion

This chapter presented an overview of the state of the art on porous media approaches, homogenization and multi-scale methods, with a final major focus

on wavelets theory. Scientific fields such as FSI, heterogeneous materials, turbulence, signal processing and operator analysis were highlighted. Despite their apparent differences, almost all the methods previously described face similar limitations. Indeed, the issues of boundary conditions and closure between resolved and unresolved scales stand out as a common denominator. Plain averaging/filtering methods or asymptotic expansions are indeed ill-posed in the vicinity of a domain boundary, and always require an *ad hoc* closure model (cf. concentration tensor, Smagorinsky eddy-viscosity model, series expansion...). Furthermore, the homogenization literature was also shown to rely on additional assumptions such as periodicity, scale separation, and linearity.

Wavelets, conversely, offer a reconstruction formula that allows to connect resolved and unresolved scales without any *ad hoc* model. This analytical closure expression also allows to properly take into account PDEs boundary conditions, and to handle, if necessary, nonlinearities. To the author's knowledge, a wavelet-based model able to tackle these major issues would be a brand new contribution in the literature of homogenization and multi-scale methods. To reach this goal, the crux of the matter is thus to explain how Continuous Wavelet Transform (CWT) may be applied onto a continuum medium PDEs, possibly exhibiting non-smooth solutions, and how the resulting spatially-filtered PDEs indeed define a homogenized continuum medium. This is the aim of the following chapter, which is dedicated to the thorough description of the wavelet-based multi-scale and homogenized model.

Chapter 3

A wavelet-based multi-scale and homogenized model

3.1 Introduction

The need for a homogenized approach of FSI...

As already highlighted in the general introduction of this manuscript, this work deals with a Fluid-Structure Interaction (FSI) phenomenon that involves numerous interfaces, and multiple spatial scales. The classical FSI approach would lead, in such a context, to cumbersome computations. To bypass both the interface and multi-scale problematics, the choice has been made to turn towards a more mesoscopic approach, in the spirit of porous media, homogenization, and multi-scale methods.

...able to connect resolved and unresolved scales, and to handle boundary conditions.

The previous chapter emphasized how the wide literature on porous media, homogenization and multi-scale methods is confronted with major challenges. The issue of closure between resolved and unresolved scales, and the treatment of boundary conditions, were especially highlighted. Additional limitations such as scale separation, periodicity and linearity have also been discussed. Thus, in order to build a self-sustained multi-scale and homogenized model, it is necessary to first, analytically connect resolved and unresolved scales without any *ad hoc* model, and second, handle the PDEs boundary conditions. In the current work, these boundary conditions play a key role as they focus the interaction between the fluid and solid media.

Why CWT is the right tool to tackle these issues ?

In this quest for a self-sustained multi-scale and homogenized model, able to account for a compressible flow within a congested solid medium, wavelets and especially CWT progressively appeared as the right tool for the task. Indeed, wavelets allow to homogenize the fluid by filtering/smoothing out all interfaces

and high-frequency phenomena. This filtering process hereafter relies on a convolution product between an analysing wavelet or scaling function, and the fluid conservation laws and equation of state. It results in PDEs governing a homogenized fluid, whose variables are now the wavelet coefficients of the original fluid variables.

Furthermore, thanks to an inverse wavelet transform, it is now possible to analytically connect the homogenized fluid (i.e. the resolved scales) to the real fluid (i.e. the unresolved scales). This also opens the way to a proper transfer of the real fluid boundary conditions into the homogenized fluid.

Last but not least, the convolution product that is here promoted between a wavelet (or scaling function) and the PDEs governing an inviscid compressible fluid, may be extended to generic PDEs.

How to choose the wavelets (or scaling function) scale parameter ?

As described in the previous chapter, wavelets are band-pass filters, while scaling functions are low-pass filters. When designing a wavelet-based multi-scale model, one can naturally wonder how to determine the relevant spatial scales that need to be computed. This is case-dependent, and requires to have some insights on the spectrum of the quantities of interest. In the current work, as turbulence effects are neglected, it is expected that the solid medium will drive the relevant spatial scales. But first, the important point is to check whether the wavelet-based multi-scale model actually converges towards a high-resolution computation (e.g. Direct Numerical Simulation) when the wavelets or scaling function catch all the possible spatial scales, i.e. when the cutoff scale s_0 tends towards zero. However, it shall be kept in mind that the wavelet explicit filtering is not independent from the mesh implicit filtering. Indeed, one cannot hope to represent all spatial scales by decreasing s_0 if the mesh size h is not refined accordingly. Compatibility conditions between s_0 and h will moreover be emphasized in order to prevent instabilities and aliasing in the numerical computations.

Why not use orthogonal wavelet bases to avoid redundancy ?

The wavelets scientific community is known to be divided between advocates of respectively continuous and discrete wavelets. When it comes to the numerical computation of PDEs, discrete wavelets seem to have taken the upper ground. Indeed, the previous chapter underlined how Discrete Wavelet Transform and orthogonal wavelet bases could be seen as an "improvement" compared to Continuous Wavelet Transform. These orthogonal bases indeed discard all redundant information, and can be used to compress linear operators into a sparse form.

However, it is here important to keep in mind that the current work aims at deriving PDEs governing an equivalent homogenized fluid, defined at the continuum medium scale. The homogenization process shall also stay as much as possible independent from any specific choice of discretization technique. The framework of Discrete Wavelet Transform and Multi-Resolution Analysis,

with its integer translations and dyadic refinements, is rather suited to finite-difference schemes and Cartesian grids.

Furthermore, it will be proven, later in this chapter, that the analysing wavelet Ψ and scaling function Φ have to possess a C^∞ smoothness, in order to properly define a convolution product with the fluid PDEs. Indeed, as compressible flows may exhibit non-smooth solutions (e.g. shock waves), the fluid equations shall be manipulated in a weak sense. This will require to work within the mathematical framework of distributions theory. Discrete orthogonal wavelets such as Daubechies' indeed possess a useful compact support, but exhibit "only" a $C^{\mu N}$ smoothness, with $\mu \approx 0.2$ and $N < +\infty$.

Finally, the non-redundancy property of orthogonal wavelets, and their resulting ability to compress linear operators into a sparse form with a low condition number (cf. the BCR algorithm highlighted in the previous chapter), is mostly relevant in the context of iterative methods and implicit schemes. The current work deals with a fast-transient wave propagation phenomenon, which is classically computed with explicit schemes. Indeed, as the time step is here constrained by the wave velocity, whether the scheme is implicit or explicit, the second option offers the advantage to avoid any matrix inversion process.

Thus, the framework of Continuous Wavelet Transform (CWT) appears here better suited for the implementation of a homogenization/filtering process.

How to choose between a real and complex wavelet ?

In parallel with the "continuous VS discrete" debate, one cannot avoid the discussion between real and complex wavelets. For 1D time signals analysis, complex analytic wavelets, with their ability to track instantaneous frequencies, definitely have the upper ground. However, in the current work, CWT aims at filtering 2D fields that do not possess any oriented feature. Indeed, both the analysing wavelet and scaling function shall be able to "observe" pressure waves propagating in different directions simultaneously (reflection/transmission on obstacles). Furthermore, it will be proven that both the analysing wavelet and scaling function shall possess a C^∞ smoothness, a good localization in the spatial domain, and a fast decay towards zero. A real wavelet such as the isotropic Mexican hat fulfills all these requirements. It also offers the advantage to lead to spatially-filtered PDEs expressed in the physical domain.

How to implement CWT on the fluid PDEs, or on generic PDEs ?

Now that the important debates on "continuous VS discrete" and "real VS complex" wavelets have been settled in the current context, one can wonder how, practically speaking, CWT will hereafter be applied to the fluid PDEs (or to generic PDEs). As described in the previous chapter, CWT can be seen as a convolution product between a signal of interest, and an analysing wavelet or scaling function. To now apply such a convolution product on PDEs which may exhibit non-smooth solutions, this manuscript puts forward the following generic procedure:

- "weak-extension": first, extend, in a weak sense, the original fluid PDEs to \mathbb{R}^2 ; this step is mandatory to ensure the proper definition of convolution product on \mathbb{R}^2 ; this extension will mostly rely on Green's formula for integration by parts and distributions theory; the treatment of the fluid boundary conditions will here play a key role;
- "weak-convolution": second, write, in a weak sense, the convolution product between the analysing wavelet or scaling function, and the extended fluid PDEs; this requires to state all the requirements that the wavelet and scaling function have to fulfill in order to properly define the convolution with a distribution; this "weak-convolution" will eventually result in spatially-filtered PDEs governing a homogenized fluid. Its variables will moreover be expressed as wavelet coefficients of the original fluid variables.

How a linear transform such as CWT may handle nonlinearities ?

Last, but not least, one may question the ability of a linear transform such as CWT to actually handle nonlinearities. There is not any magical formula allowing to express the wavelet transform of a nonlinear term, here the convective term $(\rho \underline{v} \otimes \underline{v})$, in terms of the wavelet transform of its individual components ρ and \underline{v} . Nevertheless, thanks to the reconstruction property of CWT, it is now possible to recover (up to an approximation), at each time step, the original density ρ and velocity \underline{v} from their respective wavelet coefficients $\mathcal{W}[\rho](s, \cdot)$ and $\mathcal{W}[\underline{v}](s, \cdot)$. It is thus possible to compute explicitly the wavelet coefficients $\mathcal{W}[\rho \underline{v} \otimes \underline{v}](s, \cdot)$ from the reconstructed fields. Such a process is of course expected to deteriorate the computation time.

In fluid mechanics, the nonlinear convective term is mainly responsible for turbulence effects, as detailed in the section dedicated to Large Eddy Simulation (LES). The current work considers a fast-transient phenomenon, during which turbulent dissipation is classically negligible compared to pressure gradients, given the time scale of interest. Thus, the treatment of the nonlinear convective term will hereafter be simplified, avoiding additional reconstruction processes.

All these important questions being now answered, it shall here be noted that the homogenization process will hereafter be applied in a 2D framework. Indeed, fuel assemblies inner structure needs to be accounted for only in a transverse section, while the components of the pressure waves along the axial direction can be described using standard discretization techniques (see Figure 2.2a for an illustration of a PWR fuel assembly). Spacer grids contribute little to the response of the assemblies to a transverse wave. Thus, classical regular and singular head loss models can be implemented to account for these grids, and for the friction along the rods that may impact the axial component of the waves.

Besides, as only the fluid occupies a connected domain in the problem of

interest, the choice has been made to apply the homogenization process only to the fluid. It will thus focus our modeling efforts. As for the fuel assemblies, considering the 2D modeling framework, and the focus on transverse pressure waves, the behavior of their cross section will be modeled, in first approximation, as a rigid body possessing 2 degrees of freedom, here two translations. Such an approximation is motivated by the fact that spacer grids tend to maintain a constant distance between the individual fuel rods contained within an assembly.

Throughout this third chapter, the wavelet-based multi-scale and homogenized model will progressively take shape, with the following steps:

- [3.2] the equations of both the solid and fluid media will be recalled at the microscopic scale;
- [3.3] important mathematical results regarding the non-smooth behavior of the solutions to the fluid PDEs will be recalled; this behavior will hereafter require to manipulate the fluid equations in a weak sense;
- [3.4] wavelet-based homogenization: in order to apply Continuous Wavelet Transform (CWT) to the fluid equations, the following procedure will be implemented:
 - (i) "weak-extension" of the original fluid equations to \mathbb{R}^2 ;
 - (ii) "weak-convolution" product between the extended fluid equations, and a well-designed wavelet or scaling function;
- [3.5] boundary conditions, closure, and nonlinearities: the ability of CWT to deal with these 3 important issues will be emphasized;
- [3.6] "analytical" accuracy and convergence: the model ability to converge (in a sense to be specified) towards Direct Numerical Simulation (DNS) will be discussed;
- [3.7] the analysing wavelet Ψ and scaling function Φ will be specified;
- [3.8] all the model assumptions and equations will then be summarized;
- [3.9] numerical methods: finally, the last section will describe the numerical methods chosen to implement the wavelet-based model; a special focus will be put on the problematics of stability, which is a critical point for explicit schemes, and aliasing, which is linked to the numerical implementation of wavelet transform.

3.2 Modeling at the microscopic scale

To begin this chapter, let us consider the modeling at the microscopic scale. As an illustration for the problem at study, let us consider the 2D geometry displayed on the following Figure 3.1:

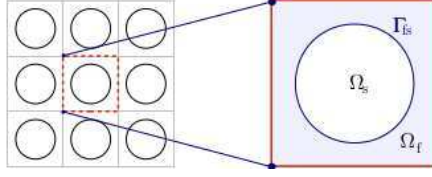


Figure 3.1: Illustration of a 2D {fluid + solid} geometry.

The whole {fluid + solid} domain thus contains:

- a fluid domain Ω_f , which is an open bounded and connected space of \mathbb{R}^2 ;
- a solid domain Ω_s , which is an open bounded and disconnected space of \mathbb{R}^2 : $\Omega_s = \cup_i \Omega_{s_i}$, with $\Omega_{s_i} \cap_{i \neq j} \Omega_{s_j} = \emptyset$.

It is important to note that no periodicity or scale separation assumption on the solid domain Ω_s will be needed in the design of the model.

3.2.1 Solid medium

As illustrated in Figure 3.1, the solid medium of interest is composed of the disjoint reunion of multiple disks, here arranged in an array representing the cross section of a fuel assembly. As spacer grids tend to maintain a constant distance between neighboring disks, the global array will be considered as a rigid body animated with two degrees of freedom, respectively horizontal and vertical translations. The behavior of the array will be modeled by a linear oscillator for each degree of freedom, whose dynamic equilibrium is governed by the following differential equation:

$$\forall i \in \{1, 2\}, m\ddot{U}_i + c\dot{U}_i + kU_i = \underline{F}_{F \rightarrow S} \cdot \underline{e}_i, \quad (3.1)$$

or equivalently:

$$\boxed{\forall i \in \{1, 2\}, \ddot{U}_i + 2\xi\omega_0\dot{U}_i + \omega_0^2 U_i = \frac{1}{m} \times (\underline{F}_{F \rightarrow S} \cdot \underline{e}_i)}, \quad (3.2)$$

where:

- $(\underline{e}_1, \underline{e}_2)$ is the orthonormal Cartesian basis of \mathbb{R}^2 ;
- $\underline{U} = (U_1 \ U_2)^T$ is the displacement (m);
- m is the mass (kg);
- c is the friction coefficient (kg.s^{-1});
- k is the system stiffness ($\text{N.m}^{-1} = \text{kg.s}^{-2}$);
- ω_0 is the system eigenfrequency, defined by: $\omega_0 = \sqrt{\frac{k}{m}}$ (rad.s^{-1});
- ξ is the (dimensionless) damping coefficient, defined by: $\xi = \frac{c}{2\sqrt{km}}$.
- $\underline{F}_{F \rightarrow S}$ is the force (N) applied by the fluid to the whole array of disks.

3.2.2 Fluid

Let us now consider the water flow. Under nominal operating conditions, the water within a PWR core is purely liquid at around 300°C under 155 bar. The flow is almost vertical, incompressible and very turbulent, with a Reynolds number around 10^5 . However, the current work deals with the propagation of a transverse pressure wave through the flow and fuel assemblies. The theory of viscous incompressible flow is therefore no longer relevant. To account for such a fast-transient phenomenon, the following modeling framework is hereafter considered:

- monophasic compressible flow;
- inviscid fluid: viscosity and turbulence effects are negligible compared to pressure gradients;
- gravity is negligible compared to pressure gradients;
- conduction heat transfer is negligible on the time scale at study;
- barotropic fluid;

Based on this modeling framework, the water flow is governed by the following Euler compressible equations:

$$\boxed{\begin{array}{rcl} \partial_t \rho + \operatorname{div}(\rho \underline{v}) & = & 0 \quad \text{in } \Omega_f(t), \\ \partial_t(\rho \underline{v}) + \operatorname{div}(\rho \underline{v} \otimes \underline{v}) & = & -\underline{\nabla} p \quad \text{in } \Omega_f(t), \\ \partial_t(\rho e) + \operatorname{div}((\rho e + p) \underline{v}) & = & 0 \quad \text{in } \Omega_f(t), \end{array}} \quad (3.3)$$

where:

- ρ is the fluid density (kg.m^{-3});
- \underline{v} is the velocity field (m.s^{-1});
- p is the pressure field (Pa);
- e is the specific total energy (J.kg^{-1}).

The system (3.3) translates respectively the conservation of mass (ρ), momentum ($\rho \underline{v}$) and energy (ρe). This system of conservation laws is here closed by a barotropic equation of state:

$$\boxed{p = p_{ref} + c_{son}^2 (\rho - \rho_{ref})}, \quad (3.4)$$

where ρ_{ref} is a reference density, $p_{ref} = p(\rho_{ref})$ the corresponding reference pressure, and $c_{son} = \sqrt{\partial_\rho p}$ the sound velocity in the fluid.

Regarding now the boundary conditions, the assumption of inviscid fluid implies:

$$\boxed{\begin{aligned} \underline{u} \cdot \underline{n}_{F \rightarrow S} &= \partial_t \underline{U} \cdot \underline{n}_{F \rightarrow S} && \text{on } \partial\Omega_f \cap \partial\Omega_s, \\ \underline{u} \cdot \underline{n}_{F \rightarrow ext} &= 0 && \text{on } \partial\Omega_f \setminus \partial\Omega_s, \end{aligned}} \quad (3.5)$$

where $\underline{n}_{F \rightarrow S}$ and $\underline{n}_{F \rightarrow ext}$ denote the outward unit normal vectors on the boundary $\partial\Omega_f$.

Thus, given an initial data, the pressure wave is completely described by Euler compressible equations (3.3), the barotropic equation of state (3.4) and the kinematic condition (3.5) on the flow boundary.

Now, before starting the wavelet-based homogenization process, the following section recalls important mathematical results regarding the non-smooth behavior of the solutions to the fluid PDEs. The focus is especially put on the role played by Rankine-Hugoniot condition with regards to the possible discontinuities.

3.3 Non-smooth behavior of the fluid PDEs

Euler compressible equations (3.3) are part of a general class of systems of PDEs, called hyperbolic systems. With such equations, the global existence (in time) of the classical solution is not guaranteed in the general case. Hence, weak solutions shall be considered. Furthermore, as hyperbolic systems may possess several weak solutions, an entropy function and its conservation law are generally added in order to select the solution physically relevant. In the case of an inviscid fluid satisfying a barotropic equation of state, the role of entropic equation is played by the energy balance equation. The interested reader may refer to [Godlewski and Raviart, 1996] for a detailed presentation on hyperbolic systems.

Regarding now the smoothness of this entropic solution, it can be determined by writing the weak formulation of (3.3) with smooth and compactly-supported test functions. Starting from an initial data $\underline{X}_0 = (\rho_0, (\rho \underline{u})_0, (\rho e)_0)$ locally bounded in Ω_f (L_{loc}^∞), it can be shown that the entropic solution $\underline{X} = (\rho, \rho \underline{u}, \rho e)$ will possess the same spatial smoothness. Moreover, the fluid domain Ω_f being bounded, a L^q spatial smoothness is satisfied for all $q \in [1, +\infty]$. Nevertheless, it can be noted that, in literature, weak solutions are generally assumed to be piecewise C^1 functions in time and space, whose jumps across surfaces of discontinuity are governed by the Rankine-Hugoniot condition. Shock waves in compressible flows are a perfect example of such discontinuities. The framework of piecewise C^1 solutions will thus be hereafter considered.

In order to recall Rankine-Hugoniot condition, let us consider the following generic hyperbolic system of p conservation laws, here written in conservative form:

$$\partial_t \underline{u}(\underline{x}, t) + \underline{\text{div}} \left(\underline{G}(\underline{u}) \right) (\underline{x}, t) = \underline{0} \quad \text{in } \mathbb{R}^d \times]0, +\infty[, \quad (3.6)$$

or equivalently:

$$\partial_t \underline{u}(\underline{x}, t) + \sum_{j=1}^d \partial_{x_j} [\underline{g}_j(\underline{u})](\underline{x}, t) = \underline{0} \text{ in } \mathbb{R}^d \times]0, +\infty[, \quad (3.7)$$

where:

- $\underline{u} = (u_1 \dots u_p)^T$ is the vector of unknown conservative variables, for instance $\underline{u} = (\rho \ \rho v_x \ \rho v_y \ \rho e)^T$ in the case of 2D Euler compressible equations;
- $\underline{G}(\underline{u})$ is a $(p \times d)$ matrix whose columns are the d flux functions g_j :

$$\underline{G}(\underline{u}) = \begin{pmatrix} G_{1,1} & \dots & G_{1,d} \\ \vdots & & \vdots \\ G_{p,1} & \dots & G_{p,d} \end{pmatrix}(\underline{u}), \quad (3.8)$$

$$= (\underline{g}_j(\underline{u}))_{1 \leq j \leq d}. \quad (3.9)$$

In the case of 2D Euler compressible equations, one has:

$$\underline{g}_1(\underline{u}) = (\rho v_x \ \rho v_x^2 + p \ \rho v_y v_x \ (\rho e + p)v_x)^T, \quad (3.10)$$

$$\underline{g}_2(\underline{u}) = (\rho v_y \ \rho v_y v_x \ \rho v_y^2 + p \ (\rho e + p)v_y)^T. \quad (3.11)$$

Following [Godlewski and Raviart, 1996], one can write, for all test functions $\underline{\varphi} \in [D(\mathbb{R}^d \times]0, +\infty[)]^p$, the weak formulation of (3.7) as follows:

$$\begin{aligned} & \left\langle \partial_t \underline{u} + \sum_{j=1}^d \partial_{x_j} [\underline{g}_j(\underline{u})], \underline{\varphi} \right\rangle_{D', D} \\ &= - \int_0^{+\infty} \int_{\mathbb{R}^d} \left(\underline{u} \cdot \partial_t \underline{\varphi} + \sum_{j=1}^d \underline{g}_j(\underline{u}) \cdot \partial_{x_j} \underline{\varphi} \right) d\underline{x} dt \\ &= 0. \end{aligned} \quad (3.12)$$

In order to emphasize why weak solutions of such hyperbolic systems have to satisfy Rankine-Hugoniot condition, one can:

- consider, for simplicity, that the solution \underline{u} , which is piecewise C^1 on $\mathbb{R}^d \times]0, +\infty[$, possesses only a single (smooth) surface Σ of discontinuity, which thus cuts the domain $\mathbb{R}^d \times]0, +\infty[$ into two subdomains Ω^+ / Ω^- ;

- split, thanks to Chasles' relation, the above weak formulation (3.12) into two integrals, one for each subdomain;
- use twice Green's formula for integration by parts in order to introduce two integrals on the boundary Σ ;
- use the fact that the solution is smooth on both Ω^+ and Ω^- , which implies that it satisfies the hyperbolic system (3.7) in a strong sense;
- and finally, bring together the two integrals on the boundary Σ , in order to obtain an equation driving the discontinuity jump of the solution across Σ , namely Rankine-Hugoniot condition;

Before going further, let us introduce some notations:

Notations 3.3.1 • $\mathbb{R}^d \times]0, +\infty[= \Omega^+ \cup \Omega^-$, such that $\Omega^+ \cap \Omega^- = \emptyset$, and $\Sigma = \partial\Omega^+ \cap \partial\Omega^-$;

- $\underline{n}_\Sigma = (n_t \ n_1 \ \dots \ n_d)^T$ denotes a normal vector of the surface Σ , oriented from Ω^+ to Ω^- ;
- $[f]_\Sigma^+ := f^+ - f^-$ denotes the jump of the function f across the surface of discontinuity Σ ;
- $\{f\}$ denotes a piecewise continuous function on $\mathbb{R}^d \times]0, +\infty[$ which coincides with the distribution f on $(\mathbb{R}^d \times]0, +\infty[) \setminus \Sigma$.

Step 1 : Chasles' relation

Following [Godlewski and Raviart, 1996], one can first write, by using Chasles' relation:

$$\begin{aligned}
 & - \int_0^{+\infty} \int_{\mathbb{R}^d} \left(\underline{u} \cdot \partial_t \underline{\varphi} + \sum_{j=1}^d \underline{g}_j(\underline{u}) \cdot \partial_{x_j} \underline{\varphi} \right) d\underline{x} dt \\
 & \quad = - \int_{\Omega^+} \left(\underline{u} \cdot \partial_t \underline{\varphi} + \sum_{j=1}^d \underline{g}_j(\underline{u}) \cdot \partial_{x_j} \underline{\varphi} \right) d\underline{x} dt \\
 & \quad \quad - \int_{\Omega^-} \left(\underline{u} \cdot \partial_t \underline{\varphi} + \sum_{j=1}^d \underline{g}_j(\underline{u}) \cdot \partial_{x_j} \underline{\varphi} \right) d\underline{x} dt. \quad (3.13)
 \end{aligned}$$

Step 2 : Green's formula for integration by parts

Then, by using Green's formula for integration by parts, the integrals on the two subdomains Ω^+ and Ω^- can be rewritten as:

$$\begin{aligned}
 & - \int_{\Omega^+} \left(\underline{u} \cdot \partial_t \underline{\varphi} + \sum_{j=1}^d \underline{g}_j(\underline{u}) \cdot \partial_{x_j} \underline{\varphi} \right) d\underline{x} dt \\
 & = \int_{\Omega^+} \{ \partial_t \underline{u} \} \cdot \underline{\varphi} d\underline{x} dt - \int_{\Sigma} \underline{u}^+(\underline{\sigma}) \cdot \underline{\varphi}(\underline{\sigma}) n_t d\underline{\sigma} + \int_{\Omega^+} \sum_{j=1}^d \{ \partial_{x_j} \underline{g}_j(\underline{u}) \} \cdot \underline{\varphi} d\underline{x} dt \\
 & \quad - \int_{\Sigma} \sum_{j=1}^d n_j \underline{g}_j^+(\underline{u}(\underline{\sigma})) \cdot \underline{\varphi}(\underline{\sigma}) d\underline{\sigma}. \quad (3.14)
 \end{aligned}$$

$$\begin{aligned}
 & - \int_{\Omega^-} \left(\underline{u} \cdot \partial_t \underline{\varphi} + \sum_{j=1}^d \underline{g}_j(\underline{u}) \cdot \partial_{x_j} \underline{\varphi} \right) d\underline{x} dt \\
 & = \int_{\Omega^-} \{ \partial_t \underline{u} \} \cdot \underline{\varphi} d\underline{x} dt - \int_{\Sigma} \underline{u}^-(\underline{\sigma}) \cdot \underline{\varphi}(\underline{\sigma}) (-n_t) d\underline{\sigma} + \int_{\Omega^-} \sum_{j=1}^d \{ \partial_{x_j} \underline{g}_j(\underline{u}) \} \cdot \underline{\varphi} d\underline{x} dt \\
 & \quad - \int_{\Sigma} \sum_{j=1}^d (-n_j) \underline{g}_j^-(\underline{u}(\underline{\sigma})) \cdot \underline{\varphi}(\underline{\sigma}) d\underline{\sigma}. \quad (3.15)
 \end{aligned}$$

By adding these last two equations, one obtains:

$$\begin{aligned}
 & - \int_0^{+\infty} \int_{\mathbb{R}^d} \left(\underline{u} \cdot \partial_t \underline{\varphi} + \sum_{j=1}^d \underline{g}_j(\underline{u}) \cdot \partial_{x_j} \underline{\varphi} \right) d\underline{x} dt \\
 & = \int_{\Omega^+} \left\{ \partial_t \underline{u} + \sum_{j=1}^d \partial_{x_j} \underline{g}_j(\underline{u}) \right\} \cdot \underline{\varphi} d\underline{x} dt + \int_{\Omega^-} \left\{ \partial_t \underline{u} + \sum_{j=1}^d \partial_{x_j} \underline{g}_j(\underline{u}) \right\} \cdot \underline{\varphi} d\underline{x} dt \\
 & \quad - \int_{\Sigma} \left(n_t [\underline{u}]_-^+ + \sum_{j=1}^d n_j [\underline{g}_j(\underline{u})]_-^+ \right) (\underline{\sigma}) \cdot \underline{\varphi}(\underline{\sigma}) d\underline{\sigma}. \quad (3.16)
 \end{aligned}$$

Step 3 : the solution is smooth in Ω^+ and Ω^-

As the solution \underline{u} is of class C^1 in both Ω^+ and Ω^- , one can state that it satisfies the conservation laws of the hyperbolic system (3.7) in a strong sense within these two subdomains. Thus, the weak formulation (3.12) of the hyperbolic system reduces to:

$$\begin{aligned}
 & \forall \underline{\varphi} \in \left[D \left(\mathbb{R}^d \times [0, +\infty[\right) \right]^p, \\
 & \int_{\Sigma} \left(n_t [\underline{u}]_-^+ + \sum_{j=1}^d n_j [\underline{g}_j(\underline{u})]_-^+ \right) (\underline{\sigma}) \cdot \underline{\varphi}(\underline{\sigma}) d\underline{\sigma} = 0, \quad (3.17)
 \end{aligned}$$

which finally leads to the well-known Rankine-Hugoniot condition driving the discontinuity jump across Σ :

Rankine-Hugoniot condition

$$\forall \underline{\sigma} \in \Sigma, \left(n_t [\underline{u}]_-^+ + \sum_{j=1}^d n_j [\underline{g}_j(\underline{u})]_-^+ \right) (\underline{\sigma}) = \underline{0}. \quad (3.18)$$

Remark 3.3.1 *Following again [Godlewski and Raviart, 1996], if $(n_1 \dots n_d)^T \neq \underline{0}$, the normal vector \underline{n}_Σ can be normalized as:*

$$\tilde{\underline{n}}_\Sigma = \frac{1}{\left\| (n_1 \dots n_d)^T \right\|_{\mathbb{R}^d}} (n_t \ n_1 \ \dots \ n_d)^T, \quad (3.19)$$

$$= (-c \ \underline{\nu})^T, \quad (3.20)$$

where $c \in \mathbb{R}$, and $\underline{\nu}$ is now a unit vector of \mathbb{R}^d . This notation allows to rewrite Rankine-Hugoniot condition as:

$$\boxed{c [\underline{u}]_-^+ = \sum_{j=1}^d \nu_j [\underline{g}_j(\underline{u})]_-^+}, \quad (3.21)$$

where c can be considered as the speed of propagation of the discontinuity, and $\underline{\nu}$ its direction of propagation.

This remark thus concludes this section dedicated to the mathematical analysis of Euler compressible equations. It was here recalled why it is necessary to manipulate the fluid PDEs in a weak sense. This section also emphasized how Rankine-Hugoniot condition plays an important role with regards to the possible discontinuities propagating within a compressible flow.

Let us now turn towards the actual wavelet-based homogenization process.

3.4 Wavelet-based homogenization

The wavelet-based homogenization process, at the core of this model, relies on the application of Continuous Wavelet Transform (CWT) to the fluid conservation laws and equation of state. The filtered equations governing the homogenized fluid are thus obtained by writing the convolution products between a wavelet family $(\Psi_s)_{s>0}$, or the associated scaling function Φ_{s_0} , and the (extended) fluid equations, as formally illustrated by equations (3.22-3.23) below:

$$(\tilde{\Psi}_s^*) * \begin{cases} \partial_t \rho + \operatorname{div}(\rho \underline{\nu}) & = 0, \\ \partial_t(\rho \underline{\nu}) + \operatorname{div}(\rho \underline{\nu} \otimes \underline{\nu}) & = -\underline{\nabla} p, \\ \partial_t(\rho e) + \operatorname{div}((\rho e + p) \underline{\nu}) & = 0, \end{cases} \quad (3.22)$$

$$\tilde{\Psi}_s^* * \{p = p_{ref} + c_{son}^2(\rho - \rho_{ref})\}. \quad (3.23)$$

It shall here be noted that, when studying a barotropic fluid, it is not necessary to solve the energy balance equation. Thus, only the mass and momentum balance equations will be hereafter considered.

Before detailing all the mathematical steps required to obtain the filtered equations governing the homogenized fluid, let us first specify the initial conditions of the problem.

3.4.1 Initial conditions: Riemann problem

As classically done in the study of hyperbolic systems, a Riemann problem (here with respect to the first component x_1) is hereafter considered. In other words, the following initial discontinuous density field is considered:

$$\forall \underline{x} \in \Omega_f, \rho_0(\underline{x}) = \begin{cases} \rho_l & \text{if } x_1 < d \\ \rho_r & \text{if } x_1 > d \end{cases} \quad (3.24)$$

$$\forall \underline{x} \in \Omega_f, (\rho \underline{v})_0(\underline{x}) = \underline{0}, \quad (3.25)$$

where ρ_l and ρ_r denote respectively the left and right initial densities, and d denotes the position of the initial density/pressure discontinuity. It is assumed that the solid medium is in equilibrium with the fluid, on the right side of the initial pressure discontinuity : $\Omega_s(0) \subset \{x_1 > d\}$.

To now implement the wavelet-based homogenization process, the following steps are required:

- (i) extend, in a weak sense, the fluid PDEs and equation of state to \mathbb{R}^2 ;
- (ii) write, in a weak sense, the convolution product between the wavelet (or scaling function) and the extended fluid equations.

3.4.2 "Weak-extension" of the fluid PDEs to \mathbb{R}^2

The extension of the original fluid equations to \mathbb{R}^2 is mandatory in order to properly define the convolution product with the analysing wavelet Ψ or scaling function Φ . As already recalled during the mathematical analysis of Euler compressible equations (3.3), the non-smooth behavior of the entropic solution requires to manipulate the equations in a weak sense. Therefore, the extension process also has to be done in a weak sense, especially as such an extension is expected to introduce discontinuities on the boundaries $\partial\Omega_s$ and $\partial\Omega_f \setminus \partial\Omega_s$. Thus, a two-steps procedure is hereafter followed to extend the fluid equations:

- [a]** first, extend the conservative fields $(\rho, \rho \underline{v}, p)$ into piecewise C^1 functions on $\mathbb{R}^2 \times]0, +\infty[$;
- [b]** second, carefully extend the mass and momentum balance equations to $\mathbb{R}^2 \times]0, +\infty[$ in a weak sense.

The "extended fluid" shall not be mistaken with the yet to come homogenized fluid. It is a first intermediary but also important step, as it will allow to properly "transfer" the boundary conditions of the real fluid into the future homogenized fluid.

Hereafter, for simplicity, same notations are used for the original and extended fields.

Basic requirements for the extension

The extension of the real fluid on Ω_s and $\mathbb{R}^2 \setminus (\Omega_f \cup \Omega_s)$ has to respect some conditions:

- the extended fluid has to coincide with the real fluid on Ω_f ;
- the extended fluid has to satisfy the barotropic equation of state on \mathbb{R}^2 :

$$p = p_{ref} + c_{son}^2 (\rho - \rho_{ref}) \quad \text{in } \mathbb{R}^2 \times]0, +\infty[. \quad (3.26)$$

- the (real) fluid located within Ω_f cannot enter the solid domain Ω_s or the exterior domain $\mathbb{R}^2 \setminus (\Omega_f \cup \Omega_s)$ (cf. kinematic boundary condition);
- the extended fluid located within the solid domain Ω_s or within the exterior domain $\mathbb{R}^2 \setminus (\Omega_f \cup \Omega_s)$ cannot enter the fluid domain Ω_f , as both the solid and exterior media are considered as closed systems, which do not exchange any matter with the real fluid;
- the extended fluid located within Ω_s , respectively $\mathbb{R}^2 \setminus (\Omega_f \cup \Omega_s)$, occupies a constant volume, respectively a fixed geometry, and thus possess a uniform density, as both the solid and exterior media are here considered as rigid and homogeneous bodies.

Thus, it can be stated that, for all $t \geq 0$:

$$\begin{aligned} \rho(\underline{x}, t) &= cst && \text{in } \Omega_s(t), \\ \rho(\underline{x}, t) &= cst && \text{in } \mathbb{R}^2 \setminus (\Omega_f \cup \Omega_s). \end{aligned} \quad (3.27)$$

As the pressure is directly linked to the density via the barotropic equation of state (3.26), one also has, for all $t \geq 0$:

$$\begin{aligned} p(\underline{x}, t) &= cst && \text{in } \Omega_s(t), \\ p(\underline{x}, t) &= cst && \text{in } \mathbb{R}^2 \setminus (\Omega_f \cup \Omega_s). \end{aligned} \quad (3.28)$$

Thus, the extended fluid trapped within the solid domain Ω_s or the exterior domain $\mathbb{R}^2 \setminus (\Omega_f \cup \Omega_s)$ can be considered as an inviscid and incompressible fluid, governed by the following Euler equations:

$$\begin{aligned} \rho (\partial_t \underline{v} + \underline{div}(\underline{v} \otimes \underline{v})) &= 0 && \text{in } \mathbb{R}^2 \setminus \Omega_f(t), \\ \underline{div}(\underline{v}) &= 0 && \text{in } \mathbb{R}^2 \setminus \Omega_f(t), \end{aligned} \quad (3.29)$$

and the following no-penetration kinematic conditions:

$$\begin{aligned} (\underline{v} - \partial_t \underline{U}) \cdot \underline{n}_{S \rightarrow F} &= 0 & \text{on } \partial\Omega_s(t) \\ \underline{v} \cdot \underline{n}_{ext \rightarrow F} &= 0 & \text{on } \partial\Omega_f \setminus \partial\Omega_s. \end{aligned} \quad (3.30)$$

Thus, the value $\underline{v}_s(t) = \partial_t \underline{U}(t)$ is an acceptable value for the extended fluid velocity within the solid domain Ω_s , while $\underline{v}_{ext} = \underline{0}$ is an acceptable value within the exterior domain.

Now, taking into account the fact that the solid medium is initially located on the right side of the pressure discontinuity, and moreover satisfies an equilibrium condition, the following extensions of the field (ρ, \underline{v}, p) can be defined:

[a] Extension of the fields (ρ, \underline{v}, p) to \mathbb{R}^2

$$\forall \underline{x} \in \mathbb{R}^2, \forall t \geq 0, \rho(\underline{x}, t) = \begin{cases} \rho(\underline{x}, t) & \text{if } \underline{x} \in \Omega_f(t) \\ \rho_r & \text{if } \underline{x} \in \Omega_s(t) \\ \rho_{ref} & \text{if } \underline{x} \in \mathbb{R}^2 \setminus (\Omega_f \cup \Omega_s) \end{cases} \quad (3.31)$$

$$\forall \underline{x} \in \mathbb{R}^2, \forall t \geq 0, \underline{v}(\underline{x}, t) = \begin{cases} \underline{v}(\underline{x}, t) & \text{if } \underline{x} \in \Omega_f(t) \\ \underline{v}_s(t) = \partial_t \underline{U}(t) & \text{if } \underline{x} \in \Omega_s(t) \\ \underline{v}_{ext} = \underline{0} & \text{if } \underline{x} \in \mathbb{R}^2 \setminus (\Omega_f \cup \Omega_s) \end{cases} \quad (3.32)$$

$$\forall \underline{x} \in \mathbb{R}^2, \forall t \geq 0, p(\underline{x}, t) = \begin{cases} p(\underline{x}, t) & \text{if } \underline{x} \in \Omega_f(t) \\ p_r & \text{if } \underline{x} \in \Omega_s(t) \\ p_{ref} & \text{if } \underline{x} \in \mathbb{R}^2 \setminus (\Omega_f \cup \Omega_s) \end{cases} \quad (3.33)$$

The previous equations thus define piecewise C^1 fields on $\mathbb{R}^2 \times]0, +\infty[$. In order to now deal with the weak-extension of the mass and momentum balance equations, an important remark shall first be stated about the different discontinuities that will affect the extension process.

Remark 3.4.1 *Important note on the discontinuities affecting the extension process*

Two different types of discontinuities shall be taken into account during the extension process:

- *on the one hand, the physical discontinuities inherent to the original Euler compressible equations and to the Riemann problem; these discontinuities propagate within the real fluid domain $\Omega_f \times]0, +\infty[$, and are governed by Rankine-Hugoniot condition, as detailed in the previous section; for simplicity, it is again assumed that there is only one surface Σ of discontinuity within $\Omega_f \times]0, +\infty[$;*

- on the other hand, the two discontinuities introduced by the extension of the fluid fields to \mathbb{R}^2 ; conversely to the physical ones, these new discontinuities do not propagate within the fluid domain: indeed, the exterior boundary $\partial\Omega_f \setminus \partial\Omega_s$ of the real fluid domain is stationary, and the inner boundary $\partial\Omega_s$ moves with the same normal velocity than the fluid.

Before starting the extension of the balance equations, let us first recall and define some notations:

Notations 3.4.1

- $\tilde{\Omega} := \Omega \times]0, +\infty[$, where the domain Ω denotes either the exterior, the fluid, or the solid domain;
- $\partial\tilde{\Omega} := \partial\Omega \times]0, +\infty[$;
- $\tilde{\sigma} = (\underline{\sigma}, t)$, with $\underline{\sigma} \in \partial\Omega$, and $d\tilde{\sigma} = d\sigma dt$;
- $\mathbb{R}^2 \times]0, +\infty[:= \tilde{\Omega}_{ext} \cup \tilde{\Omega}_f \cup \tilde{\Omega}_s$;
- Σ still denotes the unique smooth surface of discontinuity of the weak solution within $\tilde{\Omega}_f$;
- as in the previous section, the normal vectors on each surface of discontinuity will be written in the form $\underline{n} = (-c \ \nu_1 \ \nu_2)^T$, where c represents the propagation velocity of the discontinuity, and $\underline{\nu}$ its direction of propagation. Taking into account the fact that only the physical discontinuities associated to the original Euler compressible equations and Riemann problem do propagate within the fluid, one can write:

$$\tilde{\underline{n}}_{F \rightarrow ext} = \begin{pmatrix} 0 & \underline{n}_{F \rightarrow ext} \end{pmatrix}^T, \quad (3.34)$$

$$\tilde{\underline{n}}_{F \rightarrow S} = \begin{pmatrix} 0 & \underline{n}_{F \rightarrow S} \end{pmatrix}^T, \quad (3.35)$$

$$\tilde{\underline{n}}_{\Sigma} = \begin{pmatrix} -c & \nu_1 & \nu_2 \end{pmatrix}. \quad (3.36)$$

- $\{f\}$ denotes a piecewise continuous function on $\mathbb{R}^2 \times]0, +\infty[$ which coincides with the distribution f outside of the discontinuities.
- f_F , f_S and f_{ext} denote, when used on a boundary, the value of the function f respectively on the fluid, solid and exterior sides.
- F refers to the real fluid domain Ω_f , and cF to the complementary domain, i.e. either Ω_s or $\mathbb{R}^2 \setminus (\Omega_f \cup \Omega_s)$;
- $[u]_{{}^cF}^F := u_F - u_{{}^cF}$ denotes the jump of the function u across the fluid boundaries $\partial\Omega_f$;

[b] Weak-extension of the mass and momentum balance equations

Proposition 3.4.1 and 3.4.2 hereafter display the "weak-extension" of both the mass and momentum balance equations. Each proposition is followed by a proof, whose key ideas are similar to the proof of Rankine-Hugoniot condition, that is to say:

- use Chasles' relation to split the variational formulation into 3 parts, associated to the 3 subdomains $\tilde{\Omega}_{ext}$, $\tilde{\Omega}_f$ and $\tilde{\Omega}_s$;
- use Green's formula for integration by parts in order to introduce integrals on the boundaries $\partial\tilde{\Omega}_f \setminus \partial\tilde{\Omega}_s$, $\partial\tilde{\Omega}_s$, and Σ ;
- use the fact that the solution is smooth in $\tilde{\Omega}_{ext}$, $\tilde{\Omega}_f^+$, $\tilde{\Omega}_f^-$, and $\tilde{\Omega}_s$, and satisfies Rankine-Hugoniot condition on Σ ;
- bring together every term, and use the kinematic boundary conditions to simplify the equation.

Proposition 3.4.1 *Extended mass balance equation (weak form)*

$\forall \varphi \in D(\mathbb{R}^2 \times]0, +\infty[)$:

$$\boxed{\langle \partial_t \rho + \operatorname{div}(\rho \underline{v}), \varphi \rangle_{D', D} = - \int_{\partial\tilde{\Omega}_s} [\rho]_S^F (\partial_t \underline{U}(t) \cdot \underline{n}_{F \rightarrow S}(\tilde{\sigma})) \varphi(\tilde{\sigma}) d\tilde{\sigma}}. \quad (3.37)$$

Proof of Proposition 3.4.1 *To prove that the weak formulation of the mass balance equation extended to \mathbb{R}^2 writes as (3.37), let us start with the definition of the weak formulation:*

$\forall \varphi \in D(\mathbb{R}^2 \times]0, +\infty[)$:

$$\langle \partial_t \rho + \operatorname{div}(\rho \underline{v}), \varphi \rangle_{D', D} := - \int_0^{+\infty} \int_{\mathbb{R}^2} (\rho \partial_t \varphi + \rho \underline{v} \cdot \underline{\nabla} \varphi) d\underline{x} dt. \quad (3.38)$$

Step 1: Chasles' relation

This integral can be divided into three different integrals, as follows:

$$\begin{aligned} & - \int_0^{+\infty} \int_{\mathbb{R}^2} (\rho \partial_t \varphi + \rho \underline{v} \cdot \underline{\nabla} \varphi) d\underline{x} dt \\ & = - \int_{\tilde{\Omega}_{ext}} (\rho \partial_t \varphi + \rho \underline{v} \cdot \underline{\nabla} \varphi) d\underline{x} dt - \int_{\tilde{\Omega}_f} (\rho \partial_t \varphi + \rho \underline{v} \cdot \underline{\nabla} \varphi) d\underline{x} dt \\ & \quad - \int_{\tilde{\Omega}_s} (\rho \partial_t \varphi + \rho \underline{v} \cdot \underline{\nabla} \varphi) d\underline{x} dt. \end{aligned} \quad (3.39)$$

Step 2: Green's formula for integration by parts

Now, using Green's formula for each integral, and taking into account the fact that a surface Σ of discontinuity may propagate within the real fluid domain, it comes:

$$\begin{aligned}
 & - \int_{\tilde{\Omega}_{ext}} (\rho \partial_t \varphi + \rho \underline{v} \cdot \underline{\nabla} \varphi) \, d\underline{x} \, dt \\
 & = \int_{\tilde{\Omega}_{ext}} \{ \partial_t \rho + \operatorname{div}(\rho \underline{v}) \} \varphi \, d\underline{x} \, dt - \int_{\partial \tilde{\Omega}_f \setminus \partial \tilde{\Omega}_s} \rho_{ext} \times 0 \times \varphi(\tilde{\underline{x}}) \, d\tilde{\underline{x}} \\
 & \quad - \int_{\partial \tilde{\Omega}_f \setminus \partial \tilde{\Omega}_s} (\rho \underline{v})_{ext}(\tilde{\underline{x}}) \cdot \underline{n}_{ext \rightarrow F}(\tilde{\underline{x}}) \varphi(\tilde{\underline{x}}) \, d\tilde{\underline{x}}. \quad (3.40)
 \end{aligned}$$

$$\begin{aligned}
 & - \int_{\tilde{\Omega}_f} (\rho \partial_t \varphi + \rho \underline{v} \cdot \underline{\nabla} \varphi) \, d\underline{x} \, dt \\
 & = \int_{\tilde{\Omega}_f^+} \{ \partial_t \rho + \operatorname{div}(\rho \underline{v}) \} \varphi \, d\underline{x} \, dt + \int_{\tilde{\Omega}_f^-} \{ \partial_t \rho + \operatorname{div}(\rho \underline{v}) \} \varphi \, d\underline{x} \, dt \\
 & \quad - \int_{\Sigma} (-s[\rho]_-^+ + \nu_1[\rho v_x]_-^+ + \nu_2[\rho v_y]_-^+) (\tilde{\underline{x}}) \varphi(\tilde{\underline{x}}) \, d\tilde{\underline{x}} \\
 & \quad - \int_{\partial \tilde{\Omega}_f \setminus \partial \tilde{\Omega}_s} \rho_F(\tilde{\underline{x}}) \times 0 \times \varphi(\tilde{\underline{x}}) \, d\tilde{\underline{x}} - \int_{\partial \tilde{\Omega}_s} \rho_F(\tilde{\underline{x}}) \times 0 \times \varphi(\tilde{\underline{x}}) \, d\tilde{\underline{x}} \\
 & - \int_{\partial \tilde{\Omega}_f \setminus \partial \tilde{\Omega}_s} (\rho \underline{v})_F(\tilde{\underline{x}}) \cdot \underline{n}_{F \rightarrow ext}(\tilde{\underline{x}}) \varphi(\tilde{\underline{x}}) \, d\tilde{\underline{x}} - \int_{\partial \tilde{\Omega}_s} (\rho \underline{v})_F(\tilde{\underline{x}}) \cdot \underline{n}_{F \rightarrow S}(\tilde{\underline{x}}) \varphi(\tilde{\underline{x}}) \, d\tilde{\underline{x}} \\
 & \quad (3.41)
 \end{aligned}$$

$$\begin{aligned}
 & - \int_{\tilde{\Omega}_s} (\rho \partial_t \varphi + \rho \underline{v} \cdot \underline{\nabla} \varphi) \, d\underline{x} \, dt \\
 & = \int_{\tilde{\Omega}_s} \{ \partial_t \rho + \operatorname{div}(\rho \underline{v}) \} \varphi \, d\underline{x} \, dt - \int_{\partial \tilde{\Omega}_s} \rho_S \times 0 \times \varphi(\tilde{\underline{x}}) \, d\tilde{\underline{x}} \\
 & \quad - \int_{\partial \tilde{\Omega}_s} (\rho \underline{v})_S(\tilde{\underline{x}}) \cdot \underline{n}_{S \rightarrow F}(\tilde{\underline{x}}) \varphi(\tilde{\underline{x}}) \, d\tilde{\underline{x}}. \quad (3.42)
 \end{aligned}$$

Step 3: the solution is smooth in $\tilde{\Omega}_{ext}$, $\tilde{\Omega}_f^+$, $\tilde{\Omega}_f^-$ and $\tilde{\Omega}_s$ + Rankine-Hugoniot

Now, by adding the last 3 equations, and using the fact the mass balance equation is satisfied in a strong sense in $\tilde{\Omega}_{ext}$, $\tilde{\Omega}_f^+$, $\tilde{\Omega}_f^-$ and $\tilde{\Omega}_s$, and the fact that Rankine-Hugoniot condition is satisfied on Σ , it comes:

$$\begin{aligned}
 & \langle \partial_t \rho + \operatorname{div}(\rho \underline{v}), \varphi \rangle_{D', D} \\
 & = - \int_{\partial \tilde{\Omega}_f \setminus \partial \tilde{\Omega}_s} [(\rho \underline{v})]_{ext}^F(\tilde{\underline{x}}) \cdot \underline{n}_{F \rightarrow ext}(\tilde{\underline{x}}) \varphi(\tilde{\underline{x}}) \, d\tilde{\underline{x}} - \int_{\partial \tilde{\Omega}_s} [\rho \underline{v}]_S^F(\tilde{\underline{x}}) \cdot \underline{n}_{F \rightarrow S}(\tilde{\underline{x}}) \varphi(\tilde{\underline{x}}) \, d\tilde{\underline{x}} \\
 & \quad (3.43)
 \end{aligned}$$

Step 4: simplification with the kinematic boundary conditions

Finally, using the continuity of the normal component of the velocity across the boundaries, one obtains:

$$\langle \partial_t \rho + \operatorname{div}(\rho \underline{v}), \varphi \rangle_{D', D} = - \int_{\partial \tilde{\Omega}_s} [\rho]_S^F (\partial_t \underline{U}(t) \cdot \underline{n}_{F \rightarrow S}(\tilde{x})) \varphi(\tilde{x}) d\tilde{x}. \quad (3.44)$$

This concludes the proof for the extension of the mass balance equation. Let us now turn towards the momentum balance equation.

Proposition 3.4.2 *Extended momentum balance equation (weak form)*

$$\forall \underline{\psi} \in [D(\mathbb{R}^2 \times]0, +\infty[)]^2:$$

$$\begin{aligned} & \left\langle \partial_t(\rho \underline{v}) + \underline{\operatorname{div}}(\rho \underline{v} \otimes \underline{v}) + \underline{\nabla} p, \underline{\psi} \right\rangle_{D', D} \\ &= - \int_{\partial \tilde{\Omega}_s} [\partial_t \underline{U}(t) \cdot \underline{n}_{F \rightarrow S}(\tilde{x})] [\rho \underline{v}]_S^F(\tilde{x}) \cdot \underline{\psi}(\tilde{x}) d\tilde{x} \\ & \quad - \int_{\partial \tilde{\Omega}_f} [p]_{c_F}^F(\tilde{x}) \underline{n}_{F \rightarrow c_F}(\tilde{x}) \cdot \underline{\psi}(\tilde{x}) d\tilde{x}. \end{aligned} \quad (3.45)$$

Proof of Proposition 3.4.2 *This proof follows the methodology used for the mass balance equation:*

Step 1: Chasles' relation

$$\forall \underline{\psi} \in [D(\mathbb{R}^2 \times]0, +\infty[)]^2:$$

$$\begin{aligned} & \left\langle \partial_t(\rho \underline{v}) + \underline{\operatorname{div}}(\rho \underline{v} \otimes \underline{v}) + \underline{\nabla} p, \underline{\psi} \right\rangle_{D', D} \\ &= - \int_{\tilde{\Omega}_{ext}} [\rho \underline{v} \cdot \partial_t \underline{\psi} + (\rho \underline{v} \otimes \underline{v}) : \underline{\underline{\nabla}} \underline{\psi} - p \operatorname{div}(\underline{\psi})] d\underline{x} dt \\ & \quad - \int_{\tilde{\Omega}_f} [\rho \underline{v} \cdot \partial_t \underline{\psi} + (\rho \underline{v} \otimes \underline{v}) : \underline{\underline{\nabla}} \underline{\psi} - p \operatorname{div}(\underline{\psi})] d\underline{x} dt \\ & \quad - \int_{\tilde{\Omega}_s} [\rho \underline{v} \cdot \partial_t \underline{\psi} + (\rho \underline{v} \otimes \underline{v}) : \underline{\underline{\nabla}} \underline{\psi} - p \operatorname{div}(\underline{\psi})] d\underline{x} dt. \end{aligned} \quad (3.46)$$

Step 2: Green's formula for integration by parts

Thanks to Green's formula, one can write:

$$\begin{aligned} & - \int_{\tilde{\Omega}_{ext}} [\rho \underline{v} \cdot \partial_t \underline{\psi} + (\rho \underline{v} \otimes \underline{v}) : \underline{\underline{\nabla}} \underline{\psi} - p \operatorname{div}(\underline{\psi})] d\underline{x} dt \\ &= \int_{\tilde{\Omega}_{ext}} \{ \partial_t(\rho \underline{v}) + \underline{\operatorname{div}}(\rho \underline{v} \otimes \underline{v}) + \underline{\nabla} p \} \cdot \underline{\psi} - \int_{\partial \tilde{\Omega}_f \setminus \partial \tilde{\Omega}_s} 0 \times (\rho \underline{v})_{ext}(\tilde{x}) \cdot \underline{\psi}(\tilde{x}) d\tilde{x} \\ & \quad - \int_{\partial \tilde{\Omega}_f \setminus \partial \tilde{\Omega}_s} [\underline{v}_{ext} \cdot \underline{n}_{ext \rightarrow F}(\tilde{x})] (\rho \underline{v})_{ext}(\tilde{x}) \cdot \underline{\psi}(\tilde{x}) d\tilde{x} \\ & \quad - \int_{\partial \tilde{\Omega}_f \setminus \partial \tilde{\Omega}_s} p_{ext}(\tilde{x}) \underline{n}_{ext \rightarrow F}(\tilde{x}) \cdot \underline{\psi}(\tilde{x}) d\tilde{x}. \end{aligned} \quad (3.47)$$

$$\begin{aligned}
 & - \int_{\tilde{\Omega}_f} [\rho \underline{v} \cdot \partial_t \underline{\psi} + (\rho \underline{v} \otimes \underline{v}) : \underline{\nabla} \underline{\psi} - p \operatorname{div}(\underline{\psi})] \, d\underline{x} \, dt \\
 & = \int_{\tilde{\Omega}_f^+} \{ \partial_t(\rho \underline{v}) + \underline{\operatorname{div}}(\rho \underline{v} \otimes \underline{v}) + \underline{\nabla} p \} \cdot \underline{\psi} + \int_{\tilde{\Omega}_f^-} \{ \partial_t(\rho \underline{v}) + \underline{\operatorname{div}}(\rho \underline{v} \otimes \underline{v}) + \underline{\nabla} p \} \cdot \underline{\psi} \\
 & - \int_{\Sigma} \left(-s[\rho \underline{v}]_-^+ + \nu_1 \left[\left(\rho v_x^2 + p \quad \rho v_y v_x \right)^T \right]_-^+ + \nu_2 \left[\left(\rho v_y v_x \quad \rho v_y^2 + p \right)^T \right]_-^+ \right) \cdot \underline{\psi}(\tilde{\underline{x}}) \, d\tilde{\underline{x}} \\
 & \quad - \int_{\partial \tilde{\Omega}_f \setminus \partial \tilde{\Omega}_s} 0 \times (\rho \underline{v})_F(\tilde{\underline{x}}) \cdot \underline{\psi}(\tilde{\underline{x}}) \, d\tilde{\underline{x}} - \int_{\partial \tilde{\Omega}_s} 0 \times (\rho \underline{v})_F(\tilde{\underline{x}}) \cdot \underline{\psi}(\tilde{\underline{x}}) \, d\tilde{\underline{x}} \\
 & - \int_{\partial \tilde{\Omega}_f \setminus \partial \tilde{\Omega}_s} [\underline{v}_F \cdot \underline{n}_{F \rightarrow ext}] (\tilde{\underline{x}}) (\rho \underline{v})_F(\tilde{\underline{x}}) \cdot \underline{\psi}(\tilde{\underline{x}}) \, d\tilde{\underline{x}} - \int_{\partial \tilde{\Omega}_s} [\underline{v}_F \cdot \underline{n}_{F \rightarrow S}] (\tilde{\underline{x}}) (\rho \underline{v})_F(\tilde{\underline{x}}) \cdot \underline{\psi}(\tilde{\underline{x}}) \, d\tilde{\underline{x}} \\
 & - \int_{\partial \tilde{\Omega}_f \setminus \partial \tilde{\Omega}_s} p_F(\tilde{\underline{x}}) \underline{n}_{F \rightarrow ext}(\tilde{\underline{x}}) \cdot \underline{\psi}(\tilde{\underline{x}}) \, d\tilde{\underline{x}} - \int_{\partial \tilde{\Omega}_s} p_F(\tilde{\underline{x}}) \underline{n}_{F \rightarrow S}(\tilde{\underline{x}}) \cdot \underline{\psi}(\tilde{\underline{x}}) \, d\tilde{\underline{x}}. \quad (3.48)
 \end{aligned}$$

$$\begin{aligned}
 & - \int_{\tilde{\Omega}_s} [\rho \underline{v} \cdot \partial_t \underline{\psi} + (\rho \underline{v} \otimes \underline{v}) : \underline{\nabla} \underline{\psi} - p \operatorname{div}(\underline{\psi})] \, d\underline{x} \, dt \\
 & = \int_{\tilde{\Omega}_s} \{ \partial_t(\rho \underline{v}) + \underline{\operatorname{div}}(\rho \underline{v} \otimes \underline{v}) + \underline{\nabla} p \} \cdot \underline{\psi} - \int_{\partial \tilde{\Omega}_s} 0 \times (\rho \underline{v})_S(\tilde{\underline{x}}) \cdot \underline{\psi}(\tilde{\underline{x}}) \, d\tilde{\underline{x}} \\
 & - \int_{\partial \tilde{\Omega}_s} [\underline{v}_S \cdot \underline{n}_{S \rightarrow F}] (\tilde{\underline{x}}) (\rho \underline{v})_S(\tilde{\underline{x}}) \cdot \underline{\psi}(\tilde{\underline{x}}) \, d\tilde{\underline{x}} - \int_{\partial \tilde{\Omega}_s} p_S(\tilde{\underline{x}}) \underline{n}_{S \rightarrow F}(\tilde{\underline{x}}) \cdot \underline{\psi}(\tilde{\underline{x}}) \, d\tilde{\underline{x}}. \quad (3.49)
 \end{aligned}$$

Step 3/4: the solution is smooth in $\tilde{\Omega}_{ext}, \tilde{\Omega}_f^+, \tilde{\Omega}_f^-, \tilde{\Omega}_s + R.-H. + B.C.$

Now, by adding these last 3 equations, using the fact that the momentum balance equation is satisfied in a strong sense in $\tilde{\Omega}_{ext}, \tilde{\Omega}_f^+, \tilde{\Omega}_f^-$, and $\tilde{\Omega}_s$, plus the fact that Rankine-Hugoniot (R.-H.) condition is satisfied on Σ , and finally the kinematic boundary conditions (B.C.), it comes:

$$\begin{aligned}
 & \langle \partial_t(\rho \underline{v}) + \underline{\operatorname{div}}(\rho \underline{v} \otimes \underline{v}) + \underline{\nabla} p, \underline{\psi} \rangle_{D', D} \\
 & = - \int_{\partial \tilde{\Omega}_s} [\partial_t \underline{U}(t) \cdot \underline{n}_{F \rightarrow S}(\tilde{\underline{x}})] [\rho \underline{v}]_S^F(\tilde{\underline{x}}) \cdot \underline{\psi}(\tilde{\underline{x}}) \, d\tilde{\underline{x}} \\
 & \quad - \int_{\partial \tilde{\Omega}_f \setminus \partial \tilde{\Omega}_s} [p]_{ext}^F(\tilde{\underline{x}}) \underline{n}_{F \rightarrow ext}(\tilde{\underline{x}}) \cdot \underline{\psi}(\tilde{\underline{x}}) \, d\tilde{\underline{x}} \\
 & \quad - \int_{\partial \tilde{\Omega}_s} [p]_S^F(\tilde{\underline{x}}) \underline{n}_{F \rightarrow S}(\tilde{\underline{x}}) \cdot \underline{\psi}(\tilde{\underline{x}}) \, d\tilde{\underline{x}}. \quad (3.50)
 \end{aligned}$$

This concludes the proof for the extension of the momentum balance equation. Both balance equations are here written in pure Eulerian formulation. In classical FSI literature however, one can often find these equations written with an Arbitrary Lagrangian Eulerian (ALE) formulation. The interested reader may for instance refer to [Etienne et al., 2009]. The following remark hereafter details the fluid equations in ALE formulation.

Remark 3.4.2 Arbitrary Lagrangian Eulerian (ALE) formulation

The extended balance equations (3.37-3.45) could be rewritten in a more compact form, in the spirit of Arbitrary Lagrangian Eulerian (ALE) formulation. This can be done by working on the integrals involving the solid medium velocity $\partial_t \underline{U}$ in the right-hand sides of the extended equations. To this end, let us consider the following extension of the solid medium velocity $\partial_t \tilde{\underline{U}}$:

$$\forall t \geq 0, \partial_t \tilde{\underline{U}}(\cdot, t) = \begin{cases} \partial_t \underline{U}(t) & \text{in } \overline{\Omega_s} \\ \underline{0} & \text{in } \mathbb{R}^2 \setminus \overline{\Omega_s} \end{cases} \quad (3.51)$$

With such an extension, the field $(\rho \partial_t \tilde{\underline{U}})$ is uniform within the disconnected space Ω_s (cf. rigid body assumption + uniform extended density), and zero outside. Now, using once again Green's formula to define the distribution $\text{div}(\rho \partial_t \tilde{\underline{U}})$ in $\mathbb{R}^2 \times]0, +\infty[$, one can write, for all $\varphi \in D(\mathbb{R}^2 \times]0, +\infty[)$:

$$\begin{aligned} & - \int_{\tilde{\Omega}_{ext}} \rho \partial_t \tilde{\underline{U}}(\underline{x}, t) \cdot \underline{\nabla} \varphi(\underline{x}) \, d\underline{x} \, dt \\ & = \int_{\tilde{\Omega}_{ext}} \text{div}(\rho \partial_t \tilde{\underline{U}})(\underline{x}, t) \varphi(\underline{x}, t) \, d\underline{x} \, dt \\ & \quad - \int_{\partial \tilde{\Omega}_{ext}} \rho_{ext}(\tilde{\underline{x}}) \partial_t \tilde{\underline{U}}(t) \cdot \underline{n}_{ext \rightarrow F}(\tilde{\underline{x}}) \varphi(\tilde{\underline{x}}) \, d\tilde{\underline{x}}. \end{aligned} \quad (3.52)$$

$$\begin{aligned} & - \int_{\tilde{\Omega}_f} \rho \partial_t \tilde{\underline{U}}(\underline{x}, t) \cdot \underline{\nabla} \varphi(\underline{x}, t) \, d\underline{x} \, dt \\ & = \int_{\tilde{\Omega}_f} \text{div}(\rho \partial_t \tilde{\underline{U}})(\underline{x}, t) \varphi(\underline{x}, t) \, d\underline{x} \, dt - \int_{\partial \tilde{\Omega}_f \setminus \partial \tilde{\Omega}_s} \rho_F(\tilde{\underline{x}}) \partial_t \tilde{\underline{U}}(t) \cdot \underline{n}_{F \rightarrow ext}(\tilde{\underline{x}}) \varphi(\tilde{\underline{x}}) \, d\tilde{\underline{x}} \\ & \quad - \int_{\partial \tilde{\Omega}_s} \rho_F(\tilde{\underline{x}}) \partial_t \underline{U}(t) \cdot \underline{n}_{F \rightarrow S}(\tilde{\underline{x}}) \varphi(\tilde{\underline{x}}) \, d\tilde{\underline{x}}. \end{aligned} \quad (3.53)$$

$$\begin{aligned} & - \int_{\tilde{\Omega}_s} \rho \partial_t \tilde{\underline{U}}(\underline{x}, t) \cdot \underline{\nabla} \varphi(\underline{x}, t) \, d\underline{x} \, dt \\ & = \int_{\tilde{\Omega}_s} \text{div}(\rho \partial_t \tilde{\underline{U}})(\underline{x}, t) \varphi(\underline{x}, t) \, d\underline{x} \, dt - \int_{\partial \tilde{\Omega}_s} \rho_S(\tilde{\underline{x}}) \partial_t \underline{U}(t) \cdot \underline{n}_{S \rightarrow F}(\tilde{\underline{x}}) \varphi(\tilde{\underline{x}}) \, d\tilde{\underline{x}}. \end{aligned} \quad (3.54)$$

As the field $(\rho \partial_t \tilde{\underline{U}})$ is either uniform or zero, one can write, by adding the last 3 equations:

$$\begin{aligned} \langle \text{div}(\rho \partial_t \tilde{\underline{U}}), \varphi \rangle_{D', D} & := - \int_0^{+\infty} \int_{\mathbb{R}^2} \rho \partial_t \tilde{\underline{U}}(\underline{x}, t) \cdot \underline{\nabla} \varphi(\underline{x}, t) \, d\underline{x} \, dt, \\ & = - \int_{\partial \tilde{\Omega}_s} [\rho]_S^F(\tilde{\underline{x}}) (\partial_t \underline{U}(t) \cdot \underline{n}_{F \rightarrow S}(\tilde{\underline{x}})) \varphi(\tilde{\underline{x}}) \, d\tilde{\underline{x}}. \end{aligned} \quad (3.55)$$

Following the same methodology, the distribution $\underline{\text{div}}(\rho \underline{v} \otimes \partial_t \tilde{U})$ can be extended to \mathbb{R}^2 as follows:

$$\forall \underline{\psi} \in [D(\mathbb{R}^2)]^2,$$

$$\begin{aligned} \langle \underline{\text{div}}(\rho \underline{v} \otimes \partial_t \tilde{U}), \underline{\psi} \rangle_{D', D} &:= - \int_0^{+\infty} \int_{\mathbb{R}^2} (\rho \underline{v} \otimes \partial_t \tilde{U})(\underline{x}, t) : \underline{\nabla} \underline{\psi}(\underline{x}, t) d\underline{x} dt, \\ &= - \int_{\partial \tilde{\Omega}_s} (\partial_t \underline{U}(t) \cdot \underline{n}_{F \rightarrow S}(\tilde{\sigma})) [\rho \underline{v}]_S^F(\tilde{\sigma}) \cdot \underline{\psi}(\tilde{\sigma}) d\tilde{\sigma}. \end{aligned} \quad (3.56)$$

This result is obtained by using the fact that the extended velocity $\partial_t \tilde{U}$ is zero outside of $\tilde{\Omega}_s$, and the fact that the tensor $\rho \underline{v} \otimes \partial_t \tilde{U}$ is uniform within the solid domain Ω_s .

Finally, injecting equations (3.55-3.56) into (3.37-3.45), one obtains the following extended Euler compressible equations written in ALE formulation:

$$\begin{aligned} \forall \varphi \in D(\mathbb{R}^2 \times]0, +\infty[), \underline{\psi} \in [D(\mathbb{R}^2 \times]0, +\infty[)]^2 : \\ \langle \partial_t \rho(\cdot, t) + \text{div}(\rho(\underline{v} - \partial_t \tilde{U}))(\cdot, t), \varphi \rangle_{D', D} = 0. \end{aligned} \quad (3.57)$$

$$\begin{aligned} \langle \partial_t(\rho \underline{v})(\cdot, t) + \text{div}(\rho \underline{v} \otimes (\underline{v} - \partial_t \tilde{U}))(\cdot, t), \underline{\psi} \rangle_{D', D} \\ = - \langle \underline{\nabla} p, \underline{\psi} \rangle_{D', D} + \int_{\partial \Omega_f} [p]_F^{cF}(\tilde{\sigma}) \underline{\psi}(\tilde{\sigma}) \cdot \underline{n}_{F \rightarrow cF}(\tilde{\sigma}) d\tilde{\sigma}. \end{aligned} \quad (3.58)$$

In the following, the fluid extended PDEs will be written in pure Eulerian formulation, as summarized in the following Proposition 3.4.3. This choice is motivated by the fact that finite-volume schemes are classically used to solve such systems of conservation laws.

Proposition 3.4.3 *Summary of the extended fluid PDEs (weak form + Eulerian formulation)*

$$\forall \varphi \in D(\mathbb{R}^2 \times]0, +\infty[), \underline{\psi} \in [D(\mathbb{R}^2 \times]0, +\infty[)]^2 :$$

$$\boxed{\langle \partial_t \rho + \text{div}(\rho \underline{v}), \varphi \rangle_{D', D} = - \int_{\partial \tilde{\Omega}_s} [\rho]_S^F(\partial_t \underline{U}(t) \cdot \underline{n}_{F \rightarrow S}(\tilde{\sigma})) \varphi(\tilde{\sigma}) d\tilde{\sigma}.} \quad (3.59)$$

$$\boxed{\begin{aligned} \langle \partial_t(\rho \underline{v}) + \underline{\text{div}}(\rho \underline{v} \otimes \underline{v}) + \underline{\nabla} p, \underline{\psi} \rangle_{D', D} \\ = - \int_{\partial \tilde{\Omega}_s} [\partial_t \underline{U}(t) \cdot \underline{n}_{F \rightarrow S}(\tilde{\sigma})] [\rho \underline{v}]_S^F(\tilde{\sigma}) \cdot \underline{\psi}(\tilde{\sigma}) d\tilde{\sigma} \\ - \int_{\partial \tilde{\Omega}_f} [p]_F^{cF}(\tilde{\sigma}) \underline{n}_{F \rightarrow cF}(\tilde{\sigma}) \cdot \underline{\psi}(\tilde{\sigma}) d\tilde{\sigma}. \end{aligned}} \quad (3.60)$$

Proof of Proposition 3.4.3 *Summary of the previous propositions.*

The fluid equations being now extended, it is high time to consider their convolution product with the analysing wavelet Ψ or scaling function Φ . This second step will result in spatially-filtered equations governing a homogenized fluid.

3.4.3 "Weak-convolution" wavelets * extended fluid PDEs

As can be seen in Proposition 3.4.3, the extended Euler compressible equations have to be understood in a weak sense. In order to then properly define a convolution product with all the distributions present in equations (3.59-3.60), both the analysing wavelet and scaling function should ideally possess a C^∞ smoothness and a compact support. However, to the author's knowledge, such wavelets do not exist in the CWT framework. One would have to turn towards orthogonal wavelet bases such as Daubechies' in order to find a compact support. Nevertheless, as previously highlighted, these wavelets only possess a $C^{\mu N}$ smoothness, with $\mu \approx 0.2$ and $N < +\infty$.

Fortunately, the notion of compactly-supported distributions here allows to bypass the non-compact support of the wavelet and scaling function. To emphasize this point, let us first recall some properties on convolution product, before discussing compactly-supported distributions.

Properties on convolution product

Proposition 3.4.4 *Convolution product $L^1(\mathbb{R}^d) * D(\mathbb{R}^d)$*

The convolution product between a function $f \in L^1(\mathbb{R}^d)$ and a test function $\varphi \in D(\mathbb{R}^d)$ results in a C^∞ function.

Proof of Proposition 3.4.4 *See appendix A.0.1.*

Proposition 3.4.5 *Convolution product $D'(\mathbb{R}^d) * D(\mathbb{R}^d)$*

The convolution product between a distribution $T \in D'(\mathbb{R}^d)$ and a test function $\varphi \in D(\mathbb{R}^d)$ also results in a C^∞ function. Furthermore, the following equation holds:

$$\forall T \in D'(\mathbb{R}^d), \psi, \varphi \in D(\mathbb{R}^d):$$

$$\langle \psi * T, \varphi \rangle_{D', D} := \int_{\mathbb{R}^d} (\psi * T) \varphi, \quad (3.61)$$

$$= \langle T, \tilde{\psi} * \varphi \rangle_{D', D}, \quad (3.62)$$

where $\tilde{\psi}(\underline{x}) = \psi(-\underline{x})$.

In the case where the distribution T is a locally integrable function, the previous result can be obtained with Fubini's theorem:

$$\langle \psi * T, \varphi \rangle_{D', D} = \int_{\mathbb{R}^d} \left(\int_{\mathbb{R}^d} \psi(\underline{x} - \underline{y}) T(\underline{y}) d\underline{y} \right) \varphi(\underline{x}) d\underline{x} \quad (3.63)$$

$$= \int_{\mathbb{R}^d} T(\underline{y}) \left(\int_{\mathbb{R}^d} \tilde{\psi}(\underline{y} - \underline{x}) \varphi(\underline{x}) d\underline{x} \right) d\underline{y} \quad (3.64)$$

$$= \langle T, \tilde{\psi} * \varphi \rangle_{D', D} \quad (3.65)$$

Proof of Proposition 3.4.5 See appendix A.0.2.

These two propositions being recalled, let us now emphasize how the notion of compactly-supported distributions may allow to define the convolution product between the extended fluid PDEs and the analysing wavelet or scaling function.

Compactly-supported distributions

Thanks to the previous extension procedure, all the distributions of interest in the current work possess a compact support. Indeed, for all test functions $\varphi \in D(\mathbb{R}^2 \times]0, +\infty[)$ and $\underline{\psi} \in [D(\mathbb{R}^2 \times]0, +\infty[)]^2$, with compact supports included in the exterior domain $\tilde{\Omega}_{ext}$, one can write:

$$\langle \partial_t \rho + \operatorname{div}(\rho \underline{v}), \varphi \rangle_{D', D} = - \int_0^{+\infty} \int_{\mathbb{R}^2} (\rho \partial_t \varphi + \rho \underline{v} \cdot \underline{\nabla} \varphi)(\underline{x}, t) d\underline{x} dt, \quad (3.66)$$

$$= - \int_{\tilde{\Omega}_{ext}} (\rho \partial_t \varphi + \rho \underline{v} \cdot \underline{\nabla} \varphi), \quad (3.67)$$

$$= \int_{\tilde{\Omega}_{ext}} \{ \partial_t \rho + \operatorname{div}(\rho \underline{v}) \} \varphi, \quad (3.68)$$

$$= \rho_{ext} \int_{\tilde{\Omega}_{ext}} \{ \operatorname{div}(\underline{v}) \} \varphi, \quad (3.69)$$

$$= 0. \quad (3.70)$$

$$\langle \partial_t(\rho \underline{v}) + \underline{\operatorname{div}}(\rho \underline{v} \otimes \underline{v}) + \underline{\nabla} p, \underline{\psi} \rangle_{D', D} \quad (3.71)$$

$$= - \int_0^{+\infty} \int_{\mathbb{R}^2} (\rho \underline{v} \cdot \partial_t \underline{\psi} + [\rho \underline{v} \otimes \underline{v}] : \underline{\nabla} \underline{\psi} + p \operatorname{div}(\underline{\psi}))(\underline{x}, t) d\underline{x} dt, \quad (3.72)$$

$$= - \int_{\tilde{\Omega}_{ext}} (\rho \underline{v} \cdot \partial_t \underline{\psi} + [\rho \underline{v} \otimes \underline{v}] : \underline{\nabla} \underline{\psi} + p \operatorname{div}(\underline{\psi})), \quad (3.73)$$

$$= \int_{\tilde{\Omega}_{ext}} \{ \partial_t(\rho \underline{v}) + \underline{\operatorname{div}}(\rho \underline{v} \otimes \underline{v}) + \underline{\nabla} p \} \cdot \underline{\psi}, \quad (3.74)$$

$$= \rho_{ext} \int_{\tilde{\Omega}_{ext}} \left\{ \partial_t \underline{v} + \underline{\operatorname{div}}(\underline{v} \otimes \underline{v}) + \frac{1}{\rho_{ext}} \underline{\nabla} p \right\} \cdot \underline{\psi}, \quad (3.75)$$

$$= 0. \quad (3.76)$$

The last equality in both equations uses the fact that the fluid located within the exterior domain $\tilde{\Omega}_{ext}$ is considered inviscid and incompressible, and is thus governed by Euler equations.

The above results immediately imply that the supports of the distributions of interest are necessarily included in the closed and bounded subspace $\overline{\Omega_f \cup \Omega_s}$. This useful property will allow to cope with the non-compact support of the analysing wavelet and scaling function, as detailed in the following remarks and propositions.

Remark 3.4.3 *Compactly-supported distributions $\mathcal{E}'(\mathbb{R}^d)$*

The space of compactly-supported distributions $\mathcal{E}'(\mathbb{R}^d)$ offers multiple advantages. One of them is the possibility to now define the action of such a distribution $T \in \mathcal{E}'(\mathbb{R}^d)$ on a function $\psi \in C^\infty(\mathbb{R}^d)$ which does not possess a compact support. Indeed, one can write:

$$\forall T \in \mathcal{E}'(\mathbb{R}^d), \psi \in C^\infty(\mathbb{R}^d):$$

$$\langle T, \psi \rangle_{\mathcal{E}', C^\infty} := \langle T, \chi \psi \rangle_{D', D}, \quad (3.77)$$

where $\chi \in D(\mathbb{R}^d)$ is a test function which is identically equal to 1 on a compact neighborhood of the support of the distribution T . Furthermore, the above definition (3.77) does not depend on the choice of the test function χ . An illustration of such a test function in 1D is displayed in Figure 3.2 below, where K denotes the compact neighborhood of the support of the distribution T .

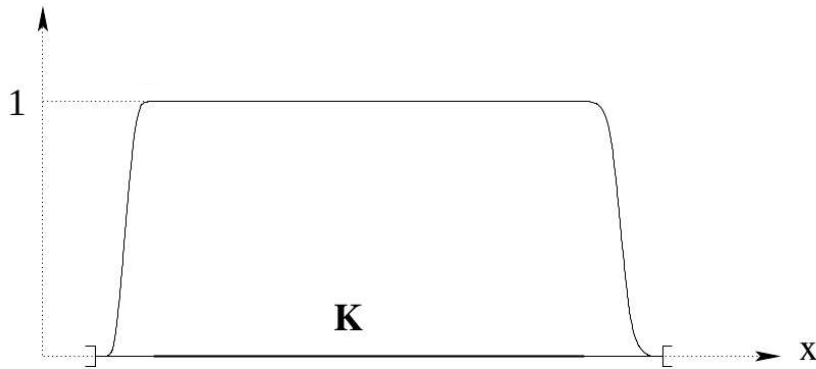


Figure 3.2: Example of a test function for compactly-supported distributions

Following the spirit of equations (3.62) and (3.77), the convolution product between the wavelets (or scaling function) and the distributions of interest is hereafter defined as follows:

Convolution (wavelets * compactly-supported distributions)

Proposition 3.4.6 *Convolution (wavelets * compactly-supported distributions)*

In the following:

- $T \in \mathcal{E}'(\mathbb{R}^2)$ denotes the distributions of interest, each possessing a compact support satisfying $\text{supp}(T) \subset \overline{\Omega_f \cup \Omega_s}$;
- $\chi \in D(\mathbb{R}^2)$ is a (compactly-supported) test function which is identically equal to 1 on a compact neighborhood K of $\overline{\Omega_f \cup \Omega_s}$, with a fast decay towards zero outside of K ;
- $(\Psi_{s,\theta})_{s,\theta}$ denotes a wavelet family of class $C^\infty(\mathbb{R}^2)$, with a fast decay towards zero outside of a well-localized spatial support.

One can write, for all $\varphi \in D(\mathbb{R}^2)$, $s > 0$, $\theta \in [0, 2\pi[$:

$$\left\langle (\chi \times \tilde{\Psi}_{s,\theta}^*) * T, \varphi \right\rangle_{D', D} = \left\langle T, (\tilde{\chi} \times \Psi_{s,\theta}^*) * \varphi \right\rangle_{D', D}. \quad (3.78)$$

Furthermore, as the product $(\chi \times \tilde{\Psi}_{s,\theta}^*)$ is of class C^∞ and also compactly-supported, the distribution $((\chi \times \tilde{\Psi}_{s,\theta}^*) * T)$ is actually a C^∞ function.

Finally, thanks to the properties of the test function χ , one can state that:

$$\forall \underline{x} \in \mathbb{R}^2, \quad (\chi \times \tilde{\Psi}_{s,\theta}^*)(\underline{x}) = \begin{cases} \tilde{\Psi}_{s,\theta}^*(\underline{x}) & \text{if } \underline{x} \in K \\ 0 & \text{if } \underline{x} \in \mathbb{R}^2 \setminus \text{supp}(\chi) \end{cases} \quad (3.79)$$

Thus, the function $(\chi \times \tilde{\Psi}_{s,\theta}^*)$ and the wavelet $(\tilde{\Psi}_{s,\theta}^*)$ coincide on the compact set K , which contains $\overline{\Omega_f \cup \Omega_s}$. Outside of K , the difference between these two functions is expected to be small. Indeed, thanks to its well-localized spatial support (localization which improves if the scale parameter decreases), the wavelet is expected to be almost zero outside of the domain of interest $\Omega_f \cup \Omega_s$. The same remark goes for the function $(\chi \times \tilde{\Psi}_{s,\theta}^*)$, thanks to the fast decay of χ from 1 to 0.

In conclusion, equation (3.78) allows to rigorously define the convolution between a compactly-supported distribution T and the function $(\chi \times \tilde{\Psi}_{s,\theta}^*)$, which happens to be very close to the wavelet $\tilde{\Psi}_{s,\theta}^*$, as further detailed in Proposition 3.4.7.

Proof of Proposition 3.4.6 *The above proposition is just an application of Proposition 3.4.5.*

Remark 3.4.4 *The above proposition also holds with a scaling function of class C^∞ and exhibiting a fast decay towards zero.*

Now, in order for the convolution product $(\chi \times \tilde{\Psi}_{s,\theta}^*) * T$ to define an actual CWT of the distribution T , one shall prove that, at least within the domain of interest $\overline{\Omega_f \cup \Omega_s}$, the following approximation, or ideally equality, holds:

$$\boxed{\forall \underline{x} \in \Omega_f \cup \Omega_s, \left((\chi \times \tilde{\Psi}_{s,\theta}^*) * f \right) (\underline{x}) \approx \left(\tilde{\Psi}_{s,\theta}^* * f \right) (\underline{x}).} \quad (3.80)$$

This point is discussed in the following proposition.

Proposition 3.4.7 Approximation $\left((\chi \times \tilde{\Psi}_{s,\theta}^*) * f \right) \approx \left(\tilde{\Psi}_{s,\theta}^* * f \right) ?$

As there is no restriction on the size of the compact domain K on which the test function χ equals 1 (as long as it is a compact neighborhood of the support of the distribution T), it can be stated that:

$$\boxed{(\chi \times \tilde{\Psi}_{s,\theta}^*) * T = \tilde{\Psi}_{s,\theta}^* * T \text{ in } \text{supp}(T).} \quad (3.81)$$

Proof of Proposition 3.4.7 *In order to prove the proximity, and even equality, between these two functions, let us consider the following 1D case:*

- $f \in L_{loc}^1(\mathbb{R})$ a distribution with a compact support $\text{supp}(f) = [-a, a]$, $a > 0$;
- $\chi \in D(\mathbb{R})$, such that χ equals 1 on $[-b, b]$, $b \geq a$, and quickly decays towards zero outside of $[-b, b]$;
- Ψ_s , $s > 0$, a wavelet of class C^∞ , well-localized on $[-c_s, c_s]$, and quickly decaying towards zero outside.

The difference between $\left((\chi \times \tilde{\Psi}_s^) * f \right)$ and $\left(\tilde{\Psi}_s^* * f \right)$ can be evaluated as follows:*

$$\forall x \in \mathbb{R}, \left[f * (\chi \times \tilde{\Psi}_s^*) - f * \tilde{\Psi}_s^* \right] (\underline{x}) = f * [(\chi - 1)\tilde{\Psi}_s^*] (\underline{x}), \quad (3.82)$$

$$= \int_{\mathbb{R}} f(x - y) (\chi(y) - 1) \tilde{\Psi}_s^*(y) dy, \quad (3.83)$$

$$= \int_{I_x} f(x - y) (\chi(y) - 1) \tilde{\Psi}_s^*(y) dy, \quad (3.84)$$

where $I_x = \{y \in \mathbb{R}, x - y \in [-a, a]\}$. Thus:

$$\left[f * (\chi \times \tilde{\Psi}_s^*) - f * \tilde{\Psi}_s^* \right] (\underline{x}) = \int_{x-a}^{x+a} f(x - y) (\chi(y) - 1) \tilde{\Psi}_s^*(y) dy. \quad (3.85)$$

As this proof is mainly interested in the behavior of the functions $((\chi \times \tilde{\Psi}_s^*) * f)$ and $(\tilde{\Psi}_s^* * f)$ within the support of f , it is hereafter assumed that $x \in [-a, a]$.

In the following, one shall distinguish two cases:

- if the domain where the test function χ equals 1 is wide enough, i.e. if $b \geq 2a$, one has:

$$\forall x \in [-a, a], \quad -b \leq x - a \leq x + a \leq b, \quad (3.86)$$

$$\forall x \in [-a, a], \quad \forall y \in [x - a, x + a], \quad \chi(y) = 1. \quad (3.87)$$

As a consequence, equation (3.85) simplifies into:

$$\forall x \in [-a, a], \quad [f * (\chi \times \tilde{\Psi}_s^*) - f * \tilde{\Psi}_s^*](\underline{x}) = 0. \quad (3.88)$$

- if the domain where the test function χ equals 1 is not wide enough, i.e. if $a \leq b < 2a$, then one shall distinguish the inner interval $[a - b, b - a]$, from the outer intervals $[-a, a - b]$ and $[b - a, a]$:

$$\forall x \in [a - b, b - a], \quad y \in [x - a, x + a], \quad [f * (\chi \times \tilde{\Psi}_s^*) - f * \tilde{\Psi}_s^*](\underline{x}) = 0. \quad (3.89)$$

$$\forall x \in [-a, a - b], \quad (3.90)$$

$$\int_{x-a}^{x+a} f(x-y) (\chi(y) - 1) \tilde{\Psi}_s^*(y) dy \quad (3.91)$$

$$= \int_{x-a}^{-b} f(x-y) (\chi(y) - 1) \tilde{\Psi}_s^*(y) dy + \int_{-b}^{x+a} f(x-y) (\chi(y) - 1) \tilde{\Psi}_s^*(y) dy, \quad (3.92)$$

$$= \int_{x-a}^{-b} f(x-y) (\chi(y) - 1) \tilde{\Psi}_s^*(y) dy. \quad (3.93)$$

Thus, when b tends towards $2a$, the error between the two functions of interest is focused in the vicinity of the boundaries of $[-a, a]$. Besides, as the wavelet Ψ_s is well-localized on $[-c_s, c_s]$ and quickly decays towards zero, the integral in (3.93) will tend towards zero if $b \gg c_s$. Indeed:

$$\forall x \in [-a, a-b], \left| \int_{x-a}^{-b} f(x-y) (\chi(y) - 1) \tilde{\Psi}_s^*(y) dy \right| \quad (3.94)$$

$$\leq \int_{x-a}^{-b} |f(x-y) (\chi(y) - 1) \tilde{\Psi}_s^*(y)| dy, \quad (3.95)$$

$$\leq \max_{y \in [x-a, -b]} |\tilde{\Psi}_s^*(y)| \times \int_{x-a}^{-b} |f(x-y)| dy, \quad (3.96)$$

$$\leq \max_{y \in [-2a, -b]} |\tilde{\Psi}_s^*(y)| \times \|f\|_{L^1(\mathbb{R})}, \quad (3.97)$$

$$\leq \max_{y \in [b, 2a]} |\Psi_s^*(y)| \times \|f\|_{L^1(\mathbb{R})}, \quad (3.98)$$

where the maximum value of the wavelet modulus $|\Psi_s|$ on $[b, 2a]$ decays towards zero when $a, b \gg c_s$.

A similar proof holds for the last interval $[b-a, a]$.

In conclusion, as long as the interval $[-b, b]$, on which χ equals 1, is wide enough compared to the support $\text{supp}(f) = [-a, a]$, or to the wavelet localization domain $[-c_s, c_s]$, the error between the functions $((\chi \times \tilde{\Psi}_{s,\theta}^*) * f)$ and $(\tilde{\Psi}_{s,\theta}^* * f)$ is either zero or close to zero. Thus, as there is no restriction on the width of the interval $[-b, b]$ (as long as it is a compact neighborhood of $[-a, a]$), it can be stated that, for a well-designed test function χ :

$$(\chi \times \tilde{\Psi}_{s,\theta}^*) * f = \tilde{\Psi}_{s,\theta}^* * f \text{ in } \text{supp}(f) \quad (3.99)$$

Remark 3.4.5 It is here recalled that the convolution product between the wavelets $(\tilde{\Psi}_{s,\theta}^*)_{s>0, \theta \in \mathbb{R}}$ (respectively the isotropic scaling function $\tilde{\Phi}_{s_0}^*$) and the function of interest is exactly the wavelet coefficient (2.132) (respectively low-frequency approximation (2.154)) of the function:

$$\mathcal{W}[f](s, \underline{u}, \theta) = (f * \tilde{\Psi}_{s,\theta}^*)(\underline{u}), \quad (3.100)$$

$$\mathcal{L}[f](s_0, \underline{u}) = (f * \tilde{\Phi}_{s_0}^*)(\underline{u}). \quad (3.101)$$

These propositions and remarks being stated, it is now high time to explicitly derive the spatially-filtered equations from the extended fluid PDEs (3.59-3.60). This is done by:

- first, considering the functions $(\tilde{\chi} \times \Psi_{s,\theta}^*) * \varphi$ or $(\tilde{\chi} \times \Phi_{s_0}^*) * \varphi$ as test functions in the extended fluid PDEs (3.59-3.60);
- second, using equation (3.78);
- third, using the fact that convolution product commutes with time and especially spatial derivatives on \mathbb{R}^2 ;
- and finally, using Fubini's theorem to rewrite the boundary integrals in the right-hand side of the balance equations.

Weak-convolution product with the extended fluid PDEs

Proposition 3.4.8 *Weak-convolution product with the fluid PDEs*

Consider $T > 0$. $\forall t \in [0, T[, s > 0, \theta \in [0, 2\pi[, \varphi \in D(\mathbb{R}^2), \underline{\psi} \in [D(\mathbb{R}^2)]^2$:

- mass balance equation:

starting with the left-hand side of equation (3.59), and using equation (3.78), one can write:

$$\left\langle \partial_t \rho + \operatorname{div}(\rho \underline{v}), (\tilde{\chi} \times \Psi_{s,\theta}^*) * \varphi \right\rangle_{D', D} \quad (3.102)$$

$$= \left\langle (\chi \times \tilde{\Psi}_{s,\theta}^*) * [\partial_t \rho + \operatorname{div}(\rho \underline{v})], \varphi \right\rangle_{D', D}, \quad (3.103)$$

$$= \left\langle \partial_t [(\chi \times \tilde{\Psi}_{s,\theta}^*) * \rho] + (\chi \times \tilde{\Psi}_{s,\theta}^*) * \operatorname{div}(\rho \underline{v}), \varphi \right\rangle_{D', D}, \quad (3.104)$$

$$= \left\langle \partial_t [(\chi \times \tilde{\Psi}_{s,\theta}^*) * \rho] + \operatorname{div}[(\chi \times \tilde{\Psi}_{s,\theta}^*) * \rho \underline{v}], \varphi \right\rangle_{D', D}. \quad (3.105)$$

In the right-hand side of equation (3.59), the boundary integral can be rewritten using Fubini's theorem:

$$\int_{\partial \tilde{\Omega}_s} [\rho]_S^F (\partial_t \underline{U}(t) \cdot \underline{n}_{F \rightarrow S}(\tilde{\sigma})) [(\tilde{\chi} \times \Psi_{s,\theta}^*) * \varphi](\tilde{\sigma}) d\tilde{\sigma} \quad (3.106)$$

$$= \int_0^{+\infty} \int_{\partial \Omega_s} [\rho]_S^F (\partial_t \underline{U}(t) \cdot \underline{n}_{F \rightarrow S}(\underline{\sigma}, t)) \left(\int_{\mathbb{R}^2} (\tilde{\chi} \times \Psi_{s,\theta}^*)(\underline{\sigma} - \underline{x}) \varphi(\underline{x}, t) d\underline{x} \right) d\underline{\sigma} dt, \quad (3.107)$$

$$= \int_0^{+\infty} \int_{\mathbb{R}^2} \left(\int_{\partial \Omega_s} (\chi \times \tilde{\Psi}_{s,\theta}^*)(\underline{x} - \underline{\sigma}) [\rho]_S^F (\partial_t \underline{U}(t) \cdot \underline{n}_{F \rightarrow S}(\underline{\sigma}, t)) d\underline{\sigma} \right) \varphi(\underline{x}, t) d\underline{x} dt \quad (3.108)$$

$$= \left\langle \int_{\partial \Omega_s} (\chi \times \tilde{\Psi}_{s,\theta}^*)(\cdot - \underline{\sigma}) [\rho]_S^F (\partial_t \underline{U}(t) \cdot \underline{n}_{F \rightarrow S}(\underline{\sigma}, t)) d\underline{\sigma}, \varphi \right\rangle_{D', D} \quad (3.109)$$

Now, bringing together both sides of the equation, one obtains:

$$\begin{aligned} & \left\langle \partial_t [(\chi \times \tilde{\Psi}_{s,\theta}^*) * \rho] + \operatorname{div}[(\chi \times \tilde{\Psi}_{s,\theta}^*) * \rho \underline{v}], \varphi \right\rangle_{D', D} \\ &= - \left\langle \int_{\partial \Omega_s} (\chi \times \tilde{\Psi}_{s,\theta}^*)(\cdot - \underline{\sigma}) [\rho]_S^F (\partial_t \underline{U}(t) \cdot \underline{n}_{F \rightarrow S}(\underline{\sigma}, t)) d\underline{\sigma}, \varphi \right\rangle_{D', D}. \end{aligned} \quad (3.110)$$

- momentum balance equation:

starting with the left-hand side of equation (3.60), one can write:

$$\left\langle \partial_t(\rho \underline{v}) + \underline{\operatorname{div}}(\rho \underline{v} \otimes \underline{v}) + \nabla p, (\tilde{\chi} \times \Psi_{s,\theta}^*) * \underline{\psi} \right\rangle_{D',D} \quad (3.111)$$

$$= \left\langle (\chi \times \tilde{\Psi}_{s,\theta}^*) * [\partial_t(\rho \underline{v}) + \underline{\operatorname{div}}(\rho \underline{v} \otimes \underline{v}) + \nabla p], \underline{\psi} \right\rangle_{D',D}, \quad (3.112)$$

$$= \left\langle \partial_t [(\chi \times \tilde{\Psi}_{s,\theta}^*) * (\rho \underline{v})] + \underline{\operatorname{div}} [(\chi \times \tilde{\Psi}_{s,\theta}^*) * (\rho \underline{v} \otimes \underline{v})] + \nabla [(\chi \times \tilde{\Psi}_{s,\theta}^*) * p], \underline{\psi} \right\rangle_{D',D}. \quad (3.113)$$

Using once again Fubini's theorem, the two boundary integrals in the right-hand side of equation (3.60) can be rewritten as follows:

$$\int_{\partial \tilde{\Omega}_s} [\partial_t \underline{U}(t) \cdot \underline{n}_{F \rightarrow S}(\tilde{\sigma})] [\rho \underline{v}]_S^F(\tilde{\sigma}) \cdot [(\tilde{\chi} \times \Psi_{s,\theta}^*) * \underline{\psi}](\tilde{\sigma}) d\tilde{\sigma} \quad (3.114)$$

$$= \int_0^{+\infty} \int_{\partial \Omega_s} [\partial_t \underline{U}(t) \cdot \underline{n}_{F \rightarrow S}(\sigma, t)] [\rho \underline{v}]_S^F(\sigma) \cdot \left(\int_{\mathbb{R}^2} (\tilde{\chi} \times \Psi_{s,\theta}^*)(\sigma - \underline{x}) \underline{\psi}(\underline{x}, t) d\underline{x} \right) d\sigma dt, \quad (3.115)$$

$$= \int_0^{+\infty} \int_{\mathbb{R}^2} \left(\int_{\partial \Omega_s} (\chi \times \tilde{\Psi}_{s,\theta}^*)(\underline{x} - \sigma) [\partial_t \underline{U}(t) \cdot \underline{n}_{F \rightarrow S}(\sigma, t)] [\rho \underline{v}]_S^F(\sigma) d\sigma \right) \cdot \underline{\psi}(\underline{x}, t) d\underline{x} dt, \quad (3.116)$$

$$= \left\langle \int_{\partial \Omega_s} (\chi \times \tilde{\Psi}_{s,\theta}^*)(\cdot - \sigma) [\rho \underline{v}]_S^F(\sigma) [\partial_t \underline{U}(t) \cdot \underline{n}_{F \rightarrow S}(\sigma, t)] d\sigma, \underline{\psi} \right\rangle_{D',D}. \quad (3.117)$$

$$\int_{\partial \tilde{\Omega}_f} [p]_{c_F}^F(\tilde{\sigma}) [(\tilde{\chi} \times \Psi_{s,\theta}^*) * \underline{\psi}](\tilde{\sigma}) \cdot \underline{n}_{F \rightarrow c_F}(\tilde{\sigma}) d\tilde{\sigma} \quad (3.118)$$

$$= \int_0^{+\infty} \int_{\partial \Omega_f} [p]_{c_F}^F(\sigma, t) \left(\int_{\mathbb{R}^2} (\tilde{\chi} \times \Psi_{s,\theta}^*)(\sigma - \underline{x}) \underline{\psi}(\underline{x}, t) d\underline{x} \right) \cdot \underline{n}_{F \rightarrow c_F}(\sigma, t) d\sigma dt, \quad (3.119)$$

$$= \int_0^{+\infty} \int_{\mathbb{R}^2} \left(\int_{\partial \Omega_f} (\chi \times \tilde{\Psi}_{s,\theta}^*)(\underline{x} - \sigma) [p]_{c_F}^F(\sigma, t) \underline{n}_{F \rightarrow c_F}(\sigma, t) d\sigma \right) \cdot \underline{\psi}(\underline{x}, t) d\underline{x} dt, \quad (3.120)$$

$$= \left\langle \int_{\partial \Omega_f} (\chi \times \tilde{\Psi}_{s,\theta}^*)(\cdot - \sigma) [p]_{c_F}^F(\sigma, t) \cdot \underline{n}_{F \rightarrow c_F}(\sigma, t) d\sigma, \underline{\psi} \right\rangle_{D',D}. \quad (3.121)$$

Now, bringing together both sides of the equation, one obtains:

$$\begin{aligned} & \left\langle \partial_t [(\chi \times \tilde{\Psi}_{s,\theta}^*) * (\rho \underline{v})] + \underline{\operatorname{div}} [(\chi \times \tilde{\Psi}_{s,\theta}^*) * (\rho \underline{v} \otimes \underline{v})] + \nabla [(\chi \times \tilde{\Psi}_{s,\theta}^*) * p], \underline{\psi} \right\rangle_{D',D} \\ &= - \left\langle \int_{\partial \Omega_s} (\chi \times \tilde{\Psi}_{s,\theta}^*)(\cdot - \sigma) [\rho \underline{v}]_S^F(\sigma) [\partial_t \underline{U}(t) \cdot \underline{n}_{F \rightarrow S}(\sigma, t)] d\sigma, \underline{\psi} \right\rangle_{D',D} \\ & \quad - \left\langle \int_{\partial \Omega_f} (\chi \times \tilde{\Psi}_{s,\theta}^*)(\cdot - \sigma) [p]_{c_F}^F(\sigma, t) \underline{n}_{F \rightarrow c_F}(\sigma, t) d\sigma, \underline{\psi} \right\rangle_{D',D}. \end{aligned} \quad (3.122)$$

Proof of Proposition 3.4.8 See Proposition 3.4.6 and equation (3.78).

Remark 3.4.6 *Commutation convolution product \longleftrightarrow spatial derivatives*

Proposition 3.4.8 used the fact that convolution product commutes with spatial (and time) derivatives on \mathbb{R}^2 . It is important to keep in mind that such a property is no longer valid on a bounded subset $\Omega \subset \mathbb{R}^2$, as already highlighted in the previous chapter when discussing Large Eddy Simulation.

Proposition 3.4.8 presented the spatially-filtered equations in a weak form. Now, using the smoothing property of the convolution product with a compactly-supported function of class C^∞ , and equation (3.81), one can write the spatially-filtered equations in a strong form:

Spatially-filtered PDEs governing the homogenized fluid (strong form)

Proposition 3.4.9 *Spatially-filtered PDEs (strong form)*

The homogenized fluid, whose conservative variables are the wavelet coefficients $(\mathcal{W}[\rho] \ \mathcal{W}[\rho v_x] \ \mathcal{W}[\rho v_y])^T(s, \underline{u}, \theta, t)$, is governed by the following spatially-filtered PDEs (here written on $\Omega_f \cup \Omega_s$) :

Consider $T > 0$. $\forall \underline{u} \in \Omega_f \cup \Omega_s$, $\forall t \in [0, T[$, $s > 0$, $\theta \in [0, 2\pi[$:

$$\begin{aligned} \partial_t \mathcal{W}[\rho](s, \underline{u}, \theta, t) + \operatorname{div}(\mathcal{W}[\rho \underline{v}](s, \underline{u}, \theta, t) \\ = - \int_{\partial \Omega_s} \tilde{\Psi}_{s,\theta}^*(\underline{u} - \underline{\sigma}) [\rho]_S^F [\partial_t \underline{U}(t) \cdot \underline{n}_{F \rightarrow S}(\underline{\sigma}, t)] \, d\underline{\sigma}. \end{aligned} \quad (3.123)$$

$$\begin{aligned} \partial_t \mathcal{W}[\rho \underline{v}](s, \underline{u}, \theta, t) + \underline{\operatorname{div}}(\mathcal{W}[\rho \underline{v} \otimes \underline{v}](s, \underline{u}, \theta, t) + \nabla \mathcal{W}[p](s, \underline{u}, \theta, t) \\ = - \int_{\partial \Omega_f} \tilde{\Psi}_{s,\theta}^*(\underline{u} - \underline{\sigma}) [p]_{c_F}^F(\underline{\sigma}, t) \cdot \underline{n}_{F \rightarrow c_F}(\underline{\sigma}, t) \, d\underline{\sigma} \\ - \int_{\partial \Omega_s} \tilde{\Psi}_{s,\theta}^*(\underline{u} - \underline{\sigma}) [\rho \underline{v}]_S^F(\underline{\sigma}) [\partial_t \underline{U}(t) \cdot \underline{n}_{F \rightarrow S}(\underline{\sigma}, t)] \, d\underline{\sigma}. \end{aligned} \quad (3.124)$$

In these PDEs, it is important to emphasize the role played by the function

$$\tilde{F}_{S \rightarrow F}(s, \underline{u}, \theta, t) := - \int_{\partial \Omega_f} \tilde{\Psi}_{s,\theta}^*(\underline{u} - \underline{\sigma}) [p]_{c_F}^F(\underline{\sigma}, t) \cdot \underline{n}_{F \rightarrow c_F}(\underline{\sigma}, t) \, d\underline{\sigma}, \quad (3.125)$$

which is a body force (per unit of length), defined across the whole space \mathbb{R}^2 , which represents the resistance that encounters the real fluid when flowing through the solid medium and impacting the outer boundaries. The

homogenization process thus transformed contact forces, localized on the fluid-structure interfaces and outer boundaries, into a body force. It also transformed PDEs governing the real fluid variables into filtered PDEs now governing the wavelet coefficients (or low-frequency approximations) of the extended fluid variables.

Finally, as the wavelet Ψ (or scaling function Φ) exhibits a well-localized support and a fast decay towards zero, it is fortunately not necessary to mesh the whole space \mathbb{R}^2 to compute the homogenized fluid. Indeed, beyond a thin layer around the initial domain boundaries $\partial(\Omega_f \cup \Omega_s)$, the homogenized fields resulting from the convolution products will be almost constant or zero, given the previous extension of the fields $(\rho, \rho \underline{v}, p)$. Besides, the current work focuses on the behavior of the homogenized fluid only within the interior domain $\Omega_f \cup \Omega_s$.

Proof of Proposition 3.4.9 See Proposition 3.4.6 for the justification of the C^∞ smoothness.

Remark 3.4.7 The spatially-filtered PDEs presented in Proposition 3.4.9 are also valid for a (real and isotropic) scaling function Φ_{s_0} of class C^∞ , with a well-localized support and a fast decay towards zero.

The spatially-filtered Euler compressible equations are completed with the following equation of state:

Equation of state for the homogenized fluid

Proposition 3.4.10 *Spatially-filtered equation of state*

Starting with the (extended) barotropic equation of state

$$p = p_{ref} + c_{son}^2(\rho - \rho_{ref}), \quad (3.126)$$

one obtains, with the analysing wavelet Ψ , the following spatially-filtered equation of state:

$\mathcal{W}[p](s, \underline{u}, \theta, t) = c_{son}^2 \mathcal{W}[\rho](s, \underline{u}, \theta, t).$

(3.127)

Now, replacing the analysing wavelet Ψ with an isotropic scaling function Φ , the filtered equation of state slightly changes:

$\mathcal{L}[p](s, \underline{u}, t) = (p_{ref} - c_{son}^2 \rho_{ref}) s \int_{\mathbb{R}^2} \Phi(\underline{y})^* d\underline{y} + c_{son}^2 \mathcal{L}[\rho](s, \underline{u}, t).$

(3.128)

Proof of Proposition 3.4.10 *Starting with the analysing wavelet Ψ , one can write, by using the linearity of convolution product on equation (3.126):*

$$\mathcal{W}[p](s, \underline{u}, \theta, t) = (p_{ref} - c_{son}^2 \rho_{ref}) \mathcal{W}[1](s, \underline{u}, \theta, t) + c_{son}^2 \mathcal{W}[\rho](s, \underline{u}, \theta, t), \quad (3.129)$$

$$= (p_{ref} - c_{son}^2 \rho_{ref}) \int_{\mathbb{R}^2} \frac{1}{s} \Psi \left(\underline{\underline{R}}_{-\theta} \frac{\underline{x} - \underline{u}}{s} \right)^* d\underline{x} + c_{son}^2 \mathcal{W}[\rho](s, \underline{u}, \theta, t). \quad (3.130)$$

Introducing the affine function $\underline{f}_{s, \underline{u}, \theta} : \underline{x} \mapsto \underline{\underline{R}}_{-\theta} \frac{\underline{x} - \underline{u}}{s}$, whose (2×2) Jacobian matrix is given by $\underline{\nabla} \underline{f}_{s, \underline{u}, \theta}(\underline{x}) = \frac{1}{s} \underline{\underline{R}}_{-\theta}$, a change of variable can be implemented in the integral of equation (3.130):

$$\int_{\mathbb{R}^2} \frac{1}{s^2} |\det(\underline{\underline{R}}_{-\theta})| \Psi \left(\underline{\underline{R}}_{-\theta} \frac{\underline{x} - \underline{u}}{s} \right)^* d\underline{x} = \int_{\mathbb{R}^2} \Psi(\underline{y})^* d\underline{y}. \quad (3.131)$$

This change of variable then leads to:

$$\mathcal{W}[p](s, \underline{u}, \theta, t) = (p_{ref} - c_{son}^2 \rho_{ref}) s \int_{\mathbb{R}^2} \Psi(\underline{y})^* d\underline{y} + c_{son}^2 \mathcal{W}[\rho](s, \underline{u}, \theta, t), \quad (3.132)$$

$$= c_{son}^2 \mathcal{W}[\rho](s, \underline{u}, \theta, t), \quad (3.133)$$

where the wavelet zero-average condition has been used to simplify the result.

When considering an isotropic scaling function Φ , this zero-average condition no longer holds. One thus obtains:

$$\mathcal{L}[p](s, \underline{u}, t) = (p_{ref} - c_{son}^2 \rho_{ref}) s \int_{\mathbb{R}^2} \Phi(\underline{y})^* d\underline{y} + c_{son}^2 \mathcal{L}[\rho](s, \underline{u}, t). \quad (3.134)$$

This last proposition finally concludes the wavelet-based homogenization process of the fluid. Now, before detailing the analysing wavelet Ψ and scaling function Φ , it is of high importance to discuss some of the critical issues associated to homogenization and multi-scale methods, that is to say the treatment of boundary conditions, the closure between unresolved and resolved scales, and nonlinearities.

3.5 Boundary conditions, closure between scales, and nonlinearities

3.5.1 Boundary conditions and closure between scales

The first step of the homogenization process, which focused on the extension of the original fluid equations, highlighted the important role played by the real fluid dynamic (and also kinematic) boundary conditions, through for instance

the following boundary integral in the extended momentum balance equation (3.60):

$$- \int_{\partial\tilde{\Omega}_f} [p]_{c_F}^F(\tilde{\sigma}) \underline{n}_{F \rightarrow c_F}(\tilde{\sigma}) \cdot \underline{\psi}(\tilde{\sigma}) d\tilde{\sigma}, \quad (3.135)$$

where it is recalled that $[p]_{c_F}^F := p_F - p_{c_F} = \begin{cases} p - p_r & \text{on } \partial\Omega_s \\ p - p_{ref} & \text{on } \partial\Omega_f \setminus \partial\Omega_s \end{cases}$.

This boundary integral could be decomposed into a first integral on the fluid-structure interface $\partial\Omega_s$, and a second integral on the outer boundary $\partial\Omega_f \setminus \partial\Omega_s$. The current work focuses only on the inner boundaries of the fluid $\partial\Omega_s$. The second integral will thus be discarded, and classical reflecting conditions will be used on the outer boundaries.

The second step of the homogenization process, which focused on the actual filtering of the extended equations, transformed contact forces, defined on the fluid-structure interfaces, into a body force defined across the whole domain:

$$\forall t \in [0, T[, s > 0, \theta \in [0, 2\pi[, \underline{u} \in \Omega_f \cup \Omega_s,$$

$$\tilde{F}_{S \rightarrow F}(s, \underline{u}, \theta, t) = - \int_{\partial\Omega_f} \tilde{\Psi}_{s,\theta}^*(\underline{u} - \underline{\sigma}) [p]_{c_F}^F(\underline{\sigma}, t) \cdot \underline{n}_{F \rightarrow c_F}(\underline{\sigma}, t) d\underline{\sigma}. \quad (3.136)$$

This body force, applied by the underlying solid obstacles to the homogenized fluid, depends on the real pressure field p , which contains all the possible spatial scales that could be caught with a DNS computation of the original fluid PDEs. However, the spatially-filtered PDEs (3.123-3.124-3.127) now only compute a band-pass $\mathcal{W}[p](s, \cdot)$ or low-pass $\mathcal{L}[p](s, \cdot)$ filtering of the original field p . A closure expression between the unresolved and resolved scales of the pressure field is thus required, as in any homogenization or multi-scale method. Conversely to plain filtering or averaging techniques, CWT and its inverse transform (2.158) bring us an analytical closure expression:

$$p(\underline{x}, t) = \frac{1}{C_\Psi} \int_0^{+\infty} \left(\int_{\mathbb{R}^2} \int_0^{2\pi} \mathcal{W}[p](s, \underline{u}, \theta, t) \times \frac{1}{s} \Psi\left(\left(\frac{\underline{R}_\theta}{s}\right)^{-1} \frac{\underline{x} - \underline{u}}{s}\right) d\theta d\underline{u} \right) \frac{ds}{s^3}. \quad (3.137)$$

If both the analysing wavelet Ψ and its scaling function Φ are real-valued and isotropic, the reconstruction formula (3.137) could also be written:

$$\boxed{p(\underline{x}, t) = \frac{2\pi}{C_\Psi} \int_0^{s_0} \left(\int_{\mathbb{R}^2} \mathcal{W}[p](s, \underline{u}, t) \times \frac{1}{s} \Psi\left(\frac{\underline{x} - \underline{u}}{s}\right) d\underline{u} \right) \frac{ds}{s^3} + \frac{\pi}{C_\Psi s_0^2} \int_{\mathbb{R}^2} \mathcal{L}[p](s_0, \underline{u}, t) \frac{1}{s_0} \Phi\left(\frac{\underline{x} - \underline{u}}{s_0}\right) d\underline{u},} \quad (3.138)$$

where s_0 denotes the cutoff scale of the low-pass filter Φ_{s_0} .

It is thus possible, thanks to CWT, to reconstruct, at each time step, the microscopic pressure field on the fluid inner boundaries, and to evaluate the body force applied by the underlying solid obstacles. In other words, the real fluid dynamic boundary conditions are transferred into a body force applied to the homogenized fluid. In a similar way, it is also possible to reconstruct the real fluid density (ρ) and momentum ($\rho \underline{v}$) at each time step, which then allow to compute the boundary integrals associated to the solid medium displacement \underline{U} in the filtered mass and momentum balance equations.

Nevertheless, one can immediately notice that, in order to compute the body force (3.136) for a single scale $s > 0$, one shall exactly reconstruct the microscopic pressure field p , and thus compute all its wavelets coefficients $\mathcal{W}[p](s, \cdot)$, for all scales $s > 0$. This would of course be too cumbersome, as it would be equivalent to a DNS computation. To bypass this difficulty, one can either:

- approximate the reconstruction formula (3.137) by using a "well-chosen" number of wavelets coefficients $(\mathcal{W}[p](s_k, \cdot))_{1 \leq k \leq N}$, selected on a "well-chosen" scale range $[s_1, s_N]$;
- discard, in equation (3.138), all wavelet coefficients $\mathcal{W}[p](s, \cdot)$ with a scale s below the cutoff scale s_0 , thus only taking into account the low-frequency approximation $\mathcal{L}[p](s_0, \cdot)$ of the pressure field:

$$\boxed{p(\underline{x}) \approx \frac{\pi}{C_\Psi s_0^2} \int_{\mathbb{R}^2} \mathcal{L}[p](s_0, \underline{u}) \frac{1}{s_0} \Phi\left(\frac{\underline{x} - \underline{u}}{s_0}\right) d\underline{u}.} \quad (3.139)$$

Both methods require to possess some *a priori* knowledge or insights on the pressure field wavelengths spectrum. Furthermore, with the approximation (3.139), the second method can be expected to present a loss of accuracy compared to the first one. Nevertheless, the computational gain is clear, as the scaling function allows to compute just once the spatially-filtered PDEs, for a given cutoff scale s_0 . Indeed, the low-frequency approximation $\mathcal{L}[p](s_0, \cdot)$ catches simultaneously all scales larger than s_0 . This also allows to avoid interactions between multiple scales in the spatially-filtered equations associated to a given scale s_i .

Besides, as wavelet coefficients decrease towards zero in regions where the field of interest is smooth, the velocity of the homogenized pressure waves could drastically increase in regions where the real fluid density is constant, thus imposing a very small time step in the numerical method.

In order not to discard the wavelet coefficients in approximation (3.139), while bypassing very small time steps, one could:

- rewrite the spatially-filtered equations so as to compute the addition of the wavelet coefficients $\mathcal{W}[f](s, \cdot)$ and the low-frequency approximation $\mathcal{L}[f](s_0, \cdot)$, with $s \in]0, s_0[$. This is done by changing the unknowns $(\tilde{\Psi}_s^* * f)$ into $[(\tilde{\Psi}_s^* + \tilde{\Phi}_{s_0}^*) * f]$ in equations (3.123-3.124-3.127).

- compute the unknowns $\left[\left(\tilde{\psi}_{s_k}^* + \tilde{\phi}_{s_0}^* \right) * f \right] = \mathcal{W}[f](s_k, \cdot) + \mathcal{L}[f](s_0, \cdot)$ for multiple $s_k \in]0, s_0[$;
- compute the low-frequency approximation $\mathcal{L}[f](s_0, \cdot)$ on its own, and then deduce the wavelet coefficients by difference:

$$\forall s_k \in]0, s_0[, \mathcal{W}[f](s_k, \cdot) = [\mathcal{W}[f](s_k, \cdot) + \mathcal{L}[f](s_0, \cdot)] - \mathcal{L}[f](s_0, \cdot). \quad (3.140)$$

Such a method would of course imply a significant increase in the computational cost.

Remark 3.5.1 *Coupling between the fluid and solid media*

The ability to reconstruct, up to an approximation, the microscopic pressure field p allows to evaluate, at each time step, and without any ad hoc model, the total force applied by the real (reconstructed) fluid to the solid medium:

$$\underline{F}_{F \rightarrow S} = \int_{\partial\Omega_s} -p(\underline{\sigma}, t) \underline{n}_{S \rightarrow F}(\underline{\sigma}, t) d\underline{\sigma}. \quad (3.141)$$

This is a mandatory step in the design of a coupled fluid-structure solver.

3.5.2 Treatment of nonlinearities

Let us now turn towards the question of nonlinearities, i.e. the convective term in the filtered momentum balance equation (3.124). It is recalled that the low-frequency approximation of the convective term writes, with an isotropic scaling function Φ :

$$\mathcal{L}[\rho \underline{v} \otimes \underline{v}](s, \underline{u}, t) = \left(\tilde{\phi}_s^* * (\rho \underline{v} \otimes \underline{v}) \right) (\underline{u}, t). \quad (3.142)$$

In LES literature, this nonlinearity is first rewritten as follows:

$$\mathcal{L}[\rho \underline{v} \otimes \underline{v}] = \mathcal{L}[\rho] \tilde{\mathcal{L}}[\underline{v} \otimes \underline{v}] \quad (3.143)$$

$$= \mathcal{L}[\rho] \tilde{\mathcal{L}}[\underline{v}] \otimes \tilde{\mathcal{L}}[\underline{v}] + \left(\mathcal{L}[\rho] \tilde{\mathcal{L}}[\underline{v} \otimes \underline{v}] - \mathcal{L}[\rho] \tilde{\mathcal{L}}[\underline{v}] \otimes \tilde{\mathcal{L}}[\underline{v}] \right), \quad (3.144)$$

where $\tilde{\mathcal{L}}$ here denotes the Favre average:

$$\tilde{\mathcal{L}}[\underline{v}] = \frac{\mathcal{L}[\rho \underline{v}]}{\mathcal{L}[\rho]}. \quad (3.145)$$

The term $(\mathcal{L}[\rho]\tilde{\mathcal{L}}[\underline{v} \otimes \underline{v}] - \mathcal{L}[\rho]\tilde{\mathcal{L}}[\underline{v}] \otimes \tilde{\mathcal{L}}[\underline{v}])$ is then transferred into the right-hand side of the filtered momentum balance equation, and gives rise to the subgrid-scale tensor, which contains the information about the energy dissipation induced by turbulence. As the current work focuses on a fast transient pressure wave within a compressible flow, viscosity and turbulence effects are considered negligible compared to pressure gradients. In the following, the nonlinear convective term will thus be approximated as follows:

$$\boxed{\mathcal{L}[\rho]\tilde{\mathcal{L}}[\underline{v} \otimes \underline{v}] \approx \mathcal{L}[\rho]\tilde{\mathcal{L}}[\underline{v}] \otimes \tilde{\mathcal{L}}[\underline{v}].} \quad (3.146)$$

In cases where turbulence effects cannot be neglected, the nonlinear term $\mathcal{L}[\rho \underline{v} \otimes \underline{v}]$ can be explicitly computed by reconstructing, at each time step, the real fluid density ρ and velocity \underline{v} via the reconstruction formula (3.139), and then computing the low-frequency approximation of the convective term $\rho \underline{v} \otimes \underline{v}$. This would of course represent a significant computational cost.

To summarize and conclude this section, the use of CWT as homogenization tool allowed to:

- rigorously derive spatially-filtered PDEs governing an equivalent homogenized fluid, whose conservative variables are the wavelets coefficients $\mathcal{W}[f](s, \cdot)$ or the low-frequency approximation $\mathcal{L}[f](s_0, \cdot)$ of the original fluid variables;
- transfer the real fluid (inner) dynamic and kinematic boundary conditions into the homogenized fluid, by means of respectively a body force applied by the underlying solid obstacles, and boundary integrals in the right-hand side of the filtered balance equations;
- evaluate, up to an approximation, this body force and these boundary integrals without any *ad hoc* model, thanks to an inverse wavelet transform connecting the unresolved and resolved scales of the fluid variables.

Now, before specifying the analysing wavelet and scaling function chosen to implement the model, and the numerical methods used for the computation of the filtered PDEs, some remarks on the model "analytical" convergence and accuracy can be highlighted.

3.6 Model convergence and accuracy criteria

The aim of this section is to:

- confirm the intuitive idea that, when the number of wavelet coefficients and the scale range $[s_{min}, s_{max}]$ increase, or equivalently, when the scaling function cutoff scale s_0 decreases towards 0, the wavelet-based model converges towards Direct Numerical Simulation (DNS);

- identify accuracy criteria to measure the analytical error between the wavelet-based model and DNS.

To reach these goals, a point-wise convergence is first proven (with respect to the cutoff scale s_0) between the wavelet-based model and DNS. Several analytical accuracy criteria are then introduced, based on a point-wise error, a L^2 -norm error, and a force-wise error.

3.6.1 Convergence towards DNS

To start with the convergence issue, it is recalled that, given a pair of real isotropic (and admissible) analysing wavelet Ψ and scaling function Φ , the error committed in reconstructing a signal $f \in L^2(\mathbb{R}^2)$ with its low-frequency approximation $\mathcal{L}[f](s_0, \cdot)$, can be evaluated as follows:

$$\begin{aligned} \forall \underline{x} \in \mathbb{R}^2, f(\underline{x}) - \frac{\pi}{C_\Psi s_0^2} \int_{\mathbb{R}^2} \mathcal{L}[f](s_0, \underline{u}) \frac{1}{s_0} \Phi\left(\frac{\underline{x} - \underline{u}}{s_0}\right) d\underline{u} \\ = \frac{2\pi}{C_\Psi} \int_0^{s_0} \left(\int_{\mathbb{R}^2} \mathcal{W}[f](s, \underline{u}) \times \frac{1}{s} \Psi\left(\frac{\underline{x} - \underline{u}}{s}\right) d\underline{u} \right) \frac{ds}{s^3}. \end{aligned} \quad (3.147)$$

Proposition 3.6.1 thoroughly proves how this error tends towards zero when the cutoff scale s_0 decreases towards zero.

Proposition 3.6.1 *Point-wise convergence towards DNS*

Consider Ψ an admissible (cf. equation (2.157)) real and isotropic wavelet, and Φ its associated real and isotropic scaling function. For all $f \in L^2(\mathbb{R}^2)$, one has the following point-wise convergence between the reconstruction based on the low-frequency approximation $\mathcal{L}[f](s_0, \cdot)$ and the function f :

$$\forall \underline{x} \in \mathbb{R}^2, \lim_{s_0 \rightarrow 0} \left| f(\underline{x}) - \frac{\pi}{C_\Psi s_0^2} \int_{\mathbb{R}^2} \mathcal{L}[f](s_0, \underline{u}) \frac{1}{s_0} \Phi\left(\frac{\underline{x} - \underline{u}}{s_0}\right) d\underline{u} \right| = 0. \quad (3.148)$$

Proof of Proposition 3.6.1 *The proof of this point-wise convergence is designed as follows:*

- step 1: apply Fourier transform to the right-hand side of equation (3.147); this first requires to justify that this term is integrable or square-integrable in order to possess a Fourier transform;
- step 2: use the wavelet admissibility condition (2.157) to prove that the obtained Fourier transform indeed converges towards zero when the cutoff scale s_0 decreases towards zero;

- step 3: apply an inverse Fourier transform and use a dominated convergence theorem to conclude.

Step 1: Fourier transform

The starting point consists in applying Fourier transform to the integral in the right-hand side of equation (3.147). To this end, let us first notice that:

$$\mathcal{W}[f](s, \underline{u}) = (f * \tilde{\Psi}_s^*)(\underline{u}). \quad (3.149)$$

$$\int_{\mathbb{R}^2} \mathcal{W}[f](s, \underline{u}) \times \frac{1}{s} \Psi\left(\frac{\underline{x} - \underline{u}}{s}\right) d\underline{u} = [\mathcal{W}[f](s, \cdot) * \Psi_s](\underline{x}). \quad (3.150)$$

As the function f belongs to the Lebesgue space $L^2(\mathbb{R}^2)$ and the wavelet Ψ to $L^1(\mathbb{R}^2) \cap L^2(\mathbb{R}^2)$, Young's inequality ensures that the function $\underline{u} \mapsto \mathcal{W}[f](s, \underline{u})$ belongs to $L^2(\mathbb{R}^2) \cap L^\infty(\mathbb{R}^2)$. Applying once again Young's inequality allows to state that the function $\underline{x} \mapsto [\mathcal{W}[f](s, \cdot) * \Psi_s](\underline{x})$ also belongs to $L^2(\mathbb{R}^2) \cap L^\infty(\mathbb{R}^2)$. One can thus apply a Fourier transform to the right-hand side of equation (3.147), which, thanks to Fubini's theorem, formally leads to:

$$\begin{aligned} \mathcal{F} \left[\int_0^{s_0} \left(\int_{\mathbb{R}^2} \mathcal{W}[f](s, \underline{u}) \times \frac{1}{s} \Psi\left(\frac{\cdot - \underline{u}}{s}\right) d\underline{u} \right) \frac{ds}{s^3} \right] (\underline{k}) \\ = \mathcal{F} \left[\int_0^{s_0} (\mathcal{W}[f](s, \cdot) * \Psi_s)(\cdot) \frac{ds}{s^3} \right] (\underline{k}), \\ = \int_0^{s_0} \mathcal{F}[\mathcal{W}[f](s, \cdot)](\underline{k}) \times \mathcal{F}[\Psi_s](\underline{k}) \frac{ds}{s^3}. \end{aligned} \quad (3.151)$$

The convergence of the integral in equation (3.151) will be proven in a few steps. To this end, one can notice that:

$$\mathcal{F}[\Psi_s](\underline{k}) = \mathcal{F}\left[\frac{1}{s} \Psi\left(\frac{\cdot}{s}\right)\right](\underline{k}), \quad (3.152)$$

$$= s \times \mathcal{F}[\Psi](s\underline{k}). \quad (3.153)$$

$$\mathcal{F}[\mathcal{W}[f](s, \cdot)](\underline{k}) = \mathcal{F}[f * \tilde{\Psi}_s^*](\underline{k}), \quad (3.154)$$

$$= \mathcal{F}[f](\underline{k}) \times s \mathcal{F}[\tilde{\Psi}^*](s\underline{k}), \quad (3.155)$$

$$= \mathcal{F}[f](\underline{k}) \times s \mathcal{F}[\Psi](s\underline{k})^*, \quad (3.156)$$

where it is recalled that $\tilde{\Psi}(\underline{x}) = \Psi(-\underline{x})$. One can now write:

$$\begin{aligned}
 \mathcal{F} \left[\int_0^{s_0} \left(\int_{\mathbb{R}^2} \mathcal{W}[f](s, \underline{u}) \times \frac{1}{s} \Psi \left(\frac{\cdot - \underline{u}}{s} \right) d\underline{u} \right) \frac{ds}{s^3} \right] (\underline{k}), \\
 = \int_0^{s_0} \mathcal{F}[f](\underline{k}) \times s^2 |\mathcal{F}[\Psi](s\underline{k})|^2 \frac{ds}{s^3}, \\
 = \mathcal{F}[f](\underline{k}) \times \int_0^{s_0} \frac{|\mathcal{F}[\Psi](s\underline{k})|^2}{s} ds. \quad (3.157)
 \end{aligned}$$

The analysing wavelet being here isotropic, the following change of variables can be used for all vector $\underline{k} \in \mathbb{R}^2 \setminus \{(0, 0)\}$:

$$\int_0^{s_0} \frac{|\mathcal{F}[\Psi](s\underline{k})|^2}{s} ds = \int_0^{s_0} \frac{|\mathcal{F}[\Psi](s\|\underline{k}\|)|^2}{s} ds, \quad (3.158)$$

$$= \int_0^{s_0\|\underline{k}\|} \frac{|\mathcal{F}[\Psi](\xi)|^2}{\frac{\xi}{\|\underline{k}\|}} \frac{1}{\|\underline{k}\|} d\xi, \quad (3.159)$$

$$= \int_0^{s_0\|\underline{k}\|} \frac{|\mathcal{F}[\Psi](\xi)|^2}{\xi} d\xi. \quad (3.160)$$

Step 2: wavelet admissibility condition

If $\underline{k} = \underline{0}$, one has in equation (3.157), thanks to the zero-average condition satisfied by the wavelet, $\mathcal{F}[\Psi](\underline{0}) = 0$. Now, using the wavelet admissibility condition (2.157), that is to say:

$$C_\Psi := \int_{\mathbb{R}^2} \frac{|\mathcal{F}[\Psi](\|\underline{k}\|)|^2}{\|\underline{k}\|^2} d\underline{k}, \quad (3.161)$$

$$= 2\pi \int_0^{+\infty} \frac{|\mathcal{F}[\Psi](r)|^2}{r^2} r dr, \quad (3.162)$$

$$= 2\pi \int_0^{+\infty} \frac{|\mathcal{F}[\Psi](r)|^2}{r} dr, \quad (3.163)$$

$$< +\infty, \quad (3.164)$$

it can be stated that the function $\xi \mapsto \frac{|\mathcal{F}[\Psi](\xi)|^2}{\xi}$, visible in equation (3.160), is integrable on $]0, +\infty[$. As a consequence, one has, for all $\underline{k} \in \mathbb{R}^2 \setminus \{(0, 0)\}$:

$$\lim_{s_0 \rightarrow 0} \int_0^{s_0\|\underline{k}\|} \frac{|\mathcal{F}[\Psi](\xi)|^2}{\xi} d\xi = \lim_{s_0 \rightarrow 0} \left(\int_0^{+\infty} \frac{|\mathcal{F}[\Psi](\xi)|^2}{\xi} d\xi - \int_{s_0\|\underline{k}\|}^{+\infty} \frac{|\mathcal{F}[\Psi](\xi)|^2}{\xi} d\xi \right), \quad (3.165)$$

$$= 0. \quad (3.166)$$

It is thus proved that, for all $\underline{k} \in \mathbb{R}^2$:

$$\lim_{s_0 \rightarrow 0} \mathcal{F} \left[\int_0^{s_0} \left(\int_{\mathbb{R}^2} \mathcal{W}[f](s, \underline{u}) \times \frac{1}{s} \Psi \left(\frac{\cdot - \underline{u}}{s} \right) d\underline{u} \right) \frac{ds}{s^3} \right] (\underline{k}) = 0. \quad (3.167)$$

Step 3: inverse Fourier transform + dominating convergence theorem

Now, using an inverse Fourier transform, one can write for all $\underline{x} \in \mathbb{R}^2$:

$$\begin{aligned} & \int_0^{s_0} \left(\int_{\mathbb{R}^2} \mathcal{W}[f](s, \underline{u}) \times \frac{1}{s} \Psi \left(\frac{\underline{x} - \underline{u}}{s} \right) d\underline{u} \right) \frac{ds}{s^3} \\ &= \mathcal{F}^{-1} \left[\mathcal{F} \left[\int_0^{s_0} \left(\int_{\mathbb{R}^2} \mathcal{W}[f](s, \underline{u}) \times \frac{1}{s} \Psi \left(\frac{\cdot - \underline{u}}{s} \right) d\underline{u} \right) \frac{ds}{s^3} \right] (\cdot) \right] (\underline{x}) \\ &= \frac{1}{(2\pi)^2} \int_{\mathbb{R}^2} \left(\mathcal{F}[f](\underline{k}) \times \int_0^{s_0} \frac{|\mathcal{F}[\Psi](s\underline{k})|^2}{s} ds \right) e^{i\underline{k} \cdot \underline{x}} d\underline{k}. \end{aligned} \quad (3.168)$$

It has already been proven that the modulus of the function within the integral in the right-hand side of equation (3.168) converges towards zero when the cutoff scale s_0 tends towards zero. Moreover, one can write, using again the wavelet admissibility constant C_Ψ , that for all $\underline{k} \in \mathbb{R}^2$:

$$\begin{aligned} & \left| \mathcal{F}[f](\underline{k}) \times \int_0^{s_0} \frac{|\mathcal{F}[\Psi](s\underline{k})|^2}{s} ds \times e^{i\underline{k} \cdot \underline{x}} \right| \\ &= |\mathcal{F}[f](\underline{k})| \times \int_0^{s_0} \frac{|\mathcal{F}[\Psi](s\underline{k})|^2}{s} ds, \\ &\leq |\mathcal{F}[f](\underline{k})| \times \frac{C_\Psi}{2\pi}. \end{aligned} \quad (3.169)$$

The Fourier transform of f is a bounded and continuous function on \mathbb{R}^2 . It is thus integrable on each compact subset of \mathbb{R}^2 . As a consequence, the function $\underline{k} \mapsto |\mathcal{F}[f](\underline{k})| \times \frac{C_\Psi}{2\pi}$ is a locally integrable and dominating function. Thanks to the dominated convergence theorem, one can now pass the limit within the integral in the right-hand side of equation (3.168):

$$\begin{aligned} & \lim_{s_0 \rightarrow 0} \int_{\mathbb{R}^2} \left(\mathcal{F}[f](\underline{k}) \times \int_0^{s_0} \frac{|\mathcal{F}[\Psi](s\underline{k})|^2}{s} ds \right) e^{i\underline{k} \cdot \underline{x}} d\underline{k} \\ &= \int_{\mathbb{R}^2} \left(\lim_{s_0 \rightarrow 0} \left(\mathcal{F}[f](\underline{k}) \times \int_0^{s_0} \frac{|\mathcal{F}[\Psi](s\underline{k})|^2}{s} ds \right) e^{i\underline{k} \cdot \underline{x}} \right) d\underline{k}, \end{aligned} \quad (3.170)$$

which finally leads to the result:

$$\lim_{s_0 \rightarrow 0} \int_0^{s_0} \left(\int_{\mathbb{R}^2} \mathcal{W}[f](s, \underline{u}) \times \frac{1}{s} \Psi \left(\frac{\underline{x} - \underline{u}}{s} \right) d\underline{u} \right) \frac{ds}{s^3} = 0. \quad (3.171)$$

This concludes the proof on the "analytical" convergence of the wavelet-based model towards Direct Numerical Simulation (DNS). It is here worth noticing that the cutoff scale s_0 is actually closely linked to the mesh size h . This link will be especially emphasized when discussing the stability of the numerical methods, later in this chapter. Thus, in order to decrease s_0 and catch all possible wavelengths, the mesh has to be refined accordingly. The convergence of the reconstruction process based on the low-frequency approximation is thus a convergence with respect to both the cutoff scale s_0 and the mesh size h .

Remark 3.6.1 *Convergence in L^2 -norm*

Thanks to the fact that CWT preserves the L^2 -norm of a finite-energy signal $f \in L^2(\mathbb{R}^2)$ (cf. energy identity (2.159)), one could also define a convergence between $\|f\|_{L^2(\mathbb{R}^2)}$ and $\|\mathcal{W}[f](s, \cdot)\|_{L^2(\mathbb{R}^2)}$.

These propositions and remarks on the model "analytical" convergence being stated, let us now detail some accuracy criteria that will be used in chapter 4 to assess the model capabilities.

3.6.2 Accuracy criteria

In the following, p_{ref} denotes a reference pressure field defined at the microscopic scale. Let us denote by λ_{min} the minimum wavelength contained within this pressure field, and s_{min} the positive scale parameter such that the cutoff wavelength of the scaling function Φ satisfies:

$$\lambda_{cutoff}(\Phi_{s_{min}}) = s_{min} \times \lambda_{cutoff}(\Phi), \quad (3.172)$$

$$\lesssim \lambda_{min}. \quad (3.173)$$

Point-wise accuracy

Given the above assumption, the low-frequency approximation $\mathcal{L}[p](s_{min}, \cdot)$ thus allows to reach the "best" approximation of the microscopic pressure field p_{ref} with equation (3.139). Thus, thanks to the reconstruction formula (3.138), one can state that:

$$p_{ref}(\underline{x}) - p_{s_{min}}(\underline{x}) \quad (3.174)$$

$$:= p_{ref}(\underline{x}) - \frac{\pi}{C_{\Psi} s_{min}^2} \int_{\mathbb{R}^2} \mathcal{L}[p_{s_{min}}](s_{min}, \underline{u}) \frac{1}{s_{min}} \Phi\left(\frac{\underline{x} - \underline{u}}{s_{min}}\right) d\underline{u}, \quad (3.175)$$

$$= \frac{2\pi}{C_{\Psi}} \int_0^{s_{min}} \left(\int_{\mathbb{R}^2} \mathcal{W}[p_{s_{min}}](s, \underline{u}) \times \frac{1}{s} \Psi\left(\frac{\underline{x} - \underline{u}}{s}\right) d\underline{u} \right) \frac{ds}{s^3}, \quad (3.176)$$

$$\approx 0. \quad (3.177)$$

Then, for any computation of the homogenized fluid at a larger cutoff scale $s_0 \geq s_{min}$, one can define the point-wise error as follows:

$$p_{ref}(\underline{x}) - p_{s_0}(\underline{x}) \quad (3.178)$$

$$:= p_{ref}(\underline{x}) - \frac{\pi}{C_\Psi s_0^2} \int_{\mathbb{R}^2} \mathcal{L}[p_{s_{min}}](s_0, \underline{u}) \frac{1}{s_0} \Phi\left(\frac{\underline{x} - \underline{u}}{s_0}\right) d\underline{u}, \quad (3.179)$$

$$\approx \frac{2\pi}{C_\Psi} \int_{s_{min}}^{s_0} \left(\int_{\mathbb{R}^2} \mathcal{W}[p_{s_{min}}](s, \underline{u}) \times \frac{1}{s} \Psi\left(\frac{\underline{x} - \underline{u}}{s}\right) d\underline{u} \right) \frac{ds}{s^3}, \quad (3.180)$$

where the wavelet coefficients $\mathcal{W}[p_{s_{min}}](s, \cdot)$ are not obtained with the computation of the spatially-filtered PDEs at a given scale $s \in [s_{min}, s_0]$, but rather directly computed from the "best" approximation $p_{s_{min}}$. One can then study the behavior of the function

$$s_0 \longmapsto \frac{2\pi}{C_\Psi} \int_{s_{min}}^{s_0} \left(\int_{\mathbb{R}^2} \mathcal{W}[p_{s_{min}}](s, \underline{u}) \times \frac{1}{s} \Psi\left(\frac{\underline{x} - \underline{u}}{s}\right) d\underline{u} \right) \frac{ds}{s^3} \quad (3.181)$$

to see how the point-wise error $|p_{ref}(\underline{x}) - p_{s_0}(\underline{x})|$ deteriorates when the cutoff scale s_0 increases, i.e. when the smaller wavelengths are progressively discarded.

L^2 accuracy

Beside this point-wise accuracy, one can also define a L^2 accuracy. Indeed, thanks to the energy identity (2.159), one can study the function (here written with an isotropic wavelet):

$$s_0 \longmapsto \|p_{ref}\|_{L^2}^2 - \frac{2\pi}{C_\Psi} \int_{s_{min}}^{s_0} \|\mathcal{W}[p_{s_{min}}](s, \cdot)\|_{L^2}^2 \frac{ds}{s^3}, \quad (3.182)$$

which shall decrease from $\|p_{ref}\|_{L^2}^2$ ($s_0 = s_{min}$) to zero ($s_0 \longrightarrow +\infty$).

Force-wise accuracy

One could also define an accuracy with respect to the force applied by the real fluid to the solid medium:

$$\forall i \in \{1, 2\},$$

$$\left| \left((\underline{F}_{F \rightarrow S})_{ref} - (\underline{F}_{F \rightarrow S})_{s_0} \right) \cdot \underline{e}_i \right| = \left| \int_{\partial\Omega_s} - (p_{ref} - p_{s_0})(\underline{\sigma}, t) (\underline{n}_{S \rightarrow F}(\underline{\sigma}, t) \cdot \underline{e}_i) d\underline{\sigma} \right|, \quad (3.183)$$

$$\leq \int_{\partial\Omega_s} |(p_{ref} - p_{s_0})(\underline{\sigma}, t) (\underline{n}_{S \rightarrow F}(\underline{\sigma}, t) \cdot \underline{e}_i)| d\underline{\sigma}, \quad (3.184)$$

where we recall that $p_{s_0} = \frac{\pi}{C_V s_0^2} \int_{\mathbb{R}^2} \mathcal{L}[p_{s_{min}}](s_0, \underline{u}) \frac{1}{s_0} \Phi\left(\frac{x-u}{s_0}\right) d\underline{u}$.

It is also possible to look at the time integration of the force applied by the real fluid to the solid medium, which contributes to its momentum:

$$\left| \int_{t_a}^{t_b} \left((\underline{F}_{F \rightarrow S})_{ref} - (\underline{F}_{F \rightarrow S})_{s_0} \right) \cdot \underline{e}_i dt \right| \leq \int_{t_a}^{t_b} \left| \left((\underline{F}_{F \rightarrow S})_{ref} - (\underline{F}_{F \rightarrow S})_{s_0} \right) \cdot \underline{e}_i \right| dt, \quad (3.185)$$

$$: = \left\| \left((\underline{F}_{F \rightarrow S})_{ref} - (\underline{F}_{F \rightarrow S})_{s_0} \right) \cdot \underline{e}_i \right\|_{L^1[t_a, t_b]}. \quad (3.186)$$

These different accuracy criteria being stated, let us finally describe the analysing wavelet and scaling function chosen to implement the model.

3.7 Analysing wavelet and scaling function

In the current work, CWT aims at filtering fields that do not possess any oriented feature. Indeed, both the analysing wavelet and scaling function shall be able to “observe” pressure waves propagating in different directions simultaneously (reflection/transmission on obstacles). Furthermore, as detailed during the derivation of the spatially-filtered Euler compressible equations, both the analysing wavelet and scaling function shall satisfy the following properties:

- C^∞ smoothness;
- good localization in the spatial domain;
- fast decay towards zero.

Thus, the Mexican hat wavelet (Figure 3.3), which is an isotropic, real-valued wavelet of class C^∞ , with a fast decay towards zero, appears perfectly suited for the model. The definition of the 2D Mexican hat is recalled below, both in the physical and spectral domains.

Definition 3.7.1 2D Mexican hat wavelet

The Mexican hat wavelet is defined, with a L^2 -normalization in the physical domain, as follows:

$$\Psi(\underline{x}) = \frac{\sqrt{2}}{\sigma\sqrt{\pi}} \left(1 - \frac{\|\underline{x}\|^2}{2\sigma^2} \right) e^{-\frac{\|\underline{x}\|^2}{2\sigma^2}}, \quad (3.187)$$

$$\mathcal{F}[\Psi](\underline{k}) = \sigma^3 \sqrt{2\pi} \|\underline{k}\|^2 e^{-\frac{\sigma^2 \|\underline{k}\|^2}{2}}. \quad (3.188)$$

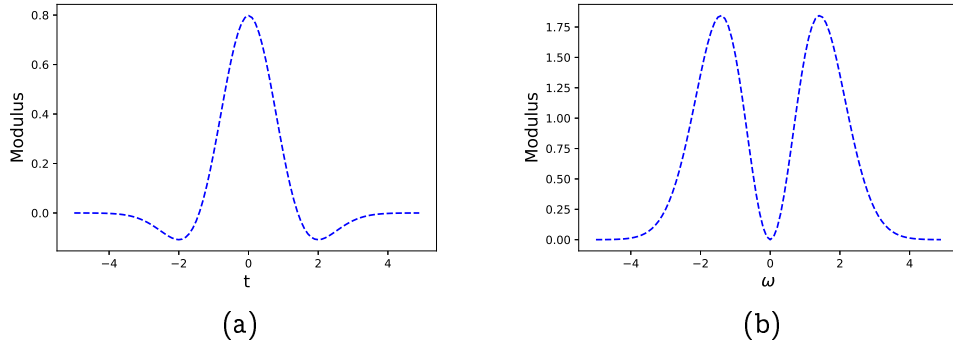


Figure 3.3: Cutaway of the 2D Mexican hat (a) and its Fourier transform (b).

This wavelet is obtained by computing the Laplacian of a Gaussian function, whose standard deviation is here denoted by $\sigma > 0$. As any analysing wavelet, the Mexican hat exhibits a band-pass behavior in the spectral domain, as detailed in Tables 3.1-3.2 (with a -3 dB bandwidth convention).

Proposition 3.7.1 *Filtering properties of the Mexican hat ($\sigma = 1$)*

Peak wave vector	Bandwidth - lower bound	Bandwidth - upper bound
$\ \underline{k}_\Psi\ = \frac{\sqrt{2}}{\sigma}$	$\ \underline{k}_\Psi\ _{min} \approx 0.875 \text{ m}^{-1}$	$\ \underline{k}_\Psi\ _{max} \approx 2.04 \text{ m}^{-1}$

Table 3.1: Filtering properties of the Mexican hat wavelet (1/2)

Peak wavelength	Bandwidth - lower bound	Bandwidth - upper bound
$\lambda_\Psi = \pi\sigma\sqrt{2}$	$(\lambda_\Psi)_{min} \approx 3.08 \text{ m}$	$(\lambda_\Psi)_{max} \approx 7.18 \text{ m}$

Table 3.2: Filtering properties of the Mexican hat wavelet (2/2)

Proof of Proposition 3.7.1 *The above results are obtained by identifying the -3 dB bandwidth on the curve of the Mexican hat Fourier transform.*

Beside its smoothness and isotropy, the Mexican hat wavelet also satisfies the admissibility condition (2.157), which is a requirement for the use of an inverse wavelet transform.

Proposition 3.7.2 *2D Mexican hat admissibility constant*

The 2D Mexican hat is an admissible wavelet, with:

$$\boxed{C_\Psi = 2\pi^2\sigma^2.} \quad (3.189)$$

Proof of Proposition 3.7.2 *Straight application of the definition of the admissibility constant in equation (2.157).*

Regarding now the scaling function associated to the Mexican hat, hereafter displayed in Figure 3.4, it is defined in the spectral domain by:

Definition 3.7.2 *2D Mexican hat scaling function*

$$\mathcal{F}[\Phi](\underline{k}) = \sigma^2 \sqrt{2\pi} \left(\|\underline{k}\|^2 + \frac{1}{\sigma^2} \right)^{\frac{1}{2}} e^{-\frac{\sigma^2 \|\underline{k}\|^2}{2}}. \quad (3.190)$$

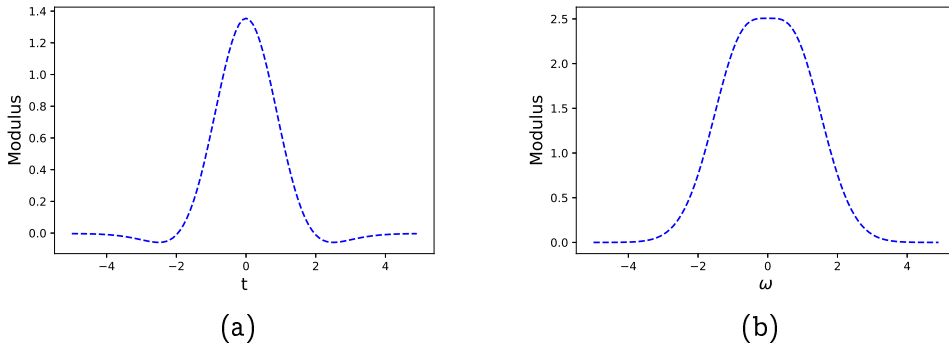


Figure 3.4: Cutaway of the 2D scaling function (a) and its Fourier transf. (b).

As the analysing wavelet Ψ , the scaling function Φ is also isotropic, real-valued, of class C^∞ , and exhibits a fast decay towards zero. However, conversely to the wavelet, it does not possess any analytical formula in the physical domain. Its representation in Figure 3.4a can thus only be obtained with an inverse Fast Fourier Transform (FFT).

Remark 3.7.1 *Approximation of the scaling function in the physical domain*

In numerical implementations, 2D FFT/FFT⁻¹ algorithms, which classically rely on successive 1D FFT/FFT⁻¹ computations, may deteriorate the isotropy of the scaling function. To prevent this phenomenon, one can approximate the scaling function behavior in the physical domain (for $\sigma = 1$) via the following analytical and isotropic formula:

$$\Phi_{approx}(\underline{x}) = \frac{\sqrt{2}}{\sqrt{1.09}} \left(1 - \frac{\|\underline{x}\|^2}{2 \left(\frac{1.785 \times 1.09 \sigma}{\sqrt{2}} \right)^2} \right) e^{-\frac{\|\underline{x}\|^2}{2(1.09\sigma)^2}}. \quad (3.191)$$

As displayed in Figure 3.5b, the approximation defined by equation (3.191) satisfies the following accuracy result:

$$|\Phi_{approx} - \Phi|(\|\underline{x}\|) \leq \frac{1}{100} \Phi(0). \quad (3.192)$$

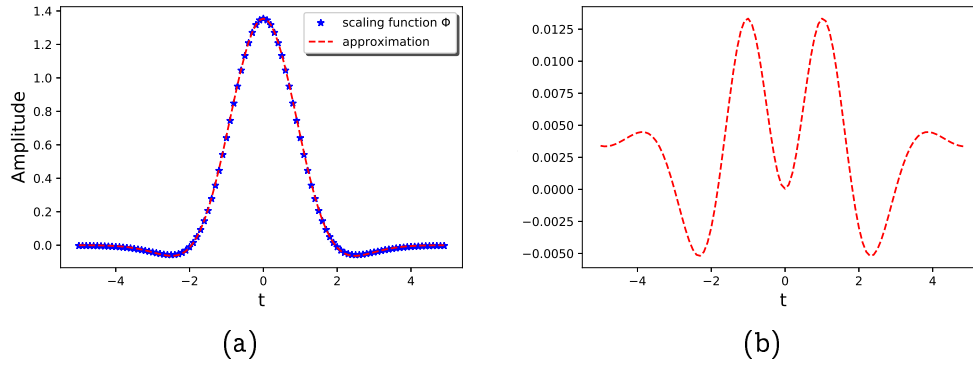


Figure 3.5: Cutaway of the scaling function Φ and its approximation Φ_{approx} (a), and their difference $\Phi_{approx} - \Phi$ (b).

Finally, conversely to the analysing wavelet Ψ , the scaling function is a low-pass filter. Its characteristics are summarized in Table 3.3 below (with a -3 dB bandwidth convention).

Proposition 3.7.3 *Filtering properties of the scaling function*

Cutoff wave vector	Cutoff wavelength
$\ \underline{k}_\Phi\ \lesssim 1.285 \text{ m}^{-1}$	$\lambda_\Phi \gtrsim 4.85 \text{ m}$

Table 3.3: Filtering properties of the scaling function ($\sigma = 1$)

Proof of Proposition 3.7.3 *The above results are obtained by identifying the -3 dB bandwidth on the curve of the scaling function Fourier transform.*

Remark 3.7.2 *Loss of isotropy caused by directional splitting*

It is here worth highlighting that the use of finite-volume schemes with directional splitting may deteriorate the isotropy of the scaling function. Indeed, with such numerical methods, only fluxes oriented along the Cartesian directions are taken into account. The impact of the cells vertices is thus neglected. Therefore, in order to transport a quantity of interest from the cell $c_{(i,j)}$ to the cell $c_{(i+1,j+1)}$, one has to transport this quantity along each Cartesian direction. If this quantity is filtered with an isotropic filter, the cutoff frequency or wave vector is thus applied along each direction. As a consequence, larger frequencies and smaller wavelengths can be taken into account by the scaling function:

$$\|\underline{k}_\Phi\|_{num} = \sqrt{k_x^2 + k_y^2}, \quad (3.193)$$

$$= \|\underline{k}_\Phi\| \sqrt{2}, \quad (3.194)$$

which leads to the following "numerical" cutoff values:

Cutoff wave vector	Cutoff wavelength
$\ \underline{k}_\Phi\ _{num} \lesssim 1.83 \text{ m}^{-1}$	$(\lambda_\Phi)_{num} \gtrsim 3.43 \text{ m}$

 Table 3.4: Scaling function cutoff values with directional splitting ($\sigma = 1$)

This remark thus concludes the section dedicated to the choice of the analysing wavelet and scaling function. It is now high time to describe the numerical methods that will be implemented to solve on the one hand, the solid medium dynamic equation, and on the other hand, the homogenized fluid filtered PDEs. To this end, let us first summarize the model assumptions and equations.

3.8 Summary of the model assumptions and equations

The wavelet-based homogenized and multi-scale model at the core of this work has been designed within a 2D framework:

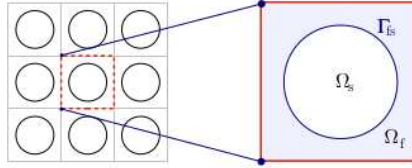


Figure 3.6: Illustration of a 2D {fluid + solid} geometry.

Assumptions on the 2D geometry

- the fluid domain Ω_f is an open bounded and connected space of \mathbb{R}^2 ;
- the solid domain Ω_s is an open bounded and disconnected space of \mathbb{R}^2 : $\Omega_s = \cup_i \Omega_{s_i}$, with $\Omega_{s_i} \cap_{i \neq j} \Omega_{s_j} = \emptyset$. No periodicity or scale separation assumptions are here required.

Assumptions and equations for the solid medium

- the solid medium is composed of the disjoint reunion of multiple disks. These disks are considered as rigid and homogeneous bodies;
- the distance between neighboring disks, while not necessarily periodic, is assumed constant (cf. spacer grids in fuel assemblies); this assumption could be easily bypassed by considering an individual displacement field for each disk (without impacts), with no change to the wavelet-based model;

- the whole array is modeled as a rigid body animated with two degrees of freedom (two translations). Its dynamic equilibrium is governed by a second order linear differential equation:

$$\forall i \in \{1, 2\}, \ddot{U}_i + 2\xi\omega_0\dot{U}_i + \omega_0^2 U_i = \frac{1}{m} \left(\underline{F}_{F \rightarrow S} \cdot \underline{e}_i \right). \quad (3.195)$$

Assumptions and equations for the fluid

- compressible single-phase flow;
- the real fluid is considered inviscid: viscosity and turbulence effects are negligible compared to pressure gradients;
- gravity is negligible compared to pressure gradients;
- conduction heat transfer is negligible on the time scale at study;
- the real fluid satisfies a barotropic equation of state.
- the homogenized fluid is shown to be governed (in a strong sense) by the following spatially-filtered Euler compressible equations within the inner domain $\Omega_f \cup \Omega_s$ (here written with an isotropic scaling function Φ):

find the homogenized fluid conservative variables $\left(\mathcal{L}[\rho](s, \cdot), \mathcal{L}[\rho \underline{v}_x](s, \cdot), \mathcal{L}[\rho \underline{v}_y](s, \cdot) \right)^T$ such that, for all $s > 0$, $\underline{u} \in \Omega_f \cup \Omega_s$, and $t \geq 0$:

$$\begin{aligned} \partial_t \mathcal{L}[\rho](s, \underline{u}, t) + \operatorname{div}(\mathcal{L}[\rho \underline{v}]) (s, \underline{u}, t) \\ = - \int_{\partial \Omega_s} \tilde{\Phi}_s^*(\underline{u} - \underline{\sigma}) [\rho]_S^F [\partial_t \underline{U}(t) \cdot \underline{n}_{F \rightarrow S}(\underline{\sigma}, t)] \, d\underline{\sigma}, \end{aligned} \quad (3.196)$$

$$\begin{aligned} \partial_t \mathcal{L}[\rho \underline{v}](s, \underline{u}, t) + \underline{\operatorname{div}}(\mathcal{L}[\rho \underline{v} \otimes \underline{v}]) (s, \underline{u}, t) + \underline{\nabla}(\mathcal{L}[p]) (s, \underline{u}, t) \\ = - \int_{\partial \Omega_f} \tilde{\Phi}_s^*(\underline{u} - \underline{\sigma}) [p]_{c_F}^F(\underline{\sigma}, t) \cdot \underline{n}_{F \rightarrow c_F}(\underline{\sigma}, t) \, d\underline{\sigma} \\ - \int_{\partial \Omega_s} \tilde{\Phi}_s^*(\underline{u} - \underline{\sigma}) [\rho \underline{v}]_S^F(\underline{\sigma}) [\partial_t \underline{U}(t) \cdot \underline{n}_{F \rightarrow S}(\underline{\sigma}, t)] \, d\underline{\sigma}. \end{aligned} \quad (3.197)$$

where it is recalled that $\mathcal{L}[f](s, \underline{u}, t) = (f * \tilde{\Phi}_s^*)(\underline{u}, t)$ denotes the low-frequency approximation of f .

- the underlying solid obstacles are shown to apply a body force to the homogenized fluid:

$$\tilde{F}_{S \rightarrow F}(s, \underline{u}, t) = - \int_{\partial \Omega_f} \tilde{\Phi}_s^*(\underline{u} - \underline{\sigma}) [p]_{c_F}^F(\underline{\sigma}, t) \cdot \underline{n}_{F \rightarrow c_F}(\underline{\sigma}, t) \, d\underline{\sigma}. \quad (3.198)$$

- for the homogenized fluid problem to be well-posed, a closure equation between resolved and unresolved scales is required for the conservative variables $(\rho, \rho \underline{v}, p)$. Thanks to an inverse wavelet transform, this analytical closure equation writes, with only an isotropic scaling function Φ :

$$p(\underline{x}) \approx \frac{\pi}{C_\psi s_0^2} \int_{\mathbb{R}^2} \mathcal{L}[p](s_0, \underline{u}) \frac{1}{s_0} \Phi\left(\frac{\underline{x} - \underline{u}}{s_0}\right) d\underline{u}, \quad (3.199)$$

$$\approx \frac{\pi}{C_\psi s_0^2} \mathcal{F}^{-1}[\mathcal{F}[\mathcal{L}[p](s_0, \cdot)](\cdot) \times s_0 \mathcal{F}[\Phi](s_0 \times \cdot)](\underline{x}). \quad (3.200)$$

- as turbulence is neglected, the treatment of the nonlinear convective term is simplified into:

$$\mathcal{L}[\rho \underline{v} \otimes \underline{v}] := \mathcal{L}[\rho] \tilde{\mathcal{L}}[\underline{v} \otimes \underline{v}], \quad (3.201)$$

$$\approx \mathcal{L}[\rho] \tilde{\mathcal{L}}[\underline{v}] \otimes \tilde{\mathcal{L}}[\underline{v}], \quad (3.202)$$

where $\tilde{\mathcal{L}}$ denotes the Favre average.

- the homogenized fluid is shown to satisfy a spatially-filtered barotropic equation of state (here written with an isotropic scaling function):

$$\mathcal{L}[p](s, \underline{u}, t) = (p_{ref} - c_{son}^2 \rho_{ref}) s \int_{\mathbb{R}^2} \Phi(\underline{y})^* d\underline{y} + c_{son}^2 \mathcal{L}[\rho](s, \underline{u}, t). \quad (3.203)$$

- as this work focuses on the behavior of the homogenized fluid within the inner domain $\Omega_f \cup \Omega_s$, only the component of the body force (3.198) associated to the fluid-structure interface $\partial\Omega_s$ is hereafter considered. The other component is discarded, and replaced by classical reflection conditions on the outer boundary $\partial\Omega_f \setminus \partial\Omega_s$.

All the model assumptions and equations being recalled, let us now detail the numerical methods.

3.9 Numerical methods

This section presents the numerical methods chosen to solve the solid and fluid equations, and gives some insights on the major numerical challenges faced by the wavelet-based model. The current section is thus organized as follows:

- the first subsection recalls the classical Newmark algorithm, here chosen to solve the solid medium linear differential equation;

- it is followed by a 1st order finite-volume scheme, here chosen to solve the homogenized fluid PDEs; this scheme is based on a Godunov's method and an explicit time integration, and uses an approximate Riemann solver (namely Rusanov) to compute the numerical fluxes;
- the third subsection then emphasizes the issue of stability, which is critical for explicit schemes;
- and finally, the focus is put on the risk of aliasing associated to the use of FFT algorithms with the scaling function Φ_{s_0} , whose support in the frequency domain may exceed the range allowed by Nyquist–Shannon sampling theorem;

3.9.1 Solid medium: Newmark method

In the current work, the solid medium is animated with two degrees of freedom, i.e. horizontal and vertical translations, which are governed by the following linear differential equation:

$$\forall i \in \{1, 2\}, m\ddot{U}_i + c\dot{U}_i + kU_i = \underline{F}_{F \rightarrow S} \cdot \underline{e}_i. \quad (3.204)$$

To simplify notations, we hereafter denote A the acceleration, V the velocity, and D the displacement. Equation (3.204) is classically computed with a Newmark algorithm:

- the solution being known at $t = t^n$, either in acceleration A_n or displacement D_n , one predicts the next values of the displacement and velocity based on the acceleration profile on the time step $[t^n, t^{n+1}]$:

$$D_{n+1} = D_n + \Delta t V_n + \frac{\Delta t^2}{2} [(1 - 2\beta)A_n + 2\beta A_{n+1}], \quad (3.205)$$

$$= \widetilde{D}_{n+1} + \beta \Delta t^2 A_{n+1}, \quad (3.206)$$

$$V_{n+1} = V_n + \Delta t [(1 - \gamma)A_n + \gamma A_{n+1}], \quad (3.207)$$

$$= \widetilde{V}_{n+1} + \gamma \Delta t A_{n+1}, \quad (3.208)$$

where \widetilde{D}_{n+1} and \widetilde{V}_{n+1} are the predicted values of the displacement and velocity, and β and γ are two parameters controlling the algorithm stability. For a displacement-oriented resolution, one can write:

$$A_{n+1} = \frac{1}{\beta \Delta t^2} (D_{n+1} - \widetilde{D}_{n+1}), \quad (3.209)$$

$$V_{n+1} = \widetilde{V}_{n+1} + \frac{\gamma}{\beta \Delta t} (D_{n+1} - \widetilde{D}_{n+1}). \quad (3.210)$$

- given the predicted values \widetilde{D}_{n+1} and \widetilde{V}_{n+1} , the equilibrium equation at $t = t^{n+1}$ writes:

$$\frac{m}{\beta \Delta t^2} (D_{n+1} - \widetilde{D}_{n+1}) + c \left(\widetilde{V}_{n+1} + \frac{\gamma}{\beta \Delta t} (D_{n+1} - \widetilde{D}_{n+1}) \right) + k D_{n+1} = F_{n+1}, \quad (3.211)$$

$$\boxed{\left[\frac{m}{\beta \Delta t^2} + \frac{\gamma c}{\beta \Delta t} + k \right] D_{n+1} = F_{n+1} + \frac{m}{\beta \Delta t^2} \widetilde{D}_{n+1} + c \left(\frac{\gamma}{\beta \Delta t} \widetilde{D}_{n+1} - \widetilde{V}_{n+1} \right)}, \quad (3.212)$$

or equivalently, in a more compact form:

$$\boxed{\widetilde{k} D_{n+1} = \widetilde{F}_{n+1}}. \quad (3.213)$$

- once D_{n+1} is computed from equation (3.213), one updates the acceleration and velocity at t^{n+1} with equations (3.209-3.210).

Depending on the values chosen for the parameters γ and β , Newmark algorithm is known to be:

- unconditionally stable if $\frac{1}{2} \leq \gamma \leq 2\beta$;
- stable if $\gamma \geq \frac{1}{2}$ and $\beta < \frac{\gamma}{2}$, under the additional condition:

$$\omega_0 \Delta t \leq \sqrt{\frac{2}{\gamma - 2\beta}}. \quad (3.214)$$

The values $\gamma = \frac{1}{2}$ and $\beta = \frac{1}{4}$ are commonly used to reach an unconditional stability.

3.9.2 Homogenized fluid: Godunov's method

Let us now turn towards the computation of the homogenized fluid PDEs. All the spatially-filtered equations, written with an isotropic scaling function Φ , are recalled below:

- the filtered mass balance equation governing $\mathcal{L}[\rho](s_0, \cdot)$:

$$\begin{aligned} & \partial_t \mathcal{L}[\rho](s_0, \cdot) + \partial_x \left(\mathcal{L}[\rho] \tilde{\mathcal{L}}[v_x] \right)(s_0, \cdot) + \partial_y \left(\mathcal{L}[\rho] \tilde{\mathcal{L}}[v_y] \right)(s_0, \cdot) \\ & = - \int_{\partial \Omega_s} \tilde{\Phi}_{s_0}^*(\underline{u} - \underline{\sigma}) [\rho]_S^F(\underline{\sigma}, t) [\partial_t \underline{U}(t) \cdot \underline{n}_{F \rightarrow S}(\underline{\sigma}, t)] \, d\underline{\sigma}, \end{aligned} \quad (3.215)$$

- the filtered momentum balance equation governing $\mathcal{L}[\rho v_x](s_0, \cdot)$:

$$\begin{aligned} & \partial_t \left(\mathcal{L}[\rho] \tilde{\mathcal{L}}[v_x] \right) (s_0, \cdot) + \partial_x \left(\mathcal{L}[\rho] \tilde{\mathcal{L}}[v_x]^2 + \mathcal{L}[p] \right) (s_0, \cdot) + \partial_y \left(\mathcal{L}[\rho] \tilde{\mathcal{L}}[v_x] \tilde{\mathcal{L}}[v_y] \right) (s_0, \cdot) \\ &= - \int_{\partial\Omega_s} \tilde{\Phi}_{s_0}^* (\cdot - \underline{\sigma}) [p]_S^F(\underline{\sigma}, t) (\underline{n}_{F \rightarrow S}(\underline{\sigma}, t) \cdot \underline{e}_x) d\underline{\sigma} \\ & \quad - \int_{\partial\Omega_s} \tilde{\Phi}_{s_0}^* (\underline{u} - \underline{\sigma}) [\partial_t U(t) \cdot \underline{n}_{F \rightarrow S}(\underline{\sigma}, t)] [\rho \underline{v} \cdot \underline{e}_x]_S^F(\underline{\sigma}, t) d\underline{\sigma}, \quad (3.216) \end{aligned}$$

- the filtered momentum balance equation governing $\mathcal{L}[\rho v_y](s_0, \cdot)$:

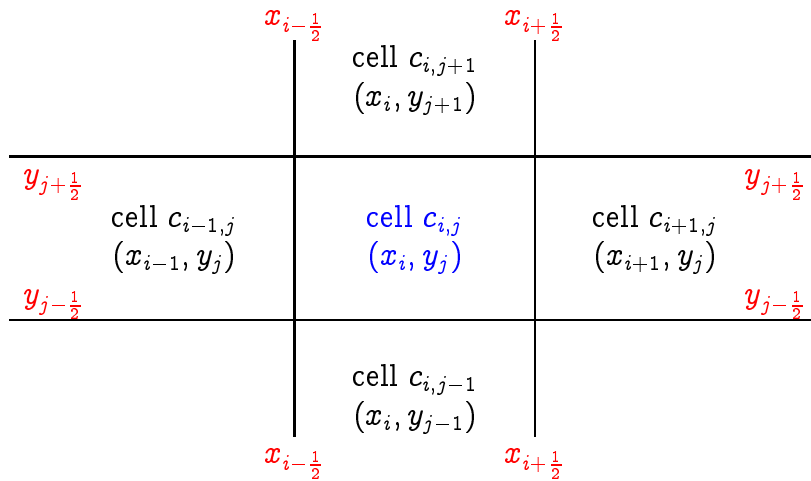
$$\begin{aligned} & \partial_t \left(\mathcal{L}[\rho] \tilde{\mathcal{L}}[v_y] \right) (s_0, \cdot) + \partial_x \left(\mathcal{L}[\rho] \tilde{\mathcal{L}}[v_y] \tilde{\mathcal{L}}[v_x] \right) (s_0, \cdot) + \partial_y \left(\mathcal{L}[\rho] \tilde{\mathcal{L}}[v_y]^2 + \mathcal{L}[p] \right) (s_0, \cdot) \\ &= - \int_{\partial\Omega_s} \tilde{\Phi}_{s_0}^* (\cdot - \underline{\sigma}) [p]_S^F(\underline{\sigma}, t) (\underline{n}_{F \rightarrow S}(\underline{\sigma}, t) \cdot \underline{e}_y) d\underline{\sigma} \\ & \quad - \int_{\partial\Omega_s} \tilde{\Phi}_{s_0}^* (\underline{u} - \underline{\sigma}) [\partial_t U(t) \cdot \underline{n}_{F \rightarrow S}(\underline{\sigma}, t)] [\rho \underline{v} \cdot \underline{e}_y]_S^F(\underline{\sigma}, t) d\underline{\sigma}, \quad (3.217) \end{aligned}$$

- the filtered barotropic equation of state (here normalized with respect to the mean of the scaling function):

$$\frac{1}{s_0 \int_{\mathbb{R}^2} \Phi(\underline{x})^* d\underline{x}} \mathcal{L}[p](s_0, \cdot) = (p_{ref} - c_{son}^2 \rho_{ref}) + \frac{c_{son}^2}{s_0 \int_{\mathbb{R}^2} \Phi(\underline{x})^* d\underline{x}} \mathcal{L}[\rho](s_0, \cdot). \quad (3.218)$$

Spatial discretization: 1st order finite-volume scheme

As classically done in the study of hyperbolic system of conservation laws, the homogenized fluid equations will hereafter be discretized in space via a finite-volume method with directional splitting. Thanks to the homogenization process, this finite-volume method can be associated to a plain 2D regular Cartesian grid, as illustrated below.



The unknowns will be approximated by constants on each cell, leading to a 1st order scheme.

Time discretization: Euler explicit scheme

As for the time discretization, an Euler explicit scheme is chosen considering the physics at study. Indeed, for the numerical method to be accurate, the time step Δt is first restricted by the pressure waves velocities, in order to prevent these waves from exiting a cell during a single time step. This restriction on Δt allows at the same time to satisfy the Courant-Friedrichs-Lewy (C.F.L.) condition which ensures the stability of the explicit scheme. The definition of this C.F.L. condition will be recalled in the following section. Finally, another advantage of explicit schemes is their ability to avoid any matrix inversion process.

Godunov's scheme

Thus, the 1st order finite-volume scheme with Euler explicit time integration can be summarized into the following Godunov's scheme:

for each cell $c_{i,j}$:

$$(\underline{L})_{i,j}^{n+1} = (\underline{L})_{i,j}^n - \frac{\Delta t^n}{\Delta x} (\underline{\mathcal{G}}_{i+\frac{1}{2},j}^n - \underline{\mathcal{G}}_{i-\frac{1}{2},j}^n) - \frac{\Delta t^n}{\Delta y} (\underline{\mathcal{H}}_{i,j+\frac{1}{2}}^n - \underline{\mathcal{H}}_{i,j-\frac{1}{2}}^n) + \Delta t^n \begin{pmatrix} S_0 \\ S_1 \\ S_2 \end{pmatrix}_{i,j}^n,$$

(3.219)

where:

- $\Delta x / \Delta y$ and Δt denote respectively the spatial and time steps;
- \underline{L} denotes the homogenized fluid conservative variables:

$$\underline{L} = \left(\mathcal{L}[\rho] \quad \mathcal{L}[\rho v_x] \quad \mathcal{L}[\rho v_y] \right)^T (s_0, \cdot); \quad (3.220)$$

- $\underline{\mathcal{G}}_{i+\frac{1}{2},j}$ and $\underline{\mathcal{G}}_{i-\frac{1}{2},j}$ denote the horizontal fluxes exchanged at the interfaces with the right and left neighboring cells;
- $\underline{\mathcal{H}}_{i,j+\frac{1}{2}}$ and $\underline{\mathcal{H}}_{i,j-\frac{1}{2}}$ denote the vertical fluxes exchanged at the interfaces with the upper and lower neighboring cells;
- $\underline{S} = \begin{pmatrix} S_0 & S_1 & S_2 \end{pmatrix}^T$ is a vector gathering the source terms of each balance equation.

Approximate Riemann solver: Rusanov flux

In order to compute the numerical fluxes $\underline{\mathcal{G}}$ and $\underline{\mathcal{H}}$ at the interfaces, an approximate Riemann solver is used, namely Rusanov flux:

$$\begin{aligned} \underline{\mathcal{G}}_{i+\frac{1}{2},j}^n = & \frac{\underline{\mathcal{G}}(\underline{L}_{i,j}^n) + \underline{\mathcal{G}}(\underline{L}_{i+1,j}^n)}{2} \\ & - \max_{k=1,\dots,3} [|(\lambda_x)_k|(\underline{L}_{i,j}^n), |(\lambda_x)_k|(\underline{L}_{i+1,j}^n)] \frac{\underline{L}_{i+1,j}^n - \underline{L}_{i,j}^n}{2}; \end{aligned} \quad (3.221)$$

$$\begin{aligned} \underline{\mathcal{H}}_{i,j+\frac{1}{2}}^n = & \frac{\underline{\mathcal{H}}(\underline{L}_{i,j}^n) + \underline{\mathcal{H}}(\underline{L}_{i,j+1}^n)}{2} \\ & - \max_{k=1,\dots,3} [|(\lambda_y)_k|(\underline{L}_{i,j}^n), |(\lambda_y)_k|(\underline{L}_{i,j+1}^n)] \frac{\underline{L}_{i,j+1}^n - \underline{L}_{i,j}^n}{2}; \end{aligned} \quad (3.222)$$

with:

- $\underline{\mathcal{G}}$ and $\underline{\mathcal{H}}$ the exact flux in the PDEs:

$$\underline{\mathcal{G}} = \begin{pmatrix} \mathcal{L}[\rho]\tilde{\mathcal{L}}[v_x] & \mathcal{L}[\rho]\tilde{\mathcal{L}}[v_x]^2 + \mathcal{L}[p] & \mathcal{L}[\rho]\tilde{\mathcal{L}}[v_y]\tilde{\mathcal{L}}[v_x] \end{pmatrix}^T; \quad (3.223)$$

$$\underline{\mathcal{H}} = \begin{pmatrix} \mathcal{L}[\rho]\tilde{\mathcal{L}}[v_y] & \mathcal{L}[\rho]\tilde{\mathcal{L}}[v_x]\tilde{\mathcal{L}}[v_y] & \mathcal{L}[\rho]\tilde{\mathcal{L}}[v_y]^2 + \mathcal{L}[p] \end{pmatrix}^T; \quad (3.224)$$

- $(\lambda_x)_{1 \leq k \leq 3}$ and $(\lambda_y)_{1 \leq k \leq 3}$ the eigenvalues associated to the non-conservative form of the hyperbolic system ($i \in \{x, y\}$):

$$(\lambda_i)_1 = \tilde{\mathcal{L}}[v_i] - \mathcal{L}[c_{son}], \quad (3.225)$$

$$(\lambda_i)_2 = \tilde{\mathcal{L}}[v_i], \quad (3.226)$$

$$(\lambda_i)_3 = \tilde{\mathcal{L}}[v_i] + \mathcal{L}[c_{son}]. \quad (3.227)$$

This concludes the numerical methods for both the solid and fluid equations. The following subsections now emphasize the critical issue of stability, before underlining the risk of an aliasing phenomenon caused by the scaling function.

3.9.3 Stability: explicit VS implicit filtering

It is well-known that explicit schemes are especially vulnerable to instability. Indeed, let us consider the classical (1D) linear advection equation

$$\partial_t u + c \partial_x u = 0, \quad (3.228)$$

where $c > 0$ denotes a constant advection velocity. An Euler explicit upwind scheme

$$\frac{u_j^{n+1} - u_j^n}{\Delta t} + c \frac{u_j^n - u_{j-1}^n}{\Delta x} = 0 \quad (3.229)$$

is known to be stable under the following Courant-Friedrichs-Lewy (C.F.L.) condition:

$$\boxed{\nu := \frac{c\Delta t}{\Delta x} \leq 1}, \quad (3.230)$$

or equivalently:

$$\boxed{\Delta t \leq \frac{\Delta x}{c}}. \quad (3.231)$$

When solving (1D) nonlinear PDEs with such explicit schemes, a safety margin is usually taken with respect to the C.F.L. condition:

$$\Delta t = C_{stab} \frac{\Delta x}{c_{max}}, \quad C_{stab} \leq 1, \quad (3.232)$$

where the constant C_{stab} is commonly chosen equal to 0.8, and c_{max} denotes the maximum velocity over the whole domain.

In the current work, two "spatial steps" coexist:

- first, the cutoff wavelength $(\lambda_{\Phi_{s_0}})_{num}$ of the scaling function Φ_{s_0} (see Table 3.4), which satisfies for all $s_0 > 0$:

$$(\lambda_{\Phi_{s_0}})_{num} = s_0 \times (\lambda_{\Phi})_{num}, \quad (3.233)$$

and acts directly onto the original Euler compressible equations, at the continuum medium scale.

- second, the spatial discretization of the 2D regular Cartesian grid:

$$h = \Delta x = \Delta y, \quad (3.234)$$

which then acts in the numerical computation of the spatially-filtered equations.

Thus, the classical C.F.L. condition associated to the mesh size h coexist with another characteristic time scale, linked to the scaling function Φ_{s_0} :

$$\Delta t_{\Phi_{s_0}} = \frac{(\lambda_{\Phi_{s_0}})_{num}}{c_{max}}. \quad (3.235)$$

Nevertheless, it shall be noticed that, conversely to the scaling function spatial scale, which is isotropic, the distance between two neighboring grid nodes is not. Thus, in order to preserve the scheme stability, the cutoff wavelength of the scaling function has to be larger than the maximum distance between two neighboring grid nodes:

$$s_0 (\lambda_\Phi)_{num} \geq \text{dist}(\text{node}_{i,j}, \text{node}_{i+1,j+1}), \quad (3.236)$$

$$\geq h\sqrt{2}, \quad (3.237)$$

which leads to the following compatibility condition between the scale parameter s_0 and the mesh size h :

$$s_0 \geq \frac{\sqrt{2}}{(\lambda_\Phi)_{num}} \times h. \quad (3.238)$$

The numerical approximation of the compatibility condition (3.238) is specified in Table 3.5:

Stability - cutoff scale VS mesh size

$$s_0 \gtrsim 0.412 \times h$$

Table 3.5: Compatibility condition between the cutoff scale s_0 and the mesh size h to ensure the stability of the explicit scheme.

This compatibility condition will be tested in the next chapter dedicated to the model implementation. But for now, let us turn towards the risk of aliasing.

3.9.4 Sampling, FFT, and aliasing

The phenomenon of aliasing is known to be explained by Shannon sampling theorem. Indeed, given a mesh size h , one has the following sampling properties:

Spatial step	Spatial sampling frequency	Shannon spatial frequency
h	$\sigma_e = \frac{1}{h}$	$\sigma_{max} = \frac{1}{2h}$

Table 3.6: Mesh sampling properties.

To satisfy Shannon theorem, the frequency range accessible with the scaling function should remain within the wave vector range defined by $[-\|k\|_{max}, \|k\|_{max}] = [-2\pi\sigma_{max}, 2\pi\sigma_{max}]$. However, it was previously highlighted that, considering the directional splitting used in the finite-volume

method, the cutoff wave vector of the scaling function is larger than its theoretical value: $\|\underline{k}_{\Phi}\|_{num} = \sqrt{2} \times \|\underline{k}_{\Phi}\|$. Thus, to ensure that the bandwidth of the scaling function Φ_{s_0} remains within the observable wave vector range, the cutoff scale parameter s_0 has to satisfy:

$$\|\underline{k}_{\Phi_{s_0}}\|_{num} \leq \frac{\pi}{h}, \quad (3.239)$$

$$\frac{\sqrt{2} \times \|\underline{k}_{\Phi}\|}{s_0} \leq \frac{\pi}{h}, \quad (3.240)$$

$$\boxed{s_0 \geq \frac{\sqrt{2} \|\underline{k}_{\Phi}\|}{\pi} \times h.} \quad (3.241)$$

Thus, if the cutoff scale s_0 is too small, the scaling function bandwidth will exceed the admissible spatial frequency range, leading to an aliasing phenomenon with the use of FFT algorithms on Φ_{s_0} . The numerical approximation of equation (3.241) is detailed in the following Table 3.7:

Aliasing - cutoff scale VS mesh size
$s_0 \gtrsim 0,579 \times h$

Table 3.7: Compatibility condition between the cutoff scale s_0 and the mesh size h to prevent aliasing in FFT computations.

Remark 3.9.1 *Aliasing and boundary conditions*

The impact of aliasing will be mainly focused on the fluid-structure interfaces. Indeed, the boundary integrals present in the right-hand sides of the filtered balance equations all require a closure expression between the resolved and unresolved scales of the fluid variables. This closure is brought by an inverse wavelet transform, which will be implemented via FFT and FFT⁻¹ algorithms applied to the low-frequency approximations $\mathcal{L}[\rho](s_0, \cdot)$, $\mathcal{L}[\rho \underline{v}](s_0, \cdot)$, $\mathcal{L}[p](s_0, \cdot)$ and the scaling function Φ_{s_0} itself. As a consequence, the reconstructed fields on the fluid-structure interfaces will exhibit high-frequency noise if the above compatibility condition (3.241) is not satisfied.

3.10 Conclusion

These important remarks thus conclude this third chapter dedicated to the thorough description of the wavelet-based model. This core chapter built step by step a self-sustained homogenized and multi-scale model, here applied to an inviscid compressible flow within a congested solid medium. It was proven how Continuous Wavelet Transform (CWT) can be used to rigorously homogenize,

at the continuum medium scale, a heterogeneous medium. The homogenization process here promoted, which may apply to generic PDEs, relies on a "weak-extension" of the original fluid PDEs, followed by a "weak-convolution" with an analysing wavelet or scaling function. To ensure the well-posedness of this convolution product, a real-valued, isotropic, smooth, well-localized and admissible wavelet, namely the Mexican hat, has been chosen. With such an analysing wavelet or scaling function, this wavelet-based convolution product, which acts as a regularizing and filtering operator, is thus able to deal with PDEs exhibiting non-smooth weak solutions. This convolution process eventually results in spatially-filtered PDEs governing a homogenized fluid, defined over the whole {fluid + solid} domain. The homogenized fluid variables were shown to be the wavelet coefficients (or low-frequency approximation) of the original fluid variables. It was also detailed how the original contact forces between the fluid and solid media are transformed into body forces defined within the whole homogenized fluid.

Furthermore, it was emphasized that CWT possesses a key advantage compared to classical homogenization and multi-scale methods, namely its ability to reconstruct, thanks to an inverse wavelet transform, the fields at the microscopic scale. This crucial point allowed to build a self-sustained model, which can connect resolved and unresolved scales without any *ad hoc* model, and properly treat the original PDEs boundary conditions. This reconstruction ability can also be used to explicitly compute, if necessary, nonlinear terms. Besides, the wavelet formalism also allowed to prove an analytical convergence (either point-wise or in L^2 -norm) between the homogenized model and Direct Numerical Simulation (DNS). To the author's knowledge, it is the first time that such a self-sustained homogenized and multi-scale model, able to deal with generic and non-smooth PDEs, closure between resolved and unresolved scales and boundary conditions (and if necessary nonlinearities), is put forward in literature. This wavelet-based model also bypasses periodicity and scale separation assumptions.

Finally, the last section of this chapter emphasized some of the challenges likely to appear during the model numerical implementation, that is to say the risks of instability and aliasing. Two compatibility conditions underlining the links between the scaling function cutoff scale s_0 (i.e. explicit filtering) and the mesh size h (i.e. implicit filtering), were put forward.

All this theoretical framework being defined, the following chapter shall now confirm, with numerical tests, these risks of instability and aliasing. These tests also aim at assessing the model actual convergence towards numerical reference solutions computed at the DNS scale, and involving 2D transverse pressure waves propagating through congested solid media composed of multiple disks.

Chapter 4

Model implementation and analysis

4.1 Introduction

In order to confront the wavelet-based model with the physics of interest, and assess its ability to tackle the challenges previously highlighted, namely instability, aliasing, and convergence towards DNS, this fourth chapter hereafter presents several 2D numerical tests, completed with preliminary experimental data. Throughout this chapter, a special focus will be put on the model ability to reconstruct 2D pressure fields, and the resulting dynamic load applied to the solid medium.

The opening section presents a wavelet analysis of a 2D reference pressure wave propagating through a 10×10 steady array of disks. This reference solution is computed at the DNS scale with EUROPLEXUS software, a fast-transient dynamics code for fluids and structures. This first study of a reference solution known at the DNS scale allows to get insights on the pressure field spectrum, in other words its most relevant wavelet coefficients and spatial scales. This information will later on guide the direct computation of the homogenized fluid PDEs.

The second section then presents a preliminary analysis on the numerical model stability and accuracy. This analysis is performed by directly computing the spatially-filtered PDEs, with the scaling function ϕ , for a 2D pressure wave propagating through a 2×2 steady array of disks. The focus is especially put on both the C.F.L. and compatibility conditions between the scaling function cutoff scale s_0 and the mesh size h .

In echo with the first wavelet analysis, the third section then presents the direct computation of a 2D transverse pressure wave propagating through a 10×10 steady array of disks. The model ability to accurately reconstruct the reference pressure field and the reference force applied to the solid medium, both computed at the DNS scale with EUROPLEXUS software, will be evaluated.

Fourth, in order to emphasize the multi-scale component of the model, the propagation of a 2D transverse pressure wave through different but equivalent steady array of disks (2×2 , 4×4 , 10×10) is considered. The aim of this test is to assess whether a more macroscopic modeling of the solid medium, and thus

a larger mesh size h and cutoff scale s_0 , allow to reconstruct a similar order of magnitude for the force applied to the solid medium.

To conclude this chapter, insights on two ongoing projects will be presented. The first one consists in a first attempt at implementing a nested grids algorithm within the numerical model. Conversely to classical multi-grid methods, this attempt does not here aim at improving an iterative method by damping both the high and low-frequency components of the error. The aim is rather to speed up the computations, by solving the homogenized fluid PDEs on a coarse grid, while keeping track of the solid medium geometry on a fine grid, in order to evaluate the different boundary integrals present in the filtered PDEs. As for the second ongoing project, it is dedicated to the coupling between the homogenized fluid and the solid medium. Experiments realized with a 10×10 array of PMMA cylinder rods submitted to a shock wave will be presented. This experimental data will be supplemented with a preliminary numerical test involving a 2×2 moving array of disks.

4.2 Wavelet analysis of a 2D reference pressure wave

In order to guide the direct computation of the spatially-filtered equations, and select wisely the cutoff scale parameter s_0 , or the number of wavelet coefficients $(\mathcal{W}[f](s_k, \cdot))_{1 \leq k \leq N}$, it is necessary to possess some insights on the pressure field spectrum. To this end, this section presents a wavelet analysis of a 2D reference pressure wave propagating through a 10×10 steady array of disks. This pressure wave is computed at the microscopic scale with EUROPLEXUS software, a fast-transient dynamics code for fluids and structures, which solves directly Euler compressible equations. This local solution allows to compute analytically the pressure field wavelet coefficients, and then fully assess the accuracy of the reconstruction process with respect to the main quantity of interest, i.e. the dynamic load applied to the solid medium, which is directly linked to the pressure gradient. The simulation is designed as shown in Figure 4.1 below. Such a 2D test case can be seen as a simplified, yet representative, version of the actual pressure loading that would impact PWR fuel assemblies during a depressurization transient.

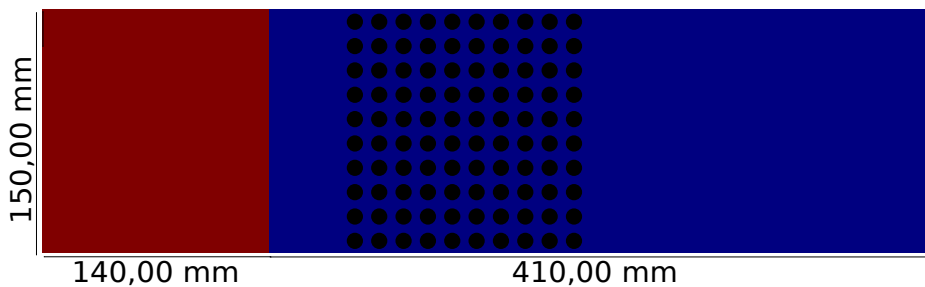


Figure 4.1: Geometry of the first reference test case.

All the simulation parameters are specified in Tables 4.1-4.2-4.3.

Lx	Ly	Disks radius	Dist. consecutive disks	Disks position
0.55 m	0.15 m	$5 \cdot 10^{-3}$ m	$5 \cdot 10^{-3}$ m	[0.2025 m, 0.3525 m]

Table 4.1: Geometry - 1st test case.

10 bar zone	1 bar zone	Discontinuity \longleftrightarrow 1st disks
[0, 0.14 m]	[0.14 m, 0.55 m]	6.75×10^{-2} m

Table 4.2: Pressure loading - 1st test case.

The fluid is considered compressible, inviscid and isothermal. It satisfies a barotropic state law:

$$p = p_{ref} + c^2(\rho - \rho_{ref}), \quad (4.1)$$

with the following numerical values:

Reference Density	Reference Pressure	Sound Velocity
$\rho_{ref} = 1000 \text{ kg} \cdot \text{m}^{-3}$	$p_{ref} = 10^5 \text{ Pa}$	$c = 1300 \text{ m} \cdot \text{s}^{-1}$

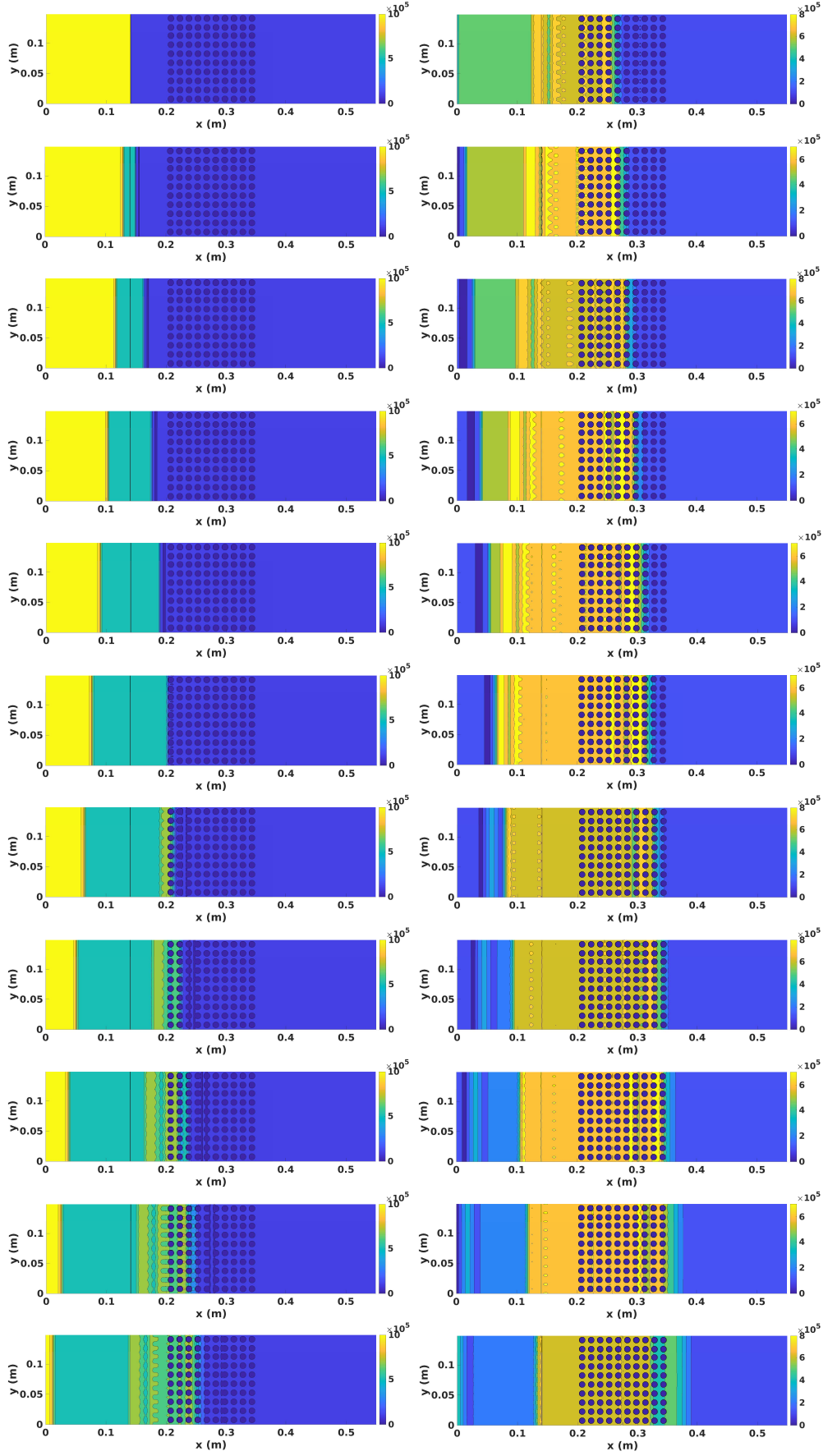
Table 4.3: Fluid parameters - 1st test case.

As for the solid medium, the disks can here be considered as rigid bodies, whose centers are kinematically blocked, so that the sum of the reaction forces to the central blockages directly provides the force applied by the fluid to the solid obstacles.

The numerical methods used to compute this 2D reference pressure wave are designed as follows:

- a finite-element method for the (linear elastic and isotropic) solid medium, with 3-noded triangle elements;
- a 2nd order cell-centered finite volume scheme for the fluid, with quadrangle elements, and a H.L.L. (Harten - Lax - van Leer) Riemann solver for the numerical fluxes;
- mesh size: $h_{epx} \in \{\frac{R}{5}, \frac{R}{8}, \frac{R}{10}, \frac{R}{12}\}$, where R denotes the disks radius;
- Euler explicit time integration for the fluid.

The reference pressure field, computed on Ω_f , is then extended over the whole domain $\Omega_f \cup \Omega_s$ by means of a linear interpolation on a 2D regular Cartesian grid with half mesh size $h = 0.5h_{epx}$. Figures 4.2 and 4.3 display the resulting pressure field computed with $h_{epx} = \frac{R}{5} = 1 \text{ mm}$. It can be noted that, during the interpolation process, the pressure is by default set to zero on the nodes located outside the fluid domain.


 Figure 4.2: Reference pressure field snapshots every $\Delta t = 1.10^{-5}$ s

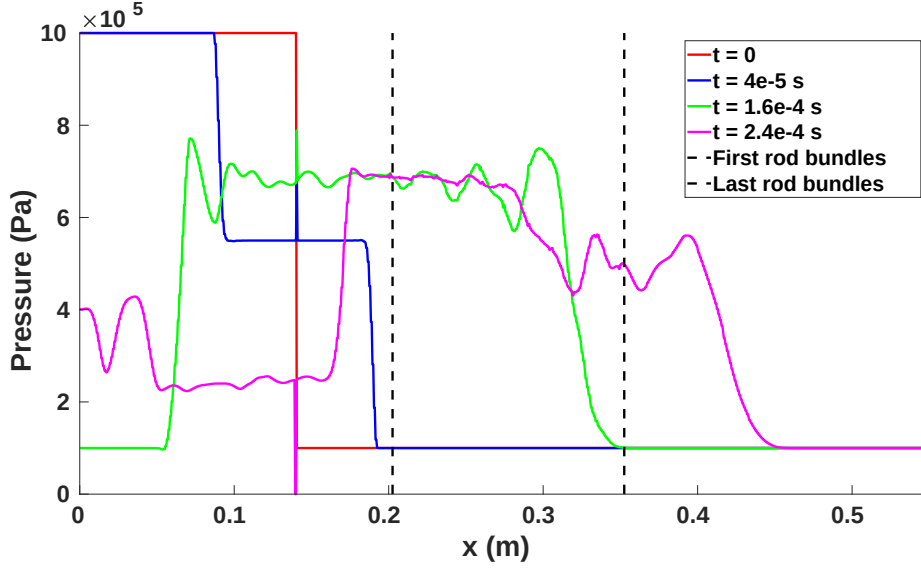


Figure 4.3: Reference horizontal pressure profile - 10×10 array ($y = \frac{L_y}{2}$).

As in a classical shock tube situation, the simulation shows two waves propagating in opposite directions from the initial discontinuity (Figure 4.2 and Figure 4.3 at $t = 4.10^{-5}$ s). The left one then bounces back on the left vertical boundary (defined with absorbing conditions) and heads back towards the solid medium (Figure 4.3, $t = 1.6 \times 10^{-4}$ s and $t = 2.4 \times 10^{-4}$ s). This left boundary condition, not very familiar in shock tube computations or experiments, does not here affect the propagation of the pressure wave within the solid medium. Indeed, the simulation stops before the reflected wave hits back the solid medium. The same is true for the wave bouncing back on the right vertical boundary.

Now, in order to determine the most relevant wavelengths within this reference pressure field, let us use some of the accuracy criteria presented in the previous chapter.

4.2.1 L^2 -accuracy

In equation (3.182), the following function was introduced:

$$s_0 \mapsto \|p_{ref}\|_{L^2}^2 - \frac{2\pi}{C_\Psi} \int_{s_{min}}^{s_0} \|\mathcal{W}[p_{s_{min}}](s, \cdot)\|_{L^2}^2 \frac{ds}{s^3}, \quad (4.2)$$

$$= \|p_{ref}\|_{L^2}^2 \left(1 - \frac{\frac{2\pi}{C_\Psi} \int_{s_{min}}^{s_0} \|\mathcal{W}[p_{s_{min}}](s, \cdot)\|_{L^2}^2 \frac{ds}{s^3}}{\|p_{ref}\|_{L^2}^2} \right), \quad (4.3)$$

$$= \|p_{ref}\|_{L^2}^2 (1 - E(s_0)), \quad (4.4)$$

where it is recalled that $\mathcal{W}[p_{s_{min}}](s, \cdot)$ denotes the wavelet coefficients computed with the Mexican hat, and $E(s_0)$ is an energy ratio increasing from 0

($s_0 = s_{min}$) to 1, which measures the percentage of the pressure field L^2 -energy that is progressively recovered by adding wavelet coefficients.

The pressure field is discretized on a regular Cartesian grid with mesh size $h = 5.10^{-4}$ m. Furthermore, it is recalled that the Mexican hat exhibits a band-pass behavior in the spectral domain, with a -3 dB bandwidth located on $[s \times 3.08 \text{ m}, s \times 7.18 \text{ m}]$. Thus, the scale parameter s allowing to catch the minimum spatial scale of the pressure field, either $\lambda_p = 5.10^{-4}$ m in the Cartesian interpolation, or $\lambda_{epx} = 1.10^{-3}$ m in the EUROPLEXUS computation, is given by:

$$s \geq \frac{\lambda}{7.18}. \quad (4.5)$$

The numerical values associated to the above equation are summarized in Table 4.4 below.

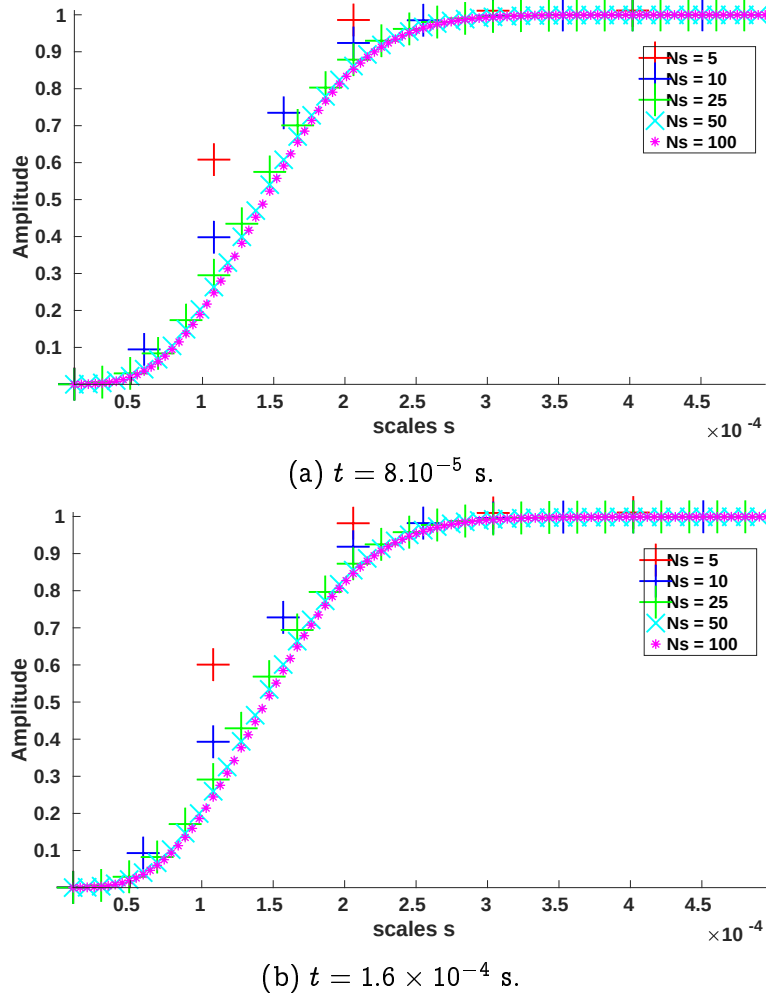
Cutoff scale associated to λ_p	Cutoff scale associated to λ_{epx}
$s_p \approx 7.10^{-5}$	$s_{epx} \approx 1.4 \times 10^{-4}$

Table 4.4: Cutoff scale of the Mexican hat wavelet - 1st test case.

These remarks being stated, Figure 4.4 displays, for two different time instants for which the pressure discontinuity is at different locations within the array of disks, the evolution of the energy ratio $E(s_0)$ for $s_0 \in [10^{-5}, 5.10^{-4}]$.

It appears that for both time instants, the scale range $s_0 \in [10^{-5}, 5.10^{-4}]$, which theoretically corresponds to wavelengths starting from $\lambda \in [3.08 \times 10^{-5}, 7.18 \times 10^{-5} \text{ m}]$ up to $\lambda \in [1.54 \times 10^{-3} \text{ m}, 3.59 \times 10^{-3} \text{ m}]$, conveys around 100% of the pressure field L^2 -energy. Thus, regardless of the location of the pressure discontinuity within the array of disks, the most energetic scales seem to be invariant and only constrained by the geometry of the array.

Nevertheless, one can notice that scales below $s_p = 7.10^{-5}$, which corresponds to the minimum spatial scale of the pressure field on the Cartesian grid, still convey around 5% of the pressure field L^2 -energy. The presence of scales s belonging to $[5.10^{-5}, 7.10^{-5}]$ (scales between 10^{-5} and 5.10^{-5} can be neglected) is explained by the fact that the amplitude of the Mexican hat Fourier transform is not immediately "almost zero" outside of its bandwidth. Thus, even with a small scale parameter s , the tail of the "Gaussian" lobes of the Mexican hat Fourier transform (cf. Figure 3.3) may catch, with a low amplitude, the pressure field smallest wavelengths. Fortunately, 95% of the pressure field L^2 -energy corresponds to scales s larger than the cutoff value s_p .


 Figure 4.4: Pressure L^2 -energy recovered - $s_0 \in [10^{-5}, 5.10^{-4}]$

Finally, it can be noted that a decrease in the number of computed wavelet coefficients N_s does not have a significant impact on the L^2 -energy recovery. Indeed, the asymptotic value still reaches around 100%, even with only five wavelet coefficients.

Let us now turn towards another accuracy criterion in order to check whether similar conclusions are reached regarding the scale range and number of wavelet coefficients.

4.2.2 Force-wise accuracy

In the previous chapter, a force-wise accuracy criterion was introduced via equation (3.183). In this subsection, a slightly different version of this criterion will be used:

$$\left((\underline{F}_{F \rightarrow S})_{ref} - (\underline{F}_{F \rightarrow S})_{N_s} \right) \cdot \underline{e}_x = (\underline{F}_{F \rightarrow S})_{ref} \cdot \underline{e}_x \left(1 - \frac{(\underline{F}_{F \rightarrow S})_{N_s} \cdot \underline{e}_x}{(\underline{F}_{F \rightarrow S})_{ref} \cdot \underline{e}_x} \right), \quad (4.6)$$

$$= (\underline{F}_{F \rightarrow S})_{ref} \cdot \underline{e}_x (1 - f(N_s)) \quad (4.7)$$

with $(\underline{F}_{F \rightarrow S})_{N_s} = \int_{\partial \Omega_s} -p_{N_s}(\underline{\sigma}, t) \underline{n}_{F \rightarrow S}(\underline{\sigma}) d\sigma$, and p_{N_s} an approximate pressure field here reconstructed only with the analysing wavelet Ψ , using N_s wavelet coefficients on a scale range $[s_1, s_{N_s}]$:

$$p_{N_s}(\underline{x}, t) = \frac{2\pi}{C_\Psi} \int_{s_1}^{s_{N_s}} \left(\int_{\mathbb{R}^2} \mathcal{W}[p_{ref}](s, \underline{u}) \times \frac{1}{s} \Psi\left(\frac{\underline{x} - \underline{u}}{s}\right) d\underline{u} \right) \frac{ds}{s^3}. \quad (4.8)$$

Figure 4.5 shows the evolution of the force ratio $f(N_s)$, evaluated on the whole array, with the number of computed scales N_s , and for three different scale ranges: $s \in [10^{-5}, 5.10^{-4}]$, $s \in [10^{-5}, 10^{-3}]$, and $s \in [10^{-4}, 10^{-3}]$.

Conversely to the L^2 -energy criterion, the scale range $s \in [10^{-5}, 5.10^{-4}]$ seems here unsuited to properly reconstruct the force applied to the solid medium microstructure, as an almost 40% overestimation can be witnessed for the time instant $t = 1.6 \times 10^{-4}$ s. Furthermore, an 8% overestimation is still visible for the time instant $t = 8.10^{-5}$ s. This significant difference between the two time instants can be explained by the following fact: as the initial pressure wave has almost exited the array of disks for $t = 1.6 \times 10^{-4}$ s, wavelengths around 5.10^{-3} m (driven by the distance between two consecutive disks), which are not taken into account in the scale range $s \in [10^{-5}, 5.10^{-4}]$, are much more present within the array of disks than for the time instant $t = 8.10^{-5}$ s.

Thus, the wider scale range $s \in [10^{-5}, 10^{-3}]$ allows to better reconstruct the force for both time instants, with, for instance, an overestimation around 10% for $t = 1.6 \times 10^{-4}$ s. Additionally, Figure 4.5c proves that the smallest scales could even be neglected without losing accuracy, thus leading to the range $s \in [10^{-4}, 10^{-3}]$, which contains wavelengths $\lambda \in [3.08 \times 10^{-4}, 7.18 \times 10^{-3}]$ m. The clear shift with respect to the scale range previously identified with the L^2 -energy criterion ($[7.10^{-5}, 5.10^{-4}]$) can be explained by the fact that the force criterion focuses on the pressure values on the fluid-structure interfaces, while the L^2 -energy takes into account the whole $\Omega_f \cup \Omega_s$ domain.

Finally, it can be noticed that $N_s = 10$ wavelet coefficients would already allow reaching a good accuracy ($\leq 10\%$ overestimation) on the force applied to the solid medium. The results on the most relevant wavelengths with respect to this physics-driven criterion are summarized in Table 4.5.

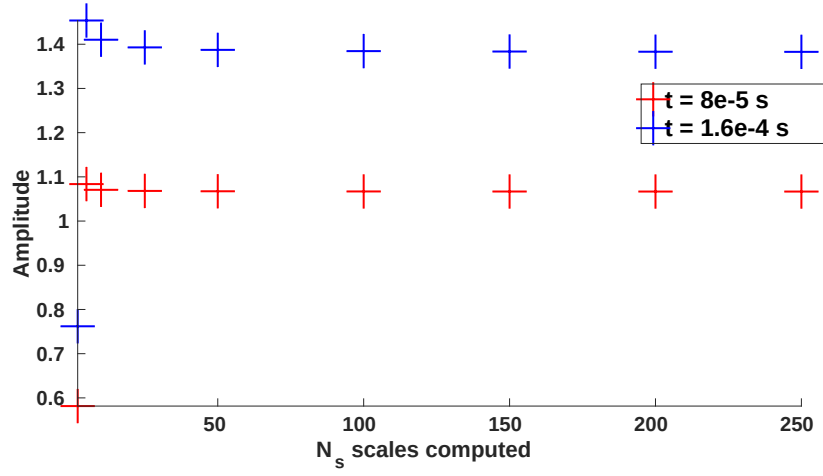
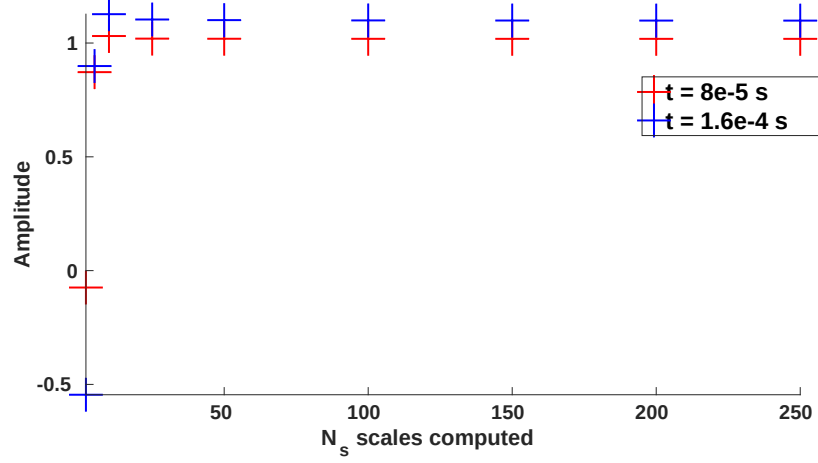
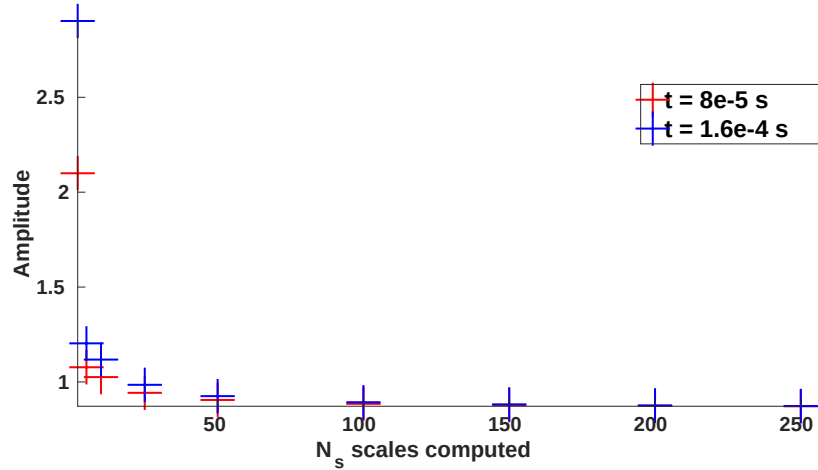

 (a) $s \in [10^{-5}, 5.10^{-4}]$.

 (b) $s \in [10^{-5}, 10^{-3}]$.

 (c) $s \in [10^{-4}, 10^{-3}]$

Figure 4.5: Evolution of the horizontal force ratio with the number of wavelet coefficients, for 3 different scale ranges.

Cutoff scales and number of wavelet coefficients		
$s_{min} = 10^{-4}$	$N_s = 10$	$s_{max} = 10^{-3}$
$\lambda \in [3.08 \times 10^{-4}, 7.18 \times 10^{-4} \text{ m}]$		$\lambda \in [3.08 \times 10^{-3}, 7.18 \times 10^{-3} \text{ m}]$

Table 4.5: Cutoff scales and number of wavelet coefficients - 1st test case.

For the sake of completeness, Figure 4.6 displays the reference and reconstructed pressure profiles along the medium horizontal axis, while Figure 4.7 displays the absolute error between the 2D reference and reconstructed pressure fields. The absolute error is logically located in the vicinity of the disks, where the reference pressure variations are maximal, but it remains small compared to the reference pressure range (less than 10% for maximum values). Furthermore, the good results obtained in terms of forces acting on the solid medium indicate that the pressure gradient is well preserved.

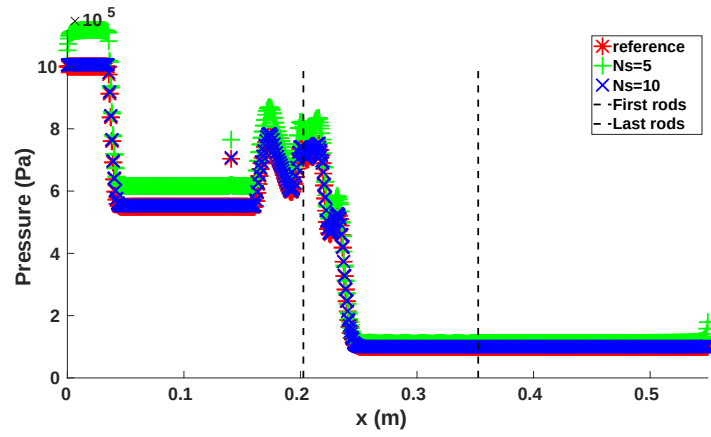
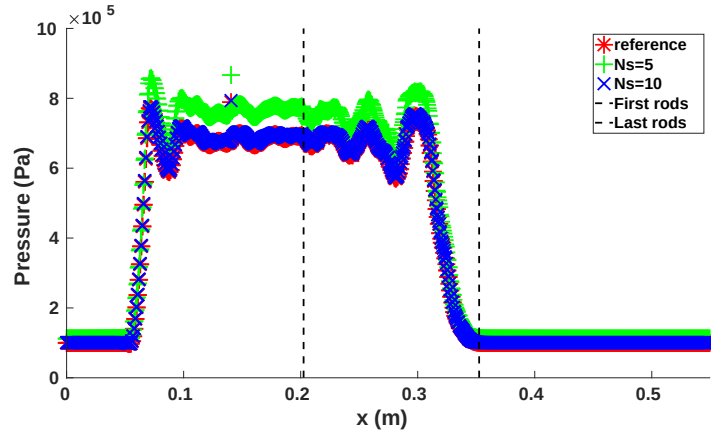

 (a) $t = 8.10^{-5} \text{ s.}$

 (b) $t = 1.6 \times 10^{-4} \text{ s.}$

 Figure 4.6: Horizontal pressure profiles $\left(y = \frac{L_y}{2}\right) - s \in [10^{-4}, 10^{-3}]$

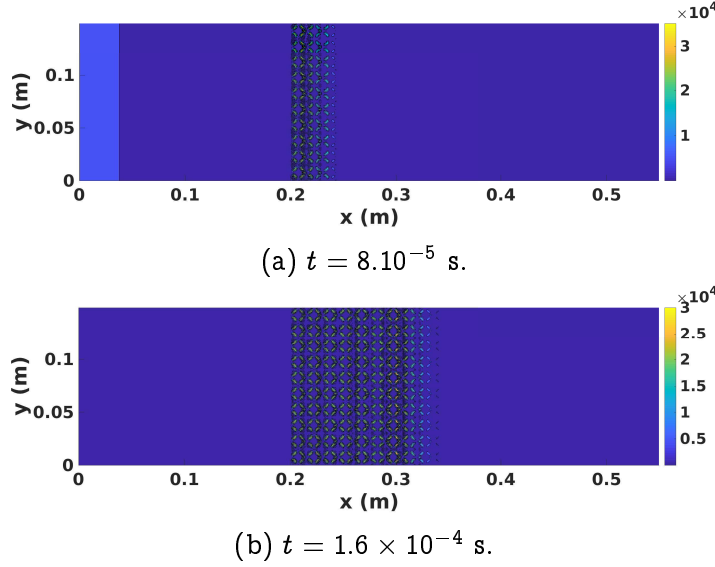


Figure 4.7: Absolute error $|p_{ref} - p_{recons}|$ (Pa) - $N_s = 10$ - $s \in [10^{-4}, 10^{-3}]$.

This first wavelet analysis of a 2D reference pressure wave, which can also be found in [Mokhtari et al., 2020], thus gave some insights on the most relevant wavelet coefficients and spatial scales. It appears that a direct computation of the homogenized fluid PDEs would require, with the Mexican hat analysing wavelet, 10 different computations to determine 10 wavelet coefficients on the scale range $s \in [10^{-4}, 10^{-3}]$. This is of course expected to represent a significant computational cost, especially as these different wavelet coefficients are linked through the boundary integrals in the right-hand side of the filtered PDEs, and the necessary closure expressions between the resolved and unresolved scales of the fluid variables.

In order to bypass this need for multiple computations, the Mexican hat wavelet is hereafter replaced by its associated scaling function. The computation of the low-frequency approximation $\mathcal{L}[f](s_0, \cdot)$, at a given cutoff scale s_0 , indeed allows us to catch simultaneously all the spatial scales larger than s_0 . But before computing a similar 2D pressure wave through a 10×10 array of disks directly with the model equations, the following section first investigates the numerical model stability and accuracy on a simpler test case.

4.3 Direct computation of the fluid filtered PDEs

4.3.1 Preliminary analysis on stability and accuracy

This preliminary analysis aims at assessing on the one hand, the stability of the explicit finite-volume scheme (3.219) designed to solve the model equations, and on the other hand, the ability of the wavelet-based model to accurately reconstruct, from the homogenized fluid, the force applied to the underlying solid medium. To this end, the propagation of a 2D pressure wave through a 2×2 steady array of disks is hereafter considered (see Figure 4.8). The solid

medium thus only acts, once again, as a boundary condition for the fluid.

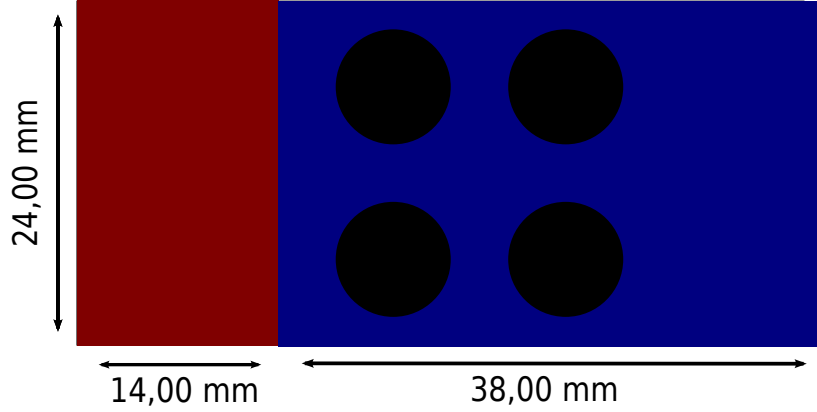


Figure 4.8: Scheme of the preliminary test.

The simulation parameters are summarized in Tables 4.6-4.7-4.8-4.9:

Lx	Ly	Disks radius	Dist. consecutive disks
52 mm	24 mm	4 mm	4 mm

Table 4.6: Geometry - 2nd test case.

10 bar zone	1 bar zone	Discontinuity \longleftrightarrow 1st disks
$[0, 14 \text{ mm}]$	$[14 \text{ mm}, 52 \text{ mm}]$	4 mm

Table 4.7: Pressure loading - 2nd test case.

Reference Density	Reference Pressure	Sound Velocity
$\rho_{ref} = 1000 \text{ kg} \cdot \text{m}^{-3}$	$p_{ref} = 10^5 \text{ Pa}$	$c = 1300 \text{ m} \cdot \text{s}^{-1}$

Table 4.8: Fluid parameters - 2nd test case.

Mesh size	Time step	Scale/mesh compatibility
$h = 1 \text{ mm}$	$\Delta t \leq C_{stab} \frac{h}{c_{max}}$	$s_0 \gtrsim 0.412 \times h$

Table 4.9: Spatial and time discretization - 2nd test case.

As a result of the homogenization process, the interfaces with the underlying solid obstacles are not taken into account via the mesh, but via a body force defined across the whole domain $\Omega_f \cup \Omega_s$. As can be seen in equation (3.136), this body force is expressed as an integral of the pressure on the boundary $\partial\Omega_s$, weighted by the analysing wavelet Ψ , or rather the scaling function Φ here. Figure 4.9 illustrates how this weight is well-localized in the vicinity of the boundary $\partial\Omega_s$.

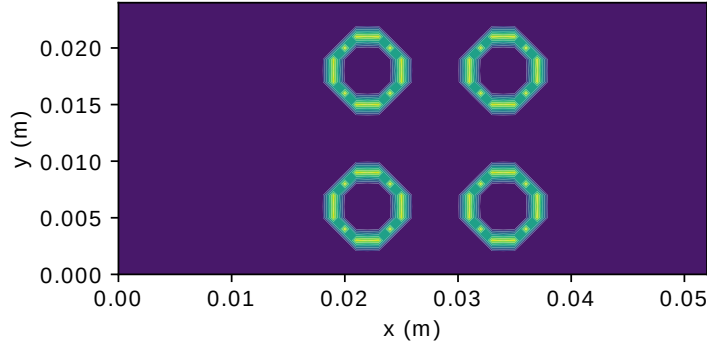


Figure 4.9: Visualization of the 2×2 array - $s_0 = 0.415 \times h$.

The simulation is initialized as a Riemann problem, with a 10 vs 1 bar pressure discontinuity, as displayed in Figure 4.10 below. It is recalled that the solid medium is initially in equilibrium with the surrounding fluid, and thus "hidden" in the 1 bar zone.

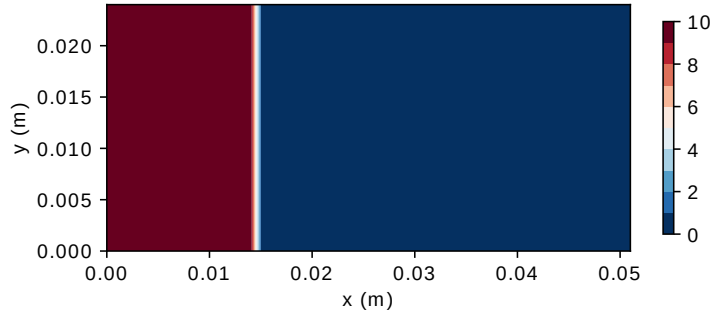


Figure 4.10: Initial pressure field (10 vs 1 bar).

Conversely to the previous analysis of a 2D reference pressure wave, in which the Mexican hat wavelet Ψ was used to detect the most relevant wavelengths, all the results hereafter presented are obtained with the scaling function Φ . All the reference data used to confront the model is obtained with EUROPLEXUS software, using the same numerical methods as described in the previous section. The reference mesh size is set to $h_{epx} = \frac{R}{4} = 1$ mm, where R denotes the disks radius. The reference pressure field is then extended to the whole domain $\Omega_f \cup \Omega_s$, by means of a linear interpolation on a 2D regular Cartesian grid with mesh size $h = 1$ mm (as opposed to 0.5 mm in the previous analysis). It is recalled that this linear interpolation artificially sets the pressure to zero on the nodes located outside the fluid domain Ω_f .

In order to assess the stability of the explicit finite-volume scheme, the impact of two possible sources of instability are hereafter studied:

- the classical C.F.L. condition between the time step Δt and mesh size h ;
- the scale/mesh compatibility condition with respect to the explicit scheme stability (3.238).

To do so, several tests are hereafter presented, depending on the value chosen for the C.F.L. stability constant C_{stab} and for the cutoff scale s_0 .

Test # 1 : $C_{stab} = 1$, and $s_0 = 0.42 \times h$

Let us start with the "worst-case" scenario, where no safety margins are taken with respect to either the C.F.L. or the scale/mesh compatibility conditions. Figure 4.11 below displays the reference and reconstructed pressure field, after 29 time steps ($\Delta t \approx 7.69 \times 10^{-7}$ s).

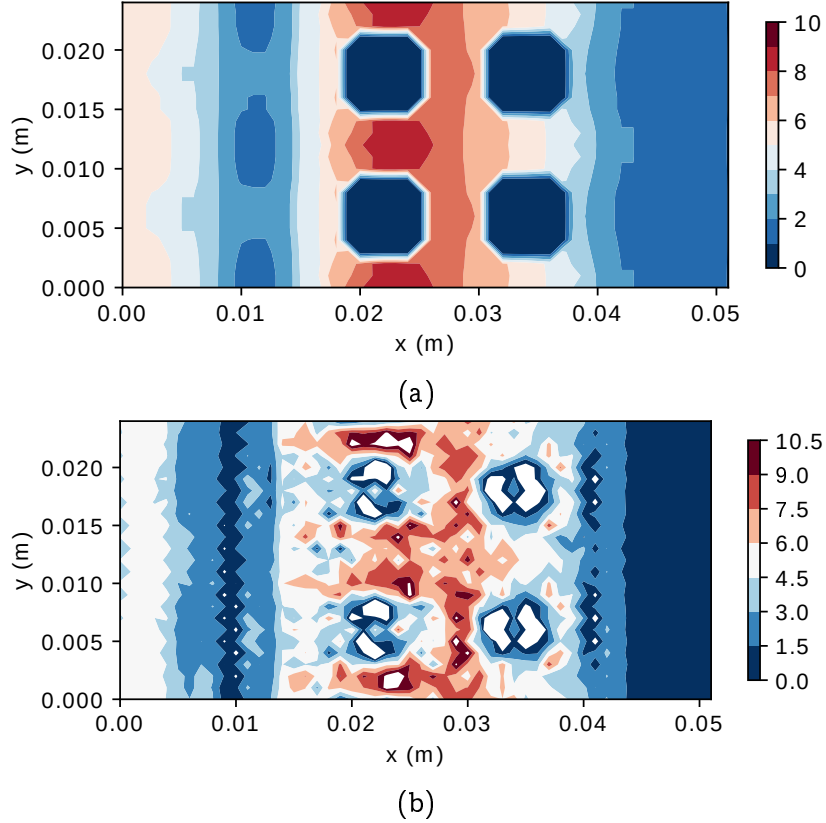


Figure 4.11: Reference (4.11a) VS reconstructed (4.11b) pressure fields - $s_0 = 0.42h$ - $C_{stab} = 1$ - $t = 2.2284 \times 10^{-5}$ s.

The pressure field reconstructed after only 29 time steps is clearly unsatisfactory. To compare more precisely the reference and reconstructed pressure fields, Figure 4.12 displays both horizontal pressure profiles, at $t = 0$ s and after 29 times steps. The vertical black lines correspond to the location of the 2×2 array of disks.

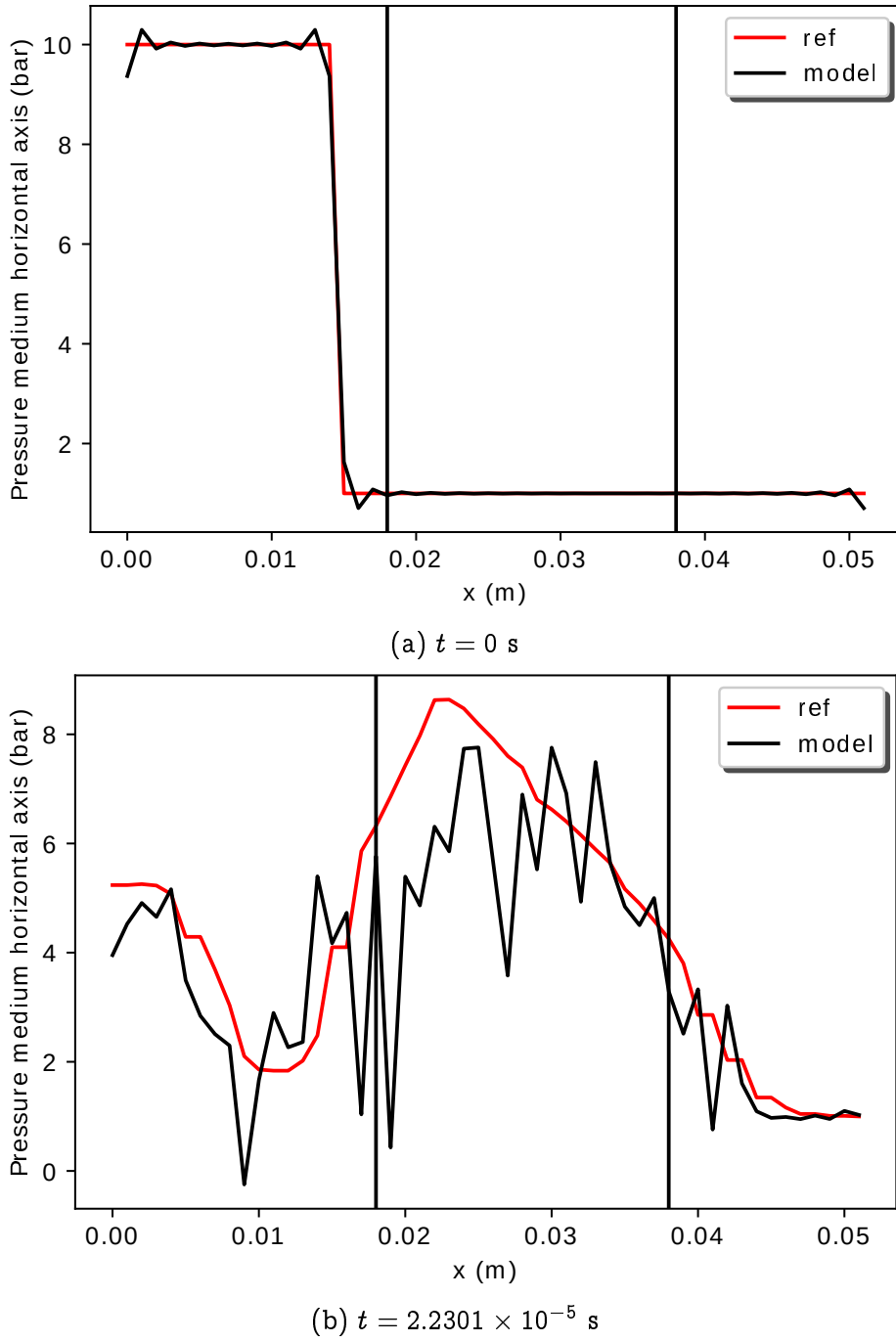


Figure 4.12: Reference VS reconstructed pressure profiles ($y = \frac{L_y}{2}$) - $s_0 = 0.42h$ - $C_{stab} = 1$

The important oscillatory, yet bounded, behavior that can be witnessed on the reconstructed pressure field finds its source on the one hand in the aliasing phenomenon caused by the scaling function Φ_{s_0} (cf. equation (3.241)), and on the other hand in the lack of safety margin with respect to both the C.F.L. and the scale/mesh compatibility conditions (3.238).

Let us now study independently the role played by the scale/mesh compat-

ibility and C.F.L. conditions.

Test # 2 : $C_{stab} = 1$, and $s_0 = 0.6 \times h$

For this second test, the C.F.L. stability constant C_{stab} is kept equal to 1, but the cutoff scale s_0 increases. As for the first test, the reference and reconstructed pressure fields are hereafter displayed in Figure 4.13, and their horizontal profiles along the medium horizontal axis in Figure 4.14.

Remark 4.3.1 *It is recalled that, during the homogenization process, the fluid artificially located within the solid medium is initially in equilibrium with the surrounding fluid, in the 1 bar zone. Thus, ideally, as the real and artificial fluid never penetrate or leave the solid medium, the pressure should ideally remain constant equal to 1 bar within Ω_s .*

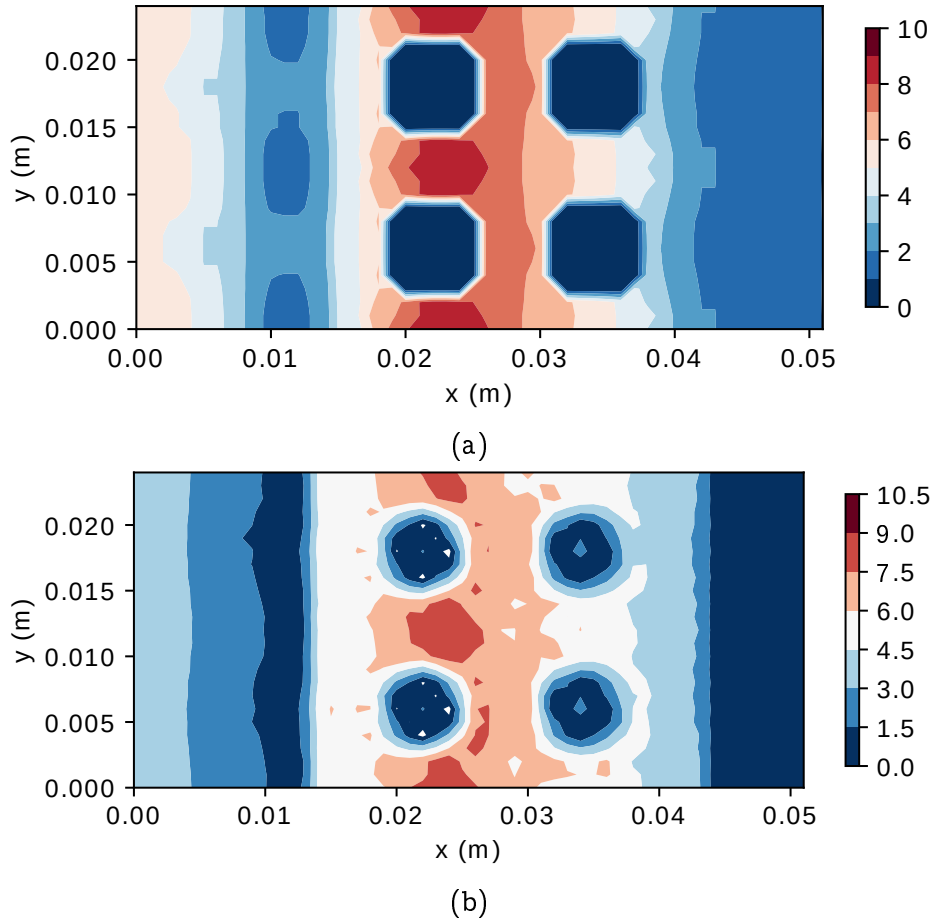


Figure 4.13: Reference (4.13a) VS reconstructed (4.13b) pressure fields - $s_0 = 0.6h$ - $C_{stab} = 1$ - $t = 2.2284 \times 10^{-5}$ s

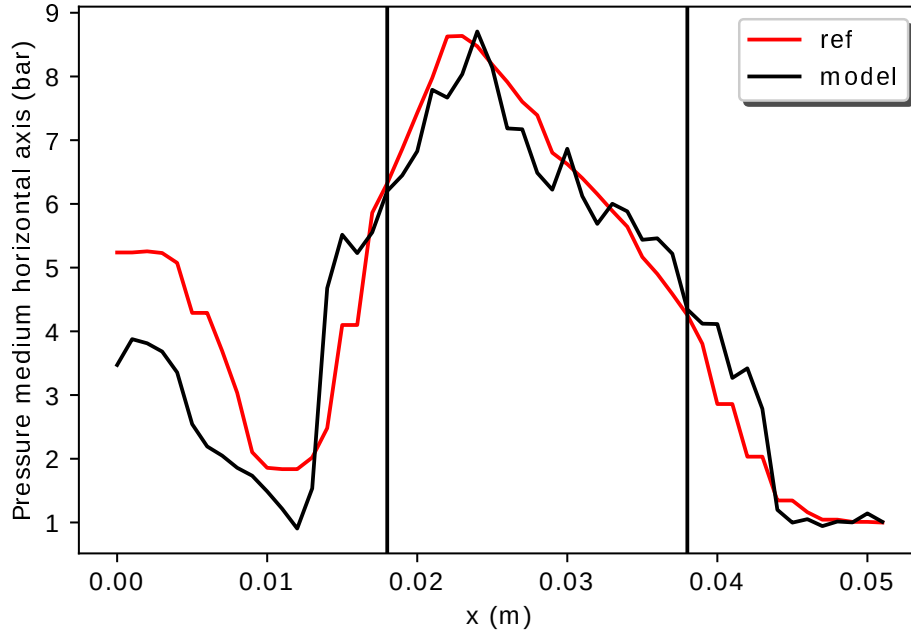


Figure 4.14: Reference VS reconstructed pressure profiles ($y = \frac{L_y}{2}$) - $s_0 = 0.6h$ - $C_{stab} = 1$ - $t = 2.2301 \times 10^{-5}$ s.

The results obtained are clearly much more satisfactory than in the worst-case scenario. The geometry of the solid obstacles is quite faithfully reconstructed in Figure 4.13b, with an artificial pressure almost uniform and close to 1 bar within Ω_s . Furthermore, the pressure profile along the medium horizontal axis is also much smoother. The small oscillations still visible in Figure 4.14 have a significantly smaller amplitude than in the previous case. This result thus supports the fact that the scaling function and the associated scale/mesh compatibility condition are the main source of instability in the model response. Such a conclusion could be expected, as the scaling function operates a first (explicit) spatial filtering of the fields, at the continuum medium scale, before the discretization step of the filtered PDEs on the 2D Cartesian grid.

Test # 3 : $C_{stab} = 0.8$, and $s_0 = 0.42 \times h$

For this third test, let us now study the role played by the C.F.L. condition. A safety margin is thus taken with respect to this condition, with C_{stab} equal to 0.8. Regarding the scale/mesh compatibility condition, the cutoff scale s_0 is once again chosen close to the critical minimum value.

Figure 4.15 displays the reference and reconstructed pressure field, the latter being obtained after 36 time steps ($\Delta t \approx 6.15 \times 10^{-7}$ s). Figure 4.16 compares both pressure profiles along the medium horizontal axis.

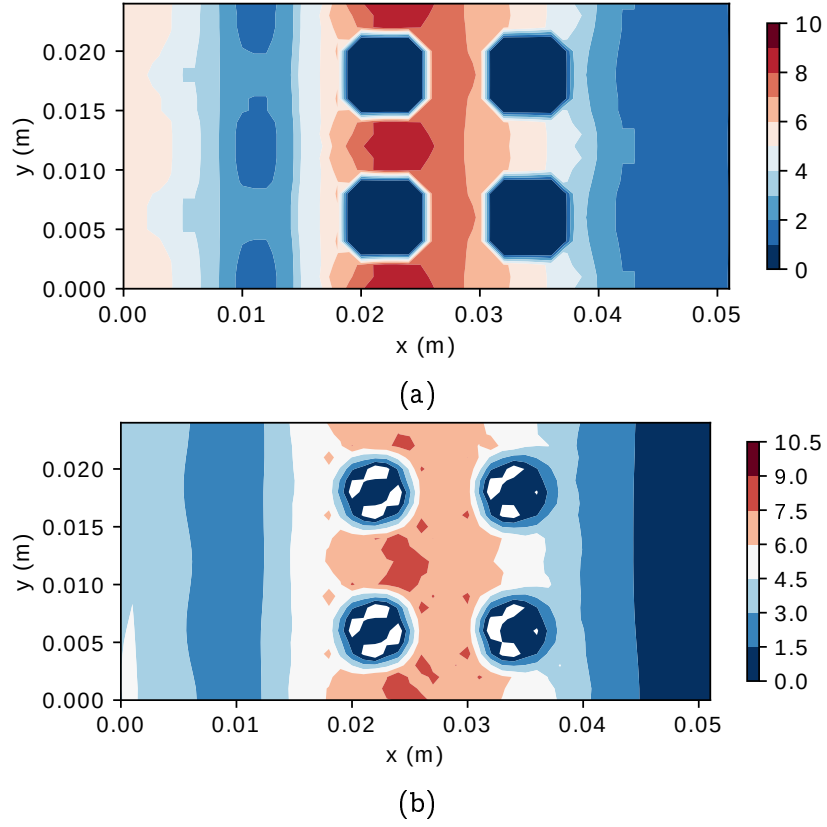


Figure 4.15: Reference VS reconstructed pressure fields - $s_0 = 0.42h$ - $C_{stab} = 0.8$ - $t = 2.2147 \times 10^{-5}$ s

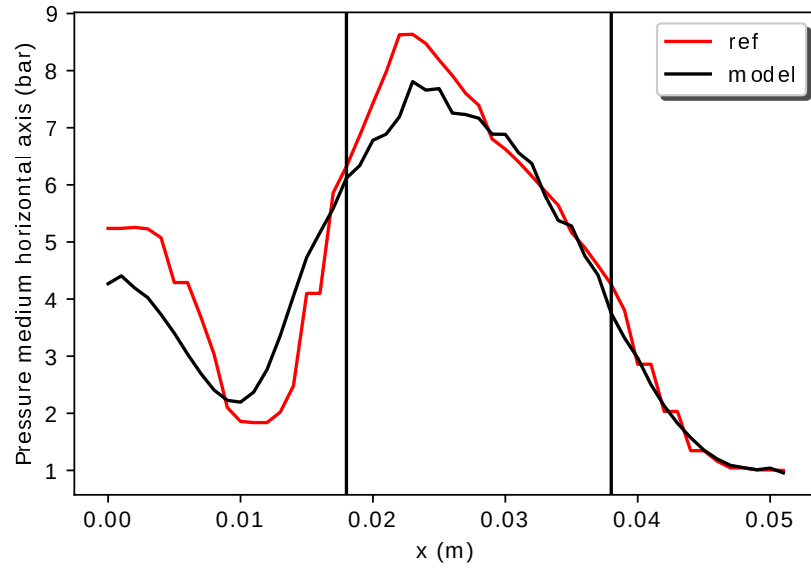


Figure 4.16: Reference VS reconstructed pressure profiles - $s_0 = 0.42h$ - $C_{stab} = 0.8$ - $t = 2.2147 \times 10^{-5}$ s.

As can be witnessed in Figure 4.16, the pressure profile along the medium horizontal axis is even smoother than in the second test, where only a safety margin with respect to the scale parameter s_0 was taken into account. Such a result could be expected. Indeed, by decreasing C_{stab} , the time step Δt is now not only below the C.F.L. condition, but also below the characteristic time scale of the scaling function (3.235).

Nevertheless, this improved stability seems to go along with a loss of accuracy. Indeed, the "white numerical artefacts" visible within the solid obstacles in Figure 4.15b clearly show that the reconstructed pressure deviates from the ideal 1 bar value within Ω_s .

In order to further investigate this link between stability and accuracy, the following test hereafter considers a force-wise accuracy criterion.

Test # 4 : $0.5 \leq C_{stab} \leq 1$, and $0.42 \times h \leq s_0 \leq h$

Figure 4.17 displays the time evolution of the horizontal force (per unit of length) applied to the solid obstacles, with a comparison between the reference and reconstructed values for $s_0 \in [0.42h, h]$. The C.F.L. stability constant C_{stab} is first chosen equal to 1. It can be noticed that, like the pressure signal, the force exhibits oscillations when the cutoff scale parameter s_0 decreases towards its minimum value. These oscillations seem nevertheless less important than the ones witnessed in the pressure signal itself. This can be explained by the fact that the force integrates the pressure on the boundaries $\partial\Omega_s$, thus filtering out the highest frequency components of the oscillations.

Furthermore, one can notice that, for $s_0 \geq 0.6h$, the reconstructed force tends to deviate from the reference signal, especially downstream each column of disks.

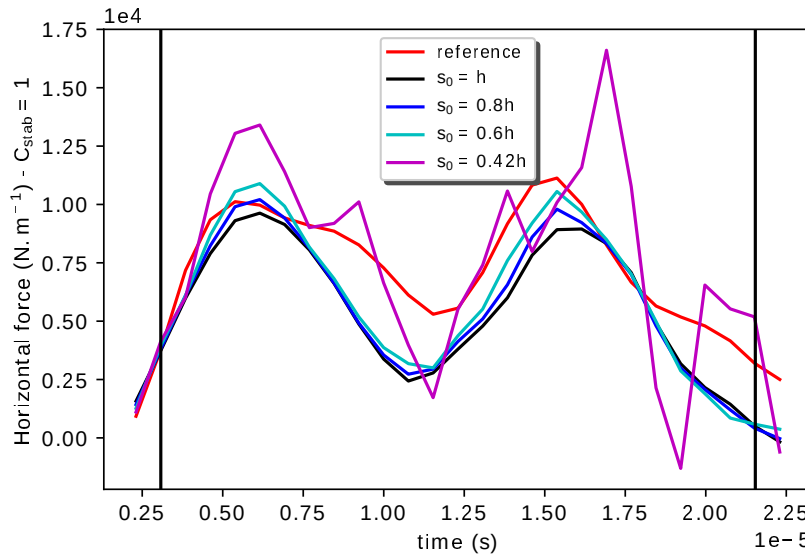


Figure 4.17: Time evolution of the horizontal force applied to the solid medium - $C_{stab} = 1$, $0.42h \leq s_0 \leq h$.

Let us now keep the cutoff scale parameter s_0 equal to $0.42 \times h$, and study the impact of the C.F.L. stability constant. Figure 4.18 displays the time evolution of the horizontal force (per unit of length) applied to the solid obstacles, with $C_{stab} \in [0.6, 1]$.

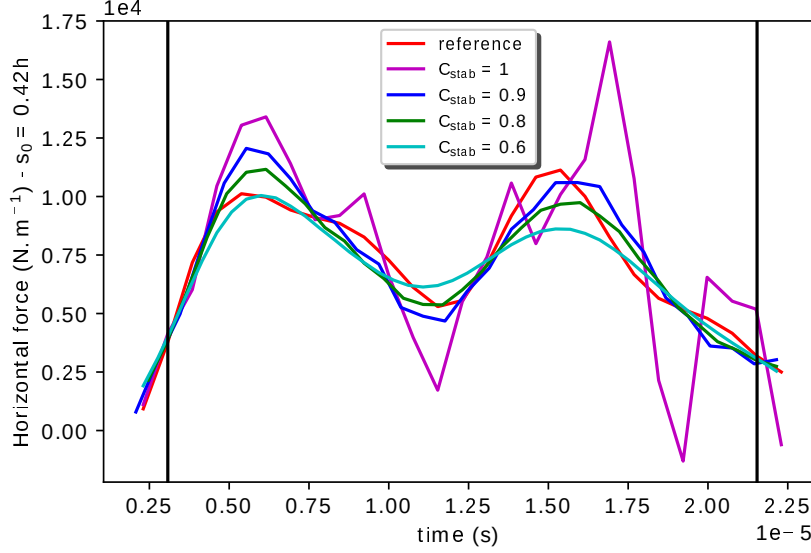


Figure 4.18: Time evolution of the horizontal force applied to the solid medium - $s_0 = 0.42h$, $0.6 \leq C_{stab} \leq 1$.

As already noticed with the pressure signal, when the cutoff scale s_0 is near its critical minimum value and the C.F.L. constant C_{stab} decreases, the force signal becomes smoother. Furthermore, it can be noticed that the reconstructed force signals in Figure 4.18 are able to follow more faithfully the reference signal than in the previous case, especially downstream each column of disks.

Nevertheless, it shall be highlighted that further decreasing the C.F.L. constant C_{stab} seems to damage the accuracy of the model response, with both over and underestimations of the reference force, as can be witnessed on the curve associated to $C_{stab} = 0.6$. This fact tends to push for a compromise between stability and accuracy.

In order to further illustrate this duality, let us now consider the force-wise accuracy criterion introduced in the previous chapter (3.186):

$$e_F = \left| \int_{t_a}^{t_b} \left((\underline{F}_{F \rightarrow S})_{ref} - (\underline{F}_{F \rightarrow S})_{s_0} \right) \cdot \underline{e}_x dt \right|, \quad (4.9)$$

$$= \left| \int_{t_a}^{t_b} (\underline{F}_{F \rightarrow S})_{ref} \cdot \underline{e}_x dt \right| \times \left| \frac{\int_{t_a}^{t_b} \left((\underline{F}_{F \rightarrow S})_{ref} - (\underline{F}_{F \rightarrow S})_{s_0} \right) \cdot \underline{e}_x dt}{\int_{t_a}^{t_b} (\underline{F}_{F \rightarrow S})_{ref} \cdot \underline{e}_x dt} \right|, \quad (4.10)$$

$$= \left| \int_{t_a}^{t_b} (\underline{F}_{F \rightarrow S})_{ref} \cdot \underline{e}_x dt \right| \times \tilde{e}_F. \quad (4.11)$$

With 26 time steps on the time range $[t_a, t_b] \approx [2.3 \times 10^{-6} \text{ s}, 2.23 \times 10^{-5} \text{ s}]$, the numerical value $\int_{t_a}^{t_b} (\underline{F}_{F \rightarrow S})_{ref} \cdot \underline{e}_x dt \approx 1.45 \times 10^{-1} \text{ kg.s}^{-1}$ is obtained

(with a rectangle method) for the time integration of the reference horizontal force.

The following Figure 4.19 displays the evolution of the relative error \tilde{e}_F on the horizontal force when decreasing the C.F.L. stability constant C_{stab} , for a mesh size $h = 1$ mm, and for $s_0 \in \{0.42h, 0.6h\}$. One can notice that the relative error \tilde{e}_F is at least divided by 3 when the cutoff scale s_0 decreases from $0.6h$ to $0.42h$. This is coherent with the *a priori* idea that the best accuracy is reached when the scaling function is designed so as to catch all the possible wavelengths that can be represented by the mesh. Thus, with the set of parameters ($s_0 = 0.42h, C_{stab} = 0.9$), which seems to be a good compromise between accuracy and stability, the model responds with a relative error \tilde{e}_F below 1%.

Nevertheless, when further decreasing the constant C_{stab} , and thus improving the numerical scheme stability, the accuracy of the model response slightly deteriorates. This confirms the duality between stability and accuracy.

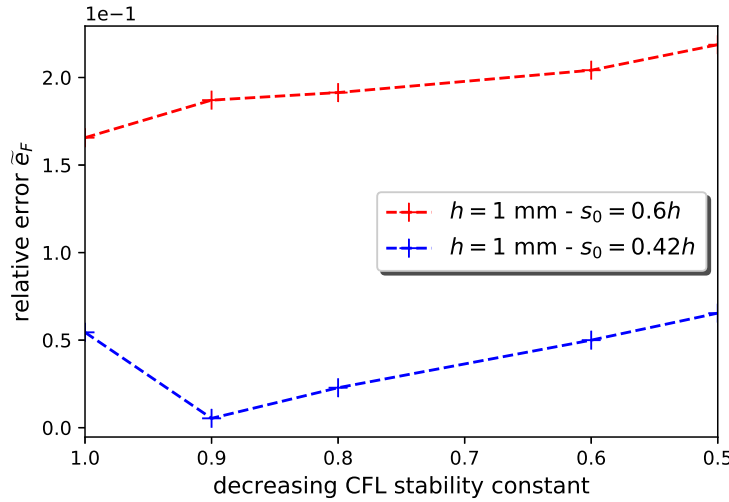


Figure 4.19: Evolution of the relative error \tilde{e}_F with C_{stab} - $h = 1$ mm.

In order to further highlight the important role played by the critical minimum value $s_0 \approx 0.412 \times h$, Figure 4.20 displays the evolution of the relative error \tilde{e}_F with the cutoff scale s_0 , and for two different mesh sizes : $h_1 = 1$ mm, and $h_2 = 0.5$ mm. One can thus distinguish two "regimes":

- when the cutoff scale s_0 decreases from the minimum value $0.412 \times h$, the relative error \tilde{e}_F increases exponentially when $C_{stab} = 1$. This is the result of both the scaling function aliasing and the numerical scheme lack of stability, which quickly deteriorate the model accuracy. When $C_{stab} = 0.9$, the improved stability is able to balance the important oscillations due to aliasing, thus preventing the relative error from drastically increasing.
- when the cutoff scale s_0 increases from the minimum value $0.412 \times h$, the relative error \tilde{e}_F first decreases, as the aliasing phenomenon weakens. However, as the cutoff scale s_0 keeps on increasing, \tilde{e}_F progressively

deteriorates, as the smallest wavelengths accessible with the mesh are progressively discarded by the scaling function.

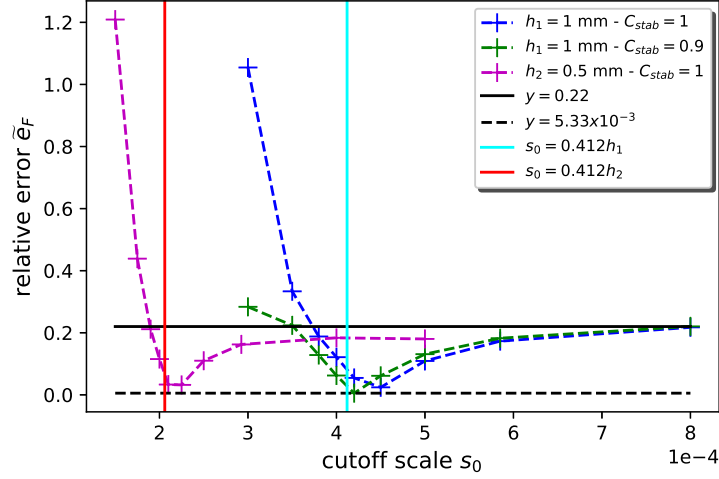


Figure 4.20: Evolution of the relative error \tilde{e}_F with the cutoff scale s_0 - $h \in \{0.5 \text{ mm}, 1 \text{ mm}\}$ - $C_{stab} \in \{0.9, 1\}$.

Finally, to conclude this preliminary analysis on the stability and accuracy of the numerical model, Figure 4.21 displays the evolution of the relative error \tilde{e}_F with a decreasing mesh size h , for $s_0 \in \{0.585h, 0.6h\}$ and $C_{stab} = 1$.

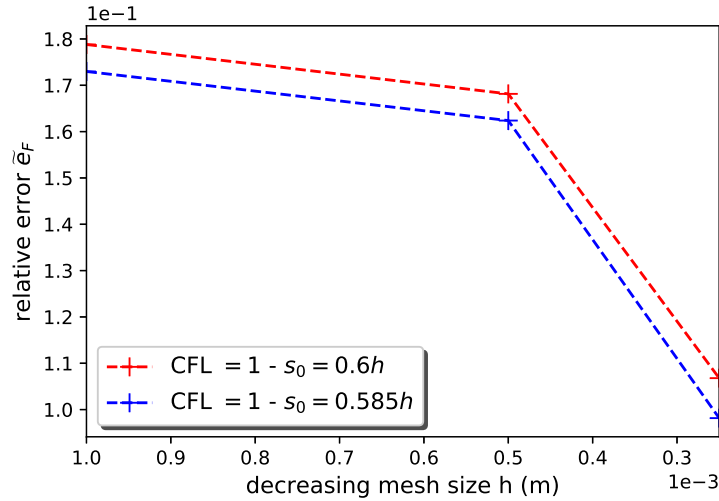


Figure 4.21: Evolution of the relative error \tilde{e}_F with the mesh size h - $C_{stab} = 1$.

The accuracy of the force reconstruction thus increases with mesh (and scale) refinements. This is coherent with the analytical convergence of the wavelet-based model towards DNS, proved in the previous chapter.

This concludes this preliminary analysis on the numerical model stability and accuracy, here assessed on a 2×2 steady array of disks submitted to a tranverse pressure wave. In order to now connect to the wavelet analysis presented in the beginning of this chapter, the following section considers the propagation of a 2D transverse pressure wave through a 10×10 steady array of disks.

4.3.2 2D pressure wave through a 10 x 10 array of disks

The test case geometry is displayed on Figure 4.22 below. The simulation parameters are then summarized in Tables 4.10-4.11-4.12-4.13.

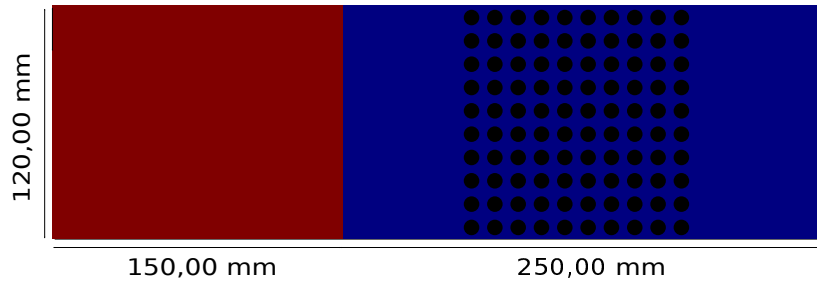


Figure 4.22: 2D pressure wave through a 10×10 steady array of disks.

Lx	Ly	Disks radius	Dist. consecutive disks
400 mm	120 mm	4 mm	4 mm

Table 4.10: Geometry - 3rd test case.

10 bar zone	1 bar zone	Discontinuity \longleftrightarrow 1st disks
$[0, 150 \text{ mm}]$	$[150 \text{ mm}, 400 \text{ mm}]$	62 mm

Table 4.11: Pressure loading - 3rd test case.

Reference Density	Reference Pressure	Sound Velocity
$\rho_{ref} = 1000 \text{ kg} \cdot \text{m}^{-3}$	$p_{ref} = 10^5 \text{ Pa}$	$c = 1300 \text{ m} \cdot \text{s}^{-1}$

Table 4.12: Fluid parameters - 3rd test case.

Mesh size	Time step	Scale/mesh compatibility
$h = 1 \text{ mm}$	$\Delta t \leq C_{stab} \frac{h}{c_{max}}$	$s_0 \gtrsim 0.412 \times h$

Table 4.13: Spatial and time discretization - 3rd test case.

The solid medium is once again taken into account in the homogenized fluid via a body force, whose maximum amplitude is localized on the fluid-structure interfaces, as displayed on Figure 4.23 below. The number of Cartesian grid nodes N used to approximate the boundary of each disk, and to compute the body force applied to the homogenized fluid (3.198), is chosen so as to satisfy:

$$N \leq \frac{2\pi R}{ds}, \quad (4.12)$$

where $ds = \sqrt{dx^2 + dy^2}$ denotes the curvilinear discretization step. In the following, $N = 16$ nodes are thus used to compute the body force.

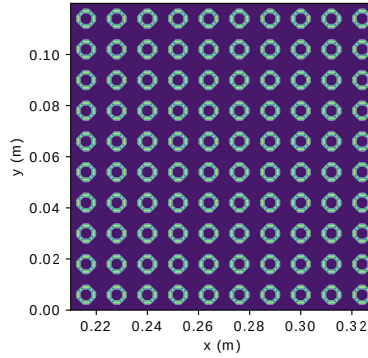


Figure 4.23: Visualization of the 10×10 array of disks.

In order to assess the model capability to reconstruct accurately a 2D pressure wave propagating through such solid obstacles, we hereafter display:

- both the 2D reconstructed and reference pressure fields, for multiple time steps (see Figure 4.24); the latter is once again computed with EUROPLEXUS software;
- the reconstructed and reference horizontal pressure profiles (see Figure 4.25).
- the time evolution of the reconstructed and reference pressure field L^2 -norm $\|p\|_{L^2}(t) = \left(\int_{\Omega_f \cup \Omega_s} |p(\underline{x}, t)|^2 d\underline{x} \right)^{\frac{1}{2}}$;
- the time evolution of the horizontal force applied to the solid medium, and the modulus of its Fourier transform.

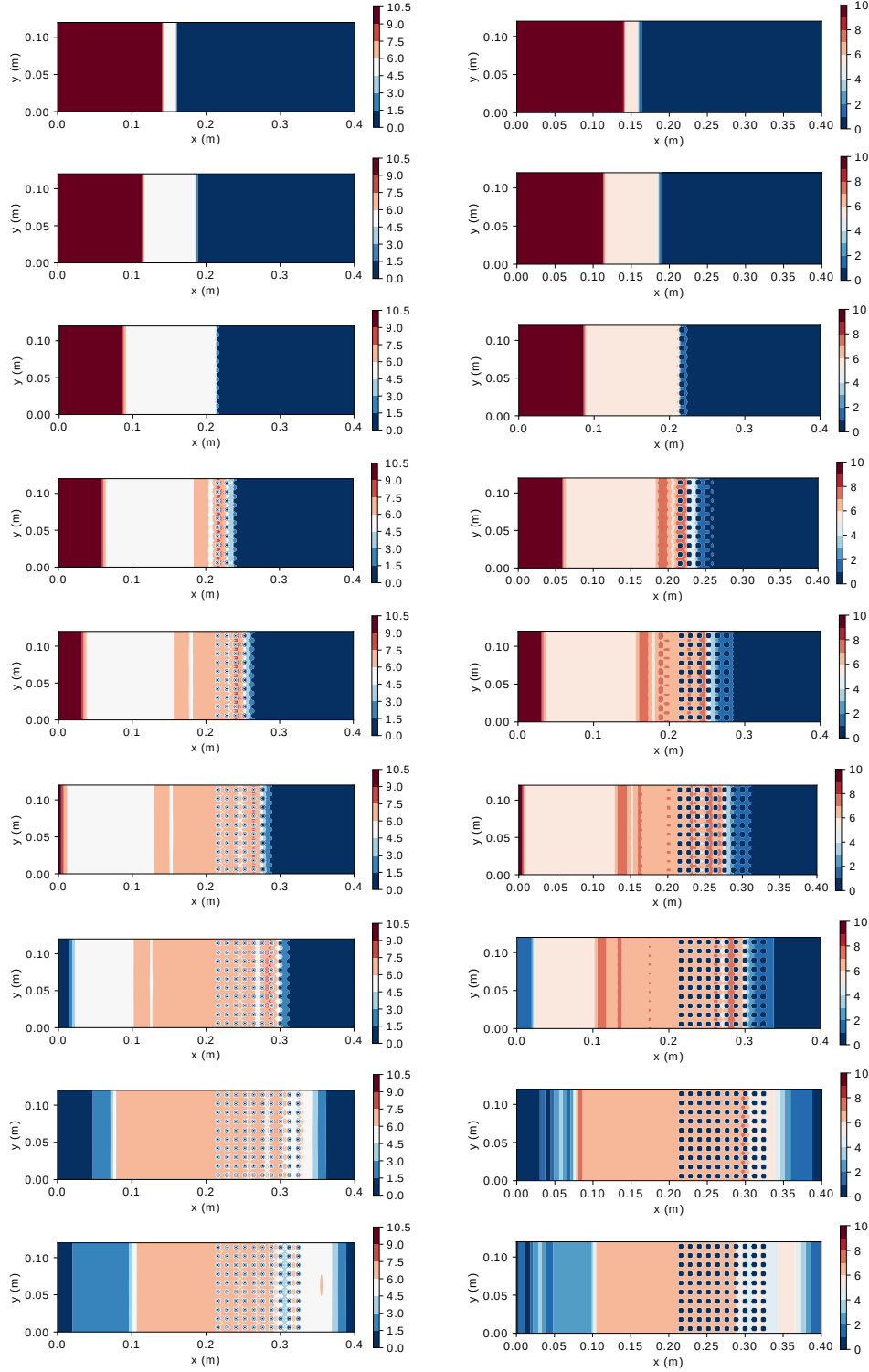
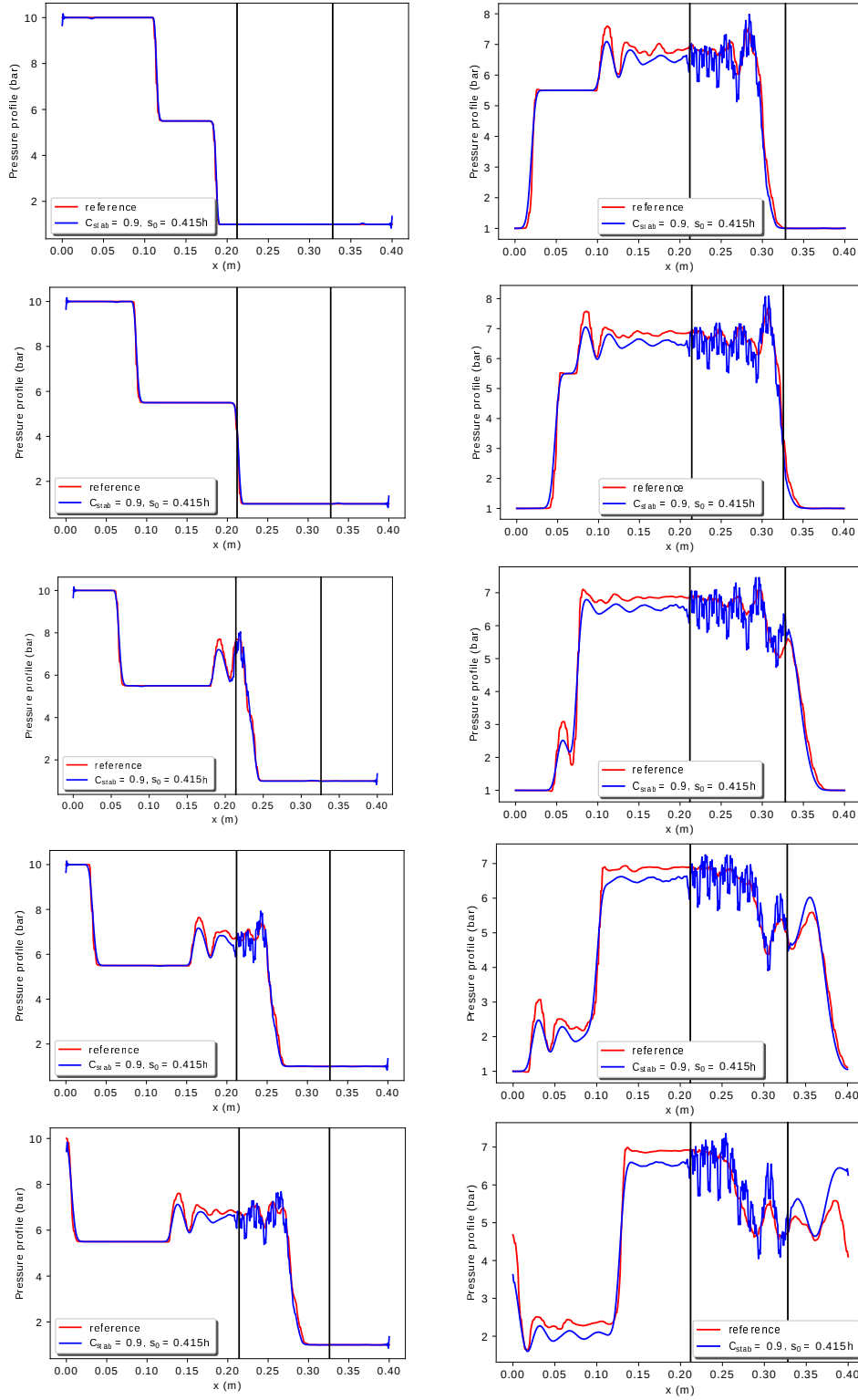
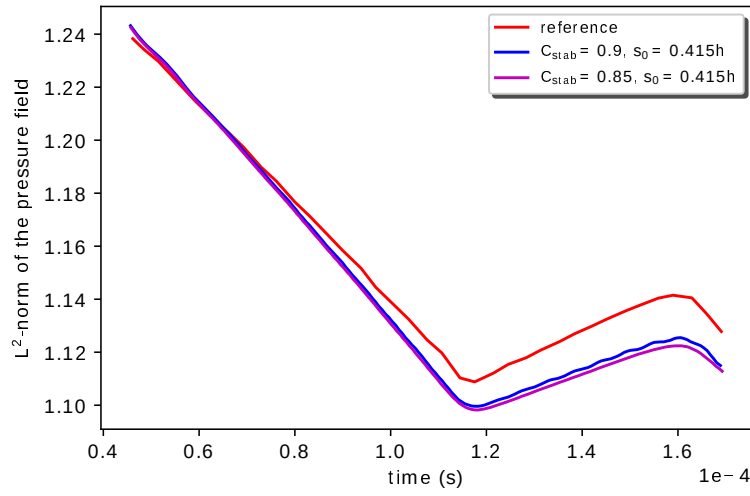


Figure 4.24: Reconstructed (left) VS reference (right) pressure fields snapshots every $\Delta t = 2.076 \times 10^{-5}$ s - $C_{stab} = 0.9$ - $s_0 = 0.415h$

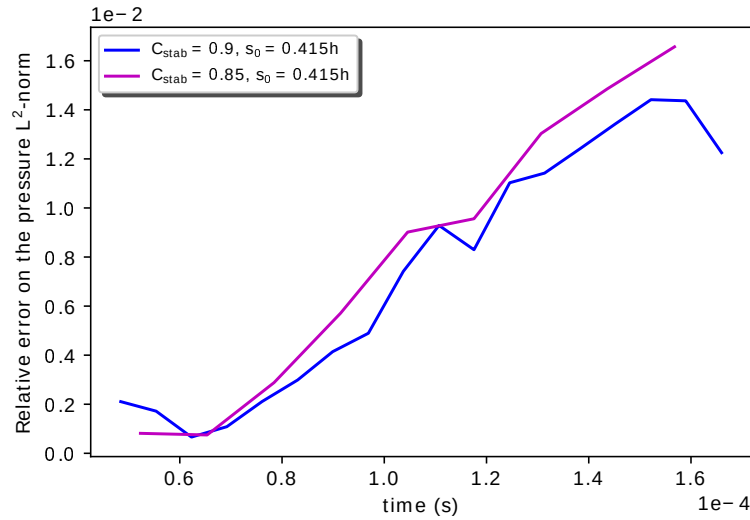

 Figure 4.25: Horizontal pressure profile - 10×10 array - $C_{stab} = 0.9$ - $s_0 = 0.415h$

The wavelet-based model thus seems able to reconstruct a horizontal pressure profile which closely fits the reference data. Nevertheless, a high frequency noise can be witnessed within the array of disks, here delimited by the vertical black lines. This phenomenon is explained by the aliasing induced by the scaling function Φ_{s_0} with the set of parameters $(C_{stab}, s_0) = (0.9, 0.415h)$. The choice of a cutoff scale $s_0 = 0.415h$ indeed allows to reach a better accuracy (while maintaining a stability safety margin with $C_{stab} = 0.9$) but results in an aliasing phenomenon, as this value does not satisfy the condition (3.241) which ensures that the scaling function bandwidth remains within the admissible Shannon frequency range.

To further investigate the accuracy of the wavelet-based model, let us now turn towards the L^2 -norm accuracy criterion.



(a) Evolution of the pressure L^2 -norm



(b) Relative error $\left| \frac{\|p_{ref}\|_{L^2} - \|p_{s_0}\|_{L^2}}{\|p_{ref}\|_{L^2}} \right|$.

Figure 4.26: L^2 -norm accuracy - 10×10 array - $C_{stab} \in \{0.85, 0.9\}$ - $s_0 = 0.415h$

Figures 4.26a-4.26b display respectively the time evolution of the L^2 -norm, for both the reconstructed and reference pressure fields, and the relative error. Two values for the C.F.L. stability constant C_{stab} are here tested. The cutoff scale s_0 is once again set to $0.415h$. It can be witnessed that the model is able to faithfully reconstruct the reference pressure field L^2 -norm, with a relative error below 1.7% for both C_{stab} values. No aliasing phenomenon is here visible. This is explained by the fact that the L^2 -norm (which integrates the square modulus of the signal over the whole domain) filters out the high frequency noise visible in the reconstructed pressure field. Nevertheless, despite this filtering, one can see that the relative error progressively increases when the wave front propagates through the solid medium. This is not a surprise, as it has already been noticed that the aliasing deteriorates the accuracy of the reconstructed pressure field within the array of disks.

To conclude this test, let us finally turn towards the main quantity of interest in the design of a coupled fluid-structure solver, i.e. the force applied to the solid medium. Figure 4.27 hereafter displays the time evolution of the horizontal force applied to the whole array, for both the reference and reconstructed pressure fields. Two different values are tested for the C.F.L. stability constant and the cutoff scale: $C_{stab} \in \{0.85, 0.9\}$ and $s_0 \in \{0.415h, 0.585h\}$.

As expected, the model response shows a better accuracy when the cutoff scale s_0 is near its minimum critical value, i.e. $s_0 = 0.415h$. A high frequency noise (due to aliasing) can once again be witnessed in the reconstructed force. Its amplitude moreover decreases when the C.F.L. constant C_{stab} decreases. This aliasing is characterized by the fact that the frequency of the oscillations visible in Figure 4.27b remains equal to the sampling frequency $(\frac{1}{2\Delta t})$, even when the time step Δt decreases with C_{stab} . The choice of a larger cutoff scale $s_0 = 0.585h$, which satisfies the aliasing compatibility condition (3.241), allows to completely suppress the high frequency noise, at the cost of a loss of accuracy.

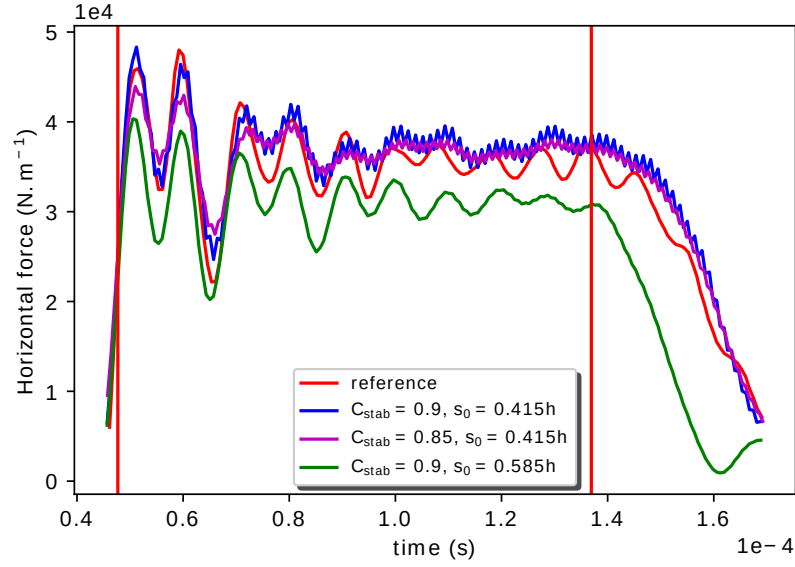
Table 4.14 summarizes the relative errors obtained on the horizontal force and the pressure field L^2 -norm. As the difference between the reference and reconstructed pressure fields is mainly focused within the array of disks, and especially in the vicinity of the fluid-structure interfaces, it is not surprising to see that a better accuracy is reach on the pressure field L^2 -norm, which takes into account the whole {fluid + solid} domain.

$s_0 = 0.415h$	Relative error \tilde{e}_F	Relative error on $\ p\ _{L^2}$
$C_{stab} = 0.9$	5.22×10^{-2}	$\lesssim 1.5 \times 10^{-2}$
$C_{stab} = 0.85$	3.70×10^{-2}	$\lesssim 1.7 \times 10^{-2}$

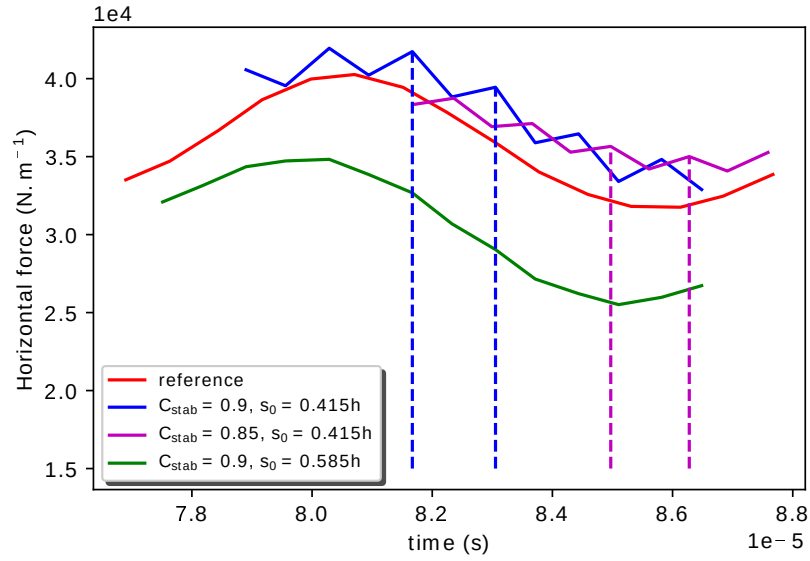
Table 4.14: Relative errors on the force and pressure field L^2 -norm.

It is here recalled that the absolute error e_F is defined by the time integration of the horizontal force:

$$e_F = \left| \int_{t_a}^{t_b} \left((\underline{F}_{F \rightarrow S})_{ref} - (\underline{F}_{F \rightarrow S})_{s_0} \right) \cdot \underline{e}_x dt \right|. \quad (4.13)$$



(a) Horizontal force applied to the solid medium (N.m^{-1})



(b) Horizontal force applied to the solid medium (N.m^{-1}) - zoom

Figure 4.27: Force-wise accuracy - 10×10 array - $C_{stab} \in \{0.85, 0.9\}$ - $s_0 = 0.415h$

Finally, to conclude this test on a 10×10 steady array of disks, it can be emphasized that the choice of a larger C.F.L. constant C_{stab} allows to better identify the solid medium characteristic spatial scale (i.e. the size of the porous cell), here $\lambda = 3R$, where $R = 4$ mm is the disks radius. Indeed, if C_{stab} decreases, the numerical model tends to attenuate all pressure and force oscillations, whether they are caused by the scaling function aliasing or the solid medium geometry. This is highlighted in Figure 4.28, which displays the FFT modulus of the horizontal force. The distance 116 mm corresponds to the horizontal distance between the first and last disks boundaries.

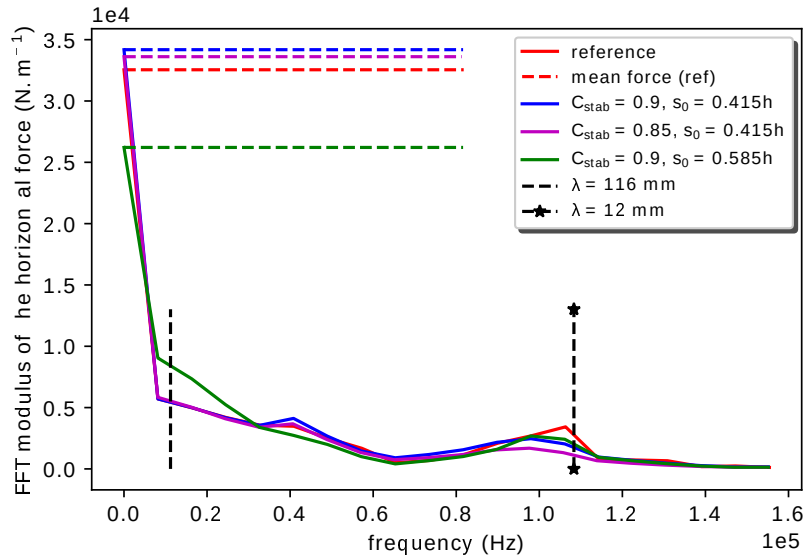


Figure 4.28: FFT modulus of the horizontal force (N.m^{-1}) - 10×10 array

This concludes this first assessment of the model capabilities, here evaluated for a 2D transverse pressure wave propagating through a 10×10 steady array of disks.

In order to now strengthen the multi-scale component of the model, the following test investigates whether a more macroscopic representation of the solid medium (and thus a larger mesh size h and cutoff scale s_0) allows to properly recover the main quantity of interest, here the horizontal force applied to the whole array. A macroscopic modeling of the solid medium would indeed allow to represent PWR fuel assemblies as a single beam, without the need to take into account their inner structure.

4.3.3 Equivalent modeling of a fuel assembly cross section

Three equivalent arrays of disks (2×2 , 4×4 , 10×10) are hereafter considered, as displayed in Figure 4.29. The (4×4) and (2×2) arrays are obtained from the (10×10) array by multiplying the radius and distance between disks by respectively 2.5 and 5. The mesh size h is adapted to each array so as to satisfy $h = \frac{R}{4}$. Furthermore, the boundary of each disk is approximated by

using 16 nodes, whether the radius is 4 mm, 10 mm or 20 mm. The C.F.L. constant C_{stab} and the cutoff scale s_0 are set to $(C_{stab}, s_0) = (0.9, 0.415h)$.

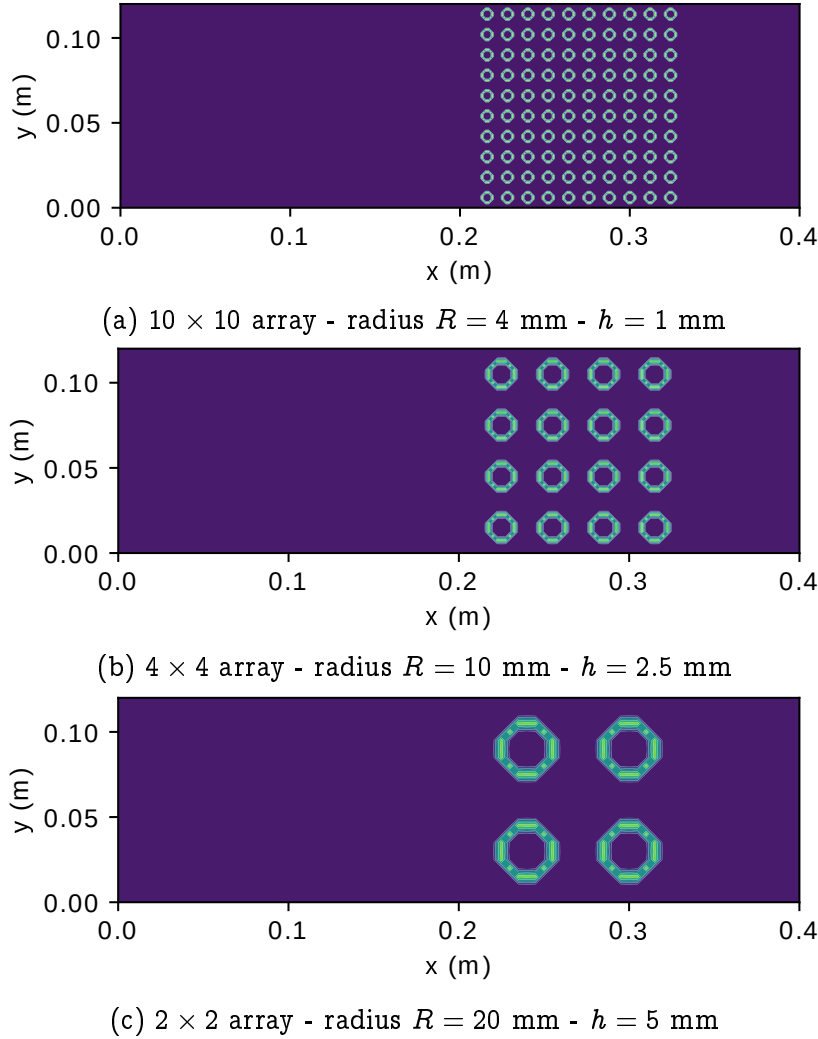


Figure 4.29: Equivalent arrays of disks (2×2 , 4×4 , 10×10)

As previously, the propagation of a 2D transverse pressure wave is computed for each array, with a 10 vs 1 bar initial pressure discontinuity, located at $x = 0.150$ m. The distance between the pressure discontinuity and the first disks is defined, for each array, by $d = 0.060 + \frac{R}{2}$ (m). As the radius changes from one array to the other, a small time delay in the pressure and force signals can be witnessed between each simulation. Figure 4.30 hereafter displays multiple snapshots of the reconstructed pressure fields for the (4×4) and (2×2) equivalent arrays.

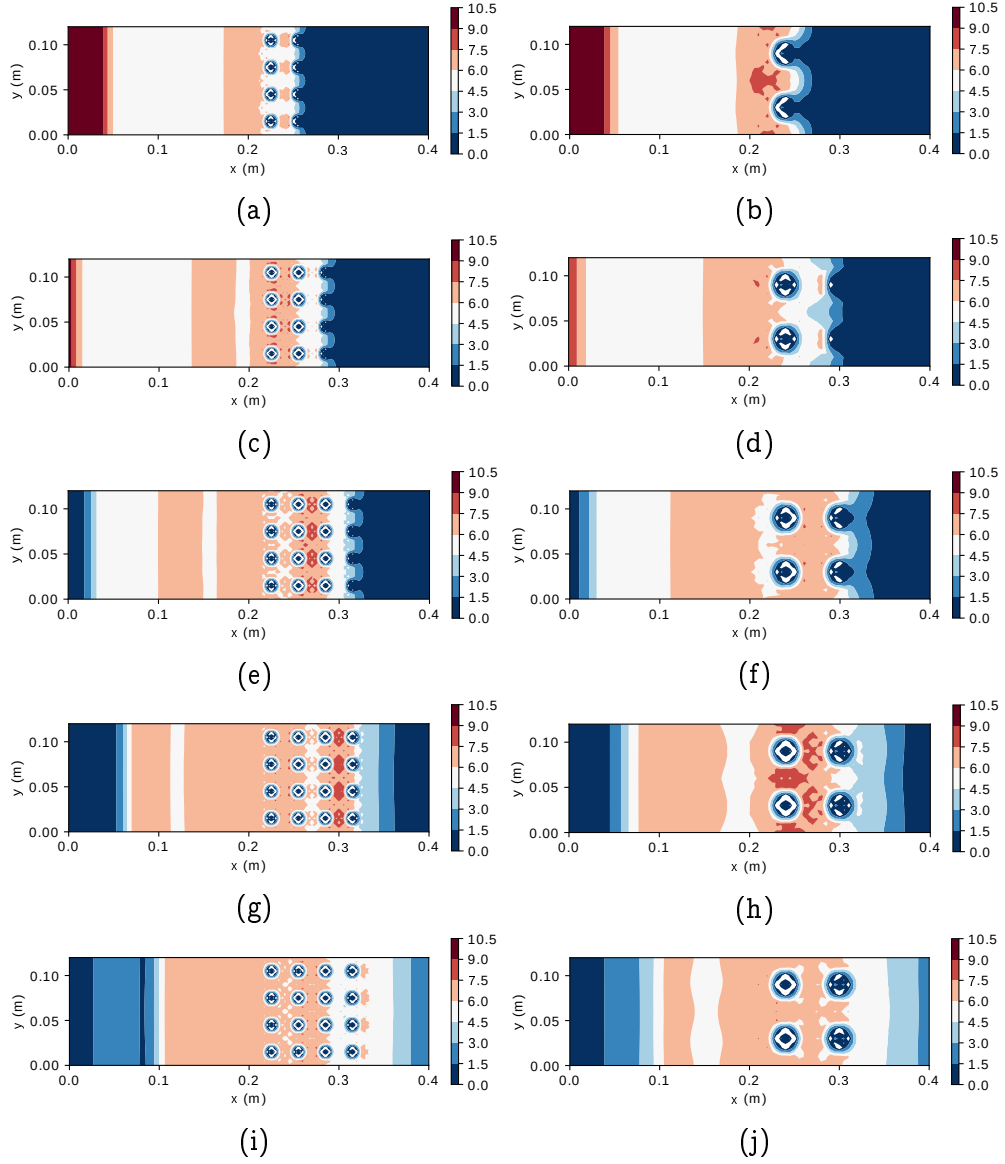
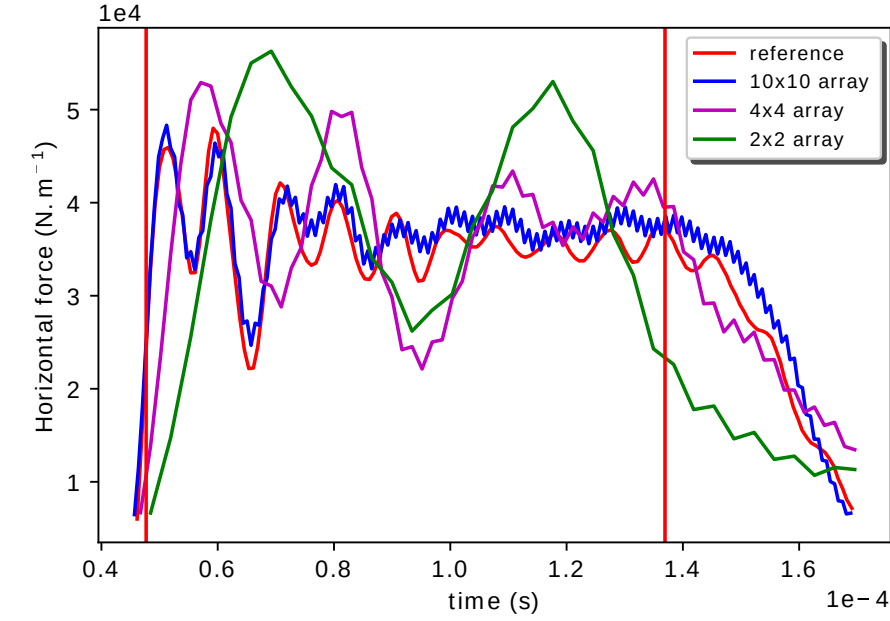
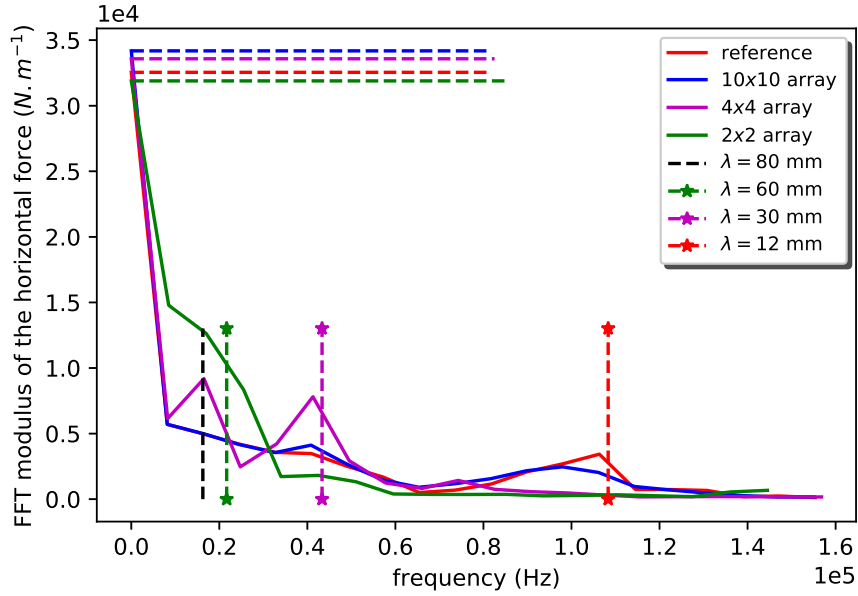


Figure 4.30: Reconstructed pressure field - equivalents arrays $(4 \times 4, 2 \times 2)$ - $h \in \{2.5 \text{ mm}, 5 \text{ mm}\}$ - $C_{stab} = 0.9$ - $s_0 = 0.415h$ - snapshots every $\Delta t = 2.77 \times 10^{-5} \text{ s}$

The following Figure 4.31 now displays both the time evolution and the FFT modulus of the horizontal force applied to each array.



(a) Horizontal force (N.m^{-1})



(b) FFT modulus of the horizontal force (N.m^{-1})

Figure 4.31: Horizontal force (N.m^{-1}) and its FFT modulus for equivalent arrays - $c_{stab} = 0.9$ - $s_0 = 0.415h$ - $h \in \{1 \text{ mm}, 2.5 \text{ mm}, 5 \text{ mm}\}$

As expected, one can first notice in Figure 4.31a that the high-frequency noise brought by the scaling function Φ_{s_0} is present for all arrays. Its frequency of course changes to match the sampling frequency of each simulation.

Furthermore, the size of the different porous cells (respectively 12 mm, 30 mm and 60 mm) is clearly visible in the horizontal force spectrum, as displayed in Figure 4.31b.

Finally, each of these equivalent arrays leads to an accurate evaluation of the time average of the horizontal force applied to the 10×10 array, as detailed in the following Table 4.15. Such a result thus supports a more macroscopic modeling of fuel assemblies within a Pressurized Water Reactor (PWR) core, for instance by simplifying the geometry to a single beam in a 3D framework.

	10×10 array	4×4 array	2×2 array
relative error \tilde{e}_F	5.22×10^{-2}	3.63×10^{-2}	1.94×10^{-2}

Table 4.15: Relative error on the horizontal force for equivalent arrays.

Now, to conclude this fourth chapter dedicated to the model implementation, two ongoing projects are hereafter presented:

- the first one consists in a first attempt at implementing a nested grids algorithm within the numerical model, with the aim of speeding up the computations;
- the second is dedicated to the coupling between the homogenized fluid and the solid medium. Experiments realized with a 10×10 array of PMMA cylinder rods submitted to a shock wave will be presented. This experimental data will be supplemented with preliminary numerical tests involving a (2×2) moving array of disks.

4.4 Ongoing works

4.4.1 First implementation of a nested grids algorithm

As multi-grid methods are generally encountered in the framework of iterative algorithms or implicit schemes, it is worthwhile to first recall the general philosophy of such methods, before detailing the specific use of nested grids in the current work.

General remarks on multi-grid methods

Multi-grid methods have been studied by an already extensive literature. Reference works on this subject can be found in [Brandt, 1977], [Stüben and Trottenberg, 1982], [Hackbusch, 1985], [Ruge and Stüben, 1987], [Wesseling, 1992], [Trottenberg et al., 2001] and [Wesseling and Oosterlee, 2001]. The development of multi-grid methods

was motivated by the will to speed up iterative algorithms, such as Jacobi's or Gauss-Seidel's, which are known to quickly reduce the high-frequency components of the error, but conversely struggle with the low-frequency components. In order to introduce the basic ideas of multi-grid methods, let us consider the following linear problem:

$$Ax = f, \quad (4.14)$$

where:

- $A \in \mathbb{R}^{n \times n}$ is a matrix, usually assumed symmetric, positive and definite;
- $x \in \mathbb{R}^n$ is the unknown vector;
- $f \in \mathbb{R}^n$ is a known vector;

Fixed-point algorithms can be used to solve iteratively equation (4.14). Jacobi's method, for instance, considers the decomposition $A = D + L + U$, where D is a diagonal matrix, and L and U are respectively strictly lower and upper triangular matrices. If the diagonal matrix D is invertible (which is true under the previous assumptions on A), one can inject the decomposition into equation (4.14) as follows:

$$Dx = f - (L + U)x. \quad (4.15)$$

$$x = D^{-1}f - D^{-1}(L + U)x. \quad (4.16)$$

Then, starting from an initial guess x^0 , the iterative algorithm writes:

$$x^{k+1} = Sx^k + D^{-1}f, \quad (4.17)$$

or with the damped form ($\omega \geq 0$):

$$x^* = Sx^k + D^{-1}f, \quad (4.18)$$

$$x^{k+1} = \omega x^* + (1 - \omega)x^k, \quad (4.19)$$

where $S = -D^{-1}(L + U)$. One then introduces the error vector e and residual vector r , defined at each iteration by:

$$e^k = x - x^k, \quad (4.20)$$

$$r^k = f - Ax^k. \quad (4.21)$$

By applying the matrix S to the error vector e^k , one obtains, with equations (4.16) and (4.17), the following iterative equation on e :

$$Se^k = Sx - Sx^k, \quad (4.22)$$

$$= -D^{-1}(L + U)x - (x^{k+1} - D^{-1}f), \quad (4.23)$$

$$= D^{-1}(f - (L + U)x) - x^{k+1}, \quad (4.24)$$

$$= D^{-1}Dx - x^{k+1} \quad (4.25)$$

$$= x - x^{k+1}, \quad (4.26)$$

$$= e^{k+1}. \quad (4.27)$$

As for the residual vector r , it is governed by the following equation:

$$r^k = f - Ax^k, \quad (4.28)$$

$$= A(x - x^k), \quad (4.29)$$

$$= Ae^k. \quad (4.30)$$

Remark 4.4.1 *Working with the residual equation (4.30) allows to improve the iterative algorithm. Indeed, when the approximation x^k is close to the solution x (for instance after a few iterations of Jacobi's method (4.17)), the error e^k will be small (in l^∞ norm), and one can thus choose the zero vector as initial guess to solve iteratively the residual equation*

$$Ae^k = r^k. \quad (4.31)$$

With the resulting approximation \tilde{e}^k of the error e^k , one can then update the unknown vector x^k as follows:

$$x^{k+1} = x^k + \tilde{e}^k. \quad (4.32)$$

Iterative algorithms such as (4.17) are known to converge if and only if the spectral radius $\rho(S)$ of the matrix S is strictly below 1. The convergence rate is also linked to $\rho(S)$: convergence is slow if $\rho(S)$ is close to 1, and becomes faster as $\rho(S)$ decreases towards zero.

Furthermore, it is well-known that such iterative algorithms, when implemented on a single grid, quickly reduce the high-frequency (non-smooth) components of the error e , but exhibit a very low damping on the low-frequency (smooth) components. The basic idea of (geometric) multi-grid methods is then to introduce multiple nested grids, so that the low-frequency components associated to a fine grid may become high-frequency components when transferred to a coarser grid. The basic example of multi-grid method is the following two-level algorithm, where two nested grids of mesh sizes h and $2h$ are considered:

Two-level algorithm:

- smoothing: compute a few iterations of the iterative scheme associated to $A^h x^h = f^h$ on the fine grid (h); this leads to an approximation \tilde{x}^h in which the high-frequency components of the error are damped;
- compute, on the fine grid (h), the residual $r^h = f^h - A^h \tilde{x}^h$;
- restriction: project the residual r^h on the coarse grid ($2h$), via a restriction operator $R : r^h \mapsto R(r^h)$;
- solve, on the coarse grid ($2h$), the residual equation $A^{2h} e^{2h} = R(r^h)$; this leads to an approximation \tilde{e}^{2h} in which the initial low-frequency components are now damped as well;
- prolongation: transfer the error \tilde{e}^{2h} on the fine grid (h) via an interpolation operator $I : \tilde{e}^{2h} \mapsto I(\tilde{e}^{2h})$;
- update the approximation \tilde{x}^h on the fine grid (h) : $\tilde{x}^h \leftarrow \tilde{x}^h + I(\tilde{e}^{2h})$.

To apply such a two-level algorithm, one needs to define the restriction R and interpolation I operators, and also the coarse grid version A^{2h} of the original (fine grid) matrix A^h . When the matrix A^h is for instance obtained through a finite-difference scheme, the construction of A^{2h} is straightforward.

These general remarks on multi-grid methods being stated, let us now turn towards the specific use of nested grids in the current work.

Specific use of nested grids

As detailed above, multi-grid methods are well-designed for (stationary) linear problems $Ax = f$ solved iteratively, or implicit schemes. However, in the current work, the homogenized fluid equations are solved with an explicit finite-volume scheme. Thus, multi-grid methods and nested grids are not here intended to improve the convergence of iterative schemes. The idea is rather to compute the homogenized fluid equations on a coarse grid, while keeping track of the rods geometry on the fine grid, in order to properly evaluate all the boundary integrals in the right-hand side of the equations. The nested grids computation is thus implemented as follows:

- the homogenized fluid variables are known on the coarse grid ($2h$) at $t = t^n$;
- the real fluid variables are reconstructed on the coarse grid ($2h$) at $t = t^n$, with a scaling function $\Phi_{s_{2h}}$ whose cutoff scale s_{2h} is linked to $2h$;
- prolongation: the real pressure field is extended from the coarse grid ($2h$) to the fine grid (h);

- the force applied by the underlying solid medium is computed on the fine grid (h), with a scaling function Φ_{s_h} whose cutoff scale is linked to h ;
- restriction: the force is transferred from the fine grid (h) to the coarse grid ($2h$);
- the homogenized fluid variables are then updated at $t = t^{n+1}$ with this source term on the coarse grid ($2h$).

Let us now specify the interpolation and restriction operators chosen to implement this nested grids algorithm. To this end, let us first introduce the following notations:

Notations 4.4.1 • $(u_{i,j}^h)_{0 \leq i,j \leq 2n}$ hereafter denotes the unknowns on the fine grid, with mesh size h ;

• $(v_{i,j}^{2h})_{0 \leq i,j \leq n}$ hereafter denotes the unknowns on the coarse grid, with mesh size $2h$.

Interpolation operator: bilinear interpolation

The interpolation (or prolongation) operator from the coarse grid to the fine grid is here defined as a bilinear interpolation, whose action on the coarse grid unknowns $(v_{i,j}^{2h})$ can be summarized into the following symbol:

$$\begin{pmatrix} \frac{1}{4} & \frac{1}{2} & \frac{1}{4} \\ \frac{1}{2} & 1 & \frac{1}{2} \\ \frac{1}{4} & \frac{1}{2} & \frac{1}{4} \end{pmatrix}.$$

More precisely, the fine grid values $(u_{i,j}^h)_{1 \leq i,j \leq 2n}$ are obtained from the coarse grid values $(v_{i,j}^{2h})_{1 \leq i,j \leq n}$ according to the following equations:

$$\forall 0 \leq i, j \leq n, u_{2i,2j}^h = v_{i,j}^{2h}. \quad (4.33)$$

$$\forall 0 \leq i \leq n-1, 0 \leq j \leq n, u_{2i+1,2j}^h = \frac{1}{2} (v_{i,j}^{2h} + v_{i+1,j}^{2h}). \quad (4.34)$$

$$\forall 0 \leq i \leq n, 0 \leq j \leq n-1, u_{2i,2j+1}^h = \frac{1}{2} (v_{i,j}^{2h} + v_{i,j+1}^{2h}). \quad (4.35)$$

$$\forall 0 \leq i, j \leq n-1, u_{2i+1,2j+1}^h = \frac{1}{4} (v_{i,j}^{2h} + v_{i+1,j}^{2h} + v_{i,j+1}^{2h} + v_{i+1,j+1}^{2h}). \quad (4.36)$$

Restriction operator: full weighting restriction

Regarding now the restriction operator, the simplest choice would be a straight injection which copies the values $(u_{2i,2j}^h)$ onto $(v_{i,j}^{2h})$. As such a choice does not take into account values corresponding to odd indices, a full weighting restriction is here chosen, whose symbol is defined by:

$$\begin{pmatrix} \frac{1}{16} & \frac{1}{8} & \frac{1}{16} \\ \frac{1}{8} & \frac{1}{4} & \frac{1}{8} \\ \frac{1}{16} & \frac{1}{8} & \frac{1}{16} \end{pmatrix}.$$

More precisely, the coarse grid values are obtained via the following equations:

$$\forall 1 \leq i, j \leq n-1,$$

$$\begin{aligned} v_{i,j}^{2h} = & \frac{1}{4}u_{2i,2j}^h + \frac{1}{8}u_{2i+1,2j}^h + \frac{1}{16}u_{2i+1,2j+1}^h + \frac{1}{8}u_{2i,2j+1}^h + \frac{1}{16}u_{2i-1,2j+1}^h \\ & + \frac{1}{8}u_{2i-1,2j}^h + \frac{1}{16}u_{2i-1,2j-1}^h + \frac{1}{8}u_{2i,2j-1}^h + \frac{1}{16}u_{2i+1,2j-1}^h. \end{aligned} \quad (4.37)$$

$$\forall 1 \leq j \leq n-1,$$

$$v_{0,j}^{2h} = \frac{1}{4}u_{0,2j+1}^h + \frac{1}{2}u_{0,2j}^h + \frac{1}{4}u_{1,2j-1}^h, \quad (4.38)$$

$$v_{n,j}^{2h} = \frac{1}{4}u_{n,2j+1}^h + \frac{1}{2}u_{n,2j}^h + \frac{1}{4}u_{n,2j-1}^h. \quad (4.39)$$

$$\forall 1 \leq i \leq n-1,$$

$$v_{i,0}^{2h} = \frac{1}{4}u_{2i-1,0}^h + \frac{1}{2}u_{2i,0}^h + \frac{1}{4}u_{2i+1,0}^h, \quad (4.40)$$

$$v_{i,n}^{2h} = \frac{1}{4}u_{2i-1,n}^h + \frac{1}{2}u_{2i,n}^h + \frac{1}{4}u_{2i+1,n}^h. \quad (4.41)$$

$$v_{0,0}^{2h} = u_{0,0}^h, \quad (4.42)$$

$$v_{n,0}^{2h} = u_{2n,0}^h, \quad (4.43)$$

$$v_{0,n}^{2h} = u_{0,2n}^h, \quad (4.44)$$

$$v_{n,n}^{2h} = u_{2n,2n}^h. \quad (4.45)$$

These two operators being defined, let us now compare the results obtained with mono-grid and multi-grid computations.

Comparison between mono-grid and multi-grid computations

The following Figure 4.32 displays the propagation of a 2D transverse pressure wave through a 2×2 steady array of disks. Two multi-grid computations are hereafter considered, respectively 2 mm/1 mm and 1 mm/0.5 mm.

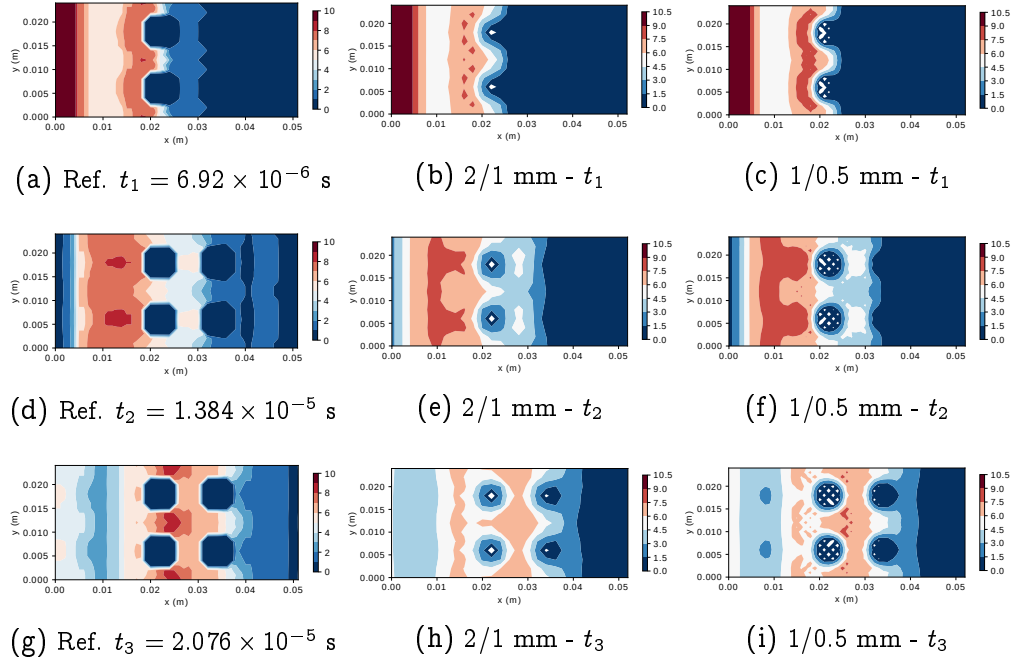


Figure 4.32: Pressure field snapshots - reference VS model with multi-grid computations (2/1 mm and 1/0.5 mm)

Figure 4.33 now displays the horizontal force obtained with both mono-grid and multi-grid computations.

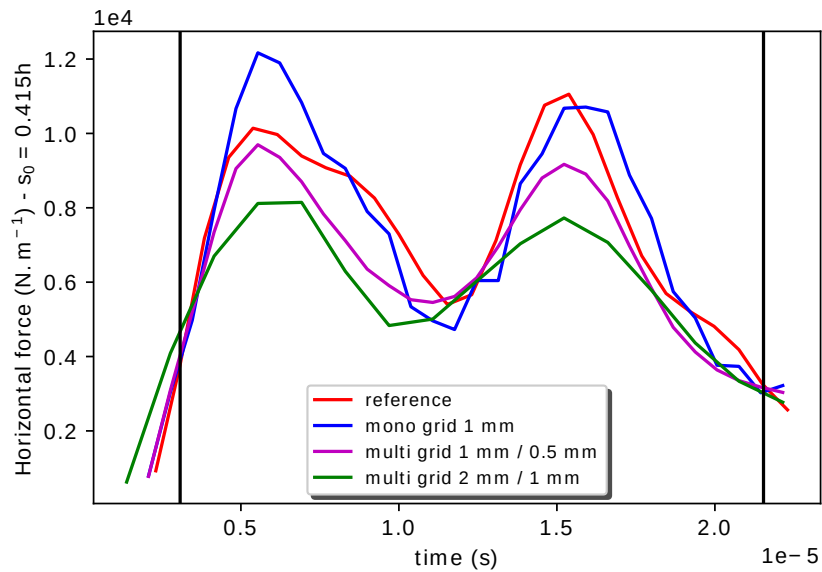


Figure 4.33: Horizontal force ($\text{N} \cdot \text{m}^{-1}$) - multi-grid - $C_{stab} = 0.9$ - $s_0 = 0.415h$

It appears that both multi-grid computations result in a loss of accuracy on the time average of the horizontal force, as detailed in Table 4.16 below. This surprising result requires additional investigations to explain such a phenomenon, especially for the nested grids 1 mm/0.5 mm, for which one would expect to obtain a better accuracy.

	Mono-grid 1 mm	1 mm / 0.5 mm	2 mm / 1 mm
relative error $\tilde{\epsilon}_F$	1.41×10^{-2}	1.11×10^{-1}	1.76×10^{-1}

Table 4.16: Relative error on the horizontal force - multi-grid computations.

These preliminary results thus conclude this first attempt at implementing a nested grids algorithm within the wavelet-based numerical model. To now conclude this chapter dedicated to the model implementation, let us finally focus on the coupling between the homogenized fluid and the solid medium dynamics.

4.4.2 Towards a coupled fluid-structure solver

Experiments on a shock tube facility

Until now, the wavelet-based homogenized model has been confronted with 2D reference solutions computed with EUROPLEXUS software, considering steady solid obstacles. In order to thoroughly assess the model capabilities, especially with regards to the coupling between the fluid and solid medium dynamics, an experimental reference solution is also mandatory. To this end, a collaborative test program has been initiated between the French Energy Commission (CEA) and the Norwegian University of Science and Technology (NTNU). This joint project aims at providing a first set of experimental results regarding transverse pressure waves propagating through a tube bundle. The SIMlab shock tube facility (SSTF), hereafter displayed in Figure 4.34, shows very interesting perspectives in this context, since the dimensions of its cross section allows implementing a simplified yet representative tube bundle specimen. This facility is also capable of generating a well-mastered and measured pressure wave loading, thus allowing to produce some significant knowledge on how the pressure signal is modified when travelling through the bundle.

In an effort to find a satisfactory balance between complexity and representativity, a bundle of 10×10 rods has been chosen for this experimental study, as can be seen in Figure 4.34g. The rods diameter and the spacing between consecutive rods are close to the regular values for PWR fuel assemblies, the preservation of the ratio between the two being a priority constraint. Such a compact test specimen is here required in order to perform 3D detailed simulations of the test, as well as optical measurements through the windows in the dedicated section of the shock tube (cf. Figures 4.34f-4.34g).

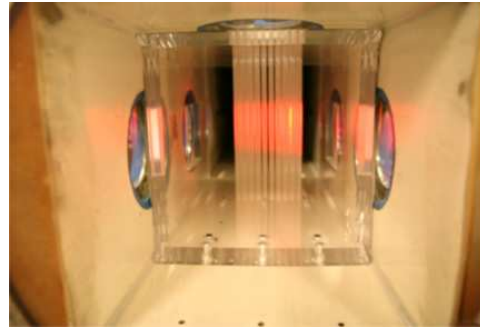
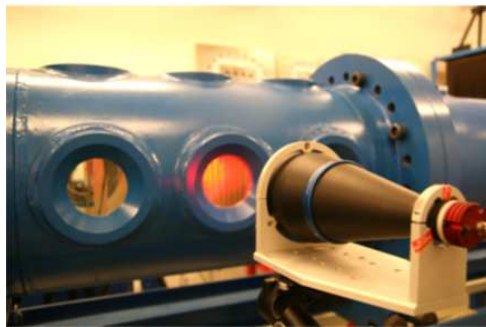
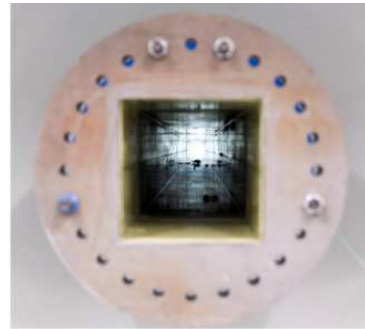
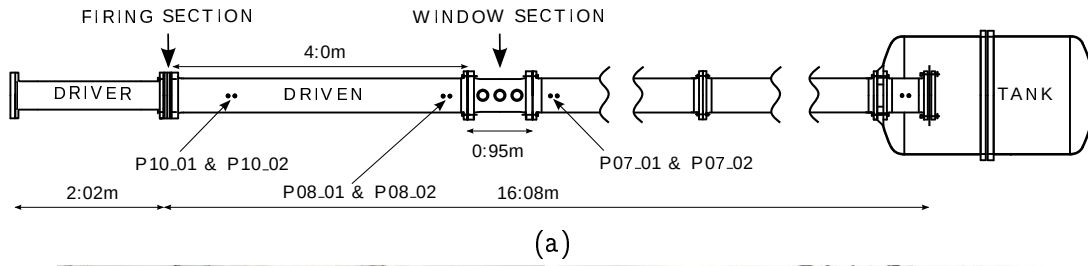


Figure 4.34: Experimental setup: sketch of the SSTF (Figure 4.34a), entire shock tube facility (Figure 4.34b), firing section with diaphragms (Figure 4.34c), close-up on camera setup (Figure 4.34d), open end and internal cross-section of the driven (Figure 4.34e), telecentric lens (Figure 4.34f), and tube bundle specimen (Figure 4.34g). Figures 4.34b and 4.34c are reprints from [Aune et al., 2016].

The driver section (cf. Figure 4.34a) is manufactured with a total length of 2.02 m and an inner diameter of 0.331 m. The driver is followed by a 0.14 m-long firing section which consists in several intermediate pressure chambers separated by diaphragms (cf. Figures 4.34a and 4.34c). This enables the total pressure difference between the driver and driven sections to be achieved stepwise. The inner cross-section in the driven section starts with a 0.6 m-long transition region from a circular to a square cross-section ($0.3 \text{ m} \times 0.3 \text{ m}$). The driven section ends with a tank of 5.1 m^3 , with an 1.6 m internal diameter.

Regarding now the test specimen, hereafter displayed in Figure 4.35, the diameter and spacing of the rods are representative of a PWR fuel assembly, in order to limit scaling effects regarding the wave propagation through the bundle. Both extremities of the rods are inserted into holes in two horizontal plates. The bottom plate is then clamped on the bottom wall of the shock tube using dedicated bolts and tapped holes. The top and bottom plates of the specimen are connected together and supported by two lateral plates of identical thickness, in which square windows are cut to allow for a direct optical access to the bundle. Indeed, telecentric lenses are used to provide a Schlieren representation of the pressure waves and the solid medium motion.

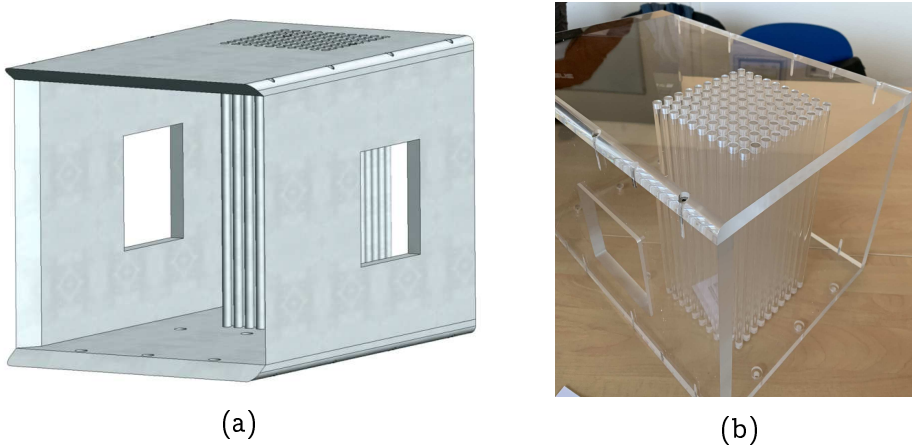


Figure 4.35: Tube bundle test specimen used in SIMlab shock tube facility

This experimental study shall be considered as part of a preliminary work, whose long-term objectives are:

- to identify experimentally, if possible, a transfer function of the bundle connecting well-chosen variables upstream and downstream the specimen;
- to see if detailed 3D simulations (i.e. at the DNS scale) are sufficiently close to the experimental data (both pressure measurements and high-speed camera images), thus allowing to use 3D simulations as numerical reference to confront a 3D extension of the wavelet-based homogenized model;
- to determine which lessons can be learned from this first series of tests to improve the experimental basis in the ongoing research dedicated to fuel assembly modeling in LOCA situation.

Remark 4.4.2 *Conversely to the actual PWR situation, the experiment has here been carried out in air given the shock tube technical conditions. This of course significantly changes the compressibility of the fluid compared to pressurized water.*

The experimental tests were operated with a maximum driver length of 2.02 m. The driven section was operated with a length of 16.08 m, with the first row of tube bundles located in the center of the window section (cf. Figures 4.34f-4.34g). The loading was varied by changing the initial pressure p_4 in the driver section, while the initial pressure in the driven section was operated at ambient conditions (p_1 and T_1). Two loading are hereafter considered, namely 2.5 bar and 5 bar overpressure. Table 4.17 below gives the complete test matrix, where each test is numbered X-Y, in which X denotes a test without (O) or with tube bundle (B) specimen. Y indicates the firing overpressure (in bar) in the driver. It is worth noting the good repeatability of the bursting characteristics of the diaphragms by comparing the firing pressure p_4 between tests with the same initial conditions in Table 4.17. The presence of tests without any tube bundle was intended to provide a comparison point (free of FSI phenomena) between the experimental shock wave within the facility and a numerical shock wave computed with EUROPLEXUS software.

Test	Overpressure p_4 in driver (kPa)	Pressure p_1 in driven (kPa)	Temp. T_1 (°C)
O02	252.08	99.60	21.67
O05	517.29	98.50	21.19
B02	255.13	100.12	21.15
B05	516.37	100.02	21.40

Table 4.17: Test matrix including initial conditions for each test. Peak pressures p_4 measured in the driver before venting.

In all tests, six sensors flush mounted in the tube roof measured the pressure behind the incident and reflected shock wave. The location of each pair of sensors is displayed in Figure 4.34a. A 10 cm spacing was used between each pair member. Sensors P10 were located 0.97 m and 1.07 m downstream the diaphragms in the firing section, P08 were located 0.22 m and 0.32 m upstream the window section, while P07 were located 0.22 m and 0.32 m downstream the window section. The delay in arrival time at each pair of sensors may then be used to determine the shock velocity and the corresponding Mach number.

In order to catch the shock wave propagation and the dynamic response of the bundles, a high-speed camera with a telecentric setup (cf. Figure 4.34d-4.34f-4.34g) was used for Schlieren photography. The sampling rate of the high-speed camera was 37 kHz. The pressure measurements were also synchronized with the camera.

Remark 4.4.3 *Failure of the specimen during the 5 bar test*

The multiple impacts of pressure waves on the bundle produced tensile stresses in the bottom plate with brittle behaviour. Very small cracks were already visible after the 2.5 bar overpressure test. The second test destroyed the specimen, starting with a straight crack near the second row of bolts and continuing with diagonal cracks in the lateral panel, leading to the release of the rear part of the specimen holding the rods (see Figure 4.36). It could fortunately be retrieved quite easily with no damage to the facility thanks to the knowledge and expertise of the local team operating the shock tube.

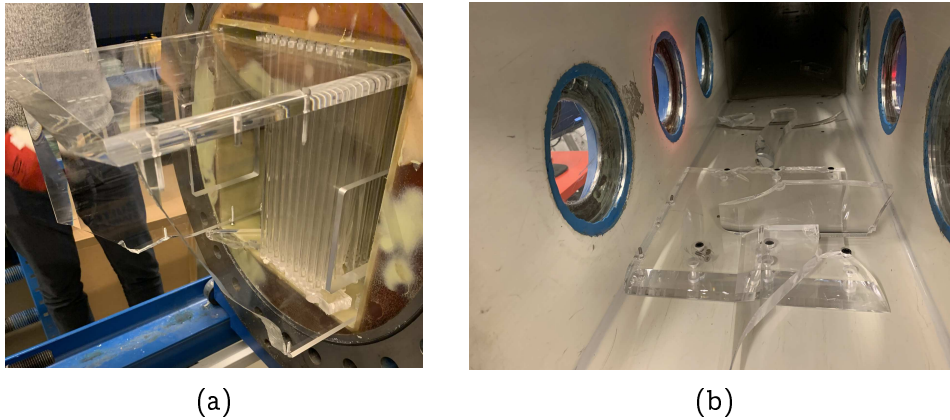


Figure 4.36: Tube bundle specimen after failure during the 5 bar test: released part (4.36a) and remaining part still connected to the facility (4.36b).

The 2.5 bar test allowed to catch, thanks to the high-speed camera, the tube bundle dynamic response to the shock wave. Figures 4.37 and 4.38 hereafter display multiple snapshots allowing to witness the impact and reflection of the shock wave on the test specimen, and the resulting motion of the first cylinder rods. The rods displacement becomes truly visible in Figure 4.38, where one can immediately notice impacts between consecutive rods. It is recalled that such impacts are not taken into account in the current 2D modeling of the solid medium.

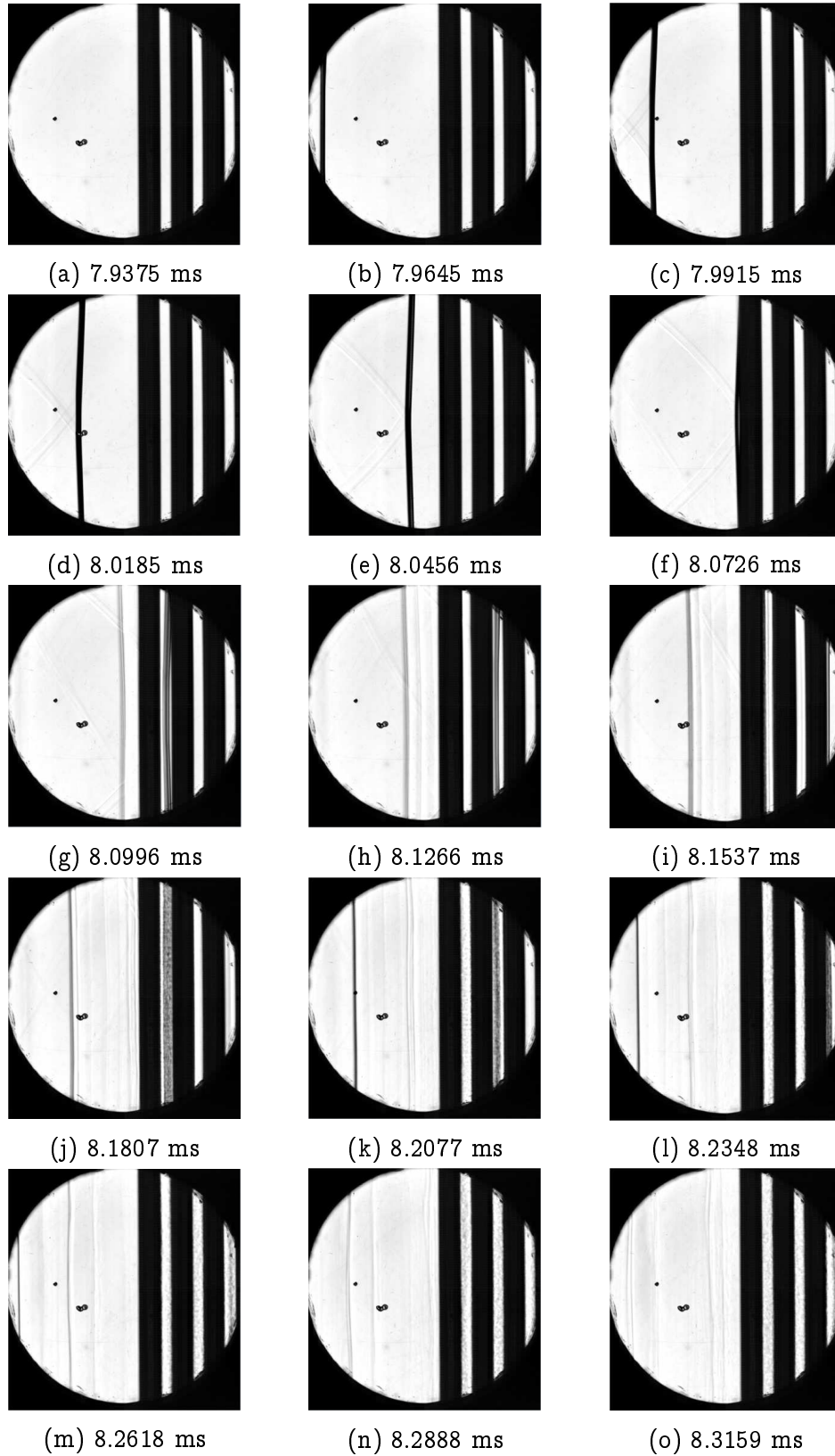


Figure 4.37: Shock wave impacting the first cylinder rods. Time ($t = 0$) is taken as the arrival of the shock wave at the pressure sensor P10_02.

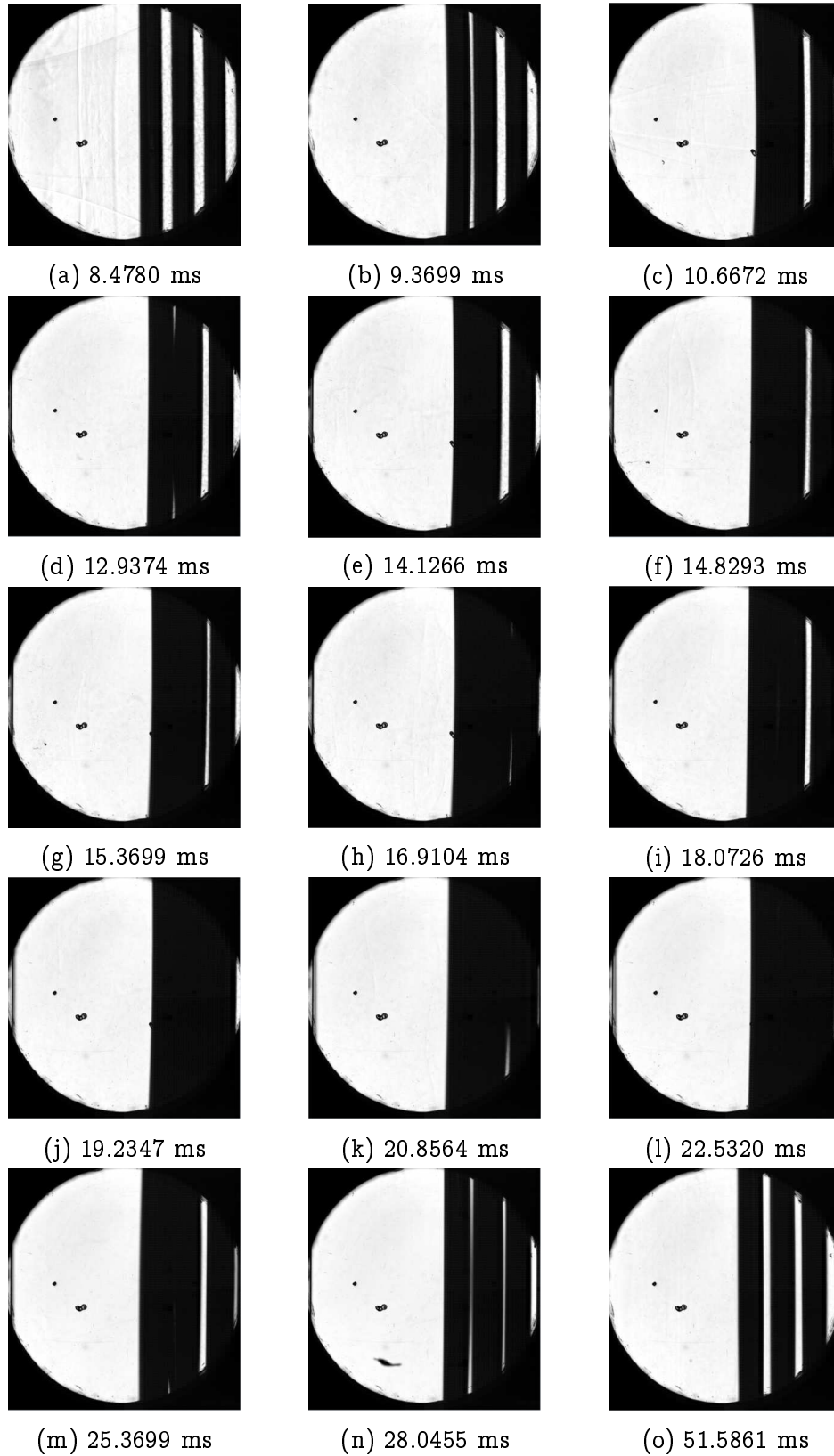


Figure 4.38: Visualization of the rods displacement. Time ($t = 0$) is taken as the arrival of the shock wave at the pressure sensor P10_02.

Given the previous snapshots, the rods displacement is then obtained by using digital image correlation to track the mid-point of the first cylinder rod in the 2.5 bars overpressure test, leading to the following curve displayed in Figure 4.39 below.

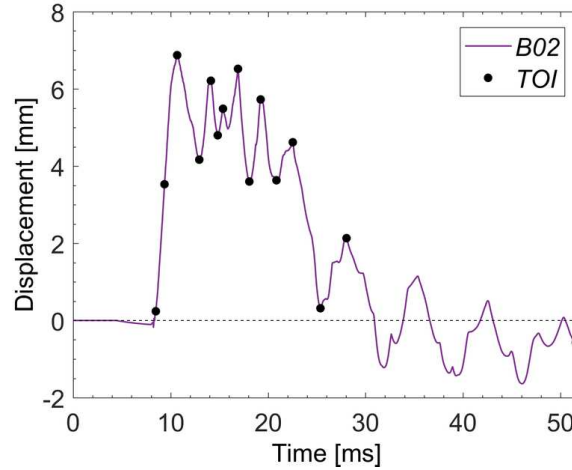


Figure 4.39: Longitudinal displacement of the mid-point of the first rod. Time ($t = 0$) is taken as the arrival of the shock wave at Sensor P10_02. Black markers correspond to the times of interest (TOI) in Figure 4.38.

The mid-point of the first row of rods thus exhibit a rapid displacement from $t = 8.4780$ ms until the point of maximum deflection at $t = 10.6672$ ms. Then, some elastic vibrations can be witnessed, followed by a significant drop in the displacement magnitude between $t = 22.5320$ ms and $t = 25.3699$ ms. The rods mid-point then seems to undergo elastic vibrations around a slightly permanent deformed configuration throughout the remaining of the test.

Now, to go along with this preliminary experimental data, it is now high time to test the wavelet-based model on a moving array of disks.

Preliminary numerical test with a moving array

For this first assessment of the model capability to treat the coupling with moving solid obstacles, the propagation of a 2D pressure wave through a 2×2 array of disks is here considered. It is recalled that the array is modeled via a linear oscillator for each degree of freedom, here two translations. Such a 2D computation is not expected to faithfully represent the 3D rods behavior observed in the shock tube facility. Indeed, impacts between consecutive rods are for instance not taken into account. The aim is here rather to recover, with the wavelet-based model equations, the theoretical behavior of a linear oscillator that would be submitted to the (reconstructed) force applied by the fluid, thoroughly investigated in the previous tests.

The simulation is designed with a 8 m long shock tube, in order to give time for the solid medium motion to take place, and also prevent reflected waves on the outer boundaries from interacting again with the solid medium. An initial

pressure discontinuity of 2.5 vs 1 bar is located at $x = 3.9$ m, as displayed in Figure 4.40.

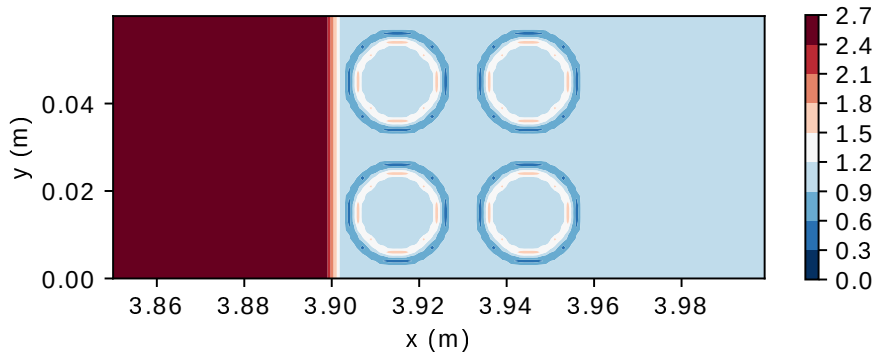


Figure 4.40: Zoom on the initial pressure field (2.5 vs 1 bar) - 2×2 moving array of disks.

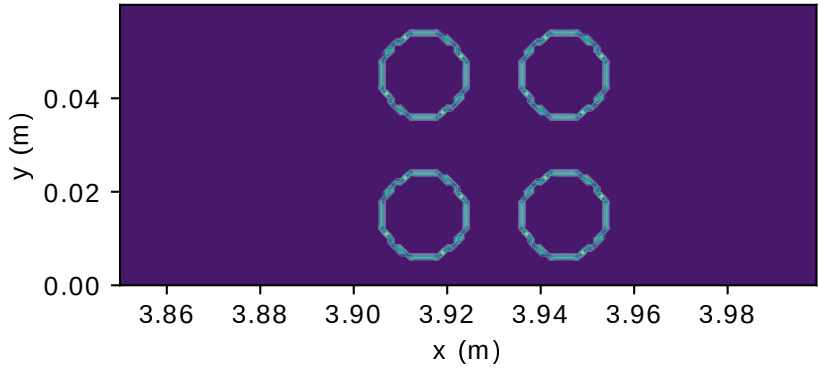


Figure 4.41: Visualization of the 2×2 moving array of disks at $t = 0$.

All the simulation parameters are summarized in the following Tables 4.18-4.19-4.20-4.21-4.22.

Lx	Ly	Disks radius	Dist. consecutive disks
8 m	$6 \cdot 10^{-2}$ m	$1 \cdot 10^{-2}$ m	$1 \cdot 10^{-2}$ m

Table 4.18: Geometry - 2×2 moving array of disks.

2.5 bar zone	1 bar zone	Discontinuity \longleftrightarrow 1st disks
$[0, 3.9 \text{ m}]$	$[3.9 \text{ m}, 8 \text{ m}]$	$5 \cdot 10^{-3}$ m

Table 4.19: Pressure loading - 2×2 moving array of disks.

Reference Density	Reference Pressure	Sound Velocity
$\rho_{ref} = 1000 \text{ kg} \cdot \text{m}^{-3}$	$p_{ref} = 10^5 \text{ Pa}$	$c = 1300 \text{ m} \cdot \text{s}^{-1}$

Table 4.20: Fluid parameters - 2×2 moving array of disks.

Eigenfrequency	Mass	Stiffness	Damping
$\omega_0 = \frac{2\pi}{5 \cdot 10^{-3}} \text{ s}^{-1}$	$m_{tot} = 1.492 \times 10^{-4} \text{ kg}$	$k_{tot} = 2.354 \times 10^2 \text{ kg} \cdot \text{s}^{-2}$	$\xi = 20\%$

Table 4.21: Solid medium parameters - 2×2 moving array of disks.

Mesh size	Time step	Scale/mesh compatibility
$h = 1 \text{ mm}$	$\Delta t = 0.9 \times \frac{h}{c_{max}}$	$s_0 = 0.585 \times h$

Table 4.22: Spatial and time discretization - 2×2 moving array of disks.

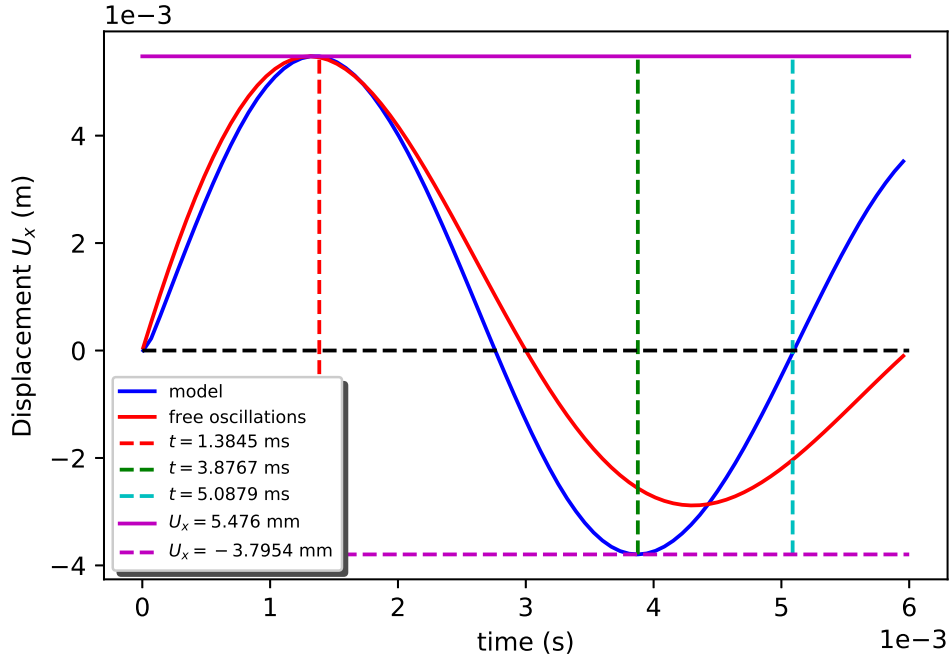
In order to be able to witness sufficient displacement of the solid medium during a limited simulation time, here 6 ms, the solid medium parameters are chosen as follows:

- [1] the (eigen-)period of the linear oscillator is set to $T_0 = 5 \text{ ms}$;
- [2] the associated eigenfrequency is then defined by $\omega_0 = \frac{2\pi}{T_0} \text{ (rad} \cdot \text{s}^{-1})$;
- [3] the solid density is set to $\rho_s = 1.188 \times 10^1 \text{ kg} \cdot \text{m}^{-3}$ (1% of PMMA density);
- [4] the disks thickness is set to $L = 10^{-2} \text{ m}$;
- [5] the resulting mass is defined by $m_{tot} = 4 \times \rho_s \pi R^2 L$;
- [6] the stiffness k_{tot} is then defined by: $k_{tot} = \omega_0^2 \times m_{tot}$;
- [7] the friction coefficient c_{tot} is finally defined by $c_{tot} = \xi \times 2\sqrt{k_{tot} m_{tot}}$, where ξ is the dimensionless damping coefficient.

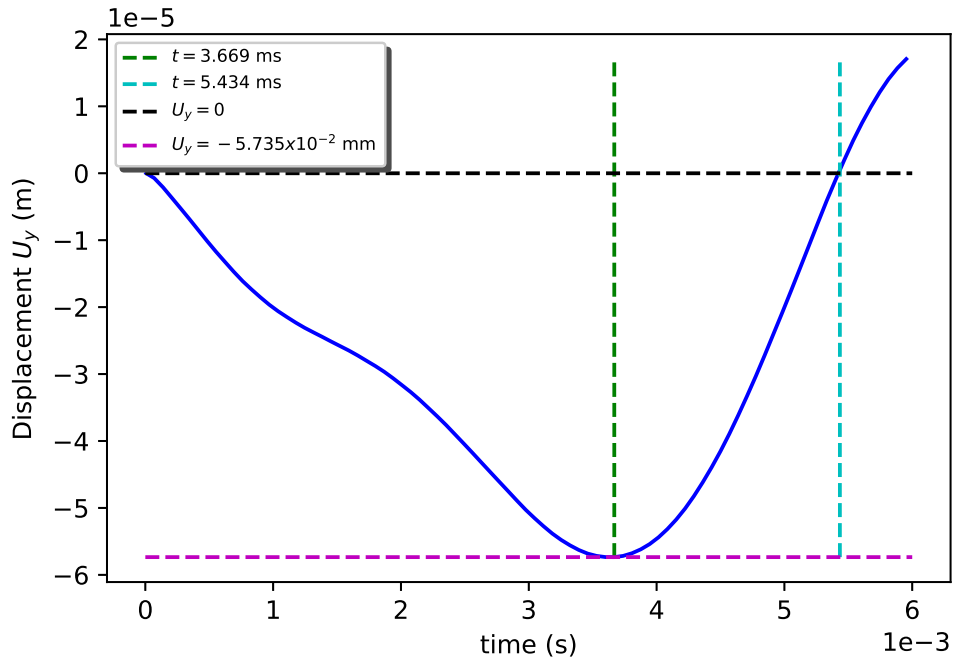
Remark 4.4.4 Influence of the structural damping

If the damping coefficient ξ is chosen too small, the coupled fluid-structure simulation may exhibit a non-physical behavior. Indeed, an increase of the pressure beyond the initial maximum value of 2.5 bar has for instance been noticed when decreasing ξ below 10%. Such a numerical phenomenon requires a parametric study on the damping coefficient ξ in order to determine its critical minimum value.

These remarks being stated, Figure 4.42 now displays the time evolution of the longitudinal and transverse displacements.



(a) Displacement U_x



(b) Displacement U_y

Figure 4.42: Displacements U_x/U_y - 2×2 moving array of disks.

The sinusoidal shape of the displacement U_x in Figure 4.42a, with a maximum displacement of 5.476 mm reached around $t = 1.3845$ ms, is coherent with the linear oscillator modeling. Indeed, the red curve visible in Figure 4.42a corresponds to the free theoretical response of a linear oscillator in pseudo-periodic regime:

$$U_x^{theo} = K e^{-\xi \tilde{\omega}_0 t} \cos \left(\tilde{\omega}_0 \sqrt{1 - \xi^2} t + \varphi \right), \quad (4.46)$$

where:

- the damping coefficient ξ is set to 20%;
- the period $\tilde{T} = \frac{2\pi}{\tilde{\omega}_0 \sqrt{1 - \xi^2}}$ is set to 6 ms;
- the phase φ is set to $-\frac{\pi}{2}$;
- the constant K is set so that U_x^{theo} coincides with the maximum displacement U_x at $t = 1.3845$ ms.

During the first phase of the simulation $[0, 1.3845 \text{ ms}]$, where the disks displacement is mainly driven by the initial shock wave, $U_x(t)$ closely fits the free theoretical response (4.46). The fact that the longitudinal displacement first responds with a period close to 6 ms can be tied back to the period of the pressure loading. Indeed, as the pressure discontinuity is initially located at $x = 3.9$ m, at only 5 mm from the first disks, the time T_{wave} necessary for a wave to impact again the disks from left to right can be evaluated as follows:

$$T_{wave} = \frac{3.9 + 3.905}{1300} - \frac{0.005}{1300} \quad (4.47)$$

$$= 6 \text{ ms}, \quad (4.48)$$

where the velocity of the pressure discontinuity has here been approximated by the sound velocity in the fluid.

During the second phase $[1.3845 \text{ ms}, 6 \text{ ms}]$, the pressure discontinuities are mostly far away from the array, leading to small pressure forces. The longitudinal displacement $U_x(t)$ is thus mainly driven by the restoring elastic force. Thus, the period of $U_x(t)$ decreases from the initial 6 ms wave period to fit its 5 ms eigen-period. Indeed, Figure 4.42a allows to estimate a period of damped oscillations around $T = 5.0879$ ms, which is coherent with the previous choices of parameters. Indeed, the frequency and period of damped oscillations satisfy:

$$\omega = \omega_0 \sqrt{1 - \xi^2}, \quad (4.49)$$

$$T = \frac{T_0}{\sqrt{1 - \xi^2}}. \quad (4.50)$$

With $\xi = 20\%$ and $T_0 = 5$ ms, it follows $T \approx 5.103$ ms.

Regarding now the transverse displacement U_y , one can notice in Figure 4.42b that it is 2 orders of magnitude below the longitudinal displacement. This is not surprising considering the transverse pressure wave impacting the solid medium. Furthermore, conversely to U_x , the displacement U_y does not at first exhibit a pure sinusoidal shape. The behavior witnessed on the time interval $[0, 3.669 \text{ ms}]$ is here explained by the vertical component of the fluid pressure forces, which is much smaller than the horizontal component, and exhibits fluctuations, with possible change of signs. For $t \geq 3.669 \text{ ms}$, after the disks have reached their maximum transverse displacement, a sinusoidal shape free of fluctuations is recovered.

Remark 4.4.5 *Important note on the way the displacement of the fluid-structure interfaces $\partial\Omega_s$ is taken into account in the boundary integrals of the model equations*

As the homogenized fluid equations are discretized on a 2D regular Cartesian grid with mesh size $h = 1 \text{ mm}$, the boundary integrals present in the right-hand sides of the balance equations are updated when the solid medium displacement reaches integer multiples of h .

To complete the displacements observed in Figure 4.42, let us now turn towards the pressure fields reconstructed for the beginning and right/left maximum positions of the disks, hereafter displayed in Figures 4.43 and 4.44.

One can immediatly notice in Figure 4.43 that the horizontal pressure profile is almost constant (around 1.75 bar) when the disks reach their maximum displacement. This is also confirmed by the 2D pressure fields displayed in Figures 4.44b-4.44c. Thus, pressure forces applied to the solid medium are almost zero, and the restoring elastic force can now freely act on the solid medium. This is coherent with the fact that the solid medium has reached its maximum displacement and will now head backwards.

Besides, it can also be noticed in Figures 4.44b-4.44c that the artificial pressure within the solid medium remains constant around 1 bar throughout the simulation. This is coherent with the assumptions at the basis of the wavelet-based homogenized model (i.e. no matter is exchanged between the fluid and solid media).

In conclusion, these preliminary results, obtained via a coupling between a 2D homogenized compressible fluid and a rigid solid medium, are in good agreement with the theoretical behavior of a linear oscillator.

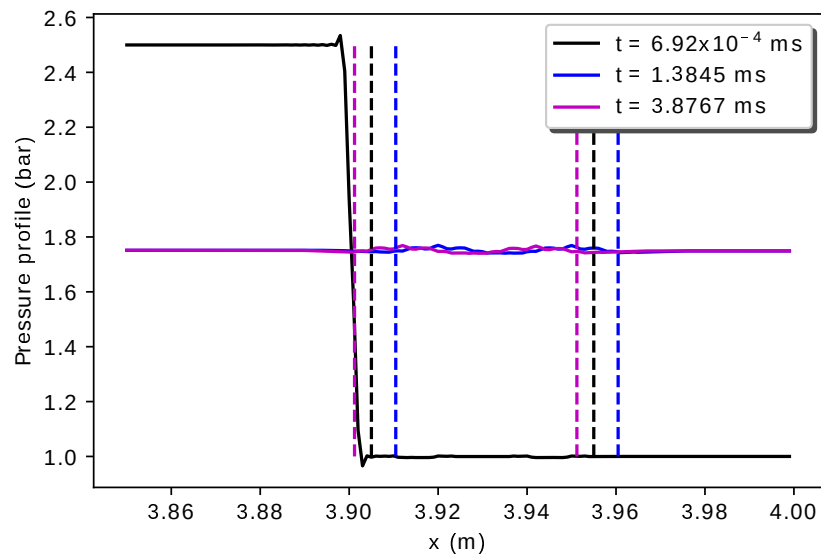


Figure 4.43: Horizontal pressure profiles for the initial and maximum positions of the disks - the vertical dashed lines indicate the position of the array.

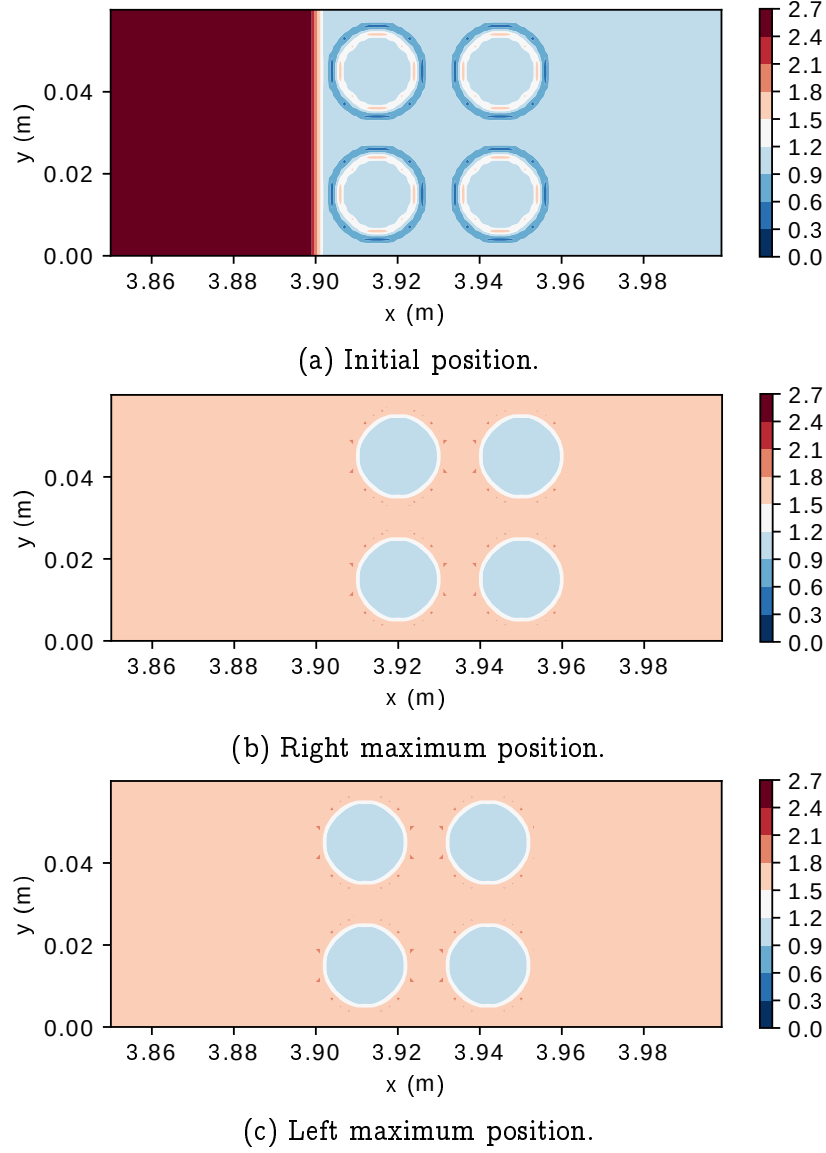


Figure 4.44: Initial and maximum positions of the 2×2 moving array of disks within the reconstructed pressure field (bar).

4.5 Conclusion

This fourth chapter, dedicated to the model implementation, allowed to assess its ability to accurately compute the physics of interest, i.e. a 2D transverse pressure wave propagating through a congested solid medium composed of multiple disks. A wavelet analysis of a reference numerical solution (10×10 steady array), computed at the DNS scale, was first presented. This first test gave insights on the pressure field spectrum, and underlined the need to replace the analysing wavelet Ψ by its associated scaling function Φ , in order to avoid multiple and cumbersome computations. A second test then confirmed the impact of both the C.F.L. and the scale/mesh compatibility conditions on the numerical model stability and accuracy. In echo with the first wavelet analysis, a 2D pressure wave propagating through a 10×10 steady array of disks was then considered. The wavelet-based model proved its ability to accurately reconstruct both the pressure field and the horizontal force applied to the solid medium. To then enhance the multi-scale component of the model, a comparison between several equivalent arrays of disks (2×2 , 4×4 , 10×10) proved that a more macroscopic modeling of the solid medium, and thus a larger mesh size h and cutoff scale s_0 , preserves the accuracy on the main quantity of interest, i.e. the dynamic load on the solid medium.

Finally, the last sections of this chapter gave some insights on two ongoing projects. The first one consists in implementing a nested grids algorithm within the numerical model. While it obviously did speed up the computations, it also exhibited an unexpected loss of accuracy. These troubling results thus require further investigations. The second project is dedicated to the design of a coupled fluid-structure solver. A collaborative test program between the French Energy Commission (CEA) and the Norwegian University of Science and Technology (NTNU) was first presented. This joint work allowed to submit a tube bundle specimen to multiple shock waves within a shock tube facility, while recording the solid medium longitudinal displacement via high-speed cameras. In addition to this preliminary experimental data, a first numerical test involving a 2×2 moving array of disks was also presented. A coupled fluid-structure simulation allowed to recover the theoretical behavior of a linear oscillator, with its classical sinusoidal displacement. These early results shall of course be completed with further testing.

Chapter 5

Conclusion

This work put forward a new contribution in the wide literature of porous media, homogenization and multi-scale methods. Guided by the need to compute transverse pressure waves within congested solid media, such as fuel assemblies within Pressurized Water Reactors (PWR), this manuscript thoroughly described a homogenized and multi-scale model able to discard all interfaces and small scale phenomena. In a will to build a self-sustained model, which can bypass the major limitations encountered in homogenization theory and multi-scale methods, this work promotes the use of Continuous Wavelet Transform (CWT). Starting with a 2D rigid and homogeneous solid medium, and an inviscid compressible fluid, it was thoroughly detailed how this wavelet formalism can be implemented on the fluid Partial Differential Equations (PDEs). The method was moreover designed to allow for an extension to generic PDEs. A two-steps process of "weak-extension" + "weak-convolution" of the original fluid PDEs with an analysing wavelet (or scaling function) was shown to result in spatially-filtered PDEs governing a homogenized fluid. The new conservative variables are moreover defined as the wavelet coefficients (or low-frequency approximation) of the original variables. In order to ensure the well-posedness of the convolution product, a real-valued, isotropic, smooth, well-localized and admissible wavelet has been chosen, namely the Mexican hat. More importantly, thanks to CWT and its reconstruction formula, the homogenized model possesses the brand new ability to connect resolved and unresolved scales without any *ad hoc* model, and to rigorously handle the original boundary conditions. It was also emphasized how the reconstruction formula can be used to explicitly compute, if necessary, nonlinear terms. To complete the wavelet-based model theoretical framework, a convergence towards Direct Numerical Simulation (DNS) was proved, along with necessary compatibility conditions between the scaling function cutoff scale s_0 and the mesh size h . To the author's knowledge, it is the first time that such a self-sustained homogenized and multi-scale model, tackling generic and non-smooth PDEs, closure between resolved and unresolved scales, boundary conditions, nonlinearities, periodicity and scale separation is put forward in literature.

In order to confront this theoretical framework with the physics of interest, several 2D numerical tests were considered, with steady micro-structures.

These tests first allowed to emphasize the impact of both the explicit scheme C.F.L. condition, and the scaling function cutoff scale, on the numerical model stability and accuracy. It was then proved, with different steady microstructures, that the wavelet-based model is able to accurately reconstruct both the pressure field, and the dynamic load applied to the solid medium. This accuracy is even preserved when a more macroscopic modeling is used to represent the solid medium. Then, in an ongoing work aiming at designing a coupled fluid-structure solver, preliminary experimental data, involving a tube bundle specimen submitted to shock waves, was presented. The longitudinal displacement observed during the experiments was then supplemented by a preliminary numerical test involving a 2×2 moving array of disks. This test, which did not aim at faithfully representing the 3D solid medium behavior observed in the shock tube facility, nevertheless allowed to recover the theoretical behavior of a linear oscillator. These early results will be completed with additional testing in order to build a robust 2D fluid-structure solver.

Finally, there obviously are improvements and challenging perspectives ahead of this work. Regarding the current vulnerabilities and possible improvements, the wavelet-based model is first confronted with risks of instability and aliasing. Besides, the use of a band-pass analysing wavelet, rather than a low-pass scaling function, was shown to significantly increase the computational cost of the method. Now, regarding the perspectives, one may think of a 3D extension of the wavelet-based homogenized model, using a 3D Continuous Wavelet Transform. Nevertheless, in a context where fuel assemblies are the solid medium of interest, such a 3D extension could rely on a "2D+1D" approach, where the homogenization process is only applied through the cross section, while classical discretization techniques are used to handle the vertical direction. If the cross section of the 3D fuel assemblies does not undergo any deformation, the assumptions made on the 2D solid medium could be easily transposed to the 3D case.

To now widen the perspectives of the current work, one could extend this wavelet-based multi-scale and homogenized model, here developed in the framework of Fluid-Structure Interaction (FSI), to other types of physics, such as heterogeneous materials and turbulence for instance. Indeed, in the spirit of the wide overview of the state of the art presented in this manuscript, this work put forward a homogenization process that can deal with generic PDEs, written at the continuum medium scale, and moreover independent from any spatial discretization technique.

Bibliography

- [Allaire, 1992] Allaire, G. (1992). Homogenization and two-scale convergence. *Journal on Mathematical Analysis*, 23(6):1482–1518.
- [Alpert et al., 2002] Alpert, B., Beylkin, G., Gines, D., and Vozovoi, L. (2002). Adaptive solution of partial differential equations in multiwavelet bases. *Journal of Computational Physics*, 182:149–190.
- [Antoine and Murenzi, 1996] Antoine, J.-P. and Murenzi, R. (1996). Two-dimensional directional wavelets and the scale-angle representation. *Signal processing*, 52:259–281.
- [Aune et al., 2016] Aune, V., Fagerholt, E., Langseth, M., and Børvik, T. (2016). A shock tube facility to generate blast loading on structures. *International Journal of Protective Structures*, 7(3):340–366.
- [Auscher, 1993] Auscher, P. (1993). Compactly supported wavelets and boundary conditions. *Journal of Functional Analysis*, 111:29–43.
- [Banerjee and Chan, 1980] Banerjee, S. and Chan, A. (1980). Separated flow models-1: Analysis of the averaged and local instantaneous formulations. *International Journal of Multiphase Flow*, 6:1–24.
- [Barsamian and Hassan, 1997] Barsamian, H. R. and Hassan, Y. A. (1997). Large eddy simulation of turbulent crossflow in tube bundles. *Nuclear Engineering and Design*, 172:103–122.
- [Bazilevs et al., 2007] Bazilevs, Y., Calo, V., Cottrell, J., Hughes, T., Reali, A., and Scovazzi, G. (2007). Variational multiscale residual-based turbulence modeling for large eddy simulation of incompressible flows. *Computer Methods in Applied Mechanics and Engineering*, 197:173–201.
- [Bensoussan et al., 1978] Bensoussan, A., Lions, J., and Papanicolaou, G. (1978). *Asymptotic Analysis for Periodic Structures*, volume 5. North-Holland.
- [Berger and Oliger, 1984] Berger, M. and Oliger, J. (1984). Adaptive mesh refinement for hyperbolic partial differential equations. *Journal of Computational Physics*, 53:484–512.

- [Berger and Collela, 1989] Berger, M. J. and Collela, P. (1989). Local adaptive mesh refinement for shock hydrodynamics. *Journal of Computational Physics*, 82:64–84.
- [Berselli et al., 2006] Berselli, L. C., Grisanti, C. R., and John, V. (2006). Analysis of commutation errors for functions with low regularity. *Journal of Computational and Applied Mathematics*, 206:1027–1045.
- [Beylkin, 1992] Beylkin, G. (1992). On the representation of operators in bases of compactly supported wavelets. *SIAM Journal on Numerical Analysis*, 29(6):1716–1740.
- [Beylkin et al., 1991] Beylkin, G., Coifman, R., and Rokhlin, V. (1991). Fast wavelet transforms and numerical algorithms I. *Communications on Pure and Applied Mathematics*, 44:141–183.
- [Bihari and Harten, 1995] Bihari, B. and Harten, A. (1995). Application of generalized wavelets: An adaptive multiresolution scheme. *Journal of Computational and Applied Mathematics*, 61:275–321.
- [Bihari and Harten, 1997] Bihari, B. and Harten, A. (1997). Multiresolution schemes for the numerical solution of 2-d conservation laws I. *Journal of Scientific Computing*, 2(18):315–354.
- [Bramkamp et al., 2004] Bramkamp, F., Lamby, P., and Müller, S. (2004). An adaptive multiscale finite volume solver for unsteady and steady state flow computations. *Journal of Computational Physics*, 197:460–490.
- [Brandt, 1977] Brandt, A. (1977). Multi-level adaptive solutions to boundary-value problems. *Mathematics of Computation*, 138:333–390.
- [Carmona et al., 1994] Carmona, R., Hwang, W., and Torr sani, B. (1994). *Identification of chirps with continuous wavelet transform*, volume 103 of *Wavelets and Statistics, Lecture Notes in Statistics*. A. Antoniadis, G. Oppenheim (Eds.), Springer.
- [Carmona et al., 1997] Carmona, R., Hwang, W., and Torr sani, B. (1997). Characterization of signals by the ridges of their wavelet transforms. In *IEEE Transactions on Signal Processing*, volume 45, pages 2586–2589.
- [Chiavassa and Liandrat, 1997] Chiavassa, G. and Liandrat, J. (1997). On the effective construction of compactly supported wavelets satisfying homogeneous boundary conditions on the interval. *Applied and computational harmonic analysis*, 4:62–73.
- [Cohen, 2000] Cohen, A. (2000). *Wavelet methods in numerical analysis*, volume 7 of *In Handbook of Numerical Analysis*. P.G. Ciarlet and J.L. Lions (Eds.), Elsevier: Amsterdam, The Netherlands.

- [Cohen et al., 1994] Cohen, A., Daubechies, I., and Vial, P. (1994). Wavelets on the interval and fast wavelet transforms. *Applied and Computational Harmonic Analysis*, 1:54–81.
- [Cohen et al., 2003] Cohen, A., Kaber, S., and Postel, M. (2003). Adaptive multiresolution for finite volume solutions of gas dynamics. *Computers and Fluids*, 32:31–38.
- [Dahmen, 1997] Dahmen, W. (1997). Wavelet and multiscale methods for operator equations. *Acta Numer.*, 6:55–228.
- [Dahmen et al., 2013] Dahmen, W., Gotzen, T., Melian, S., and Müller, S. (2013). Numerical simulation of cooling gas injection using adaptive multiresolution techniques. *Computers and Fluids*, 71:65–82.
- [Daubechies, 1988] Daubechies, I. (1988). Orthonormal bases of compactly supported wavelets. *Communications on Pure and Applied Mathematics*, 41:909–996.
- [De Giorgi and Spagnolo, 1973] De Giorgi, E. and Spagnolo, S. (1973). Sulla convergenza degli integrali dell’energia per operatori ellittici del secondo ordine. *Boll. Un. Mat. Ital.*, 4(8):391–411.
- [Delhay et al., 1993] Delhay, J. M., Giot, M., and Riethmuller, M. L. (1993). *Thermohydraulics of two-phase systems for industrial design and nuclear engineering*. A von Karman Institute Book. Hemisphere Publishing Corporation, McGraw-Hill Book Company, New York, Chapters 5 and 7.
- [Delprat et al., 1992] Delprat, N., Escudie, B., Guillemain, P., Ronland-Martinet, R., Tchamichian, P., and Torrèsani, B. (1992). Asymptotic wavelet and gabor analysis: extraction of instantaneous frequencies. In *IEEE Transactions on Information Theory*, volume 38, page 644–664.
- [Dunca et al., 2003] Dunca, A., John, V., and Layton, W. J. (2003). The commutation errors of the space averaged navier-stokes equations on a bounded domain. *Journal of Mathematical Fluids Mechanics*, 20:1–27.
- [Eshelby, 1959] Eshelby, J. (1959). The elastic field outside an ellipsoidal inclusion. In *Proceedings of the Royal Society of London*, volume 252 of *Series A, Mathematical and Physical Sciences*, pages 561–569.
- [Etienne et al., 2009] Etienne, S., Garon, A., and Pelletier, D. (2009). Perspective on the geometric conservation law and finite element methods for ale simulations of incompressible flow. *Journal of Computational Physics*, 228:2313–2333.
- [Etienne and Pelletier, 2012] Etienne, S. and Pelletier, D. (2012). The low reynolds number limit of vortex-induced vibrations. *Journal of Fluids and Structures*, 31:18–29.

- [Faucher et al., 2014] Faucher, V., Crouzet, F., and Debaud, F. (2014). Mechanical consequences of loca in pwr: Full scale coupled 1d/3d simulations with fluid-structure interaction. *Nuclear Engineering and Design*, 270:359–378.
- [Faucher and Kokh, 2013] Faucher, V. and Kokh, S. (2013). Extended vofire algorithm for fast transient fluid–structure dynamics with liquid–gas flows and interfaces. *Journal of Fluids and Structures*, 39:102–125.
- [Flandrin, 1989] Flandrin, P. (1989). Some aspects of non-stationary signal processing with emphasis on time-frequency and time-scale methods. Technical report, ICPI TS-8802. also, in Wavelets, J. M. Combes, A. Grossmann, and P. Tchamitchian (Eds.), Berlin: Springer-Verlag, pp: 68-98.
- [Flandrin, 1999] Flandrin, P. (1999). *Time-Frequency/Time-Scale Analysis*, volume 10 of *Wavelet Analysis and its Applications*. Academic Press, San Diego (CA).
- [Flandrin, 2005] Flandrin, P. (2005). *Temps-Fréquence — Concepts et Outils*, chapter Temps-Fréquence Energétique — Quelques Introductions, pages 23–41. *Traité IC2 "Information, Communications, Contrôle"*. F. Auger et F. Hlawatsch, eds., Hermes.
- [Flandrin, 2018] Flandrin, P. (2018). *Explorations in Time-Frequency Analysis*. Cambridge University Press, Cambridge (UK).
- [Fontaine and Politopoulos, 2000] Fontaine, B. and Politopoulos, I. (2000). A non linear model for the pwr fuel assembly seismic analysis. *Nuclear Engineering and Design*, 195:321–329.
- [Frohlich and Schneider, 1997] Frohlich, J. and Schneider, K. (1997). An adaptive wavelet-vaguelette algorithm for the solution of pdes. *Journal of Computational Physics*, 130:174–190.
- [Fureby and Tabor, 1997] Fureby, C. and Tabor, G. (1997). Mathematical and physical constraints on large-eddy simulations. *Theoretical and Computational Fluid Dynamics*, 9:85–102.
- [Ghosal and Moin, 1995] Ghosal, S. and Moin, P. (1995). The basic equations for the large eddy simulation of turbulent flows in complex geometry. *Journal of Computational Physics*, 118:24–37.
- [Godlewski and Raviart, 1996] Godlewski, E. and Raviart, P.-A. (1996). *Numerical approximation of hyperbolic systems of conservation laws*. Applied Mathematical Sciences. Springer: Berlin/Heidelberg, Germany.
- [Gonnet and Torrèsani, 1994] Gonnet, C. and Torrèsani, B. (1994). Local frequency analysis with two-dimensional wavelet transform. *Signal Processing*, 37:389–404.

- [Grossmann and Morlet, 1984] Grossmann, A. and Morlet, J. (1984). Decomposition of hardy functions into square integrable wavelets of constant shape. *SIAM Journal on Mathematical Analysis*, 15:723–736.
- [Grossmann et al., 1985] Grossmann, A., Morlet, J., and Paul, T. (1985). Transforms associated to square integrable group representations i. general results. *Journal of Mathematical Physics*, 26:2473–2479.
- [Haar, 1910] Haar, A. (1910). Zur theorie der orthogonalen funktionensysteme. *Mathematische Annalen*, 69:331–371.
- [Hackbusch, 1985] Hackbusch, W. (1985). *Multi-Grid Methods and Applications*. Springer, Berlin.
- [Harten, 1994] Harten, A. (1994). Adaptive multiresolution schemes for shock computations. *Journal of Computational Physics*, 115:319–338.
- [Hashin and Shtrikman, 1963] Hashin, Z. and Shtrikman, S. (1963). A variational approach to the theory of the elastic behaviour of multiphase materials. *Journal of the Mechanics and Physics of Solids*, 11:127–140.
- [Hill, 1963] Hill, R. (1963). Elastic properties of reinforced solids: some theoretical principles. *Journal of the Mechanics and Physics of Solids*, 11:357–372.
- [Hughes et al., 1998] Hughes, T., Feijoo, G. R., Mazzei, L., and Quincy, J.-B. (1998). The variational multiscale method - a paradigm for computational mechanics. *Computer Methods in Applied Mechanics and Engineering*, 166:3–24.
- [Hughes et al., 2000] Hughes, T., Mazzei, L., and Jansen, K. E. (2000). Large eddy simulation and the variational multiscale method. *Computing and Visualization in Science*, 3(47).
- [Hughes et al., 2001] Hughes, T., Mazzei, L., and Oberai, A. A. (2001). The multiscale formulation of large eddy simulation: Decay of homogeneous isotropic turbulence. *Physics of Fluids*, 13(2).
- [Jaffard, 1991] Jaffard, S. (1991). *Wavelets and analysis of partial differential equations*. In Probabilistic and Stochastic Methods in Analysis, with Applications. NATO ASI Series; Springer: Berlin/Heidelberg, Germany.
- [Jawerth and Sweldens, 1994] Jawerth, B. and Sweldens, W. (1994). An overview of wavelet based multiresolution analyses. *SIAM Review*, 36(3):377–412.
- [Koobus and Farhat, 2004] Koobus, B. and Farhat, C. (2004). A variational multiscale method for the large eddy simulation of compressible turbulent flows on unstructured meshes - application to vortex shedding. *Computer Methods in Applied Mechanics and Engineering*, 193:1367–1383.

- [Ladevèze, 2004] Ladevèze, P. (2004). Multiscale modelling and computational strategies for composites. *International Journal for Numerical Methods in Engineering*, 60:233–253.
- [Ladevèze et al., 2001] Ladevèze, P., Loiseau, O., and Dureisseix, D. (2001). A micro-macro and parallel computational strategy for highly heterogeneous structures. *International Journal for Numerical Methods in Engineering*, 52:121–138.
- [Ladevèze and Nouy, 2003] Ladevèze, P. and Nouy, A. (2003). On a multiscale computational strategy with time and space homogenization for structural mechanics. *Computer Methods in Applied Mechanics and Engineering*, 192:3061–3087.
- [Lazaar et al., 1994] Lazaar, S., Ponenti, P., Liandrat, J., and Tchamitchian, P. (1994). Wavelet algorithms for numerical resolution of partial differential equations. *Computer Methods in Applied Mechanics and Engineering*, 116:309–314.
- [Le and Argoul, 2004] Le, T.-P. and Argoul, P. (2004). Continuous wavelet transform for modal identification using free decay response. *Journal of Sound and Vibration*, 277:73–100.
- [Lemarié and Meyer, 1986] Lemarié, P.-G. and Meyer, Y. (1986). Ondelettes et bases hilbertiennes. *Revista Matematica Iberoamericana*, 2:1–18.
- [Leonard et al., 2007] Leonard, S., Terracol, M., and Sagaut, P. (2007). Com-mutation error in large eddy simulation with time-dependent filter width. *Computers and Fluids*, 36:513–519.
- [Lesieur, 2008] Lesieur, M. (2008). *Turbulence in fluids*. Fluid Mechanics and Its Applications. Springer: Berlin/Heidelberg, Germany.
- [Liandrat et al., 1992] Liandrat, J., Perrier, V., and Tchamitchian, P. (1992). *Numerical resolution of non linear partial differential equations using the wavelet approach*. Wavelets and their applications. Jones and Barlett (Eds.).
- [Lighthill, 1960] Lighthill, M. J. (1960). Note on the swimming and slender fish. *Journal of Fluid Mechanics*, 9:305–317.
- [Lighthill, 1986] Lighthill, M. J. (1986). Fundamentals concerning wave loading on offshore structures. *Journal of Fluid Mechanics*, 173:667–681.
- [Lilly and Olhede, 2009] Lilly, J. and Olhede, S. (2009). Higher-order prop-erties of analytic wavelets. In *IEEE Transactions on Signal Processing*, volume 57.
- [Mallat, 1989a] Mallat, S. (1989a). Multifrequency channel decompositions of images and wavelet models. In *IEEE Transactions on Acoustic, Speech, and Signal Processing*, volume 37, pages 2091–2110.

- [Mallat, 1989b] Mallat, S. (1989b). Multiresolution approximations and wavelet orthonormal bases of $l^2(\mathbb{R})$. In *Transactions of the American Mathematical Society*, volume 315, pages 69–87.
- [Mallat, 1989c] Mallat, S. (1989c). A theory for multiresolution signal decomposition: The wavelet representation. In *IEEE Transactions on Pattern Analysis and Machine Intelligence*, volume 11, pages 674–693.
- [Mallat, 2008] Mallat, S. G. (2008). *A Wavelet Tour of Signal Processing*. Academic Press: Cambridge, MA, USA.
- [Martin and Flandrin, 1985] Martin, W. and Flandrin, P. (1985). Detection of changes of signal structure by using the wigner-ville spectrum. *Signal Processing*, 8:215–233.
- [Mehraeen and Chen, 2006] Mehraeen, S. and Chen, J.-S. (2006). Wavelet galerkin method in multi-scale homogenization of heterogeneous media. *International Journal for Numerical Methods in Engineering*, 66:381–403.
- [Meyer, 1990] Meyer, Y. (1990). *Ondelettes et opérateurs, I: Ondelettes, II: Opérateurs de Calderon-Zygmund, III: (with R. Coifman), Opérateurs multilinéaires*,. Hermann, Paris. English translation of first volume published by Cambridge University Press.
- [Meyer, 1992] Meyer, Y. (1992). Ondelettes sur l'intervalle. *Revista Mathematica Iberoamericana*, 7:115–133.
- [Miehe, 2002] Miehe, C. (2002). Strain-driven homogenization of inelastic microstructures and composites based on an incremental variational formulation. *International Journal for Numerical Methods in Engineering*, 55:1285–1322.
- [Mokhtari et al., 2020] Mokhtari, S., Ricciardi, G., Faucher, V., Argoul, P., and Adélaïde, L. (2020). Multiscale filtering of compressible wave propagation in complex geometry through a wavelet-based approach in the framework of pressurized water reactors depressurization transient analysis. *Fluids*, 5(64).
- [Monasse and Perrier, 1995] Monasse, P. and Perrier, V. (1995). Wavelet bases on the interval adapted for boundary conditions. In *Comptes rendus de l'Académie des sciences*, volume 321 of *Série I. Mathématique*, pages 1163–1169.
- [Murat and Tartar, 1997] Murat, F. and Tartar, L. (1997). *Topics in the mathematical modeling of composite materials*, chapter H-Convergence. Progress in Nonlinear Differential Equations and their Applications. A. Cherkaev and R.V. Kohn (Eds.).
- [Müller, 2003] Müller, S. (2003). *Adaptive multiscale schemes for conservation laws*, volume 27 of *Lecture Notes in Computational Science and Engineering*. Springer, Heidelberg.

- [Nemat-Nasser and Hori, 1993] Nemat-Nasser, S. and Hori, M. (1993). *Micromechanics : overall properties of heterogeneous materials*. North Holland.
- [Païdoussis, 1966] Païdoussis, M. P. (1966). Dynamics of flexible slender cylinders in axial flow part 1 theory. *Journal of Fluids Mechanics*, 26:717–736.
- [Païdoussis, 1969] Païdoussis, M. P. (1969). An experimental study of vibration of flexible cylinders induced by nominally axial flow part 1 theory. *Nuclear Science and Engineering*, 35:127–138.
- [Païdoussis, 2006] Païdoussis, M. P. (2006). Real-life experiences with flow induced vibration. *Journal of Fluids and Structures*, 22:741–755.
- [Piquemal and Liandrat, 2005] Piquemal, A. S. and Liandrat, J. (2005). A new wavelet preconditioner for finite difference operators. *Advances in computational Mathematics*, 22:125–163.
- [Pisapia et al., 2003] Pisapia, S., Collard, B., Bellizzi, S., and Mori, V. (2003). Modal testing and identification of a pwr fuel assembly. In *Transactions of the 17th International Conference on Structural Mechanics in Reactor Technology (SMIRT 17)*, Prague, Czech Republic.
- [Ponte Castañeda, 1991] Ponte Castañeda, P. (1991). The effective mechanical properties of nonlinear isotropic composites. *Journal of the Mechanics and Physics of Solids*, 39:45–71.
- [Ponte Castañeda and Suquet, 1998] Ponte Castañeda, P. and Suquet, P. (1998). Nonlinear composites. *Advances in Applied Mechanics*, 34:171–302.
- [Ricciardi, 2016] Ricciardi, G. (2016). Fluid-structure interaction modelling of a pwr fuel assembly subjected to axial flow. *Journal of Fluids and Structures*, 62:156–171.
- [Ricciardi et al., 2009] Ricciardi, G., Bellizzi, S., Collard, B., and Cochelin, B. (2009). Row of fuel assemblies analysis under seismic loading: Modelling and experimental validation. *Nuclear Engineering and Design*, 239:2692–2704.
- [Ricciardi and Boccaccio, 2015] Ricciardi, G. and Boccaccio, E. (2015). Modelling of the flow induced stiffness of a pwr fuel assembly. *Nuclear Engineering and Design*, 282:8–14.
- [Robbe and Bliard, 2002] Robbe, M.-F. and Bliard, F. (2002). A porosity method to describe the influence of internal structures on a fluid flow in case of fast dynamics problems. *Nuclear Engineering and Design*, 215:217–242.
- [Roussel and Schneider, 2005] Roussel, O. and Schneider, K. (2005). An adaptive multiresolution method for combustion problem: Applications to flame ball-vortex interaction. *Computers and Fluids*, 34:817–831.

- [Roussel et al., 2003] Roussel, O., Schneider, K., Tsigulin, A., and Bockhorn, H. (2003). A conservative fully adaptive multiresolution algorithm for parabolic pdes. *Journal of Computational Physics*, 188:493–523.
- [Ruge and Stüben, 1987] Ruge, J. and Stüben, K. (1987). *Algebraic Multigrid (AMG)*, volume 5 of *Multigrid Methods, Frontiers in Applied Mathematics*. S.F. Mc.Cormick (Ed.), SIAM, Philadelphia, PA.
- [Sanchez-Palencia, 1980] Sanchez-Palencia, E. (1980). *Non-Homogeneous Media and Vibration Theory*, volume 127 of *Lecture Notes in Physics*. Springer.
- [Schneider et al., 2001] Schneider, K., Farge, M., Koster, F., and Griebel, M. (2001). *Adaptive wavelet methods for the Navier-Stokes Equations*, volume 75 of *In Notes on Numerical Fluid Mechanics*. Springer: Berlin/Heidelberg, Germany.
- [Smagorinsky, 1963] Smagorinsky, J. (1963). General circulation experiments with the primitive equations. *Monthly Weather Review*, 91:216–241.
- [Strömberg, 1981] Strömberg, J. O. (1981). A modified franklin system and higher order spline systems on \mathbb{R}^n as unconditional bases for hardy spaces. In B. et al., e., editor, *Conference on Harmonic Analysis in Honor of Antoni Zygmund*, volume 2, pages 475–494. Univ. of Chicago Press.
- [Stüben and Trottenberg, 1982] Stüben, K. and Trottenberg, U. (1982). *Multigrid methods: fundamental algorithms, model problem analysis and applications*, volume 960 of *Multigrid Methods, Lecture Notes in Mathematics*. W. Hackbusch, U. Trottenberg (Eds.), Springer, Berlin.
- [Tanaka and Mori, 1972] Tanaka, K. and Mori, T. (1972). Note on volume integrals of the elastic field around an ellipsoidal inclusion. *Journal of Elasticity*, 2(3):199–200.
- [Tartar, 1979] Tartar, L. (1979). Compensated compactness and partial differential equations. In *Nonlinear Analysis and Mechanics: Heriot-Watt Symposium*, volume 4, pages 136–212.
- [Taylor, 1952] Taylor, G. (1952). Analysis of the swimming of long and narrow animals. In *Proceeding of the Royal Society London A214*, pages 158–184.
- [Tchamitchian, 1996] Tchamitchian, P. (1996). Inversion de certains opérateurs elliptiques à coefficients variables. *SIAM Journal on Mathematical Analysis*, 27(6):1680–1703.
- [Terada et al., 1998] Terada, K., Ito, T., and Kikuchi, N. (1998). Characterization of the mechanical behaviors of solid-fluid mixture by the homogenization method. *Computer Methods in Applied Mechanics and Engineering*, 153:223–257.

- [Tognevi et al., 2016] Tognevi, A., Guerich, M., and Yvonnet, J. (2016). A multi-scale modeling method for heterogeneous structures without scale separation using a filter-based homogenization scheme. *International Journal for Numerical Methods in Engineering*, 108:3–25.
- [Torrésani, 1992] Torrèsani, B. (1992). Some time-frequency aspects of continuous wavelet decompositions. In *International conference Wavelets and applications*, Toulouse, France.
- [Torrésani, 1995] Torrèsani, B. (1995). *Analyse continue par ondelettes*. Savoirs actuels/Série Physique. CNRS Editions/EDP Sciences.
- [Torrésani, 1998] Torrèsani, B. (1998). An overview of wavelet analysis and time-frequency analysis (a minicourse). In *International Workshop on Self-Similar Systems*, pages 9–34. V.B. Priezzhev and V.P. Spiridonov, Dubna, Russia.
- [Trottenberg et al., 2001] Trottenberg, U., Oosterlee, C. W., and Schüller, A. (2001). *Multigrid*. Academic Press Inc., San Diego, CA. With contributions by A. Brandt, P. Oswald and K. Stüben.
- [Vasilyev et al., 1998] Vasilyev, O., Lund, T., and Moin, P. (1998). A general class of commutative filters for LES in complex geometries. *Journal of Computational Physics*, 146:82–104.
- [Wesseling, 1992] Wesseling, P. (1992). *An Introduction to Multigrid Methods*. Pure and applied mathematics. Chichester, Wiley.
- [Wesseling and Oosterlee, 2001] Wesseling, P. and Oosterlee, C. (2001). Geometric multigrid with applications to computational fluid dynamics. *Journal of Computational and Applied Mathematics*, 128:311–334.
- [Willis, 1981] Willis, J. (1981). Variational and related methods for the overall properties of composites. *Advances in Applied Mechanics*, 21:1–78.
- [Yu et al., 2016] Yu, K.-R., Etienne, S., Scolan, Y.-M., Hay, A., Fontaine, E., and Pelletier, D. (2016). Flow-induced vibrations of in-line cylinder arrangements at low reynolds numbers. *Journal of Fluids and Structures*, 60:37–61.
- [Yu et al., 2018] Yu, K.-R., Hay, A., Pelletier, D., and Etienne, S. (2018). Two degrees of freedom vortex-induced vibration responses with zero mass and damping at low reynolds number. *Journal of Fluids and Structures*, 83:218–237.
- [Yvonnet and Bonnet, 2014] Yvonnet, J. and Bonnet, G. (2014). A consistent nonlocal scheme based on filters for the homogenization of heterogeneous linear materials with non-separated scales. *International Journal of Solids and Structures*, 51:196–209.

Appendices

Appendix A

Convolution product

Proposition A.0.1 *Convolution product $L^1(\mathbb{R}^d) * D(\mathbb{R}^d)$*

The convolution product between a function $f \in L^1(\mathbb{R}^d)$ and a test function $\varphi \in D(\mathbb{R}^d)$ results in a C^∞ function.

Proof of Proposition A.0.1 *Let us first start with the definition of convolution product. For a priori almost all $\underline{x} \in \mathbb{R}^d$:*

$$(f * \varphi)(\underline{x}) := \int_{\mathbb{R}^d} f(\underline{x} - \underline{y}) \varphi(\underline{y}) d\underline{y}, \quad (\text{A.1})$$

$$= \int_{\mathbb{R}^d} \tilde{f}(\underline{y} - \underline{x}) \varphi(\underline{y}) d\underline{y}, \quad (\text{A.2})$$

$$= \int_{\mathbb{R}^d} \tau_{\underline{x}}(\tilde{f})(\underline{y}) \varphi(\underline{y}) d\underline{y}, \quad (\text{A.3})$$

$$= \langle \varphi, \tau_{\underline{x}}(\tilde{f}) \rangle, \quad (\text{A.4})$$

where $\tilde{f}(\underline{x}) = f(-\underline{x})$, and $\tau_{\underline{x}}(\tilde{f})(\cdot) = \tilde{f}(\cdot - \underline{x})$ denotes a translation of f .

One can first notice that, for all $f \in L^1(\mathbb{R}^d)$, the function:

$$\tau_{\tilde{f}} : \begin{array}{ccc} (\mathbb{R}^d, \|\cdot\|_{\mathbb{R}^d}) & \longmapsto & (L^1, \|\cdot\|_{L^1}) \\ \underline{x} & \longmapsto & \tau_{\underline{x}}(\tilde{f}) \end{array}, \quad (\text{A.5})$$

is continuous. This point is proven by using the density of continuous and compactly-supported functions in the Lebesgue space L^p , for $1 \leq p < +\infty$. Furthermore, the linear form:

$$l_\varphi : \begin{array}{ccc} L^1(\mathbb{R}^d) & \longmapsto & \mathbb{R}^d \\ f & \longmapsto & \langle \varphi, f \rangle \end{array} \quad (\text{A.6})$$

is also continuous. Indeed, since $\varphi \in D(\mathbb{R}^d) \subset L^\infty(\mathbb{R}^d)$, Hölder inequality implies that $f \times \varphi \in L^1(\mathbb{R}^d)$, and:

$$|l_\varphi(f)| := \left| \int_{\mathbb{R}^d} f \varphi \right| \quad (\text{A.7})$$

$$\leq \int_{\mathbb{R}^d} |f| \times |\varphi|, \quad (\text{A.8})$$

$$\leq \|\varphi\|_{L^\infty} \|f\|_{L^1}. \quad (\text{A.9})$$

Finally, one can state that for all $f \in L^1(\mathbb{R}^d)$ and $\varphi \in D(\mathbb{R}^d)$, the function:

$$\begin{aligned} \mathbb{R}^d &\longmapsto \mathbb{R}^d \\ \underline{x} &\longmapsto (f * \varphi)(\underline{x}) = (l_\varphi \circ \tau_{\tilde{f}})(\underline{x}) \end{aligned} \quad (\text{A.10})$$

is continuous. The C^∞ smoothness is then obtained thanks to the theorem allowing to differentiate parameter-dependent integrals, with the differentiation being applied on the test function φ .

Proposition A.0.2 *Convolution product $D'(\mathbb{R}^d) * D(\mathbb{R}^d)$*

The convolution product between a distribution $T \in D'(\mathbb{R}^d)$ and a test function $\varphi \in D(\mathbb{R}^d)$ also results in a C^∞ function. Furthermore, the following equation holds:

$$\forall T \in D'(\mathbb{R}^d), \psi, \varphi \in D(\mathbb{R}^d):$$

$$\langle \psi * T, \varphi \rangle_{D', D} := \int_{\mathbb{R}^d} (\psi * T) \varphi, \quad (\text{A.11})$$

$$= \langle T, \tilde{\psi} * \varphi \rangle_{D', D}. \quad (\text{A.12})$$

In the case where the distribution T is a locally integrable function, the previous result can be obtained with Fubini's theorem:

$$\langle \psi * T, \varphi \rangle_{D', D} = \int_{\mathbb{R}^d} \left(\int_{\mathbb{R}^d} \psi(\underline{x} - \underline{y}) T(\underline{y}) d\underline{y} \right) \varphi(\underline{x}) d\underline{x} \quad (\text{A.13})$$

$$= \int_{\mathbb{R}^d} T(\underline{y}) \left(\int_{\mathbb{R}^d} \tilde{\psi}(\underline{y} - \underline{x}) \varphi(\underline{x}) d\underline{x} \right) d\underline{y} \quad (\text{A.14})$$

$$= \langle T, \tilde{\psi} * \varphi \rangle_{D', D} \quad (\text{A.15})$$

Proof of Proposition A.0.2 With some minor change in the proof A.0.1, one can extend the previous proposition to the convolution product $L^1_{loc}(\mathbb{R}^d) * D(\mathbb{R}^d)$, and then use the fact that $L^1_{loc}(\mathbb{R}^d) \subset D'(\mathbb{R}^d)$.